Université de Strasbourg

UNIVERSITÉ DE STRASBOURG

EDSC École Doctorale des Sciences Chimiques

ÉCOLE DOCTORALE DES SCIENCES CHIMIQUES

Institut de Chimie de Strasbourg, UMR 7177

THÈSE

présentée par :

Jing ZHANG

soutenue le : **16th December 2021**

pour obtenir le grade de : **Docteur de l'Université de Strasbourg**

Discipline/ Spécialité : **Chimie**

Chiral Organometallic Concave Compounds: Luminescence and Supramolecular Properties

THÈSE dirigée par :

M. CHAMBRON Jean-Claude	Directeur de Recherche CNRS, Université de Strasbourg

RAPPORTEURS :

M. BROTIN Thierry	Directeur de Recherche CNRS, Ecole Normale Supérieure de Lyon
Mme GOSSE Isabelle	Professeur, Université de Bordeaux

AUTRES MEMBRES DU JURY :

Mme DESAGE-EL MURR Marine	Professeur, Université de Strasbourg

Acknowledgments

I would like to express my gratitude to all those who helped me during my thesis work and the writing up of this manuscript.

First, I would like to thank “Scientific Advisory Board of the FRC Foundation and the CSC Graduate School”, for financial support of my thesis.

My deepest gratitude goes first and foremost to Dr Jean-Claude Chambron, my supervisor who has offered me valuable suggestions in the academic studies, for his constant encouragement and guidance. He has walked me through all the stages of the writing of this thesis. Without his consistent and illuminating instruction, this thesis could not have reached its present form.

I want to thank Dr. BROTIN Thierry, Prof. GOSSE Isabelle, Prof. DESAGE-EL MURR Marine for accepting to be my thesis referees and examiners and for the time they spent on promoting my work.

My thesis work was also the subject of fruitful collaborations with Dr. Emmanuelle LEIZE-WAGNER and Nathalie ZORN (CMC/Université de Strasbourg) for the mass spectrometry studies, and Dr. Nicolas VANTHUYNE and Marion JEAN for the chiral HPLC and chiroptical measurements, whom I warmly thank for their invaluable contribution. I would like to thank also the persons who brought their expertise in various techniques: The personel of the Fédération de Recherche Chimie, Dr. Bruno VINCENT, Maurice COPPE, and Dr. Lionel ALLOUCHE (NMR facility), Dr. Martine HEINRICH (luminescence spectroscopy), and Noémie SCHNEIDER (elemental analyses). I am also grateful to Thomas WEISSENBERGER (Faculté de Chimie) for the use of a spectrofluorimeter and an IR spectrophotometer, Dr. Mélanie LE GROS (Institut Charles Sadron) for her help with DLS experiments, and of Dr. Eloïse DEVAUX (ISIS) for her help with the acquisition of STEM images.

I would like to express my heartful gratitude to the professors for their direct and indirect help in the laboratory of Chimie des Ligands à Architecture Contrôlée (CLAC): Jean WEISS, Romain RUPPERT, Jennifer WYTKO, Christophe JEANDON. In

addition, all the PhD students, Raphaël LAMARE, Maxime VONESCH, Jordan APPLETON, Jean JOSEPH, Vincent SILBER who have given me a lot of favors in the past three years.

“Thank you” to my good friends, Yang LI, Li RAN, Haijun PENG, Fule WU and Yongxiang ZHENG for their unconditional support, caring and encouragment. Thank you for always being by my side when I need you.

I should finally like to express my gratitude to my beloved parents and brother who have always been helping me out of difficulties and supporting without a word of complaint all through these years.

Table of Contents

List of Abbreviations and Symbols: 1

General Introduction 3

1. Cyclotribenzylenes: General Features 5

1.1 Structures and Chirality 5

1.2 Synthesis of Cyclotribenzylenes 7

1.2.1 The Trimerization Route A 7

1.2.2 The Trimerization Route B 8

1.2.3 Condensation of Suitable Diphenylmethanes with Benzene Derivatives 9

1.2.4 Chemical Transformation of the Peripheral Substituents 9

1.3 Cyclotribenzylene Complexes 10

1.3.1 Encapsulation of Fullerenes 10

1.3.2 Encapsulation of Biological Ammoniums 11

1.3.3 Encapsulation of Metal Cations 12

2. Cryptophanes: General Features 13

2.1 Structures and Chirality 13

2.2 Synthesis of Cryptophanes 14

2.2.1 The “Template” Method 14

2.2.2 The Direct Method or Two-Step Method 14

2.2.3 The Tripod-Tripod Coupling Method 15

2.2.4 Transformation and Functionalization of Cryptophanes: Water-Soluble Cryptophanes and Monofunctionalized Cryptophanes 16

2.3 Conformers of Cryptophanes 17

2.4 Binding Properties of Organic Cryptophanes 18

2.4.1 Complexation of Small Neutral Molecules 19

2.4.2 Complexation of Ammonium Guests 20

2.4.3 Complexation of Metal Cations 21

2.4.4 Complexation of Anion Guests 22

2.4.5 Chiral Discrimination of Cryptophanes 23

2.4.6 Complexation of Xenon 24

3. Metallo-Organic Cryptophanes 25

3.1 Cis-Linked M_3L_2 Cages 25

3.2 Trans-Linked M_3L_2 Cages 26

3.3 Complexation of Neutral Guests 28

3.4 3-D Triply Interlocked [2]Catenane from Metallo-Cryptophanes 29

3.5 Emissive Ir^{III} Metallo-Cryptophanes 30

4. Objectives 33

Part I: Gold Alkynyl-Substituted CTBs as Potential Precursors of Organometallic Cryptophanes Based on Aurophilic Interactions 35

1. Introduction and Objectives of Part I 37

1.1 Intramolecular Aurophilic Interactions 37

1.2 Intermolecular Aurophilic Interactions 40

1.3 The Luminescent Properties of Gold Phosphine Alkynyl Complexes 41

1.4 The Applications of Gold(I) Alkynyl Complexes 43

1.5 Objectives 45

2. Synthesis, Characterization, Purification and Resolution of the Precursors CTB(H,C_2H) and CTB(OMe,C_2H), and of the Gold Alkynyl CTBs C1 – C9 47

3. Investigations on the Nuclearity of the Gold CTBs in Solution and Gas Phase 56

3.1 Investigations on the Nuclearity of the Gold CTBs in Solution by NMR Spectroscopy 56

3.2 Investigations on the Nuclearity of the Gold CTBs in Solution and Gas Phase by Mass Spectrometry 60

3.3 Reactivity of the Gold CTBs in the Gas Phase: Lessons form Scrambling Experiments 64

4. Evaluation of the CTBs as Hosts for NEt_4I Using ^{1}H NMR Titration and DOSY 68

5. Basic Photochemistry and Photophysics of the Gold CTBs 71

5.1 Electronic Absorption Spectroscopy 71

5.2 Electronic Emission Spectroscopy 76

6. Solvent-induced Supramolecular Assembly 85

6.1 Electronic Spectroscopy (Absorption, Emission and ECD) Studies in Solvent Mixtures 85

6.2 Dynamic Light Scattering (DLS) and Scanning Tunneling Electron Microscopy (STEM) 102

6.3 Discussion 105

7. Conclusion 109

Part II: Towards Organometallic/Coordination Hybrid Cryptophanes 111

1. Introduction and Objectives of Part II 113

2. Synthesis, Characterization and Resolution of an Asymmetric CTB Alkynyl Ligand Precursor 121

3. Preparation of the Precryptophanes Based on [(-C_2)$_2$Pt(PEt_3)$_2$] (12) and [(-C_2)$_2$Pt(dppp)] (13) Hinges. First Attempts of Cryptophane Formation 127

4. Synthesis and Characterization of Cu-Free Precryptophanes 143

5. Analytical Chiral HPLC Separation of Compound 18 152

6. Cryptophane Formation Starting from Cu-Free Precryptophanes 156

6.1 Photophysical Properties of **18** and **20** in $CHCl_3$, CH_2Cl_2 and $C_2H_2Cl_4$ 156

6.2 Photophysical Properties of **18** Coordinated with Pt(dppp)$(OTf)_2$ 157

7. Conclusion 159

Experimental Part 161

General Conclusion 235

Appendix 241

References 245

List of Abbreviations and Symbols:

@: represents the inclusion of the guest in the host

α: optical rotation angle

δ: chemical shift

ε: molar extinction coefficient

λ: wavelength

CTB: cyclotribenzylene

CH_2Cl_2: dichloromethane

$CHCl_3$: chloroform

CyH: cyclohexane

d: doublet

DMF: *N*, *N*-dimethylformamide

DLS: dynamic light scattering

DOSY: diffusion ordered spectroscopy

dppp: 1,3-Bis(diphenylphosphino)propane

ee: enantiometric excess

equiv: equivalents

EtOAc: ethyl acetate

Et_3N: triethylamine

$Et_4N^+I^-$: tetraethylammonium iodide

ECD: electronic circular dichroism

Et_2O: diethyl ether

HPLC: High performance liquid chromatography

IR: infrared

J: coupling constant

K: association constant

m: multiplet

mp: melting point

Me: methyl

MeOH: methanol

NMR: nuclear magnetic resonance

ppm: part per million

PEt_3: triethylphosphine

rac: racemic

STEM: scanning transmission electron microscopy

TLC: thin layer chromatography

THF: tetrahydrofuran

THT: tetrahydrothiophene

UV: ultra violet

VT: variable temperature

General Introduction

1. Cyclotribenzylenes: General Features

1.1 Structures and Chirality

Cyclotribenzylene (CTB) is a macrocyclic trimer of veratrole presenting a bowl-shaped conformation. The first synthesis of the CTB was achieved independently by Ewins and Robinson[1,2] in 1909 and 1915, respectively. In 1965, Lindsey, Erdtman, and Goldup[3–5] proposed a revised structure, describing a macrocyclic trimer of benzyl rings (**Figure 1**). Since then, various CTB analogues have been obtained by changing the nature of the R_1/R_2 substituents of the aromatic rings.[6–8] Cyclotribenzylene and its analogues represent a class of relatively rigid pyramidal macrocyclic molecules with a C_3 symmetric bowl-shaped electron-rich and hydrophobic shallow cavity, the large rim of which can be functionalized by various groups.

The CTB derivatives shown in **Figure 1** are chiral when the two substituents R_1 and R_2 are different, and the racemic mixtures could be resolved either by fractional crystallization of the diastereomers obtained by derivatization with chiral auxiliaries[9,10] or by using chiral HPLC.[7,11] Chiral CTB derivatives give a well-defined electron circular dichroism (ECD) spectrum. The optical activity of these compounds is attributed to the important deviation of the transition dipole moments of the long and short axes of the benzene ring from the symmetrical position due to the presence of two different substituents R_1 and R_2. In the usual high energy region of the electronic spectrum, two $\pi \rightarrow \pi^*$ transitions of the benzene ring are considered, the B_{2u} and B_{1u} transitions. Both are symmetry forbidden, and they have different polarization directions and energies: B_{1u} has the highest energy (230–260 nm) and is polarized along the long axis of the benzene ring; B_{2u} has the lowest energy (260–310 nm) and is polarized along the short axis of the benzene ring. Due to the rigid geometry of the system and the relatively strong dipole strength of the transition, even small distortions can produce a strong ECD, which in turn provides useful information about the effect of substituents on the properties of aromatic chromophores. The sign and magnitude of the rotation depend on the relative magnitude of the spectroscopic moments of the R_1

and R_2 substituents. When the CTB is viewed from the wide rim, if R_2 has priority over R_1 according to the Cahn-Ingold-Prelog rules, the orientation is anticlockwise: The chirality descriptor is called *M*, otherwise, it is called *P*.[12–14]

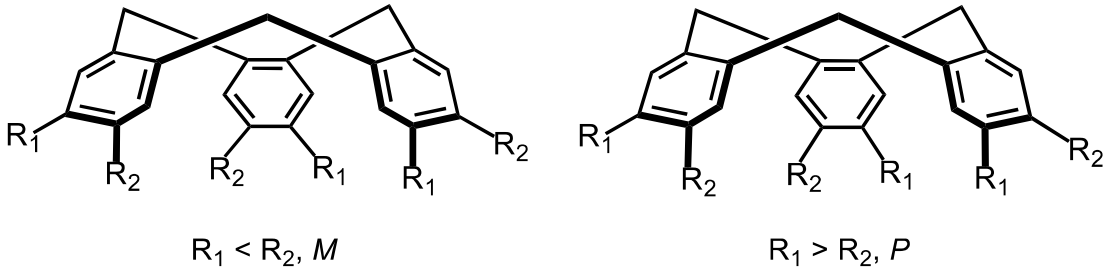


Figure 1. Structures of CTB derivatives.

The CTB derivatives can adopt two different conformations, a rigid crown, shown in **Figure 1**, and a flexible saddle. In most CTB derivatives, the saddle is much less stable than the crown, apparently due to repulsive interactions between the inward pointing methylene hydrogen and the opposite benzene ring (**Figure 2**).[15,16] It has been estimated that the saddle conformation is at least 12-16 kJ/mol higher in energy than the crown conformation. The saddle conformation results from the destabilization of the crown conformation due to steric hindrance between neighboring rings, which occurs when the substituents of the benzene rings are bulky. The racemization of chiral CTB derivatives is all the more favored as the saddle conformation is stabilized.[8] In fact, there is an equilibrium between the crown and saddle conformations in solution. Higher temperatures greatly favor the saddle conformer. At room temperature or below room temperature, the equilibrium will favor the crown form. Even if the isomerization is extremely slow, there is still a chance to observe at least a small amount saddle form. But it seems that there was no report claiming the observation of the saddle form in solution so far at room temperature.[17]

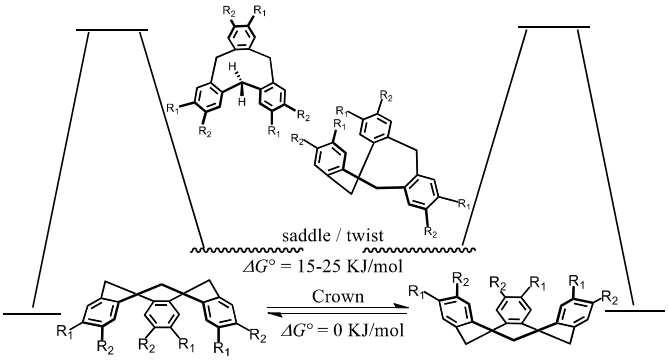


Figure 2. Energy profile for the inversion of the crown conformations of CTBs leading to the enantiomerization through saddle-twist exchanges.

1.2 Synthesis of Cyclotribenzylenes

There are three general methods for the preparation of functionalized CTBs: (i) the 'trimerization route', which itself can be employed in two different ways (A and B), and which resembles Robinson's procedures; (ii) the condensation of suitable diphenylmethanes with benzene derivatives and (iii) the chemical transformation of the peripheral substituents.

1.2.1 The Trimerization Route A

The trimerization route A is an acid-catalyzed condensation of an aromatic compound with formaldehyde. It provides a simple access to CTB derivatives. It seems that this method would be restricted to 1,2-disubstituted benzenes bearing two electron donating groups, such as catechol ethers. In addition, as shown in **Figure 3**, unless the starting material aromatic compound is symmetric, the initial cross-condensation of the two regioisomeric benzylic cations (a) and (b) is expected to eventually form a mixture of two racemic cyclic trimers with C_1 and C_3 symmetry.[18,19]

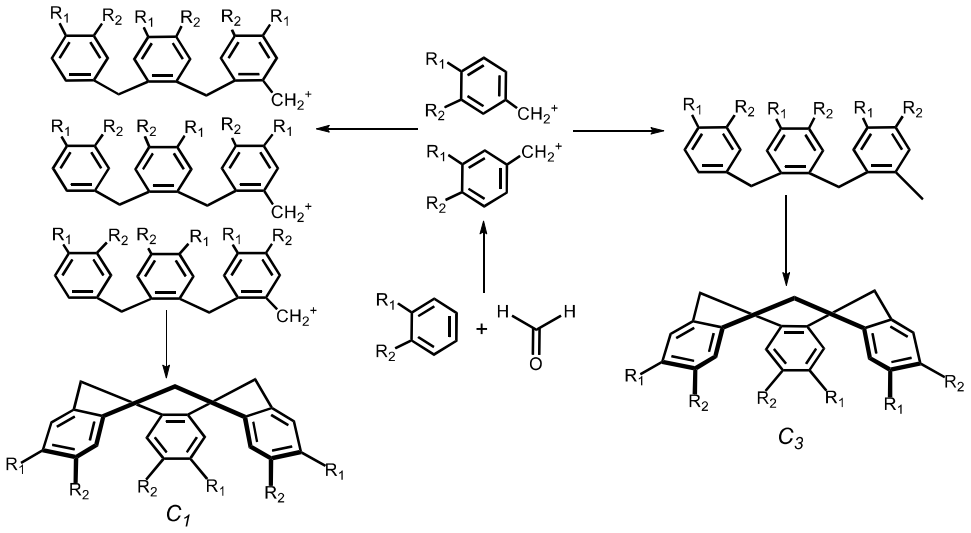


Figure 3. The trimerization route A for the preparation of CTBs from 1,2-disubstituted benzene derivatives.

1.2.2 The Trimerization Route B

Another way is to form C_3 symmetrically substituted CTB derivatives by aromatic electrophilic substitution of 3,4-disubstituted benzyl alcohol derivatives as starting materials. This approach is more effective for obtaining a C_3-substituted CTB derivative as a single product than method A since a single benzylic cation is generated in the first step. The trimerization reaction is well-known to be efficient and regioselective when the substituents in positions 3 and 4 are both donating groups, a methoxy group in position 3 being the most common situation. Such a substituent could be replaced by various electron withdrawing groups via substitution reactions or more efficiently by organometallic coupling reactions.[20,21]

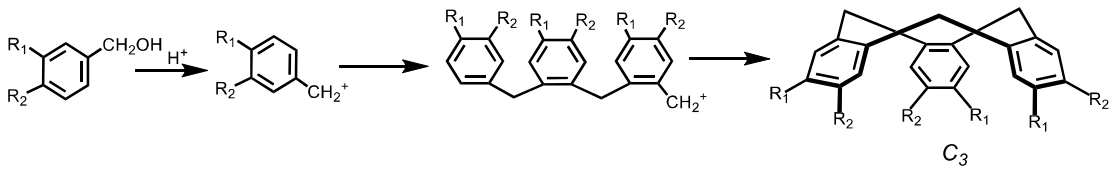


Figure 4. The trimerization route B for the preparation of CTBs from 3,4-disubstituted benzyl alcohol derivatives.

1.2.3 Condensation of Suitable Diphenylmethanes with Benzene Derivatives

The second method is the condensation of suitable diphenylmethanes with benzene derivatives to give trimers. It was originally described by Lindsey, but Sato's group extended this reaction to the synthesis of CTB derivatives without methoxy substituents. For example, in the presence of sulfuric acid, the condensation of diol derivatives with benzene under high dilution conditions could provide parent hydrocarbon **L1 - L3**. This method was the first to give access to the parent hydrocarbon cyclotribenzylene as shown in **Figure 5**. It was found that this method could be used to synthesize asymmetric CTBs as well when the groups of diphenylmethanes differ from benzene.[22–24]

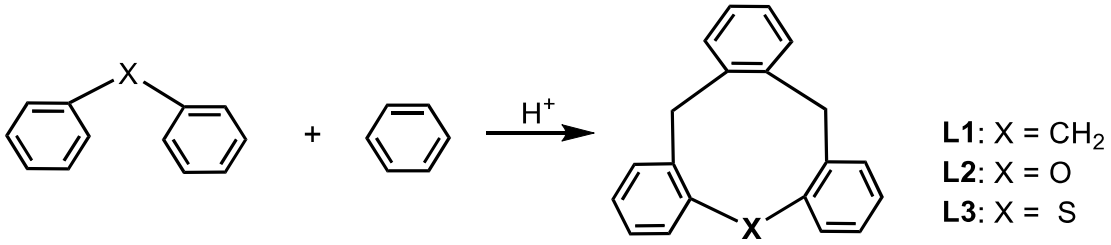


Figure 5. The preparation of CTBs by condensation of diphenylmethanes, ethers or thioethers with benzene derivatives.

1.2.4 Chemical Transformation of the Peripheral Substituents

Actually it is sometimes difficult to obtain a suitable substituted benzyl alcohol. In these cases C_3-symmetric cyclotriguaiacylene (CTG), which it is not possible to synthesize directly by trimerization of vanillyl alcohol, while it can be prepared from the tris(*o*-allyl)ether **L4** in one step as shown in **Figure 6**, is an interesting intermediate.[9] CTG having its three OH groups can be then engaged into functional group transformations which could be used for the preparation of C_3-symmetric substituted CTB derivatives. For example, treatment the acid chloride of 3-fluoro-4-pyridine carboxylic acid with CTG in a basic environment would yield (tris(fluoro-iso-nicotinoyl)cyclotriguaiacylene, **L5**.[25]

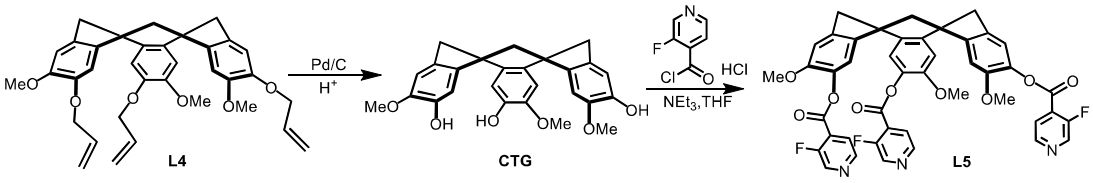


Figure 6. The synthesis of CTG and CTB derivatives by chemical transformation of the peripheral substituents.

1.3 Cyclotribenzylene Complexes

CTB-based compounds have raised much interest because of their C_3-symmetry, their electron-rich molecular concavity, and the possibility to functionalize its wide rim with diverse chemical groups. The molecular cavity of CTB derivatives could capture a relatively large number of guest molecules and ions as illustrated below.

1.3.1 Encapsulation of Fullerenes

C_3-substituted CTB derivatives have been developed for the efficient recognition of electron-deficient fullerenes in solution and in the solid state.[26–28] CTG was functionalized with three 4-ureidopyrimidinone (UPy) side-arms to form CTB-UPy **L6**, which was designed to form hydrogen bonded dimeric capsules as shown in **Figure 7**. The CTB-based hydrogen bonded dimer was shown to encapsulate a fullerene molecule within its large cavity as a (CTB-UPy)$_2$•fullerene complexe. Moreover, the system displayed an excellent selectivity for the encapsulation of C_{70} over C_{60}. Since the hydrogen bonds are easily broken apart by changing the polarity of the solvent, CTB-UPy can be applied to the separation of fullerene mixtures. This method could be used to extract higher-order fullerenes from a fullerite mixture. It was shown that CTB-UPy could extract C_{70} selectively when the ratio between CTB-UPy and fullerite was about 50-60%, while the ratio of about 5-15% could be used to recognize C_{84}.[29,30]

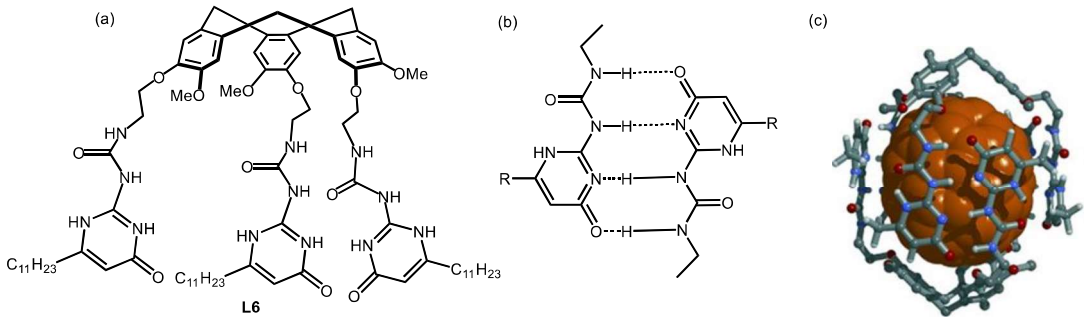


Figure 7. (a) CTB-UPy; (b) The quadruple hydrogen bond motif that can be established between two UPy motifs; (c) The hydrogen-bonded homochiral capsule formed from CTB-UPy in the presence of a C_{70} guest.

1.3.2 Encapsulation of Biological Ammoniums

C_3-substituted CTB derivatives were designed as fluorescent probes for acetylcholine (ACh) and choline (Ch) by Gosse and co-workers. The fluorescent probe **L7** having a hydrophobic concavity is substituted by three phosphonate and three methoxy electron donor groups (**Figure 8**). At neutral pH, the charged phosphonate group will ensure the water solubility and ionic interaction of the ammonium guest. The recognition was mainly due to cation–π interactions between the CTB aryl groups and the ammonium part of the guest. The binding ratio was 1:1 and the binding constant was around 70 M^{-1}, as determined by NMR and fluorescence titrations.[31,32]

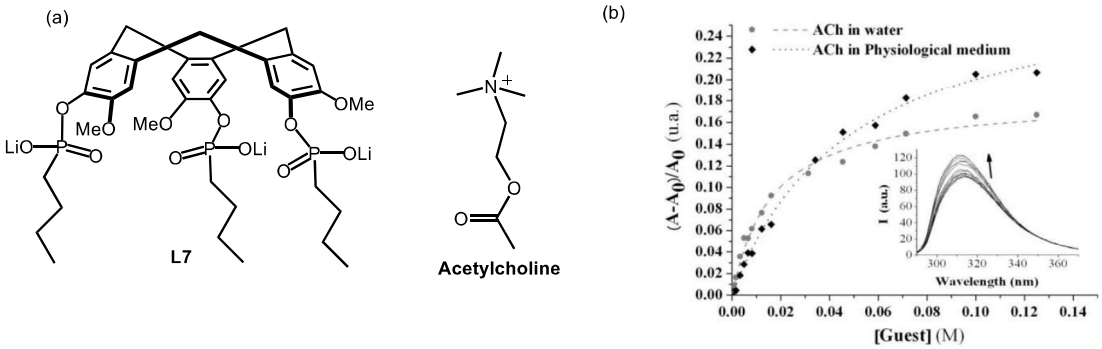


Figure 8. (a): The structure of **L7** and Ach; (b): relative fluorescence area of **L7** with increasing Ach concentration in water and physiological medium. Inset: fluorescence emission of **L7** upon ACh addition in a physiological medium.

1.3.3 Encapsulation of Metal Cations

Recently, Takayo and his co-workers developed a CTB derivative with 8-quinolinyl (8Q) groups (**L8**) as a fluorescence-enhanced probe for the highly selective sensing of Cu^{2+} ions. Usually, because of their incompletely filled d orbitals, Cu^{2+} ions can strongly quench the fluorescence emission of fluorescent compounds. Therefore, the extinction of fluorescence is used to detect the Cu^{2+} ions. The 8Q-substituted CTB derivative **L8** is not luminescent because of electron transfer between the methoxy substituents and the excited state of the 8Q subunits. However, in the presence of Cu^{2+} ions the emission of fluorescence is enhanced, which indicates that the metal cation is linked to the methoxy groups, making the latter no longer available for electron donation. Also, the **L8** showed highly selectivity for Cu^{2+} in the presence of other co-existing ions.[33]

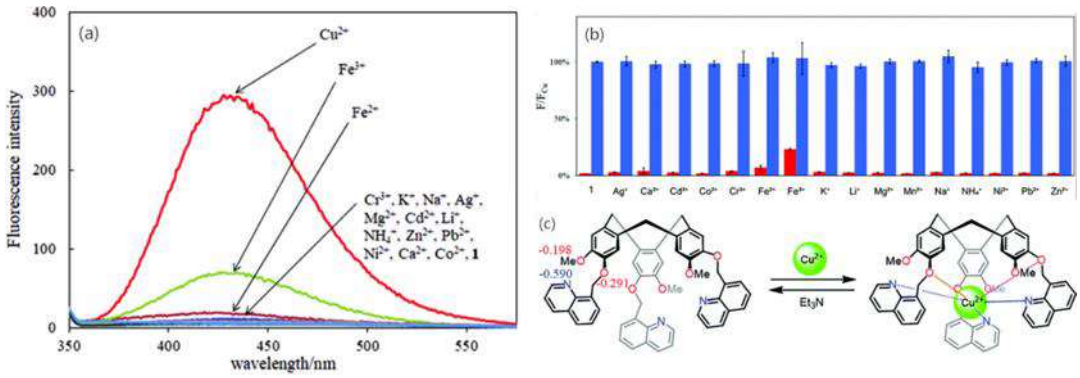


Figure 9. (a) Fluorescence spectra of **L8** in the presence of various cations; (b) Changes in the fluorescence intensity of **L8** toward the Cu^{2+} ions in the presence of other co-existing ions (c) Proposed binding mechanism of Cu^{2+} by **L8**. (Reproduced from Ref [33])

2. Cryptophanes: General Features

2.1 Structures and Chirality

The CTBs have been used mainly as building blocks for the construction of molecular cages, named cryptophanes, in which two CTB derivatives are connected by three linkers in a head-to-head arrangement.[8, 34–36] There are also examples of higher order molecular cages, such as a cube, made from six CTBs and a triply interlocked [2]catenane, made from two cryptophane subunits, hence incorporating four CTBs. In the classical cryptophanes, the linkers are positioned around the CTB bowl in a C_3-symmetric arrangement. Therefore, the connection of two identical CTB units with opposite chiralities (*M*, *P*) results in the so-called "syn" form, where the R_1/R_2 groups are positioned on the same side of the linkers (**Figure 10**). If the three linkers are the same, the cryptophanes will exhibit C_{3h} symmetry and be achiral (*meso*). The connection of identical CTB units of the same chirality (*M*, *M* or *P*, *P*) will produce chiral "*anti*" diastereomers, where the R_1/R_2 groups are on opposite sides of the linkers. If, in addition, the three linkers are the same, the cryptophanes will exhibit D_3 symmetry.[37–39]

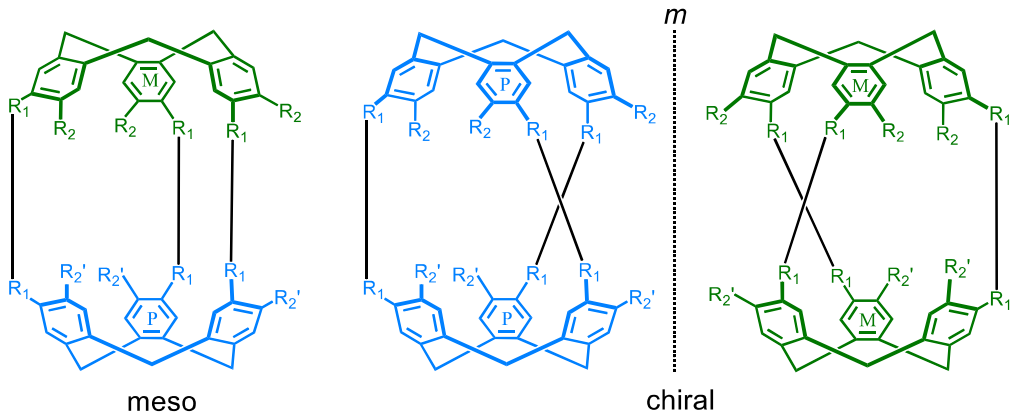


Figure 10. Schematical representations of the molecular structures of the (a) achiral *syn* and (b) chiral *anti* forms of the cryptophanes. The straight lines in black stand for organic linkers in classical cryptophanes, but they could also represent other kinds of bonds in self-assembled systems.

2.2 Synthesis of Cryptophanes

So far, there have been three main methods for preparing cryptophane hosts: the direct method or two-step method, the template method and the tripod-tripod coupling method.

2.2.1 The "Template" Method

The second method is called the template method. As shown in **Figure 11A**, the two cyclotribenzylene units are formed sequentially at two different stages of the synthesis. The terms "template" refers to the precursor CTB, which is functionalized with the three linkers bearing benzyl alcohol terminal groups. The latter will produce the second CTB unit of the cryptophane structure when submitted to the cyclization reaction conditions. Therefore, in this method, the CTB precursors play the role of an organic, permanent template that preorganizes the benzyl alcohol reactants intramolecularly. Also, as mentioned before, the efficiency of the trimerization reaction of the benzyl alcohol moieties requires electron-donating substituents on their *meta* and *para* positions. Cryptophane-A was also synthesized by using the template method.[40–42]

2.2.2 The Direct Method or Two-Step Method

The direct method (**Figure 11B**) requires the preliminary preparation of bis(vanillyl alcohol) derivatives, which are then reacted in formic acid ($\sim 10^{-2}$ M) to form the desired cryptophanes. The cryptophanes are separated by column chromatography from the side-product polymeric materials that are formed predominantly. However, the yields of this method are usually low, as large amounts of by-products were formed at the same time. Also, it is necessary to note that, as for the synthesis of CTBs, this reaction requires strong electron-donating groups in the *meta* and *para* positions of the benzylic alcohol. *Anti*-cryptophane-A and *anti*-cryptophane-E were synthesized by using the direct method.[8, 43–45]

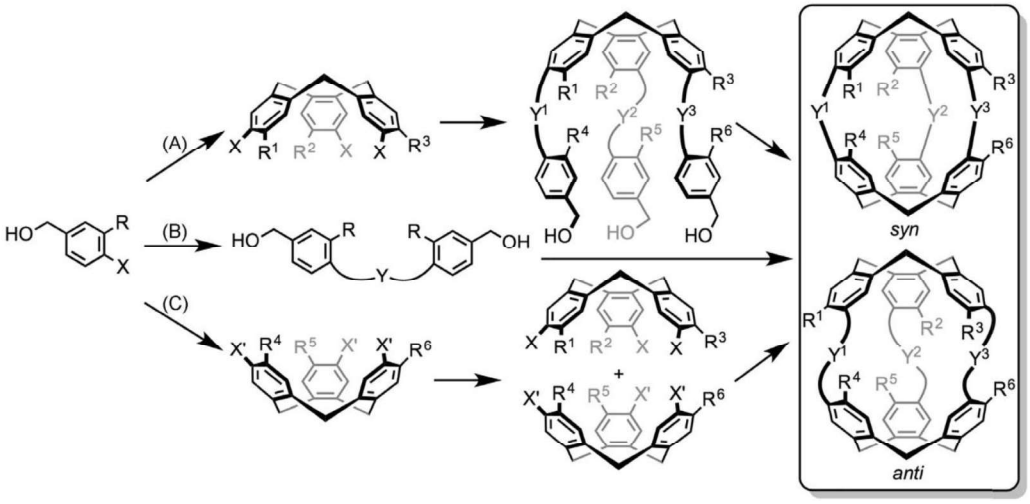


Figure 11. The three methods employed for cryptophane synthesis: (A) template method, (B) two-step method, and (C) tripod-tripod coupling method. (Reproduced from Ref [39])

2.2.3 The Tripod-Tripod Coupling Method

A third synthetic route, first described by Cram and co-workers, was used to synthesize cryptophanes with linkers containing terminal acetylenic units, which were then engaged in the Glaser-Hay reaction. The tripod-tripod coupling method was later used for the formation of cryptophanes incorporating dynamic covalent bonds (e.g., imine, disulfide) (**Figure 11C**), metal–ligand coordination bonds, and hydrogen bonds (see section 1.3.1). The tripod-tripod couplig method was extensively used for the preparation of metallo-cryptophanes. These compounds are cryptophane analogues in which the CTB components are connected by metal complex fragments. They were first described by Shinkai and co-workers, who used *meta*-pyridyl functionalised CTB analogues, which were linked together via *cis*-protected Pd(II) complex fragments. The *meso* and chiral forms were both observed and the exchange between these two forms were investigated.[46–49] Disulfide-bridged cryptophanes had been reported by Chambron and his coworkers. As shown in **Figure 12**, the conversion of **L9** into cryptophane **R1** depended on the size of the alkali metal cation strongly, the largest ones inhibiting the process. So in the presence of Li^+, only one of the diastereomers was observed; it was supposed to be the pair of *anti* enantiomers.[49]

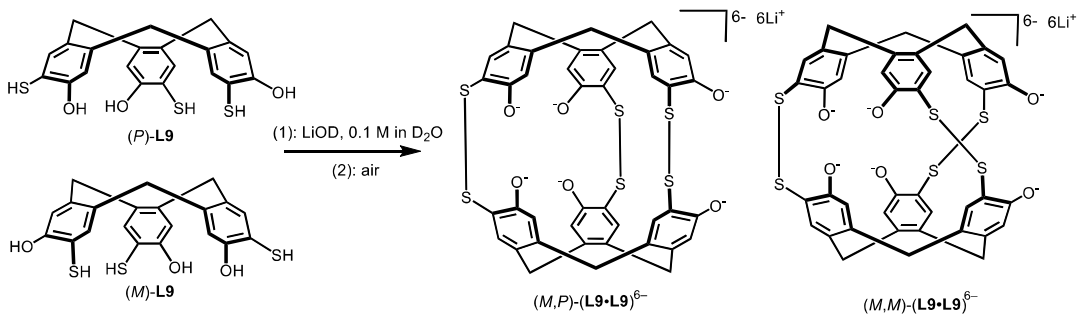


Figure 12. Oxidative dimerization of a racemic mixture of **L9** to diastereomeric cryptophanes **R1**.

2.2.4 Transformation and Functionalization of Cryptophanes: Water-Soluble Cryptophanes and Monofunctionalized Cryptophanes

Most of the known cryptophanes synthesized in the past had C_3 and D_3 symmetry. In order to obtain functionalized cryptophanes, post-synthetic modifications were developed. Collet and co-workers reported the first chemical transformation of cryptophanes using lithium diphenylphosphide (PPh_2Li) for the selective demethylation of the six methoxy groups without affecting the O-$(CH_2)_n$-O bridges in cryptophanes. In this way, several hexahydroxy cryptophanes were obtained with good yields.[50–52] Later, the group of Brotin and Dutasta proposed new strategies for the synthesis of functionalized cryptophanes, focusing on the preparation of the mono hydroxy cryptophanol. The key step is to synthesize the mono-protected alkylated cryptophane, which can be easily converted into the mono hydroxy cryptophanol molecule. The latter was subsequently used as intermediate for the preparation of other functionalized cryptophanes, like bis-cryptophanes, biosensors and enantiopure cryptophanes. For example, cryptophanol-A molecule **R3** could be synthesized by bis-functionalization of CTG, which was treated with 2 equiv of benzyl alcohol to give rise to the disubstituted derivative **L10**. Then the condensation of **L10** with a protected vanillyl alcohol derivative provided cryptophane precursor **L11**, which was stirred in a 1:1 mixture of chloroform and formic acid to give cryptophane **R2**. It is easy to obtain cryptophanol-A **R3** by the deallylation reaction.[53,54]

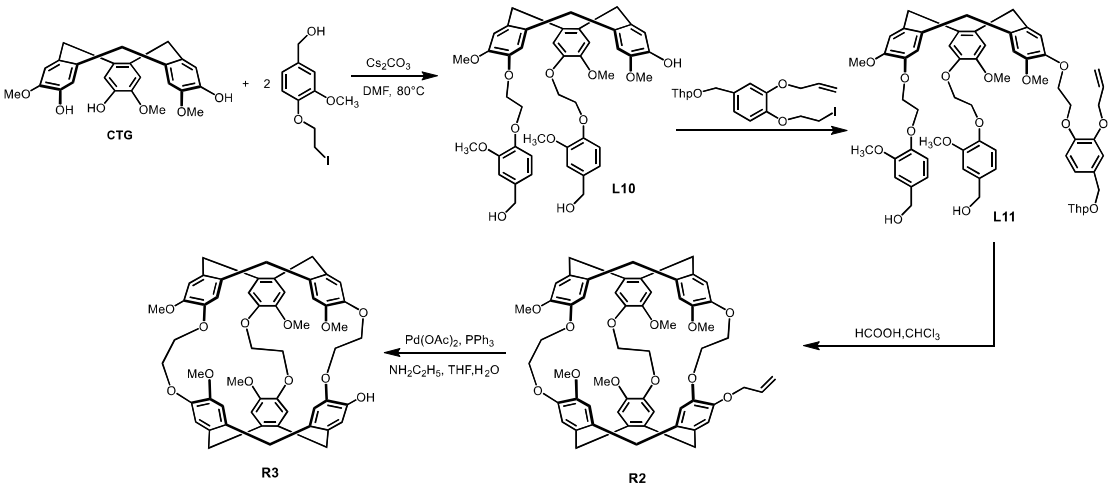


Figure 13. Preparation of cryptophanol A **R3** starting from CTG.

2.3 Conformers of Cryptophanes

CTB moieties in the cone conformation are essential to ensure the formation of a cavity and should be rigid enough to maintain the spheroidal structure of the molecule. In addition to the *syn-anti* configurational isomerism, the molecular structure of cryptophanes can encompass various conformations. As the CTB moieties, because of their flexibility in the conditions described in section 1.1, can invert or adopt a saddle twisted conformation[44,55], it is necessary to consider the existence of the out-out, in-in, in-out, and out-saddle conformers of the cryptophanes, as defined in **Figure 14**. The existence of these conformational isomers may not only be due to the greater flexibility of the molecules but also depend on the environment.

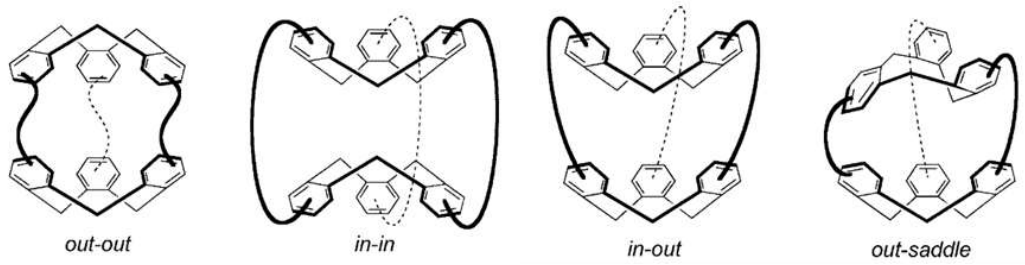
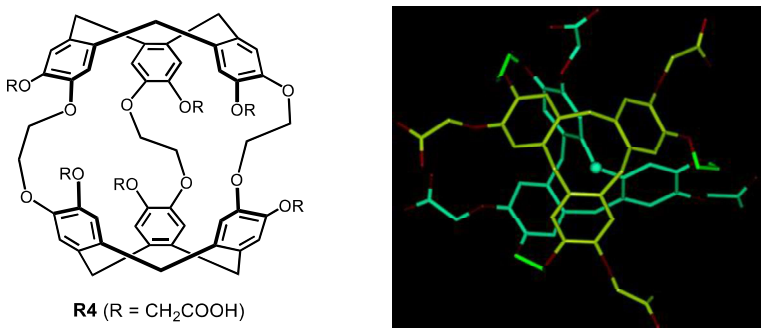


Figure 14. Conformers of cryptophanes (Reproduced from Ref [17]).

For example, the hydrophobic force has a significant influence on the molecular structure of water-soluble cryptophanes. Collet and colleagues reported the first evidence of CTB unit reversal in cryptophanes with long -O(CH_2)$_n$O- (n≥ 6) spacers. The starting out-out cryptophane could slowly equilibrate in solution at room temperature with the in-out cryptophane.[56] It was proven that, under degassed conditions, in the aromatic region of a cryptophane **R4** bearing OCH_2COOH groups in place of the methoxy groups (O(CH_2)$_n$O-, n = 2, 3), one of the CTB units exhibited the typical ^{1}H NMR signal of the saddle conformation in water. Since the cryptophanes have D_3 symmetry, the aromatic rings are all equivalent and **R4** should show only two singlets for the aromatic protons. However, the ^{1}H NMR spectrum of **R4** not only showed these two main signals, but also showed twelve smaller signals with similar intensities. These features indicated that cryptophane **R4** coexisted with an asymmetric conformation **R5**. It was confirmed that one of the CTBs had adopted an asymmetric saddle conformation. The isomerization process bewteen these two conformations was followed at 293 K with a half-life time of 5 days.[57]



R4 (R = CH_2COOH)

Figure 15. The structure of cryptophane **R4** and its corresponding saddle conformation (Reproduced from Ref [57])

2.4 Binding Properties of Organic Cryptophanes

Cryptophanes present remarkable recognition properties toward small neutral molecules like short chain alkanes (methane, isobutane, etc), haloalkanes ($CHCl_3$, CH_2Cl_2), epoxydes, organic cations like quaternary ammoniums, of synthetic (NMe_4^+) and natural (choline) origins, and inorganic soft cations, such as Cs^+ and Tl^+. Rare are examples of cryptophanes complexing anions.[43,45,50,58,59] Small size cryptophanes

were also found to complex the Xe atom, which led to the development of promising tools for bioimaging. The electron-rich and hydrophobic cavity enclosed in the six aromatic rings of the cryptophanes represents a perfect environment for the interaction with guests through dispersion and/or multipole-multipole interactions. The electronic structure and symmetry of the guest, the electron density of the host aromatic ring and the solvation effects are also important factors that may affect the formation of the complex.

NMR spectroscopy and isothermal microcalorimetry (ITC) have proven to be the tools of choice for studying the thermodynamics of the complexation properties of cryptophanes in solution. NMR spectroscopy was also extensively used for the determination of the kinetic parameters of the guest inclusion processes. The solvent must be considered as a potential substrate, which could compete with the guest, so bulky solvent molecules, which could not enter the cavity of the cryptophanes, were searched for, such as 1,1,2,2-tetrachloroethane. As the rate of the formation of the host-guest complex (kinetics of guest encapsulation) depends on the accessibility of the molecular cavity, the size of the substituents of the cryptophanes, which control the openings of the three portals of the host cavity, is an important parameter. In addition, the conformation of the cryptophane might change once the guest enters the cavity to form the host-guest complex.[34,60,61]

2.4.1 Complexation of Small Neutral Molecules

The first evidence of guest encapsulation was reported for cryptophanes-A, -C, and -E with neutral molecules such as $CHCl_3$, CH_2Cl_2, CHFClBr, and CH_4. ^1H NMR experiments proved the complexation of methane by cryptophane-A, which was characterized by the high-field chemical shift of the average signal of free and bound CH_4 in fast exchange at 298 K.[62–65] The complexation of alkanes under slow exchange conditions at 210 K was reported by Akabori and colleagues, who used cryptophanes with xylene or diethylenetrioxy linkers. The encapsulation efficiency of the cryptophane hosts depended largely on their *syn* or *anti* configuration, and on the

substitution of aromatic linkers.[64] EPR was also used for the investigation of the complexation of piperidine-derived aminooxy radicals **A-D** in water by the water-soluble cryptophane **R6** (**Figure 16**). EPR spectroscopy is particularly suitable for studying the exchange process because it is slow on the EPR time scale. Compared with bulk water, since the N-O• function in the cryptophane cavity is in a hydrophobic environment, the hyperfine coupling of the free radical nitrogen in the complex is lower than that in the free state.[66] Actually, it was difficult to determine the binding constant by calculation of EPR spectra. However, competitive experiments were carried out to provide their reliable binding constants. The higher binding constant of **A** was due to the absence of hydrophilic group compared to **C-D**. In addition, the ratio between the volume of the guest to the volume of the cavity is optimal, because it is close to the value of 0.55 occupancy established by Rebek and coworkers'.[67]

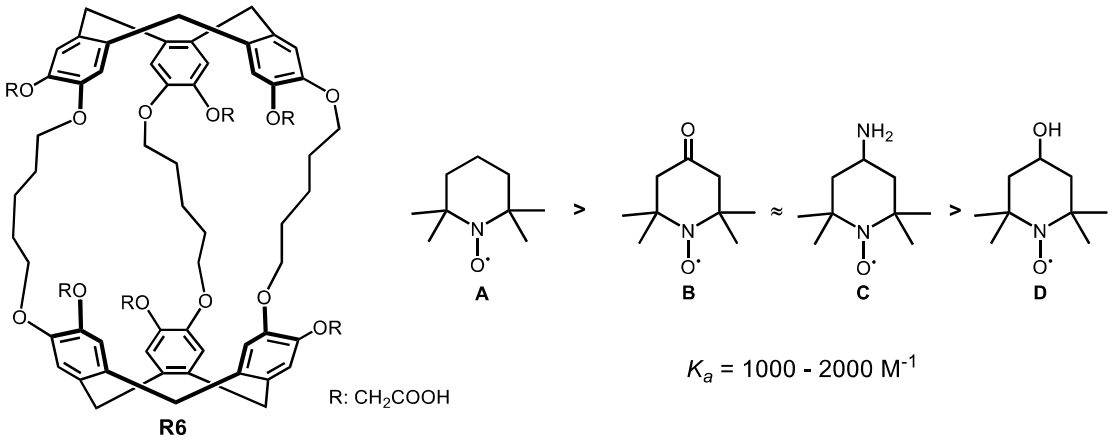


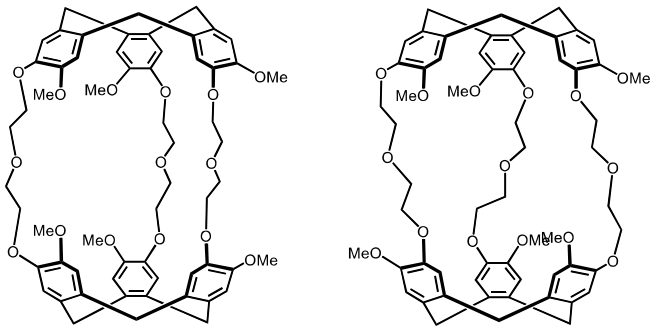
Figure 16. Water-soluble cryptophane host **R6** and guests **A-D** investigated by EPR spectroscopy.

2.4.2 Complexation of Ammonium Guests

In addition to the encapsulation of volatile organic compounds (VOCs) such as halomethane and small alkanes, cryptophanes are able to host organic ammonium cations of appropriate size. In general, ammonium cations have stronger binding power than neutral guests when using water-soluble hosts. For example, cryptophane-E strongly binds to tetramethylammonium at 293 K with unprecedented binding constant of K_a = 475000 M^{-1}, while the binding constant between cryptophane-E and Me_3NH^+

was significantly reduced to 1600 M^{-1}.[68]

It is assumed that cation-π interactions are responsible for the stabilization of the complexes of organic ammoniums and cryptophanes.[43,58] In fact, the association of ammonium guests involves other factors, as it was clearly shown that ammonium cations also interact with the oxygen or sulfur atoms of the cryptophane structure. Comparison of the thermodynamic parameters of complexation of organic ammoniums and haloalkanes shows that the complexation of the former is strongly entropy driven, while the complexation of haloalkanes is enthalpy driven in $C_2D_2Cl_4$.[58] In relation with these studies, Akabori and colleagues studied the extraction of alkylammonium ions from aqueous solutions to the organic phase by using diastereomeric cryptophanes **R7** and **R8** with diethyleneoxy bridges as shown in **Figure 17**. Interestingly, they observed that the extraction efficiency decreased concomitantly with both the size and the lipophilicity of the ammonium ions, i.e. it followed the order $(CH_3)_4N^+ > (CH_3)_3NH^+ > (CH_3)_2NH_2^+ > CH_3NH_3^+ > NH_4^+$.[58] Also, the extraction abilities of *meso* cryptophane **R8** was more efficient than the *anti* form **R7** for $(CH_3)_4N^+$.



R7 meso form **R8** *anti* form

Figure 17. The structures of cryptophanes **R7** and **R8**.

2.4.3 Complexation of Metal Cations

There is only a small number of reports on the complexation of metal cations by cryptophanes, because it is difficult to find a suitable solvent, which dissolves the metal salt and does not compete with the metal for complexation by the cryptophane. The first example was discovered by Akabori and co-workers in 1996. In CH_2Cl_2 solution, the

cavity of cryptophane bearing diethylenetrioxy linkers could be used to extract alkaline metals from water. Noteworthy, the efficiency of extraction was related to the configuration of cryptophane, for example, *meso* isomer **R7** showed relatively higher extraction abilities toward the cesium cation by comparison with anti isomer **R8**, their extraction abilities from the aqueous to the organic phase were 43.3% and 21.4% respectively.[58] A tailor-made cryptophane **R9** bearing three endo-carboxylic acid groups was synthesized by Weber et al. for recognizing alkali and alkali-earth metal cations inside the cryptophane cavity (**Figure 18**). The *syn* achiral isomer could be used to extract a variety of metal ions. Its binding ability to different metals followed the order: Ca^{2+} ~ Sr^{2+} > Mg^{2+}> Ba^{2+}> Cs^{+}> Na^{+}. Therefore, the binding ability to Ca^{2+} and Sr^{2+} was the largest, and Na^{+} was almost not recognized at all. The strong binding ability to Ca^{2+} and Sr^{2+} is consistent with their stronger interaction with the carboxylate anions. It presumably results from the preorganization of the host, in which the endo-oriented carboxylic acid functions are favorable for the formation of 1:1 complex. Further, based on the same reason, the ability of this cryptophane to extract the lanthanides ions Yb^{3+} and Eu^{3+} is also very effective.[69]

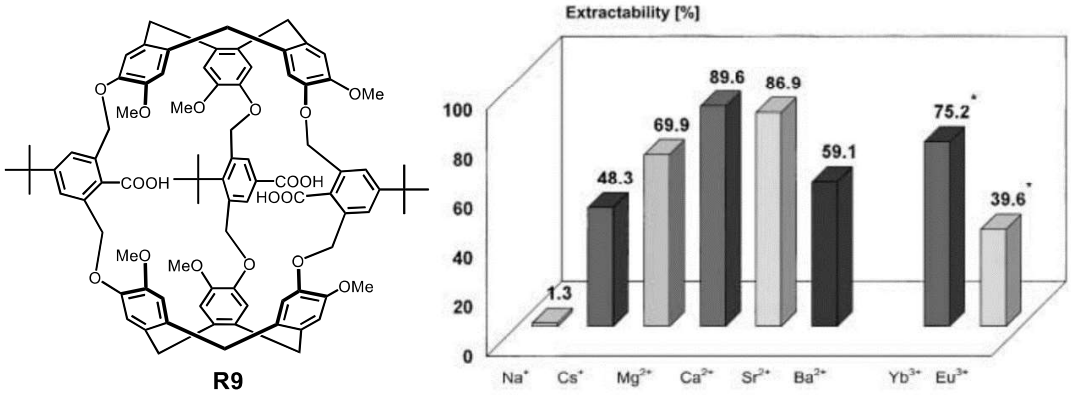


Figure 18. The structure of cryptophane **R9** and its extractability of metal ions.

2.4.4 Complexation of Anion Guests

Because of the electron rich character of CTBs, the cavities of cryptophanes are not suitable for recognition of anionic guests. Holman and coworkers have modified the outer aryl faces of cryptophane-E by η^6-coordination of cationic, electron withdrawing

[Cp*Ru(II)]$^{+}$ moieties. The resulting hexacationic cryptophane **R10** exhibits a strong binding ability in nitromethane solution to soft non-coordinating anions, such as PF_6^-, SbF_6^-, $CF_3SO_3^-$, and BF_4^-, while hydrophilic anions like halide ions difficultly interact with the cryptophane cavity. In this latter case, ion-pairing with the positively charged cryptophane induces precipitation. X-ray crystal structures clearly show that the anions SbF_6^- and $CF_3SO_3^-$ fill the cavities. The resulting complexes are stabilized by anion···π interactions, the aromatic ring being located between the anion and the cationic metals centers. As for neutral and cationic species, the binding affinity is related to the size of the anionic guest. Given the relatively large diameter of the guest and its high binding affinity, the fact that the exchange rate of the guest at room temperature was very slow is not surprising. As a consequence, anion competition experiments take several weeks to reach equilibrium.[70]

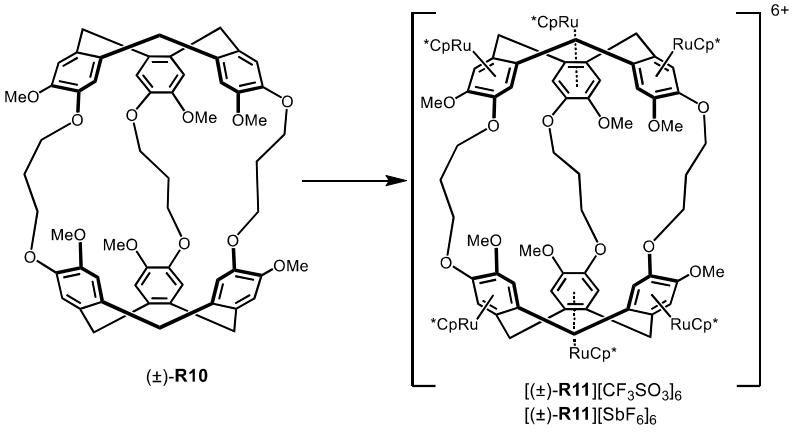


Figure 19. Chemical modification of cryptophane **R10** by grafting of six [Cp*Ru(II)]$^{+}$ complex moieties with either triflate or hexafluoroantimonyl counter-anions.

2.4.5 Chiral Discrimination of Cryptophanes

Chiral cryptophane-C was used to recognize the two enantiomers of CHFClBr, one of the smallest chiral molecules.[60] When enantiomerically enriched (+)-cryptophane-C was added to the racemic mixture of CHFClBr in organic solution, the resulting ^{1}H NMR spectrum showed two sets of doublets for the C*H*FClBr protons, where the splitting was due to scalar coupling with the fluorine atom. In addition, in $C_2D_2Cl_4$

solution, (+)-CHFClI and (–)-CHFClI form diastereomeric complexes with (±)-Cryptophane-E-$(SCH_3)_6$, which were characterized by ^{1}H- and ^{19}F-NMR spectroscopy. However, low enantioselectivity of the chiral recognition was observed at 300 K.[71]

2.4.6 Complexation of Xenon

The complexation of noble gases, such as helium, xenon or even radon by organic molecules in solution represented a challenge for chemists until recently. This research field currently goes beyond the basic research of supramolecular chemistry, as the development of receptors for the complexation of helium and xenon concerns applications in magnetic resonance imaging (MRI). At present, only a few hosts only were reported to bind the xenon atom, such as cucurbit[6]uril[72], hemicarcerands[73,74], and self-assembled capsules.[75] However, some cryptophanes exhibit among the highest xenon-binding constants.[76–79] The first Xe@cryptophane complex was reported by Collet, Bartik and their co-workers in 1998, who studied the interaction of xenon with anti-cryptophane **R12** by ^{129}Xe NMR spectroscopy in $C_2D_2Cl_4$. The binding constant of the Xe@cryptophane **R12** complex was estimated to be K_a= 3900 at 278 K.[79] The cryptophane **R11** with the smallest cavity volume, exhibit the highest binding constants (K_a= 28000) in $C_2D_2Cl_4$ at 278 K.[77] This is due to the fact that its cavity is complementary to the xenon. The cavities of cryptophanes **R11** and cryptophane **R12** are 70 Å^3 and 85 Å^3 respectively, while the volume of xenon is 42 Å^3. So it could explain why cryptophane **R12** showed weaker interaction with Xe.

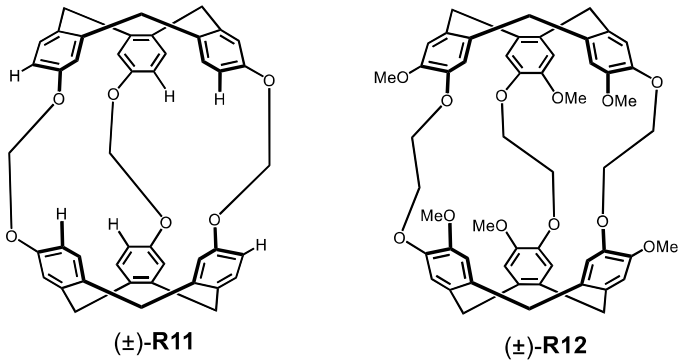


Figure 20. The structures of cryptophanes **R11** and **R12**.

3. Metallo-Organic Cryptophanes

3.1 Cis-Linked M_3L_2 Cages

Metallo-cryptophanes or metal-organic cryptophanes are molecular cages obtained by face-to-face dimerization of CTBs using coordination bonds. Thus, two modified CTB ligands (L) are linked by metal cations (M^{n+}) to form M_3L_2 cage species. The first metallo-cryptophanes were reported by Yamaguchi and Shinkai in 2001. They were designed by linking two 4-pyridyl- substituted CTB-ligands (**L12**) with three *cis*-protected square planar $[Pd(P\text{^}P)]^{2+}$ complex fragments, where P^P = bis(diphenylphosphino)ethane (dppe) or bis(diphenylphosphino)propane (dppp). Interestingly, these P^P chelates led to different self-assembly behaviors. For $[Pd_3(dppe)_3(CTB)_2]^{6+}$ **R13**, the ratio of *meso* form (PM and MP) and chiral (PP or MM) increased gradually from 1:1 to 2.5:1 in $C_2D_2Cl_4$. But for $[Pd_3(dppp)_3(CTB)_2]^{6+}$ **R14**, the initially formed *anti*-chiral isomer gradually disappeared until the *meso* form dominated.[47]

Hardie's group had reported tris[3,5-bis(methyl)benzoic acid]cyclotricatechylene (**HL13**), which was synthesized from cyclotricatechylene. A mixture of $Cu(OAc)_2$ and **HL13** in DMF and 3:1 ratio was heated at 90 °C for 48 hours, then slowly cooled to room temperature, which provided greenish blue crystals of $[Cu_3(\mathbf{L13})_2(DMF)_3]2(DMF)$ **R14**. Single crystal X ray diffraction analysis showed that the complex was composed of a trimer of Cu(II) centers, in which the CTBs were arranged in a head-to-head fashion. Four carboxylate oxygen atom donors were arranged in an approximate square and around each Cu(II), the axial position being occupied by a DMF ligand to provide a square pyramid geometry. The structure of **HL13** and the crystal structure of **R14** are shown in **Figure 21**.[80]

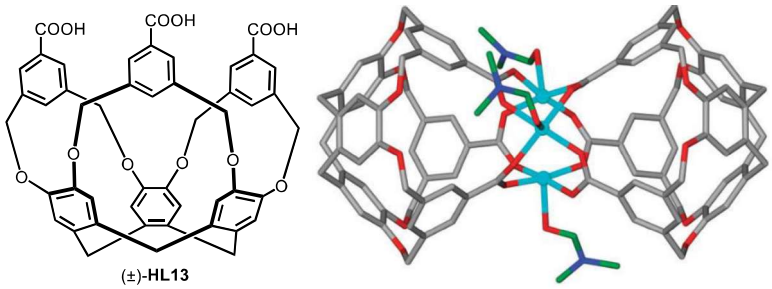


Figure 21. The structure of **HL13** and the crystal structure of **R14**.

Our laboratory reported a series of $[M_3(dppp)_3L_2]^{6+}$ (M = Pd or Pt) metallo-cryptophanes, based on the weaker M^{2+}–carbonitrile interactions, which could be obtained via self-assembly of chiral cyclotricyanobenzylene with $[M(dppp)](OTf)_2$ in 2:3 ratios in chlorinated solvents. No matter what kind of chlorinated solvent was used, only *anti*-chiral cryptophanes were formed at room temperature, while *syn*-achiral cryptophanes became the main products at low temperatures in CD_2Cl_2. Crystallization of the metallo-cryptophanes from $CHCl_3$ produced X-ray quality crystals in which the complexes had the *anti*-chiral forms and encapsulated a chloroform molecule.[81]

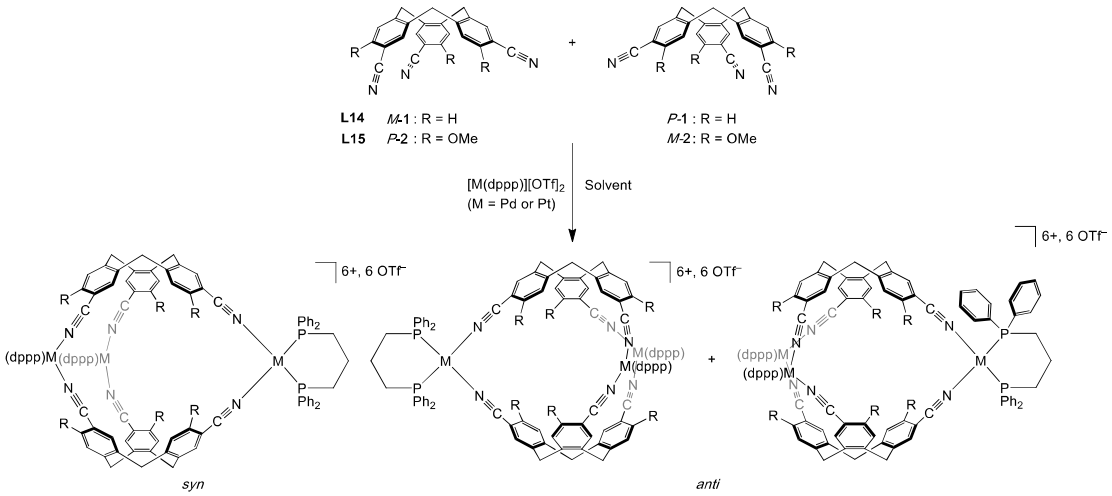


Figure 22. Self-assembly reaction of cyclotricyanobenzylenes **L14** or **L15** with $[Pd(dppp)]^{2+}$ and $[Pt(dppp)]^{2+}$ metal complex fragments into metallo-cryptophanes (Reproduced from Ref [81]).

3.2 Trans-Linked M_3L_2 Cages

T*rans*-metal complexes can also coordinate with CTB derivatives to form metallo-cryptophanes in a 3:2 ratio. As shown in **Figure 23**, Hardie and coworkers reported the

trans-linked metallo-cryptophane by mixing *trans*-[$PdCl_2(MeCN)_2$] and CTB derivatives **L16** bearing benzimidazole coordinating subunits together in polar solvents. The cryptophane, which crystallized from a DMF solution, had the composition [Pd_3Cl_6(**L16**)$_3$·(H_2O)]·1.5H_2O·3DMF as identified by single crystal X-ray crystallography.[25]

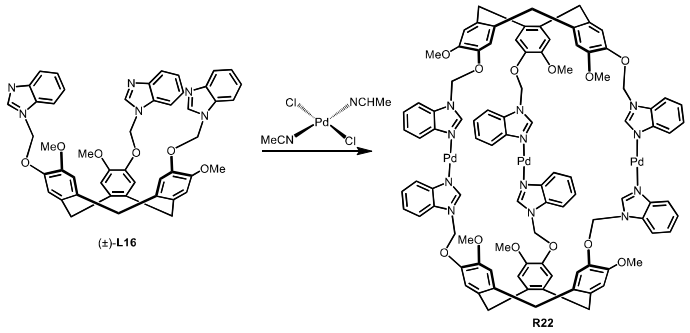


Figure 23. Self-assembly of a [($PdCl_2$)$_3$(**L16**)$_3$] neutral metallo-cryptophane from CTB **L16** functionalized with pendent benzimidazole monodentate ligands and [$PdCl_2(MeCN)_2$].

M_3L_2 metallo-cryptophanes have also been synthesized by trans-coordination of metal centers exhibiting a linear geometry. Pyrimidine-functionalised CTB derivative **L17** self-assembles with Ag^I or Cu^I to form M_3L_2 capsules in the solid state as isomorphic complexes. These molecular cages appear as *anti*-cryptophanes **23**, in which the two CTB ligands are homochiral, but the complexes crystallize as racemates since the starting CTB are in racemic form. The preferred formation of the *anti*-isomer is probably the result of the linear coordination geometry of the metal cation with the N atom at the 3-position of the aromatic ring.[82] However, it is worth noting that if the functional group of the CTB derivative changes even a little, the coordination mode of the metal will be affected. When tris(3-pyridylmethyl)amino CTB **L18** coordinated with Ag^I, instead of a M_3L_2 metallo-cryptophane, the metal-organic capsule-like assembly of M_2L_2 **R24** was formed in the crystalline state. In this assembly, each Ag^+ cation is in a tetrahedral coordination geometry, being bound by two pyridyl moieties of one CTB, one of the other, the fourth ligand being a solvent molecule.[83]

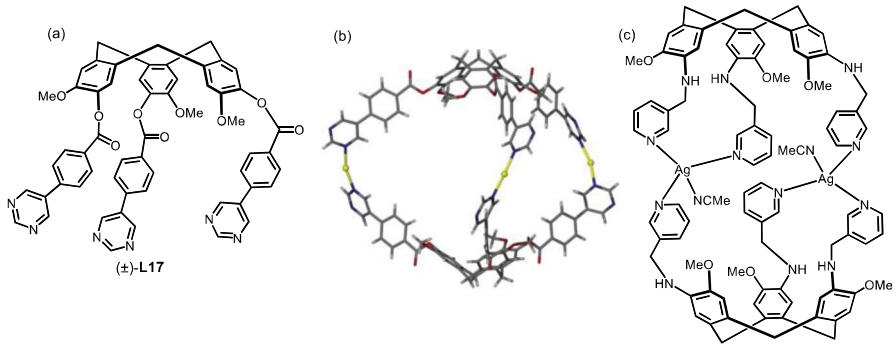


Figure 24. (a): The structure of **L17**; (b): Crystal structure of chiral *anti*-$[Ag_3(\mathbf{L17})_2]^{3+}$ **R23** (reproduced from Ref [82]); (c): Structure of $[Ag_2(\mathbf{L18})_2(CH_3CN)_2]^{2+}$ **R24** (Reproduced from Ref [83]).

3.3 Complexation of Neutral Guests

Hardie and her coworkers had employed several different chelate motifs to form metallo-cryptophanes with *cis*-arrangement of coordination groups. In particular they were the first to report the use of a bis-N-heterocyclic carbene (bis-NHC-nap) as a *cis*-protecting ligand for the self-assembly of metallo-cages from a CTB bearing pyridyl ligands **L19**. Compared with the more commonly used phosphine-based *cis*-protected ligands, the use of bis-NHC stabilized an otherwise unstable *syn* metallo-cryptophane assembly probably because of the face-to-face π-π stacking interaction between the pyridyl group on the CTB-ligand and naphthyl group of the bis-NHC-nap ligand. Although the X-ray crystal structure of $[Pd_3(\text{bis-NHC-nap})_3(\mathbf{L19})_2]\cdot 6(BF_4)$ **R25** has no obvious porous structure, the material can be still used to absorb dichlorobenzene and I_2 by single crystal-to-single crystal (SCTSC) fashion. As shown in **Figure 25**, most of the diodine molecules are included inside the metallo-organic cages. Compared to the traditional porous organic cages, once I_2 was absorbed, it was difficult to extract it from the cavity. Such materials could be used for the sequestration of radioactive I_2.[84]

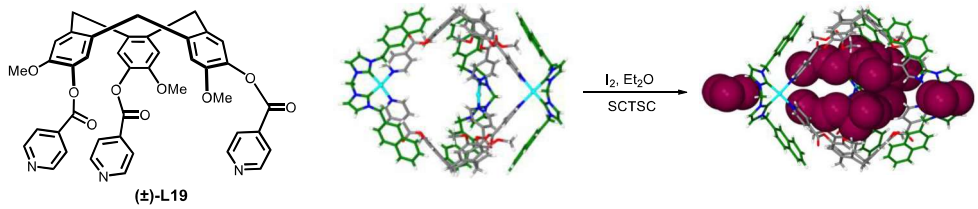


Figure 25. The structure of **L19** and inclusion of I_2 into a corresponding metallo-organic cryptophane **R25** in the solid state.

3.4 3-D Triply Interlocked [2]Catenane from Metallo-Cryptophanes

In recent years, threaded molecules such as catenanes and rotaxanes have received widespread attention[85–88], as well as 3-D metallo-supramolecular assemblies, which can form various prismatic and polyhedral structures. The first metallo-supramolecular assembly of a [2]catenane from CTB derivatives was reported by Hardie and her coworkers. The [2]catenane assembly was composed of two triply interlocking *syn*-$[Zn_3(\mathbf{L20})_2(NO_3)_3]^{3+}$ metallo-cryptophanes made from (±)-tris-(4-(4'-methyl-2,2'-bipyridyl)-benzyloxy)cyclotriguaiacylene **L20** and $Zn(NO_3)_2$ in DMSO solution. In this example, although the synthesized $[Zn_3(\mathbf{L20})_2(NO_3)_3]^{3+}$ metallo-cryptophanes are *syn* isomer, that is, they are composed of two CTB enantiomers, the helical chirality of the bis-bipyridyl coordination environment of the Zn^{2+} cations makes the metallo-cryptophane components, hence their assembly into a [2]catenane, chiral. It must be noted that the [2]catenane has six weak hydrogen bonds between the unbound O of the nitrate ligand and the pendant methyl group on the bpy moieties of one of the two types of ligand, which may play a role in templating its formation.[89]

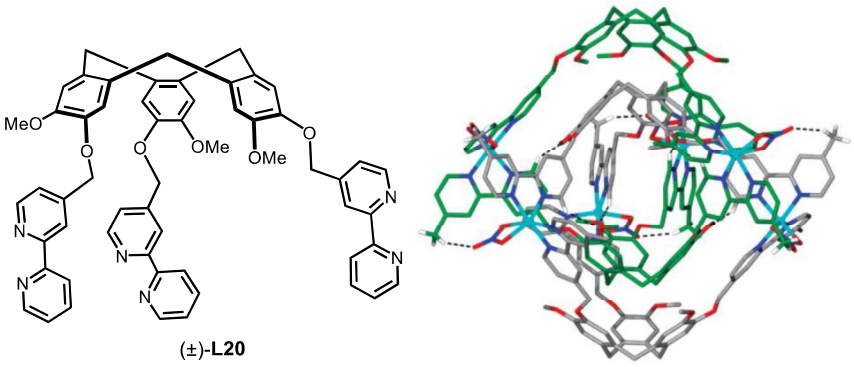


Figure 26. The structure of **L20** and X-ray crystal structure of the triply-interlocked [2]catenane **R26** (±)-$[Zn_3(\mathbf{L20})_2(NO_3)_3]^{3+}$(Reproduced from Ref [89]).

The reaction of (±)-tris-(3-pyridylmethyloxy)-cyclotriguaiacylene with silver(I) perchlorate in *N*,*N*'-dimethylformamide (DMF) solution was studied by Hardie and her coworkers. The expected *anti*-chiral metallo-cryptophane was formed upon self-assembly of two homochiral CTB ligands, although it was not the only product. In addition, the formation of a chiral [2]catenane, formed by triple interlocking of two

metallo-cryptophanes, was observed. It was obtained as a 1:1 mixture of (PPPP)-$[Ag_6(\mathbf{L21})_4]^{6+}$ and (MMMM)-$[Ag_6(\mathbf{L21})_4]^{6+}$ **R27** enantiomers. This result is completely different from the previously reported $[Zn_3(\mathbf{L20})_2(NO_3)_3]_2^{6+}$ [2]catenane structure, in which the *syn* diastereoisomer is formed. No significant intermolecular interactions between the two cages of the [2]catenane were observed, except the bowl-in-bowl arrangement of the ligands, which was relatively unusual since templation and structure directing supramolecular interactions such as π–π stacking or hydrogen bonding play an important role in the formation of catenanes or other interlocked molecular species. Another important finding was that when the pyridyl substituents on the CTB in **L21** were changed, to phenylpyrimidyl in **L22** reaction of the latter with $[Ag(CH_3CN)_4]BF_4$, afforded a single-cage $[M_3(\mathbf{L22})_2]^{n+}$ metallo-cryptophane **R28**, as could be observed in DMSO (**Figure 27**, right).[82]

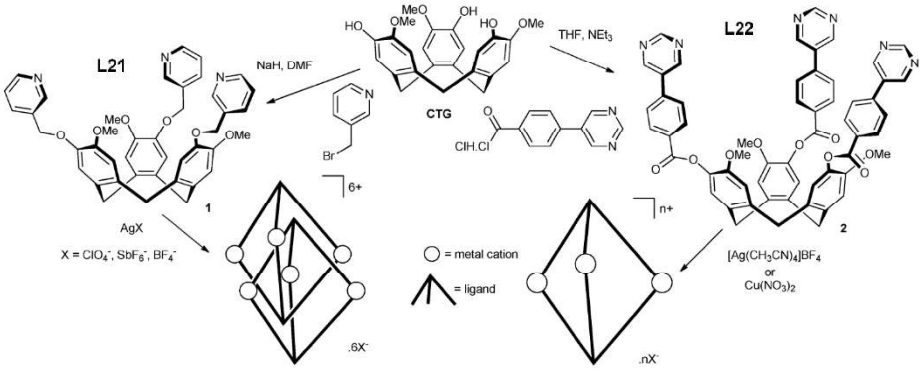


Figure 27. Synthesis of ligands **L21** and **L22**, and cartoon of [2]catenane and single cage formation (Reproduced from Ref [82]).

3.5 Emissive Ir^{III} Metallo-Cryptophanes

Luminescent metal cages have been reported, which owe their activity to the ligand moieties.[90–92] By contrast, rare are examples of cages exhibiting luminescence originating from metal-to-ligand charge transfer (MLCT). However, whatever they are organic cryptophanes or metallo-cryptophanes, almost no such examples have been reported. Hardie and her coworkers synthesized (±)-tris(isonicotinoyl)-cyclotriguaiacylene (**L23**) and (±)-tris(4-pyridyl-methyl)-cyclotriguaiacylene (**L24**),

which were reacted with $[Ir(ppy)_2(MeCN)_2]\cdot BF_4$ to form $[\{Ir(ppy)_2\}_3(L)_2]^{3+}$ metallo-cryptophanes, in which the bridges are cyclometallated Ir^{III} metal complexes. Since the $[Ir(ppy)_2]^+$ moieties are chiral, the combination of the chirality of the three metal-complex bridges and the chirality of the two CTBs will afford 12 stereoisomeric cages in solution. After equilibration for several months, these cages have undergone a ligand exchange process and have exhibited a significantly high degree of homochiral self-sorting of CTB ligands and metal complex bridges. However, when $[\{Ir(ppy)_2\}_3(\mathbf{L23})_2]^{3+}$ **R29** and $[\{Ir(ppy)_2\}_3(\mathbf{L24})_2]^{3+}$ **R30** were mixed, very slow exchange between **L23** and **L24** was observed, the near equilibrium being reached in a few months. These two metallo-cryptophanes are emissive in CH_2Cl_2 and in the solid state. $[\{Ir(ppy)_2\}_3(\mathbf{L1})_2]^{3+}$ showed a broad and unstructured emission both in solution and solid state which arose probably from a mixed ^{3}MLCT/^{3}LLCT state. The photoluminescence spectrum showed that the solution luminescence (λ_{max} = 604 nm) was red shifted in the solid state (λ_{max} = 648 nm). Compared to $[\{Ir(ppy)_2\}_3(\mathbf{L23})_2]^{3+}$, the photoluminescence spectrum of the metallo-cryptophane $[\{Ir(ppy)_2\}_3(\mathbf{L24})_2]^{3+}$ was more structured. In addition, a blue shift was observed, which could be explained by the absence of the electron-withdrawing ester moieties in **L24**. The photophysical properties of the two molecular cages are very different, indicating that they can be changed by adjusting the ligand CTB. This provides ideas for the application of metallo-cryptophanes, such as the detection of some small molecule guests through spectroscopy, photocatalysis, etc.[93]

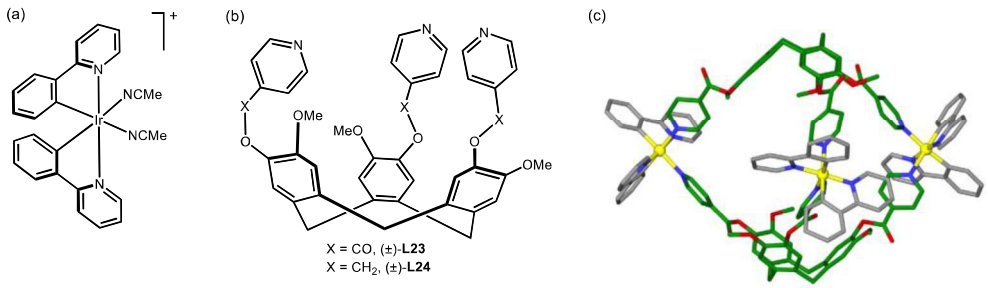


Figure 28. (a): The structure of $[Ir(ppy)_2(MeCN)_2]\cdot BF_4$; (b): the structure of **L23** and **L24**; (c): X-ray crystal structure of $[\{Ir(ppy)_2\}_3(\mathbf{L23})_2]^{3+}$ **R29** (Reproduced from Ref [93]).

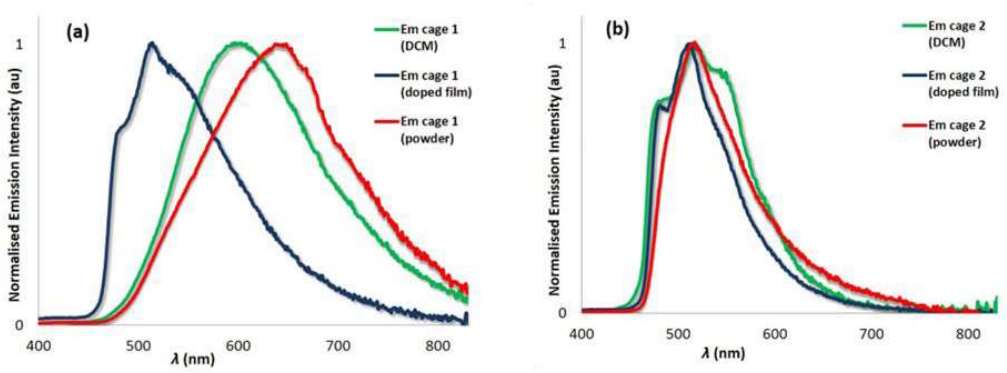


Figure 29. Emission spectra of the metallo-cryptophanes (a) $[\{Ir(ppy)_2\}_3(\mathbf{L23})_2]^{3+}$ **R29** and (b) $[\{Ir(ppy)_2\}_3(\mathbf{L24})_2]^{3+}$ **R30** in different media: CH_2Cl_2 solution and solid state (either film or powder) (Reproduced from Ref [93]).

4. Objectives

Originally, cryptophanes are organic hosts that were designed by André Collet in the early 1980s, and that are able to encapsulate species as diverse as the xenon atom, alkanes, halogenated solvents, quaternary ammoniums, and the fullerenes. Importantly also, enantioselective recognition has been observed when chiral cryptophanes were used as hosts. But actually, there was no luminescent metallo-cryptophanes reported excepted the Ir^{III} metallo-cryptophanes, which were synthesized and studied by Hardie and her coworkers. However, the research on the recognition properties of its host and guest has not been studied by electronic spectroscopy. In this thesis, we synthesized and studied two different series of light-emitting molecular precursors of metallo-cryptophanes:

(1) Gold alkynyl-substituted CTBs as potential precursors of organometallic cryptophanes based on aurophilic interactions.

The molecular structures and the chemistry of gold(I) phosphine alkynyl complexes have attracted growing attention, in part due to the reports on their rich luminescence properties and also because of the similarity in energy and directionality between aurophilic interactions and hydrogen bonds. Aurophilicity plays a key role in molecular aggregation in both solid state and solution. Our first objective was to design, synthesize, and study gold alkynyl-substituted CTBs bearing phosphine terminal ligands as potential precursors of luminescent organogold cryptophanes.

(2) The pre-cryptophanes: Towards metallo-cryptophanes combining robust, organometallic bonds and labile coordination bonds

The metallo-organic cryptophanes will be constructed from asymmetric CTBs containing two identical monodentate metal binding sites forming weak coordination bonds (carbonitrile function (RCN)) and a monodentate binding site capable of establishing strong organometallic bonds (terminal alkyne function (RCCH)). Platinum (II)-acetylide was selected because of the remarkable properties of the complexes

constructed from this metal-carbon bond. The pre-cryptophanes will then be converted into the corresponding organometallic cryptophanes by a simple coordination of $[PdL]^{2+}$ or $[PtL]^{2+}$ metal complex fragments to the nitrile groups.

Part I: Gold Alkynyl-Substituted CTBs as Potential Precursors of Organometallic Cryptophanes Based on Aurophilic Interactions

1. Introduction and Objectives of Part I

Gold(I) has a [$5d^{10}$] closed-shell electronic configuration. Therefore, gold (I) centers contained in a given molecule or different molecules undergo attractive interactions to reach an intra- or inter-molecular equilibrium distance in the range of 2.50–3.50 Å, much less than the sum of their van der Waals radii (3.80 Å). The terms "aurophilic interaction" were introduced by Schmidbaur in 1990 to qualify the Au···Au bond, which has a strength of 5–10 kcal/mol, that is, similar to that of hydrogen bonds.[94–96] In the past few decades, metal alkynyl complexes and their potential applications in molecular electronics and materials science have attracted a lot of interest and more and more work has been reported, especially for gold(I) derivatives. Gold(I) alkynyl complexes with phosphine auxiliary ligands arose interest not only because of their rich luminescence properties among which, some are related to aurophilic interactions, but also because of their linear coordination geometry, which prolongates the linearity of the π-unsaturated acetylide unit. A lot of mono-, di-, tri-, and polynuclear gold(I) complexes have been reported, in particular by the groups of Yam and Che. These complexes show strong phosphorescence and have rich photophysical and luminescent properties in which Au···Au interactions play a significant role. Normally, an increase in the Au···Au interaction leads to a shift of the emission to a lower energy, mainly in the yellowish-green to red region. A wide variety of transitions, e.g. (metal-perturbed) intra-ligand transitions, metal-centered transitions and metal-to-ligand charge transfer, are thought to be responsible for these luminescent properties.[97–101]

1.1 Intramolecular Aurophilic Interactions

Intramolecular $Au^{I}\cdots Au^{I}$ interactions can be observed in molecules and molecular ions containing more than one gold atom, and can be identified by short Au···Au distances in the solid state or limited structural flexibility in solution. These interactions are favored when the gold atoms are connected by molecular frameworks that allow them to approach each other. Therefore, they are supported by preorganization. This "template" effect is illustrated in **Figure 30** for the most common cases, where two

linearly two-coordinate gold(I) atoms are intramolecularly bound by aurophilic interactions.[94]

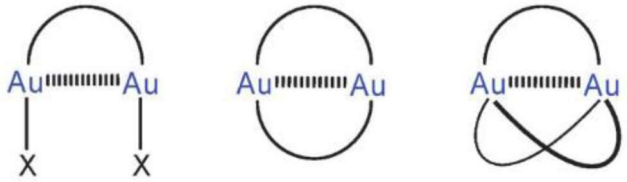


Figure 30. Three possibilities of intramolecular aurophilic interactions in (a) open, (b) macrocyclic, and (c) macrobicyclic systems.

We review, in this paragraph, several examples of gold complexes exhibiting intramolecular aurophilic interactions. For complex $[Au_4(tppb)(C{\equiv}CPh)_4]$ **R31** (tppb is 1,2,4,5-tetrakis(diphenylphosphino)-benzene, **Figure 31**) short intramolecular Au···Au contacts between adjacent Au units in the X-ray molecular structure were observed. The distances between two gold atoms were 3.15 Å, which was similar to Au···Au distances in other Au phosphine complexes and shorter than the sum of the van der Waals radius of Au^I. As shown by the X-ray crystal structure in **Figure 31**, The shape of this molecule is a little distorted, which is probably due to the steric hindrance. By the rotation of P-C σ bonds, the phenyl rings on the neighboring PPh_2 groups are far from each other so that the two gold atoms are able to approach each other.[102]

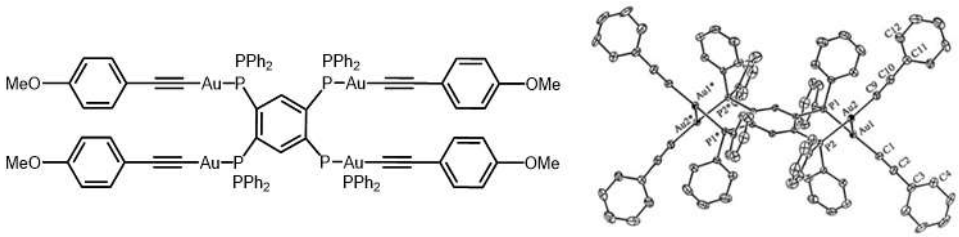


Figure 31. Molecular and X-ray crystal structure of $[Au_4(tppb)(C{\equiv}CPh)_4]$ **R31**.

The binuclear gold(I) complex $[(bpyC{\equiv}CAu)_2(\mu\text{-dppf})]$ **R32** (**Figure 32**) was reported by Chen and his coworkers. Because of the ferrocenyl platform, the two phosphine ligands were *cis*-arranged, so that the binuclear gold complex showed an Au···Au interaction at a short distance of 3.255 Å. Noticeably, the aurophilic interaction

was broken with the addition of two equiv of $Er(hfac)_3$ that forced the *trans*-conformation by coordination of Er^{3+} with 2,2′-bipyridyl.[103]

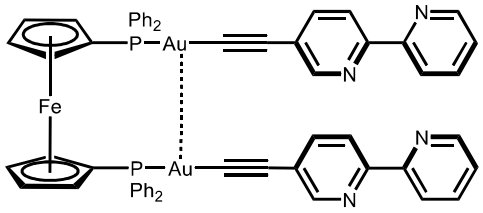


Figure 32. Structure of [(bpyC≡CAu)$_2$(μ-dppf)] **R32** showing the intramolecular aurophilic interactions.

The trinuclear gold(I) complex cation [(dppm)$_2$Au$_3${C≡CC(=CH$_2$)Me}$_2$][Au{C≡CC(=CH$_2$)Me}$_2$] **R33** consists of three gold(I) atoms arranged in a triangular array. The view of its X-ray molecular structure reproduced in **Figure 33** shows the three short Au···Au contacts of 3.1152(9), 3.1538(9) and 3.1490(9) Å, which are indicative of the presence of weak Au···Au interactions. Two of the gold (I) atoms are coordinated to an alkynyl carbon and one phosphorus atom, while the other gold (I) atom is coordinated to two phosphorus atoms of two dppm ligands.[104]

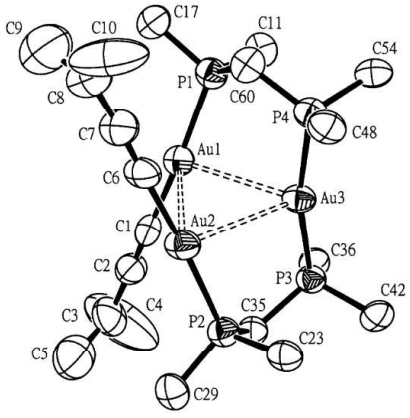


Figure 33. ORTEP view of the trinuclear cationic gold(I) complex [(dppm)$_2$Au$_3${C≡CC(=CH$_2$)Me}$_2$] (Reproduced from Ref [104]).

1.2 Intermolecular Aurophilic Interactions

Evidence for intermolecular Au···Au short contacts has not only been found by investigating simple mononuclear gold(I) complexes, but also dinuclear or multinuclear complexes. The gold atoms of these complexes are bridged by different ligands, and they may or may not be engaged in intramolecular aurophilic interactions. Experimental evidence showed that aurophilic interactions can be neither limited to a particular direction nor limited in number if there is no steric hindrance between the gold atoms. As a consequence, not only dimers, but also larger aggregates and polymers could be formed, as shown in **Figure 34**.[94]

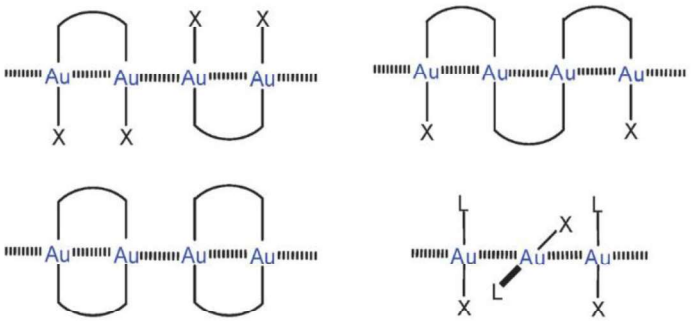


Figure 34. Different possibilities of intermolecular aurophilic interactions (Reproduced from Ref [94]).

We now illustrate the occurrence of intermolecular Au···Au interactions with two examples taken from the literature. Complex [$Me_3PAuC{\equiv}CC_6H_2Me_2C{\equiv}CAuPMe_3$] **R34** showed a polymeric structure in the crystal, the rod-shaped molecules, held together by relatively short aurophilic interactions forming a zig-zag chain. The intermolecular Au···Au distance in this organometallic polymer is 3.1361 Å. Noteworthy, the aurophilic interactions were unsupported, no π-stacking of the aromatic rings being observed since the distance between two adjacent aromatic rings was quite large (9.18 Å).[99]

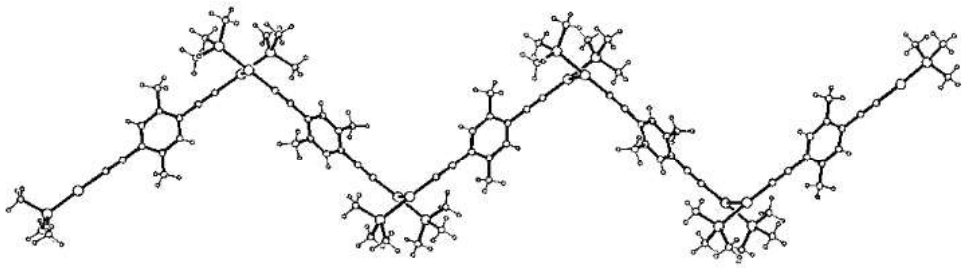


Figure 35. ORTEP view of the X-ray crystal structure of the complex [$Me_3PAuC{\equiv}CC_6H_2Me_2C{\equiv}CAuPMe_3$] **R34**. Intermolecular Au···Au contacts between adjacent molecules lead to a polymeric zigzag chain structure (Reproduced from Ref [99]).

An interesting observation was performed in the dinuclear complex {[Au(C≡CPh)]}$_2$[(μ-dppe)] **R35**. Although this complex, in which two gold atoms are bridged by 1,2-bis(diphenylphosphino)ethane is dinuclear, it did not exhibit any intramolecular aurophilic interaction. However, according to X-ray crystal structure analysis, two molecules of {[Au(C≡CPh)]}$_2$[(μ-dppe)] **R35** are arranged *anti* to each other through intermolecular aurophilic interactions. The distance between two gold atoms is 3.15 Å, which is of the same order of magnitude as the one measured in the case presented above.[105]

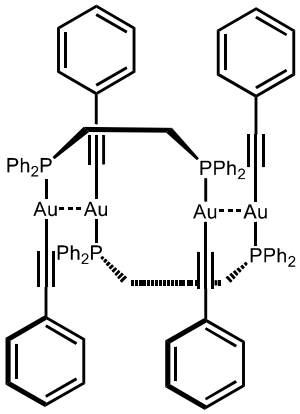


Figure 36. Schematical drawing of the molecular structure of {[Au(C≡CPh)]}$_2$[(μ-dppe)] **R35** observed in the solid state.

1.3 The Luminescent Properties of Gold Phosphine Alkynyl Complexes

Generally, the emission bands in gold(I) alkynyl complexes around 400 nm are observed. Emission quenching under oxygen, and the large Stokes shift relative to the

absorption band (250-350 nm) indicate that this emission originates from a triplet excited state. The heavy atom effect caused by the introduction of the $AuPR_3$ subunit into the organic alkynyl backbone increases the possibility of observing triplet emission at ambient temperature.[95,96]

The Yam and Che groups reported on the synthesis of series of mono-, di- and poly-nuclear gold(I) complexes and on the study of their luminescence. This studies showed that both phosphine and alkynyl ligands have an effect on the absorption and emission properties of the complexes. The high-energy absorption bands were assigned as phosphine-centered intraligand (IL) transitions and $\pi\rightarrow\pi^*(C\equiv C)$ transitions. The low energy absorption bands were tentatively assigned as metal-perturbed IL $\pi\rightarrow\pi^*(C\equiv C)$ transitions with metal-to-ligand charge transfer (MLCT) character. In the solid state, the lowest energy emission over 500 nm was tentatively assigned to the Au···Au interaction which originated from $^3(d_\sigma^*\rightarrow p_\sigma)$ or $^3(d_\delta^*\rightarrow p_\sigma)$.[97,104,106–108]

For example, the dinuclear complex $[Me_3PAuC\equiv CC_6H_2Me_2C\equiv CAuPMe_3]$ **R34** showed strong emission bands at 415 nm in solution upon excitation at 350 nm which were assigned to $^3(\pi^*\rightarrow\pi)$ or $^3(\pi^*\rightarrow\sigma)$ transitions, but in the solid state, a dramatic red shift happened. Emission bands were observed at 540 nm, as in other complexes exhibiting Au···Au interactions.[99]

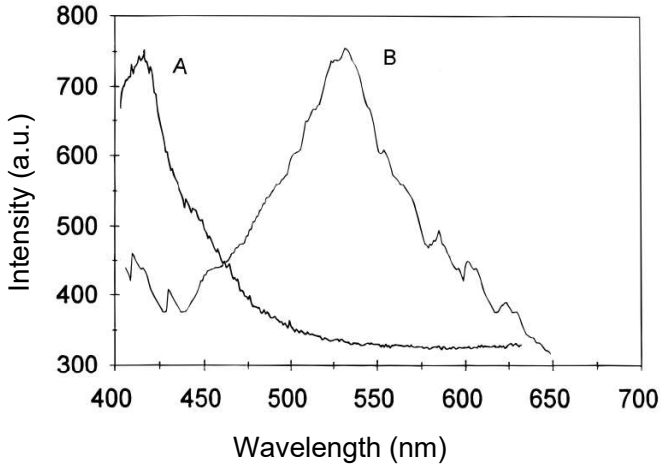


Figure 37. Emission spectra of the alkynyl complex **R34** at 298 K; (A) in CH_2Cl_2 solution and (B) in the solid state (Reproduced from Ref [99]).

Among the dinuclear gold(I) alkynyl complexes synthesized in the Yam group, two of them showed intramolecular Au···Au interactions with distances of 2.84 (**R37**) and 3.07 Å (**R38**). The luminescence lifetimes were in the microsecond range, indicating that their emissions corresponded to phosphorescence. A red shift in emission energy of **R36** relative to **R37** (**R36**: λ_{em} = 615 nm; **R37**: λ_{em} = 539 nm) was attributed probably to the presence of the less electron-rich diphosphine ligands. The slightly red shifts in emission energy of **R37** relative to **R38** (**R38**: λ_{em} = 493 nm) probably had a relationship with the strength of intramolecular Au···Au interactions, as reflected by the shorter Au···Au contacts in the X-ray structure.[109]

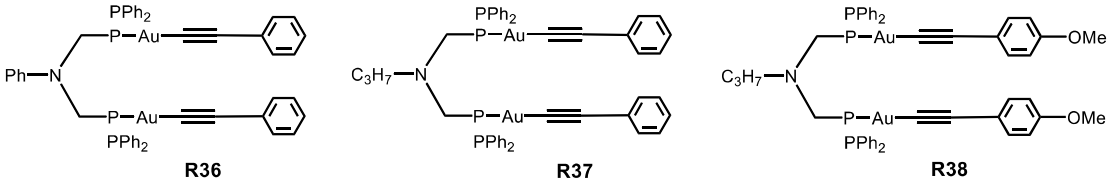


Figure 38. The structures of dinuclear gold(I) alkynyl complexes **R36**, **R37** and **R38**.

1.4 The Applications of Gold(I) Alkynyl Complexes

Puddephatt and his group discovered the first organometallic catenanes by self-assembly from oligomeric dinuclear phosphine gold alkynyl complexes. The studies showed that phosphine ligands played a significant role on determining how the self-assembly provided [2]catenane [1+1], [2+2], and [4+4] assemblies. X-ray crystal structure analysis showed intramolecular aurophilic interactions at distances of 3.19 and 3.14 Å, which templated the [2]catenane **R39** [1+1] assembly. Importantly the [2]catenanes were chiral and their formation from achiral precursors could be monitored by ^{31}P NMR spectroscopy in solution. These discoveries showed that it is possible to predict the nature of the self-assembly at least in a series of closely related compounds, which could be used to design and synthesize more functional materials.[110]

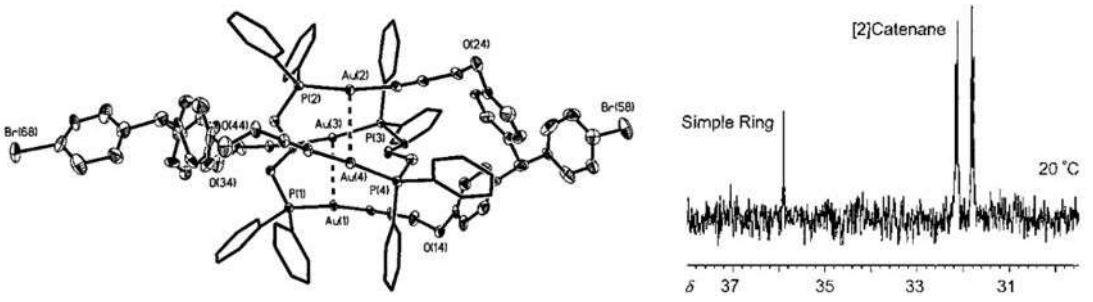


Figure 39. ORTEP view of the X-ray crystal structure of a [2]catenane **R39** complex exhibiting aurophilic interactions and its ^{31}P NMR spectrum (Reproduced from Ref [110]).

The establishing of aurophilic interactions could be also used for chemosensing purposes. Chao and his group developed a tripodal gold(I) acetylide complex **R40** that was used as luminescent sensor to detect cations. The studies showed that this complex had an excellent selectivity for Ag^+. Upon the addition of Ag^+, a new emission band at 472 nm appeared, and its intensity increased with the increase of the Ag^+ concentration. In addition, the luminesence of the solution under UV irradiation changed dramatically from blue-violet in DMSO solution to blue-green (**Figure 40**). The electronic absorption and luminescence titration experiments allowed the authors to determine that the binding stoichiometry was 1:1, and the log *K* of the association constant was 4.56 ± 0.21. The "closed clamp" conformation of the Ag^+ adduct shown in **Figure 40** was established by ^{1}H NMR titration experiments.[111]

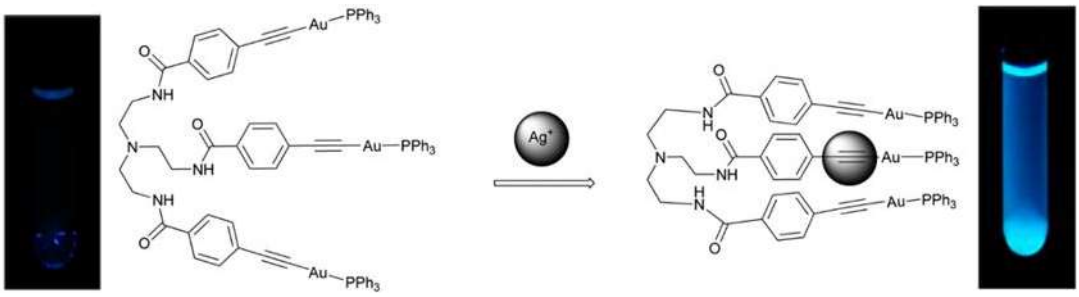


Figure 40. Schematic representation of the luminescent tripodal gold(I) acetylide sensor **R40**, and the selective recognition of Ag^+. Photographs of the test tubes containing a solution of the sensor without (left) and in the presence of Ag^+ (right) under UV light irradiation (Reproduced from Ref [111]).

Chao and his coworkers also synthesized a series of mononuclear gold acetylide complexes incorporating a diphenylurea group, which was used to recognize anions (**Figure 41**). They showed that the functional groups R substituting the terminal phenyl substituent of the urea moiety had an effect on the anion binding constants, which decreased with the increasing electron-donating character of R, but the phosphine ligands of gold showed only a weak influence on the anion binding ability of these urea receptors. In addition, the interactions between the gold acetylide complexes and anions were carried out in different solvents. In the less polar solvent THF, the binding constants span a wider range of values than in DMSO. However in this more polar solvent, complex **R41** (R = NO_2) showed a stronger color change in the presence of F^-, providing an easy means for the detection of F^- with the naked eye.[112]

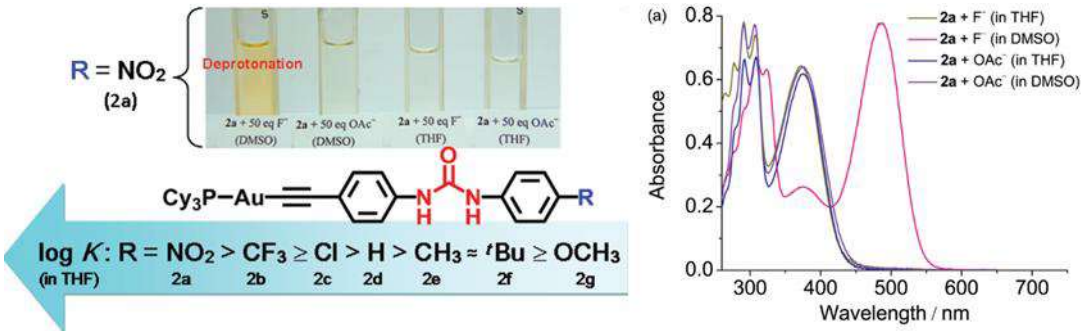
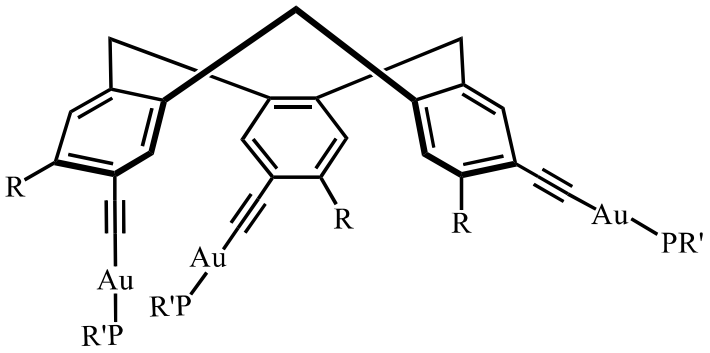


Figure 41. The recognition of F^- with the naked eye and the UV–vis absorption spectra of the gold(I) acetylide complex **R41** in THF or DMSO in the presence of F^- and OAc^- (Reproduced from Ref [112]).

1.5 Objectives

As mentioned in the Introduction chapter, cryptophanes were originally organic hosts. Nevertheless, in the last 20-25 years, self-assembly approaches to cryptophanes, by means of coordination bonds and dynamic covalent chemistry, were developed. Alkynyl-substituted CTBs were known[113–115], but were not used for the preparation of organometallic derivatives. In addition, rare are reports on luminescent cryptophanes as well. In this first part of our thesis work, we report on a series of gold(I) acetylide CTB complexes. These complexes, shown in **Figure 42**, were synthesized in order to test if it would be possible to form organogold cryptophanes by self-dimerization of

gold(I) acetylide CTBs based on aurophilic interactions. Such an appraoch would expand the diversity of methods used for the assembly of cryptophanes based on metal coordination. In addition, it would take advantage of the luminescence of the gold(I) alkynyl complex subunits to create original luminescent metallo-cryptophane receptors, which could be used for the recognition and detection of guests by electronic emission spectroscopy. When gold CTB complexes are written CTB(3R; $2C_2AuPR'$, C_2AuPR'') (R = H, OMe), it means that one of the phosphine ligands is replaced by another different phosphine ligand. **C8** stands for CTB(3H; $2C_2AuPPh_3$, C_2H), one of the gold phosphine ligands being replaced by a proton.



Series 1:
C1: R = H, R' = Ph_3
C2: R = H, R' = Ph_2Me
C3: R = H, R' = $PhMe_2$
C7: R = H, R' = Et_3
C9: R = H, R' = Cy_3

Series 2:
C4: R = OMe, R' = Ph_3
C5: R = OMe, R' = Ph_2Me
C6: R = OMe, R' = $PhMe_2$

Figure 42. Molecular structures of the gold(I) alkynyl CTB complexes synthesized and investigated in Part I.

2. Synthesis, Characterization, Purification and Resolution of the Precursors CTB(H,C_2H) and CTB(OMe,C_2H), and of the Gold Alkynyl CTBs C1 – C9

CTB(H,C_2H) was synthesized from the known **CTB(H,OTf)**[116] by Sonogashira cross-coupling reaction[117] with trimethysilylacetylene ($TMSC_2H$), using $[Pd(PPh_3)_2Cl_2]$ as catalyst and Et_3N as base, followed by removal of the TMS protecting groups with tetrabutylammonium fluoride. The yield was 80% for the two steps. The known **CTB(OMe,C_2H)** was obtained in two steps from **CTB(OMe,I)**[31] according to the literature in 45% overall yield.[118]

The trinuclear gold alkynyl CTB complexes **CTB(R,C_2AuPR')** (**C1:** R = H, R' = Ph; **C2:** R = H, R' = Ph_2Me; **C3:** R = H, R' = $PhMe_2$; **C4:** R = OMe, R' = Ph; **C5:** R = OMe, R' = Ph_2Me; **C6:** R = OMe, R' = $PhMe_2$; **C7:** R = H, R' = Et; and **C9:** R = H, R' = Cy), were prepared by nucleophilic substitution of [ClAuPR'] (Method A) (R' = Ph, Ph_2Me, $PhMe_2$, Et_3, and Cy_3) by **CTB(H,C_2H)** and **CTB(OMe,C_2H)** using sodium methoxide as base.[104,119] As attempts to purify some of these complexes by silicagel column chromatography led to partial decomposition, which was also noted in the literature[111], they were isolated by precipitation from CH_2Cl_2 solutions by addition of cyclohexane or methanol, and were obtained in good yields (**Table 1**). Following other literature approaches, **C1 – C6** were also prepared from insoluble polymer precursors **[CTB(R,C_2Au)]**$_n$ (Method B), which are obtained by reaction of **CTB(R,C_2H)** with $[Au(SMe_2)Cl]$ or [Au(THT)Cl] in the presence of sodium acetate. The organometallic polymers were then reacted with the stoichiometric amount of phosphine ligands at room temperature in CH_2Cl_2, which afforded **C1 – C6** after purification as reported above.[120–122] The yields are collected in **Table 1**. It is important to note that **C7** and **C9** were not obtained in these conditions since the polymer intermediates were decomposed after the addition of PEt_3 and PCy_3. These complexes were air stable and soluble in chlorinated solvents such as CH_2Cl_2 and $CHCl_3$.

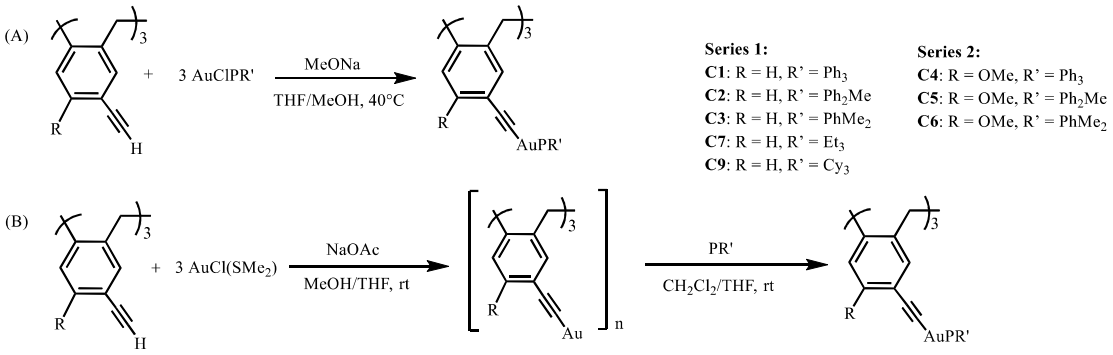


Figure 43. The two synthetic routes to gold alkynyl CTB complexes (a) Through nucleophilic substitution of [AuClPR'$_3$] by **CTB(R,C$_2$H)** in the presence of a base; (b) Through the intermediate organogold polymer **[CTB(R,C$_2$Au)]**$_n$.

Table 1. Yields of the Au(I) CTB complexes obtained by method A and method B.

	C1	**C2**	**C3**	**C4**	**C5**	**C6**	**C7**	**C9**
Method A	60%	43%	/	76%	80%	60%	68%	72%
Method B	78%	80%	53%	/	60%	72%	/	/

The CTBs of this study being C_3-symmetric, they are chiral. Therefore, it was interesting to investigate them by HPLC on chiral stationary phases. Examination of the ligand precursor **CTB(H,C$_2$H)** by analytical chiral HPLC (Chiralpak IB, heptane/ethanol/dichloromethane (70/10/20, v/v) as eluent) showed two elution peaks, at 5.38 and 6.44 min. Accordingly, racemic **CTB(H,C$_2$H)** could be separated into its two enantiomers using a preparative Chiralpak IB column and eluting with the solvent mixture heptane/ethanol/dichloromethane (70/10/20), v/v. The fractions were examined by polarimetry, which indicated that the optical rotary powers (**Table 2**) of the first and second eluted enantiomers of **CTB(H,C$_2$H)** had a negative and a positive sign, respectively. As shown in **Figure 44**, The ECD spectra of (+)-**CTB(H,C$_2$H)** and (–)-**CTB(H,C$_2$H)** in dichloromethane show features that are perfect mirror images of each other. The yields of each enantiomer (–)/(+)-**CTB(H,C$_2$H)** were both 35%. The rate constant for the inversion of **CTB(H,C$_2$H)** was $k_{\text{enantiomerisation}} = 1.40 \times 10^{-6}$ s^{-1}. The energy barrier for enantiomerization was $\Delta G^{\neq} = 111.9$ kJ/mol and the corresponding half-time was $t_{1/2} = 69$ hours at 40 °C in dichloromethane.

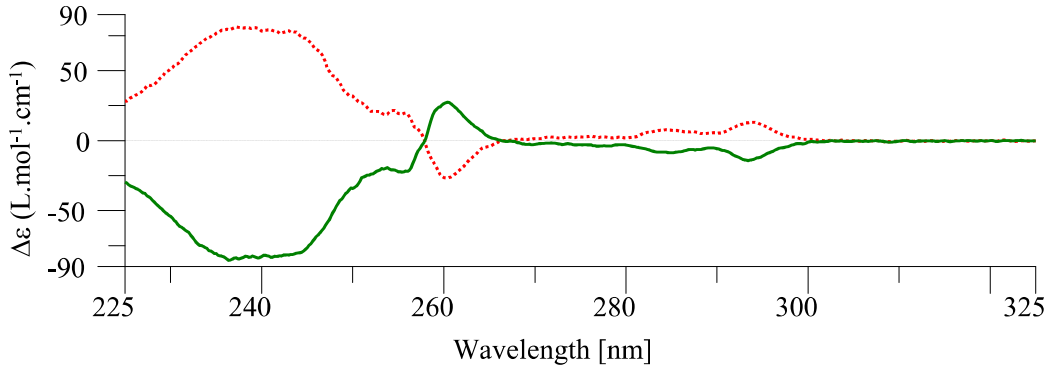


Figure 44. ECD spectra of optically pure **CTB(H,C$_2$H)** in dichloromethane. The green solid line is the spectrum of the first eluted enantiomer, **(–)-CTB(H,C$_2$H)**; the red dotted line, the one of the second eluted enantiomer, (+)-**CTB(H,C$_2$H)**.

The other ligand precursor, **CTB(OMe,C$_2$H)**, was also subjected to analytical chiral HPLC (Chiralpak ID, heptane/ethanol/dichloromethane (40/30/30, v/v.) as eluent). It also showed two elution peaks, at 4.01 and 5.49 min. Preparative chiral HPLC afforded the separate enantiomers, the yield of each enantiomer was 51% for (–)-**CTB(OMe,C$_2$H)** and 34% for (+)-**CTB(OMe,C$_2$H)**. The corresponding optical rotations are given in **Table 2** and the ECD spectra are shown in **Figure 45**. The polarimetry data indicate that the first eluted enantiomer (green solid line) is (–)-**CTB(OMe,C$_2$H)**, and that the second eluted enantiomer (red dotted line) is (+)-**CTB(OMe,C$_2$H)**. According to kinetic measurements, the rate constant for the inversion of **CTB(OMe,C$_2$H)** is $k_{\text{enantiomerisation}} = 3.74 \times 10^{-5}$ s^{-1}, the energy barrier $\Delta G^{\neq}$ for enantiomerization being 110.8 kJ/ mol and the corresponding half-time $t_{1/2}$, 154 min at 62 °C in chloroform.

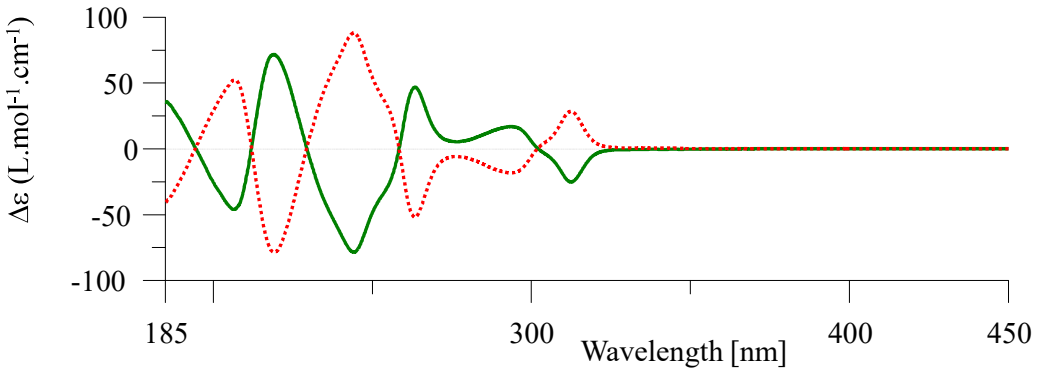


Figure 45. ECD spectra of optically pure **CTB(OMe,C$_2$H)** in acetonitrile. The green solid line is the spectrum of the first eluted enantiomer, **(–)-CTB(OMe,C$_2$H)**; the red dotted line, the one of the second eluted enantiomer, (+)-**CTB(OMe,C$_2$H)**.

In principle, the optically pure **CTB(R,C$_2$AuPR')** complexes could also be obtained by resolution of the corresponding racemates by column chromatography on a chiral phase. **C1** and **C5** were successfully resolved into their respective enantiomers. However, for **C1**, noticeable decomposition was observed as shown in the chromatogram of **Figure 46**: According to analytical chiral HPLC (using Chiralpak IF as column and heptane/ethanol/dichloromethane 20:40:40 v/v as eluent), the gold CTB complex **C1** showed two elution peaks, at 3.97 and 6.34 min. In addition, two other elution peaks, with weaker intensity, were observed at 3.74 and 5.42 min. As shown by polarimetry, they had opposed signs, and thus corresponded to another a pair of enantiomers (called **C8**). As a consequence, the resolution of **C1** was performed in two steps. First, using a Chiralpak IF column and eluting with heptane/ethanol/dichloromethane 20:40:40 v/v, optically pure (+)-**C1** and (+)-**C8** were obtained. Then the mixture of (−)-**C1** and (−)-**C8** was injected on the (*S*,*S*)-Whelk-O1 column, which showed two elution peaks, at 7.55 and 9.94 min, eluting with heptane/ethanol/dichloromethane 40/30/30 v/v. The procedure provided the optically pure (−)-**C1**, and (−)-**C8**, which was confirmed to be CTB(3H;2C$_2$AuPPh$_2$,C$_2$H) by ^{1}H NMR and ESI-MS. The yield of optically pure (–)-**C1** was 21%, (+)-**C1** was 27%, (–)-**C8** was 6%, and (+)-**C8** was 4%.

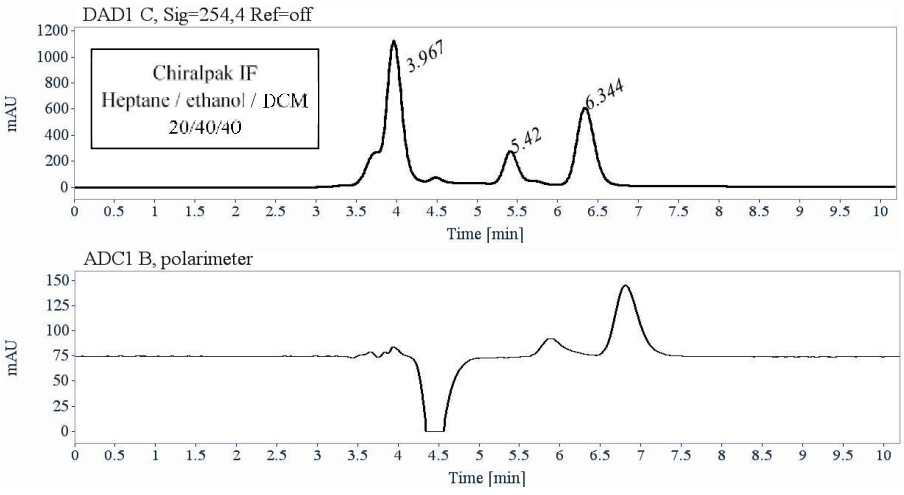


Figure 46. Chromatograms of the mixture of **C1** and **C8** preparative HPLC on Chirapak IF and polarimetry at 254 nm.

In the case of **C5**, no decomposition was observed. Analytical chiral HPLC using Chiralpak IB as column and heptane/ethanol/dichloromethane 40:40:20 v/v as eluent showed two elution peaks, at 9.31 and 16.65 min. The enantiomers were subsequently separated by preparative chiral HPLC, the conditions being the same as for the analytical separation. The yield of each enantiomer was 39% for (–)-**C5**, and 35% for (+)-**C5**. The polarimetry data of **C5** are collected in **Table 2**. They indicate that the first eluted enantiomer of **C5** is (–)-**C5**, and that the second eluted enantiomer is (+)-**C5**.

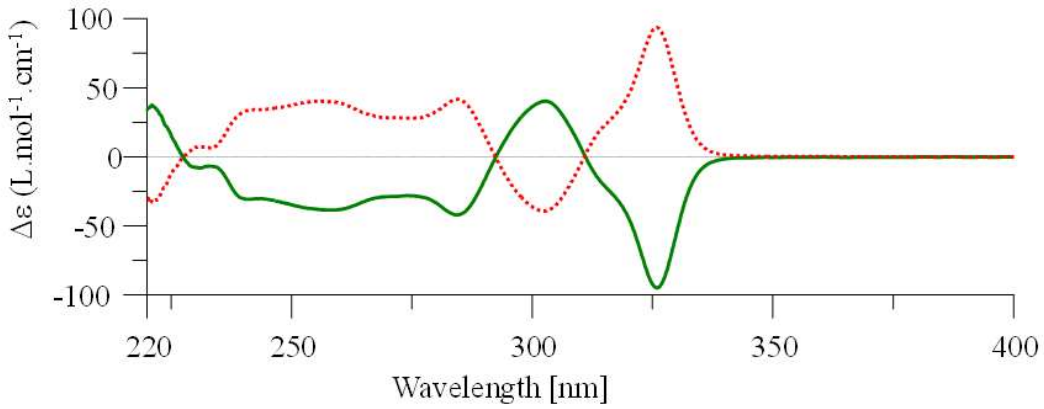


Figure 47. ECD spectra of optically pure **C5** in acetonitrile. The green solid line is the spectrum of the first eluted enantiomer, (–)-**C5**; the red dotted line, the one of the second eluted enantiomer, (+)-**C5**.

Table 2. Specific rotations of CTBs and gold(I) CTB complexes in CH_2Cl_2 at 298 K.

Compound	Concentration (g/mL)	λ (nm)					
		589	578	546	436	405	365
CTB(H,C$_2$H)	1st eluted (C = 0.121)	– 634	– 659	– 771	– 1479	/	/
	2nd eluted (C = 0.067)	+633	+660	+769	+1482	/	+2800
CTB(OMe,C$_2$H)	1st eluted (C = 0.112)	– 139	– 149	– 180	/	/	/
	2nd eluted (C = 0.128)	+ 138	+ 148	+ 178	/	/	/

Table 2 (Continued)

Compound	Concentration (g/mL)	λ (nm)					
		589	578	546	436	405	365
C4	1st eluted (C = 0.073)	+273	+287	+348	+772	/	/
	2nd eluted (C = 0.071)	– 273	– 287	– 348	– 772	/	/
C5	1st eluted (C = 0.073)	– 220	– 231	– 275	– 619	– 901	/
	2nd eluted (C = 0.071)	+ 220	+ 231	+ 275	+ 619	+ 901	/
C6	1st eluted (C = 0.095)	+ 262	+ 276	+ 334	+ 736	/	/
	2nd eluted (C = 0.04)	– 265	– 280	– 338	– 745	/	/

The gold alkynyl CTB complexes were characterized by ^{1}H, ^{13}C, and ^{31}P NMR spectroscopies, ESI-TOF mass spectrometry, IR spectroscopy, and elemental analysis. Upon metallation of **CTB(H,C$_2$H)** and **CTB(OMe,C$_2$H)**, the singlet of the alkynyl proton at 3.02 and 3.24 ppm, respectively, disappeared, which provided a convenient method for monitoring the reaction by ^{1}H NMR spectroscopy. The ^{1}H NMR spectra of **CTB(H,C$_2$H)** and **CTB(OMe,C$_2$H)** showed the typical pairs of doublets for the diastereotopic axial (a) and equatorial (e) protons of the methylene bridges, the classical patterns of the α (d), γ (dd) and α' (d) protons for singly γ'-C substituted **CTB(H,C$_2$H)**, and a singlet for each of the α and α' protons of doubly substituted **CTB(OMe,C$_2$H)**. The same patterns were of course observed in the spectra of the corresponding gold complexes. The chemical shifts of the protons of the ligand precursors and of the complexes are collected in **Table 3**. Complexation-induced shifts were observed. The general trends are the following: The protons α-H, γ-H, a-H and e-H in all the complexes were shielded by comparison with the corresponding ligand precursors. The protons γ-H and α-H were more and more shielded upon going from less (PPh_3) to more (PCy_3) electron donor phosphines. For the series **CTB(H,C$_2$AuPR')**, the α'-H protons were gradually shielded in the order **C1** < **C2** < **C3** < **C7** < **C9**, that is, followed the

electron-donating order of the phosphine terminal ligand: PPh_3 < PPh_2Me < $PPhMe_2$ < PEt_3 < PCy_3. The shifts are illustrated for the case of **C1** in **Figure 48**.

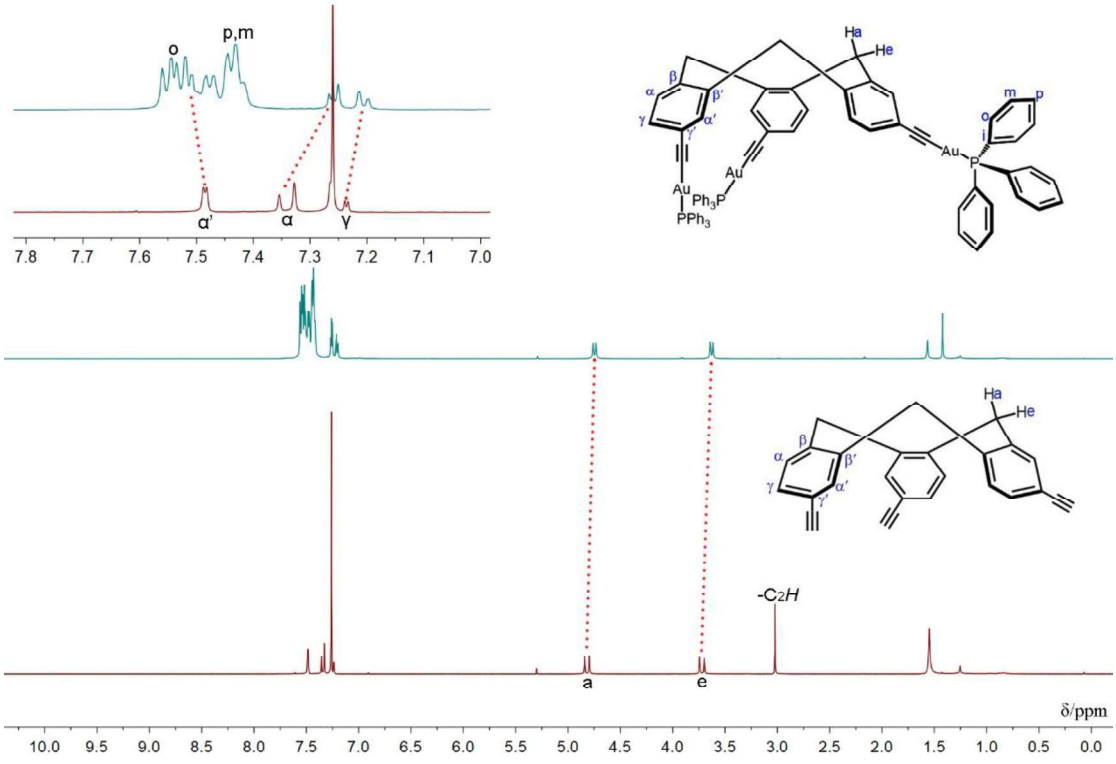


Figure 48. Comparison of the ^{1}H NMR spectra of **CTB(H,C$_2$H)** and **C1** in $CDCl_3$ at 298K.

For the series **CTB(OMe,C$_2$AuPR')**, the chemical shift of α-H protons almost did not change when the phosphine ligands changed; by contrast, α'-H protons were more and more deshielded upon going from less (PPh_3) to more ($PPhMe_2$) electron donor phosphines. The ^{31}P NMR data, also collected in **Table 3**, were in agreement with literature observations[123–126], that is, the chemical shifts of the bound phosphine ligands decreased in the order PCy_3 > PPh_3 > PEt_3 > PPh_2Me > $PPhMe_2$. The ^{13}C NMR spectra also showed interesting changes along both series of complexes. In particular, for all 8 complexes, strong downfield shifts for the alkynyl carbon ($\Delta\delta$ = ~ 20 ppm) and small upfield shifts for γ' ($\Delta\delta$ = ~ 2 ppm) were observed because of Au(I) coordination effects. Small downfield shifts were observed for β carbon, but no significant shifts were observed for the other carbons. Chemical shifts δ and CIS $\Delta\delta$ of selected carbons of the CTBs were collected in **Table 4**. The IR spectra of all the complexes showed the

characteristic, but weak signal corresponding to $\tilde{\nu}_{C\equiv C}$ at ~ 2100 cm^{-1}, which did not significantly differ from the corresponding band in the spectra of the CTB precursors. Investigations by ESI-TOF mass spectrometry showed that the molecular peak of the gold(I) CTB complexes could be observed by protonation, therefore corresponded to the singly charged ion $[M+H]^+$. They were best observed when the samples were dissolved in an acidic solvent mixture ($CHCl_3$/*i*PrOH/HCO_2H 1.00:0.99:0.01, v/v/v) before injection.

Table 3. ^1H[a] and ^{31}P[b] NMR data: Chemical shifts δ and CIS $\Delta\delta$ of selected protons of the CTBs.

Compound\H, P	**α'**	**α**	**γ**	**a**	**OMe**	**e**	**C_2H**	**P**
CTB(H,C_2H)	7.484	7.338	7.248	4.815		3.717	3.020	
C1	7.510	7.258	7.206	4.746		3.629		42.97
$\Delta\delta$	+0.026	–0.080	–0.042	–0.069		–0.088		
C2	7.490	7.247	7.186	4.742		3.624		27.19
$\Delta\delta$	+0.006	–0.091	-0.062	–0.073		–0.093		
C3	7.480	7.244	7.177	4.743		3.624		14.24
$\Delta\delta$	–0.004	–0.094	–0.071	–0.072		–0.093		
C7	7.459	7.215	7.163	4.715		3.595		37.22
$\Delta\delta$	–0.025	–0.123	–0.085	–0.100		–0.122		
C9	7.473	7.209	7.182	4.704		3.584		56.77
$\Delta\delta$	–0.011	–0.129	–0.102	–0.111		–0.133		
CTB(OMe,C_2H)	7.425	6.837		4.724	3.897	3.625	3.243	
C4	7.485	6.789		4.679	3.898	3.550		42.97
$\Delta\delta$	+0.060	–0.048		–0.045	+0.001	–0.075		
C5	7.468	6.783		4.679	3.888	3.591		27.15
$\Delta\delta$	+0.043	–0.054		–0.045	–0.009	–0.034		
C6	7.461	6.785		4.681	3.889	3.548		14.16
$\Delta\delta$	+0.036	–0.052		–0.043	–0.008	–0.077		

[a] δ, ppm downfield from TMS,setting the residual $CHCl_3$ signal to 7.26 ppm. [b] δ, ppm *vs* 85% aqueous H_3PO_4.

Table 4. ^{13}C[a] NMR data: Chemical shifts δ and CIS $\Delta\delta$ of selected carbons of the CTBs.

Compound\C	γ	β	α'	*o*	*p*	β'	*i*	*m*	γ'	α	C≡C	O*C*H$_3$	*C*H$_2$
CTB(H,C$_2$H)	131.1	140.0	133.9			139.1			121.1	130.4	83.5		36.9
C1	131.1	138.1	131.6	134.5	131.6	138.8	129.7	129.3	123.4	130.3	104.5/104.3		37.1
$\Delta\delta$	0	–1.9	–0.3			–0.3			2.3	–0.1	21		0.2
C2	131.0	138.1	134.1	133.0	131.6	138.8	131.6	129.3	123.4	130.2	104.7/104.5		37.1
$\Delta\delta$	–0.1	–1.9	0.2			–0.3			2.3	–0.2	21.2		0.2
C3	131.0	138.1	134.2	132.1	131.7	138.8	132.8	129.3	123.5	130.2	104.9/104.6		37.0
$\Delta\delta$	–0.1	–1.9	0.3			–0.3			2.4	–0.2	21.4		0.1
C7	130.9	138.0	134.1			138.8			123.5	130.2	104.3/104.1		37.0
$\Delta\delta$	–0.2	–2.0	0.2			–0.3			2.4	–0.2	20.9		0.1
C9	130.9	137.9	134.2			138.7			123.6	130.2	103.9/103.7		37.1
$\Delta\delta$	–0.2	–2.1	0.3			–0.4			2.5	–0.2	20.4		0.2
CTB(OMe,C$_2$H)	159.6	141.9	135.6			130.8			112.3	110.3	80.9/80.0	56.3	36.7
C4	159.4	139.8	135.8	134.5	131.6	130.6	129.8	129.2	112.7	111.9	99.9/99.7	56.3	37.1
$\Delta\delta$	0.2	–2.1	0.2			–0.2			0.4	0.6	19	0	0.4
C5	159.4	139.9	135.7	133.0	131.6	130.6	132.0	129.2	112.7	111.9	100.2/99.9	56.3	37.1
$\Delta\delta$	0.2	–2.0	0.1			–0.2			0.4	0.6	19.3	0	0.4
C6	159.4	139.9	135.7	132.2	131.7	130.6	132.9	129.2	112.8	111.9	100.3/100.1	56.3	37.1
$\Delta\delta$	0.2	–2.0	0.1			–0.2			0.5	0.6	19.4	0	0.4

[a] δ, ppm *vs* downfield from TMS,setting the residual $CHCl_3$ signal to 77.16 ppm.

3. Investigations on the Nuclearity of the Gold CTBs in Solution and Gas Phase

3.1 Investigations on the Nuclearity of the Gold CTBs in Solution by NMR Spectroscopy

We investigated if the gold CTBs could form face-to-face dimers through the interpenetration of $AuPR_3$ metal complex fragments and the establishment of aurophilic interactions. We chose to focus on **C1, C3** and **C4** for the following reasons: From the electronic viewpoint, triphenylphosphine is the less electron-rich among the phosphine ligands used and should be the most able to favor Au···Au interactions; from the steric viewpoint, the best compromise should be the use of $PPhMe_2$, which is much smaller than PPh_3, while being less electron-donor than PEt_3, for instance. Different techniques were involved, in particular ^1H NMR spectroscopy for the solution studies, and ESI-TOF MS for the gas phase studies. First, the ^1H NMR spectra of **C1** and **C4** in $CDCl_3$ were recorded at different concentrations, from 0.9×10^{-3} to 1.5×10^{-2} M. All the signals of **C1** were sharp and well resolved in diluted conditions, but as the concentration increased, the aromatic protons broadened. However, we did not observe significant chemical shift variations, whatever the proton signals considered. The change in concentration had hardly any effect on the protons of complex **C4**. Then the ^1H NMR spectrum of **C1** in CD_2Cl_2 was recorded at different temperatures between 298 and 193 K (**Figure 49**). At 298 K, the signals of the protons (α, α', γ, a and e-H) of the CTB part were sharp, while the signals of the protons of the triphenylphosphine ligand (o, o'; m, m'; p-H) were relatively broad. However, the latter proton signals became sharper gradually as the temperature decreased to 208 K. At the same time, the proton signals of the CTB moiety gradually broadened. In addition, weak upfield shifts of the signals of all the protons were observed, from – 0.03 ppm for α, α', γ, and e-H to – 0.07 and – 0.08 ppm for a-H and (o, o')-H, respectively. The changes of ^1H at different concentrations, and VT NMR for **C1** indicated that there was a fast exchange between monomer and dimer, if any, and the exchange was only slightly slowed down when the

temperature decreased.

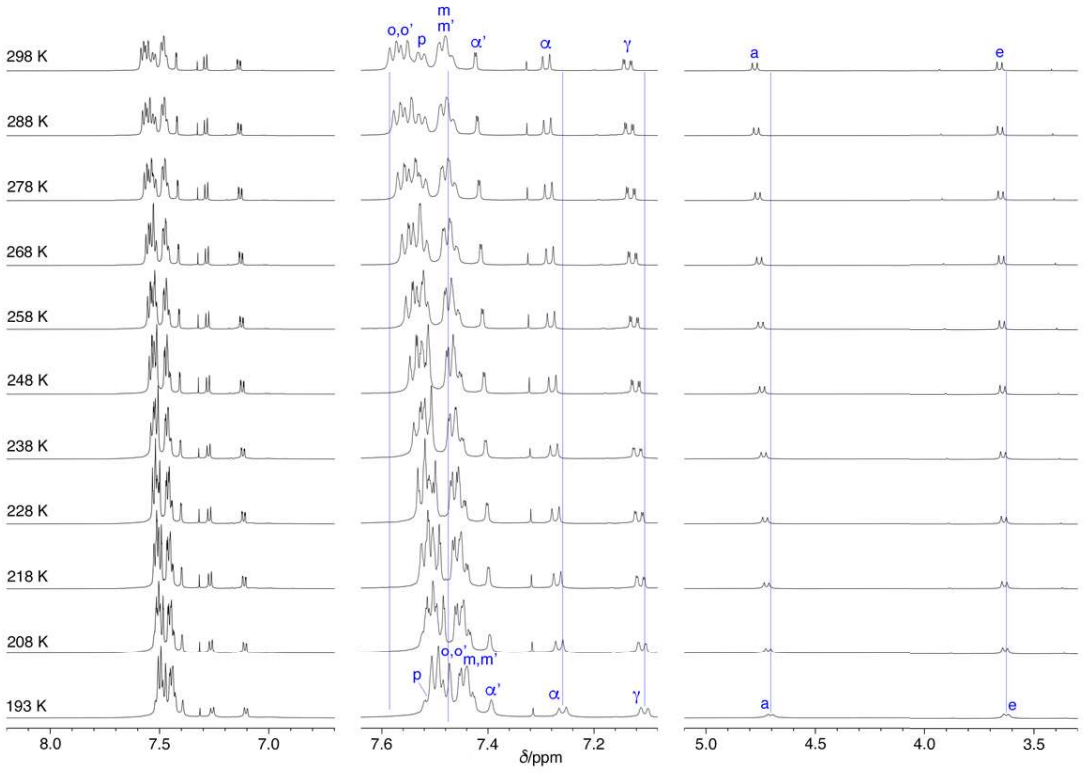


Figure 49. Variable temperature ^{1}H NMR spectra (CD_2Cl_2, 600 MHz) of **C1**. The vertical lines in blue show the upfield shifts of the proton signals.

Next, the starting **CTB(H,C$_2$H)** and the five complexes **C1**, **C3**, **C4**, **C7** and **C9** were studied by diffusion ordered spectroscopy (DOSY). The complexes **C7** and **C9** were used as references, being highly likely that they would not form dimers, because of the strong electron-donor character of PEt_3 and PCy_3, and, for the latter, its bulkiness. Our reasoning was the following: We made the hypothesis that all the Au(I) CTBs formed cryptophane-like dimers, and compared the hydrodynamic volumes obtained by the diffusion data (v_H) with the geometrical volumes (v_M). According to Corey-Pauling-Koltun (CPK) models, the overall shape of a virtual cryptophane obtained by interpenetration of two Au(I) CTBs, the concavities of which are placed face-to-face, is that of an oblate spheroid of equatorial radius *a* and polar radius *b*, or, if the bridging metal complex fragments contain large-size auxiliary ligands, is closer to that of a cylinder of diameter $d = 2a$ and length $L = 2b$ (The dimer model of **C1** is shown in

Figure 50).

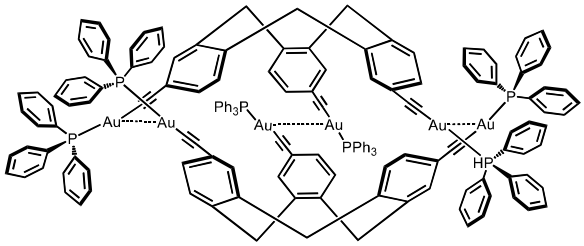


Figure 50. The dimer model of **C1**.

The geometrical characteristics of the virtual CTB dimers were estimated using CPK molecular models. The hydrodynamic radii were obtained from the measured translational diffusion coefficients D_t, using the general Stokes-Einstein equation (1):

(1) $$r_H = (1/cf_s)(kT/\pi\eta D_t)$$

in which η is the solvent viscosity, D_t the diffusion coefficient, c, the size correction factor, and f_s, the shape friction correction factor.[127] The factor c depends on the ratio between r_s, the van der Waals radius of the solvent, and r_H of the diffusing species; f_s depend on the model (spheroid or cylinder) selected. The r_H value was first optimized using an iterative procedure.[128] Then it was used to calculate the volume v_H of the sphere equivalent to the model of geometrical volume v_M. If the model was correct, v_M and v_H would be equal. The results are summarized in **Table 5**. The case of **CTB(H,C$_2$H)** is particular, because it cannot dimerize into a cryptophane. Therefore, when two **CTB(H,C$_2$H)** molecules are placed face-to-face the resulting virtual dimer could be viewed as a spheroid. The corresponding v_H/v_M ratio (0.6) was close to 0.5, in agreement with the monomeric nature of **CTB(H,C$_2$H)**. Surprinsingly, in the case of complex **C9**, the bulky PCy_3 ancillary phosphine ligands of which being strongly unfavorable for Au···Au interactions because of steric and electronic reasons[129], as explained above, the v_H/v_M ratio was 1.00 for the spheroid, whereas its value for the cylinder model (0.68) was closer to that expected for a monomer! In fact, because of the large size of PCy_3, the shape of the virtual dimer would significantly depart from

the spheroid and be best described by the cylinder model. The accuracy of the spheroid model could be diminished by the interpenetration of the CTBs, which would make the volume of the dimer very close to that of the monomer. For complex **C7** with smaller PEt_3 ancillary ligands, the v_H/v_M ratios are 0.77 and 0.52 for the spheroid and cylinder models, respectively, indicating that the spheroid better describes the behavior of **C7** by comparison with **C9**, and the cylinder is still the best model. These observations indicate that the differences between the spheroidal and cylindrical models arise from the interplay between the size of the phosphine ligands and the interpenetration of the CTBs in the virtual dimer, the latter minimizing the size variation on going from the CTB to the virtual dimer. In the case of **C1**, the experiments were run at 0.9 mM and 10 mM concentrations. In diluted conditions, the v_H/v_M ratios were 0.78 and 0.52 for the spheroid and cylinder models, respectively, and in concentrated conditions the same ratios were 0.98 and 0.65. In diluted conditions, the corresponding v_H/v_M ratio of 0.52 would confirm that **C1** is actually monomeric. Its increase to 0.65 at 10 mM concentration could attest to the presence of small amounts of dimer in fast exchange. In the case of **C3**, the experiments were run at 0.2 mM and 10 mM concentrations. In diluted solution the v_H/v_M ratios were 0.74 and 0.49 for the spheroid and cylinder models, attesting for the monomer nature of **C3** in these conditions. When the concentration was increased to 10 mM, the v_H/v_M ratios for the spheroid and cylinder models were 0.83 and 0.55, respectively, indicating that **C3** was still monomeric even in concentrated solution. In the case of **C4**, there was no significant change in its diffusion coefficient whether was observed in diluted and concentrated concentrations. In diluted conditions, the v_H/v_M ratios were calculated to be 0.79 and 0.54 for the spheroid and cylinder models, which meant there was no dimer in the diluted solution, when the concentration was increased to 10 mM, the v_H/v_M ratios for the spheroid and cylinder models were increased slightly 0.87 and 0.59, respectively. By comparison with **C1**, these data indicated that the dimerization of **C4** was more difficult, which is probably due to the electron-rich methoxy substituents.

Table 5. Selected DOSY data

Compound (a, b, c/Å) [b]	Spheroid v_m/Å^3 [c]	Cylinder v_m/Å^3 [d]	$D_t/10^{10}$ m^{2}s^{-1}	v_H /Å^3 [e]	v_H/v_m
CTB(H,C$_2$H) (7.6, 6.8, 7.6)	1645	-	8.64	988	0.60
C1 (15.2, 6.4, 15.2)	6190	9291	4.23 3.89	4820 5970 4900 6080	0.78 [f] 0.96 [g] 0.53 [f] 0.65 [g]
C3 (12.8, 6.4, 12.8)	4392	6588	5.06 4.83	3240 3640 3210 3610	0.74 [f] 0.83 [g] 0.49 [f] 0.55 [g]
C4 (15.2, 6.4, 15.2)	6190	9291	4.20 4.05	4900 5380 4990 5480	0.79 [f] 0.87 [g] 0.54 [f] 0.59 [g]
C7 (12.8, 6.4, 12.8)	4392	6588	4.96	3400 3370	0.78 0.51
C9 (15.2, 6.4, 15.2)	6190	9291	3.87	6050 6160	0.98 0.66

[a] $CDCl_3$ at 298 K (solvent viscosity: $\eta = 5.39\ 10^4$ Nsm^{-2}). [b] Model dimensions. For the oblate ellipsoid model, a = c; for the cylinder model, a = c = d, b = L/2. [c] $v_m = (4/3)\pi a^2 b$. [d] $v_m = 2\pi a^2 b$. [e] $v_H = (4/3)\pi r_H^3$; r_H is calculated according to equation (1). [f] 0.9 mM concentration. [g] 10 mM concentration.

3.2 Investigations on the Nuclearity of the Gold CTBs in Solution and Gas Phase by Mass Spectrometry

Finally, the gold CTBs **C1 – C9** were studied by mass spectrometry. The data–were obtained by the electrospray ionization time-of-flight technique (ESI-TOF). The expected isotopic distribution patterns for the molecular peak, which corresponded to the [CTB(R, C_2AuPR')H]$^+$ proton adduct ([M + H]$^+$) in all nine cases, including **C8**. **Figure 51** showed the ESI-MS spectra of **C5** and the detail of the evolution of the molecular peak as a function of E_{coll}.

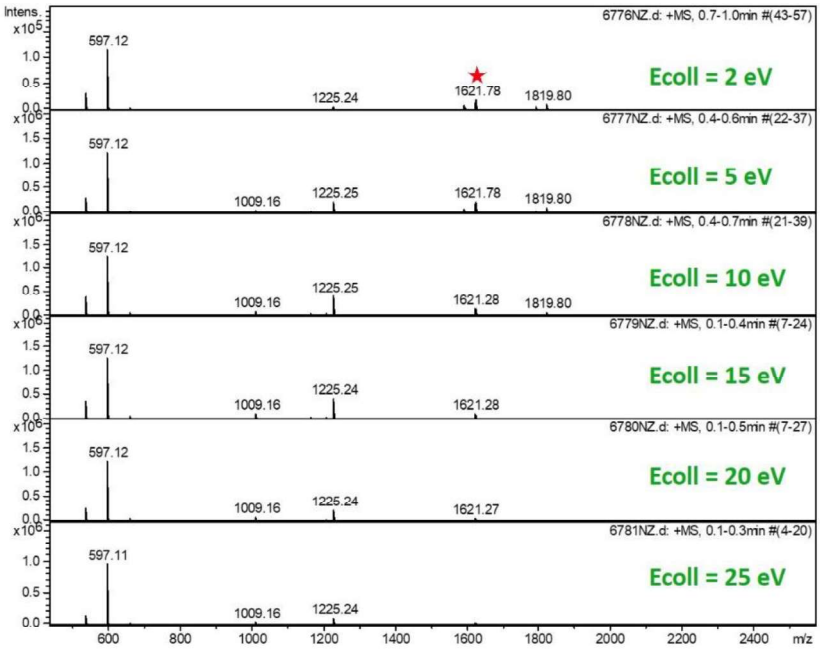


Figure 51. ESI-MS of **C5**: Detail of the evolution of the molecular peak as a function of E_{coll}.

Comparison of complexes **C1 – C3**, **C7** and **C9** shows that the intensity of the signal of $[M + H]^+$ in all the spectra and the intensity of the signal of the $[M + H]^+$ for the same "in source collision induced dissociation energy" (ISCID = E_{coll}), 5 eV, for example, decreases in the order **C9** > **C7** > **C3** > **C2** > **C1**. In the case of **C4 – C6**, the intensity of the signal of the $[M + H]^+$ for the same E_{coll} value, 5 eV, for example, decreases in the order **C6** > **C5** > **C4**. These trends could be explained by electronic considerations. The complexes are better detected when the ancillary phosphine ligands are more electron-rich, and easier to protonate: Therefore, the ranking of the complexes [**CTB(R,C$_2$AuPR')**] follow the order of decreasing basicity of phosphine ligands: PCy_3 > PEt_3 > $PPhMe_2$ > PPh_2Me > PPh_3. Remarkably, signals corresponding to doubly-charged dimers of composition [(**CTB(R,C$_2$AuPR')**H)$_2$]$^{2+}$ were observed and they displayed the expected isotopic distributions. The intensity of the signals of these doubly-charged dimers $[2(M + H)]^{2+}$ decrease with the increase of E_{coll}. Their evolution is shown in **Figure 52** in the case of **C5** as an example.

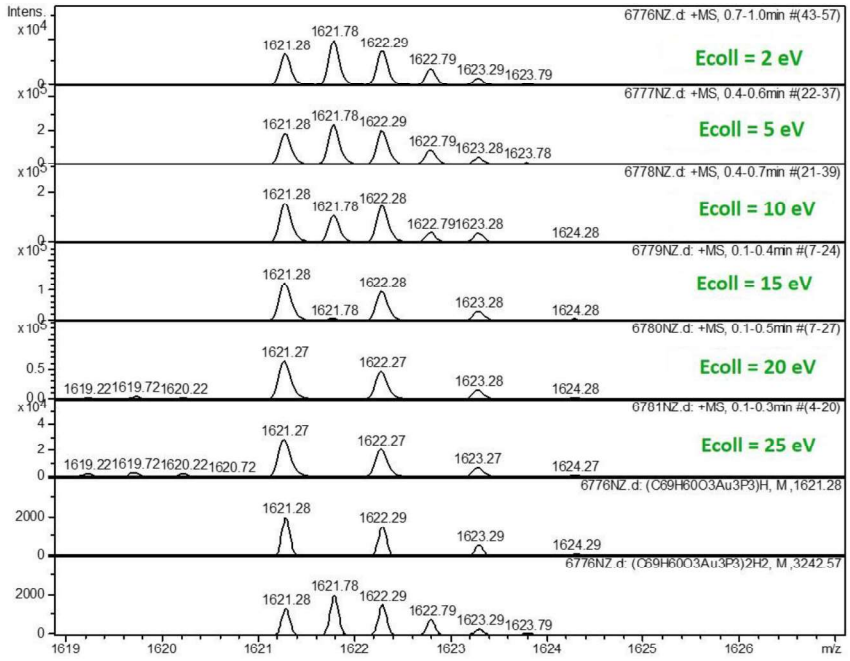


Figure 52. ESI-MS of **C5**: Detail of the evolution of the profile of the molecular peak as a function of E_{coll}. The theoretical profiles of $[M + H]^+$ and $[2M + 2H]^{2+}$ are shown in the bottom lines.

The percentage of dimers were calculated, the calculation process of the proportion of dimers is shown in the Annex and a plot of their proportion with respect to the corresponding monomers *vs* E_{coll} is shown in **Figure 53**. When E_{coll} was higher than 20 eV, there was no dimer at all, whatever the complex considered. In the case of the complexes **CTB(H,C$_2$AuPR')** (*i.e.*, series **C1**, **C2**, **C3**, **C7**, and **C9**), in the same conditions, **C2** showed the highest proportion of dimers, and the proportion of dimers decreased in the order **C2** > **C1** > **C3** > **C9** > **C7**. In the case of the complexes **CTB(OMe,C$_2$AuPR')** (*i.e.*, series **C4**, **C5**, and **C6**), when E_{coll} was less than 5 eV, **C5** showed the highest proportion of dimers, which decreased in the order **C5** > **C4** > **C6**. However, when E_{coll} was over 10 eV, the highest ratio between the signal corresponding to the dimer and the signal corresponding to the monomer was observed in the case of **C4**. Therefore, as E_{coll} increases, the dimer of **C4** is more stable than **C5**. The trends observed could be explained by a combination of electronic and steric effects, the dimer formation by aurophilic Au···Au interactions being favored by electron-deficient phosphines and disadvantaged by the use of sterically hindering phosphines. In this respect, the PPh$_2$Me ligand is likely to offer the best compromise between favorable

electronic effects (phenyl substituent) and minimized unfavorable steric effects (two methyl substituents). Finally, comparison of the two series of Au(I) CTB complexes **C1 – C3** and **C4 – C6**, indicated that the methoxy substituted complexes **C4**, **C5**, and **C6** dimerized more easily than the unsubstituted ones (*i.e.*, **C1**, **C2**, and **C3**) in the gas phase. In addition to the signal of the doubly protonated dimer, we observed signals of doubly charged dimers corresponding to the $AuPR_3^+$ single and double adducts $[2M+AuPR'+H]^{2+}$ and $[2M+2AuPR']^{2+}$, however, the intensities of these signals were extremely weak.

In the case of our Au(I) CTB complexes, in addition to these signals, signals corresponding to singly charged CTB species in which one $[AuPR']^+$ metal complex fragment had been replaced by a proton, *i.e.* $[M - AuPR' + 2H]^+$, were detected. Interestingly, in the case of **C8** = **CTB(3R;2C$_2$AuPR',C$_2$H)**, examination of the changes of the molecular peak (corresponding to $[M + H]^+ = [M' - AuPR'_3 + 2H]^+$, where $M = M' - AuPR'^+ + H^+$) with E_{coll} showed that no doubly-charged dimer appeared neither at high or low E_{coll}. However, the mass spectra of **C8** showed the signals of the doubly-charged adducts $[2M + AuPR' + H]^{2+}$ and $[2M + 2AuPR']^{2+}$, which, unlike $[2M + 2H]^{2+}$, could be formed by bridging of the CTBs with an $[Au(PR')]^+$ complex fragment bound by Au···Au interactions.

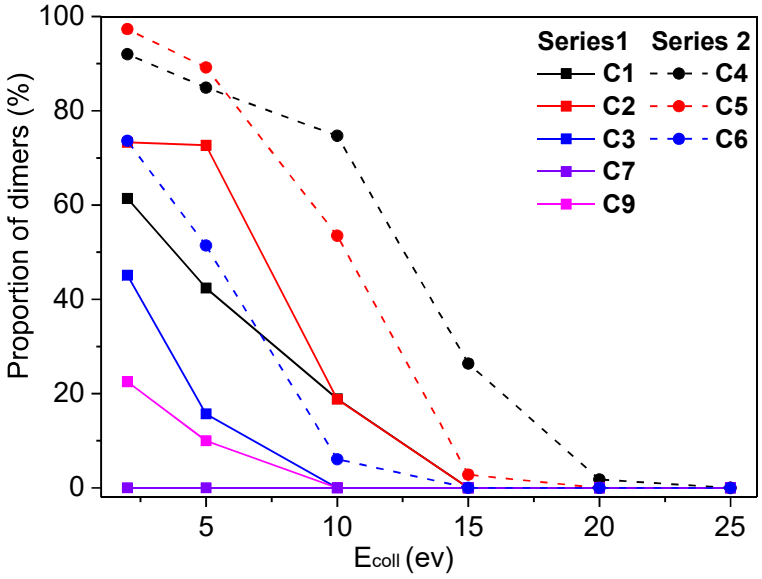


Figure 53. Plot of the proportions of dimers $[2M + 2H]^{2+}$ in the dimer/monomer mixture for the Au(I) CTB complexes **C1 – C9**, except **C8**, which does not show any dimer, as **C7**.

3.3 Reactivity of the Gold CTBs in the Gas Phase: Lessons form Scrambling Experiments

Actually, phosphine ligand exchange reactions have been studied by the Tykwinski's group, who showed that the *cis*-bis(acetylide) complexes of Pt(II) are easily obtained via ligand exchange from their *trans*-counterparts.[130,131] Inspired by their works, two series of scrambling experiments of gold CTBs were studied by mass spectrometry.

First, scrambling experiments of gold CTBs with the same precursor CTBs (**C1**/**C2**, **C2**/**C3**, **C3**/**C1**, **C4**/**C5**, **C5**/**C6** and **C6**/**C4**) were studied. In the case of **C1**/**C2** (**Figure 54**), signals of singly-charged monomer and doubly-charged dimers of **C1** and **C2** both were observed, and the intensities of doubly-charged dimers decreased with the increase of E_{coll} which was consistent with previous results. Interestingly, in addition to these two homo dimers, the doubly-charged dimer of composition (**C1**, **C2**) [(**CTB(H,C$_2$AuPPh$_3$)**/(**CTB(H,C$_2$AuPPh$_2$Me)**) + 2H]$^{2+}$ was observed and the intensity of the dimer decreased with the increase of E_{coll}, until E_{coll} was above 10 eV, the dimer completely disappeared. Another important finding was that phosphine ligand exchange reactions between PPh_3 and PPh_2Me were observed, which produced the asymmetric gold CTBs **CTB(3H;2C$_2$AuPPh$_3$,C$_2$AuPPh$_2$Me)** (**C1'**) and **CTB(3H;C$_2$AuPPh$_3$,2C$_2$AuPPh$_2$Me)** (**C2'**) as their proton adducts; their corresponding doubly-charged dimers were also observed and their intensities decreased gradually when E_{coll} increased as well. In addition, the asymmetric doubly-charged dimers corresponding to (**C1**, **C1'**) and (**C2**, **C2'**) were discovered and disappeared when E_{coll} exceeded 10 eV. When E_{coll} was above 15 eV, only four singly-charged monomers corresponding to **C1**, **C1'**, **C2** and **C2'** were observed. The other scrambling experiments (**C2**/**C3**, **C3**/**C1**, **C4**/**C5**, **C5**/**C6** and **C6**/**C4**) all showed similar observations. Scrambling experiments of **C2**/**C3** showed that the intensity of the signal of the hetero-dimer was the weakest and the intensities of the signals of the doubly-charged dimers of asymmetric gold CTBs **C2'** and **C3'** were very weak as well, since the precursor **CTB(H,C$_2$H)** and $PPhMe_2$ were both less favorable to the formation of aurophilic reactions.

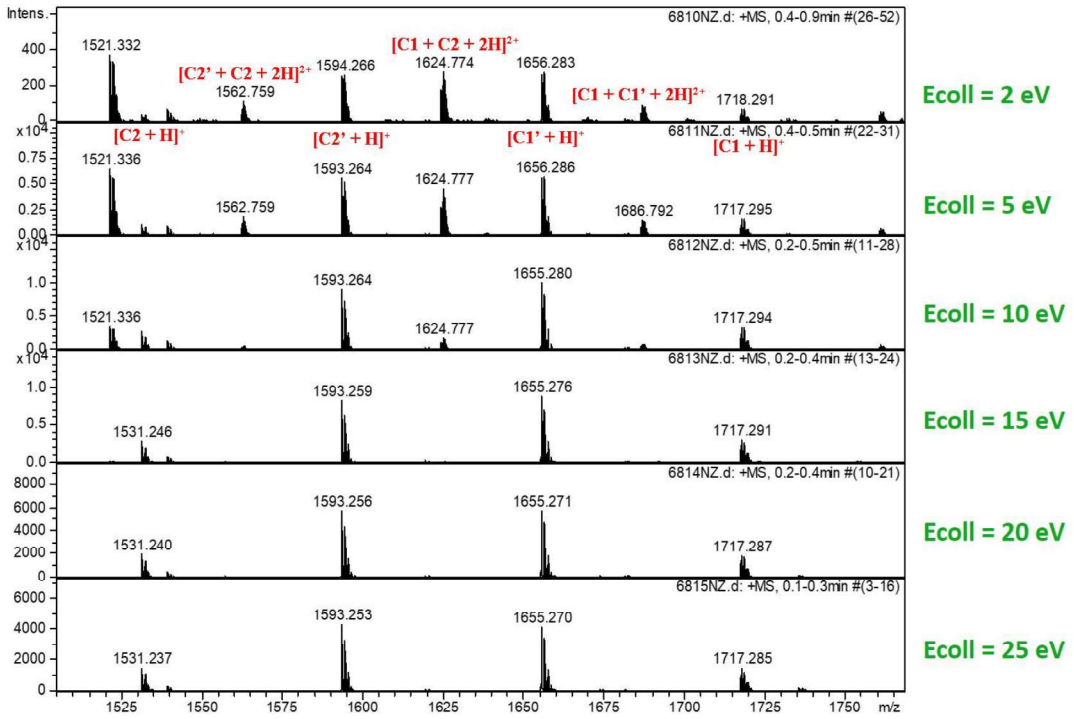


Figure 54. ESI-MS of **C1** with **C2**: Detail of the evolution of the molecular peaks as a function of E_{coll}.

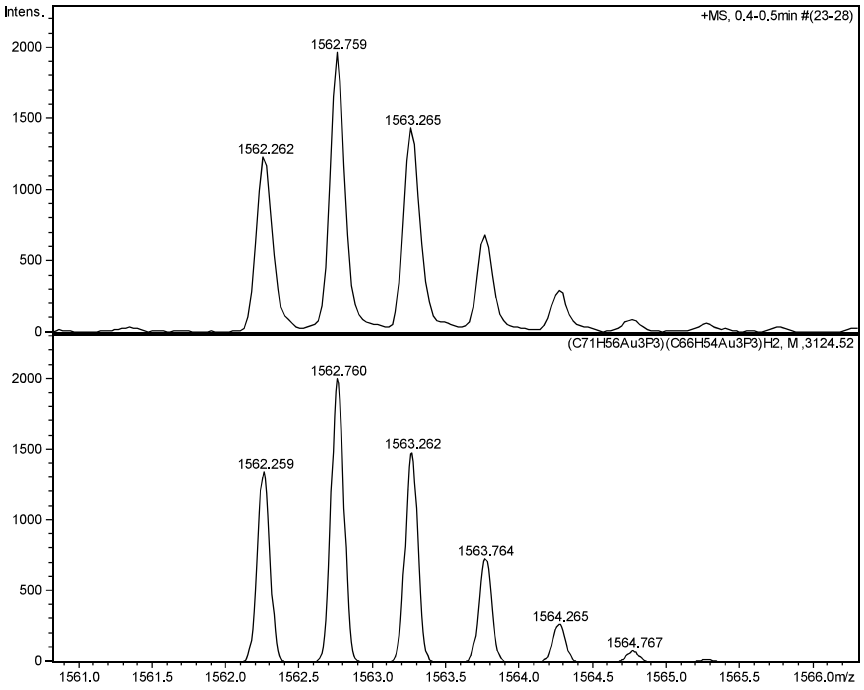


Figure 55. ESI-MS of doubly-charged dimers of composition **C2** with **C2'**: Detail of the profile of the molecular peak. The theoretical profile of [**C2** + **C2'** + 2H]$^{2+}$ is shown in the bottom lines.

The second series of scrambling experiments were studied by mixing **C1** with **C4**, **C2** with **C5** and **C3** with **C6**, that is, CTBs which contained the same phosphine ligands.

Taking the mixture of **C1** and **C4** as an example (**Figure 56**), analysis of the ESI-MS showed that the intensities of the signal of $[M + H]^+$ and $[2M + 2H]^+$ were higher than those of **C1**, the proportion of the doubly-charged dimer of **C4** being also higher than the one of **C1**. Both decreased with the increase of E_{coll}, which was agreement with in the previous observation. In addition to the homo-dimers of **C1** and **C4**, the hetero-dimer (**C1**, **C4**) was also observed. The signal of the doubly changed species [**CTB(H,C$_2$AuPPh$_3$)/CTB(OMe,C$_2$AuPPh$_3$)** + 2H]$^{2+}$ disappeared when E_{coll} was above 15 eV. Because **C1** and **C4** contain the same phosphine ligand, no ligand exchange was detected. The scrambling experiments of **C2** with **C5** and **C3** with **C6** gave similar results, except the mixture of **C3** with **C6** for which the intensity of the hetero-dimer was much weaker by comparison with the one of (**C2**, **C5**) and (**C1**, **C4**). Because PPhMe$_2$ is more electron-rich, Au···Au interactions are less favorable, which is also consistent with the previous results.

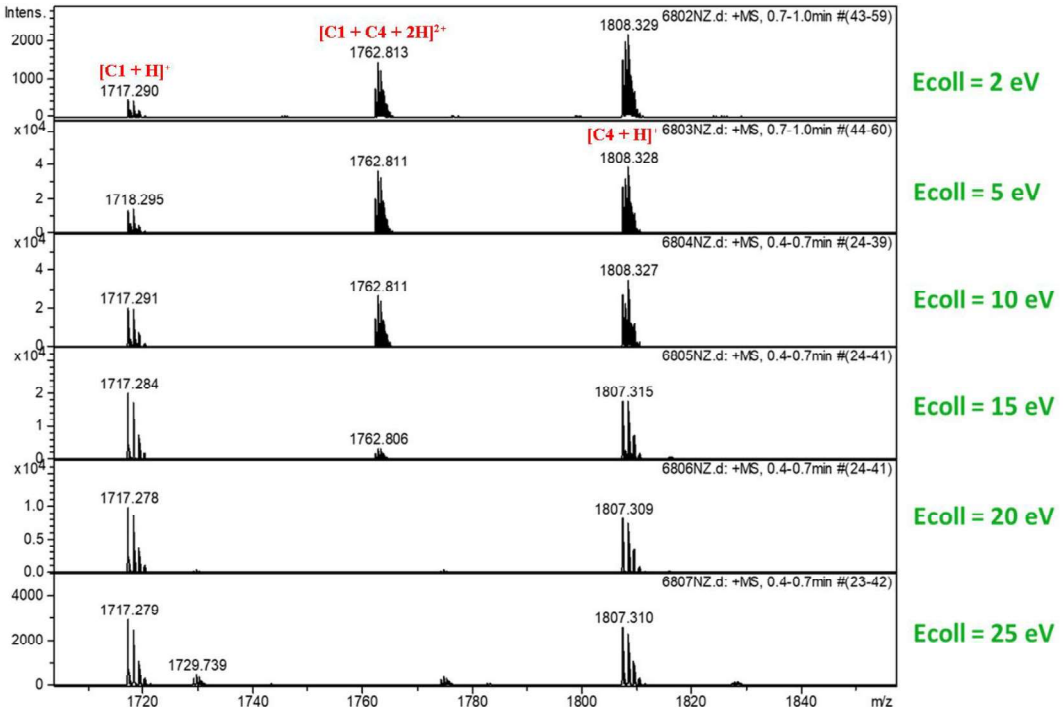


Figure 56. ESI-MS of **C1** with **C4**: Detail of the evolution of the molecular peaks as a function of E_{coll}.

An obvious interpretation of these results, which was brought up in the DOSY section, is that the dimers would result from face-to-face interpenetrated associations

of the CTBs driven by aurophilic interactions. In the solution, it seems that all the complexes existed as monomers in diluted solution; when the concentration increased, there was a very fast exchange between monomer and dimer but the monomer was the major species. However in the gas phase, all the complexes, except **C7**, showed dimerization. The proportion of dimer vs monomer was related to the nature of the precursor CTB, the terminal phosphine ligands and E_{coll}. As a matter of fact, such 1:1 associations have been observed by mass spectrometry in the case of C_3-symmetric trischelate metal complexes of triphenylphosphine gold alkynyl-functionalized bipyridine ligands.[132] The two series of scrambling experiments both proved that the doubly-charged dimer could be a metallo-cryptophane because of the Au···Au interactions. The study of mixtures of gold CTBs showing the same precursor proved that phosphine ligand exchange reactions could happen in the gas phase as well, and the scrambling experiments involving gold CTBs containing the same phosphine ligand indicated that the methoxy substituted complexes **C4**, **C5**, and **C6** dimerized more easily than the unsubstituted ones (*i.e.*, **C1**, **C2**, and **C3**) in the gas phase. Both series of experiments confirmed that the formation of Au···Au interactions were related to the electronic effects of phosphine ligand and precursors CTBs.

4. Evaluation of the CTBs as Hosts for NEt_4I Using ^1H NMR Titration and DOSY

As discussed in the general introduction, cryptophanes are good candidates for identifying organic ammonium cations of appropriate size. For example, cryptophane-E showed a very strong binding constant towards tetramethylammonium with K_a = 475000 M^{-1} at 293 K.[68] A lower binding constant, K_a = 6400 M^{-1} was observed between cryptophane **R6** and tetraethylammonium at 300 K.[52] In addition, CTB derivatives were developed by Gosse and coworkers as fluorescent molecular probes to recognize biological ammonium species such as choline (Ch) and acetylcholine (Ach). For instance, the probe CTB(OMe, C_2Ph-*p*COONa) could discriminate acetylcholine from choline, with respective binding constants of 540 and 240 M^{-1} in PBS buffered saline solution.[113] Binding constants of 23.5 ±1 M^{-1} between CTB(OMe,PO_3H) and Ach and 66 ± 4 M^{-1} between CTB(OMe,PO_3H) and Ch were found by emission titration.[31]

In order to study the recognition properties of the gold CTBs for ammonium cations (NEt_4I), ^1H NMR titration and DOSY experiments were undertaken in the case of **C1**. To a solution of NEt_4I in $CDCl_3$ were added concentrated solutions of **C1** (**Figure 57**). A fast host–guest exchange was observed on the NMR time scale, the chemical shifts of the protons of NEt_4I varying when the ratio **C1**/NEt_4I varies. Compared to the spectrum of pure NEt_4I, the signals of methylene and methyl ammonium protons are shifted upfield gradually by about 0.45 and 0.64 ppm respectively, when the **C1** amount increases from 0 to 4.5 equivalents, which is consistent with the complexation of a guest in an electron-rich host. In addition, the signals of these protons became broader and broader, which could be explained by the variations of the exchange rate of the guest between the inside and the outside. Concerning the host, the signals of the protons of **C1** are almost unaffected by the presence of NEt_4I. Assuming a 1 : 1 stoichiometry, the binding constant (K_a) was calculated to be 8908 ± 320 M^{-1} by the software BindFit.[133]

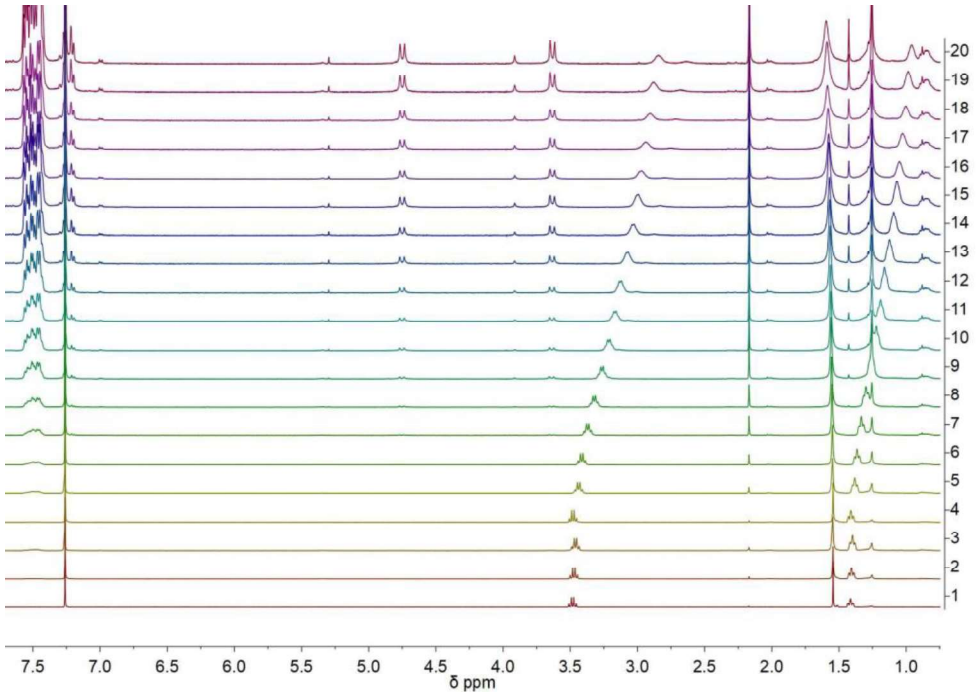


Figure 57. Evolution of the ^{1}H NMR spectra (400 MHz, 298 K, $CDCl_3$) of NEt_4I upon addition of **C1** (from bottom to top), 1: pure NEt_4I.

Further structural confirmation of the complexation was achieved through diffusion-ordered spectroscopy (DOSY). The diffusion coefficients (*D* values) of NEt_4I and **C1** were 9.00×10^{-10} and 4.15×10^{-10} m^2/s respectively. Then the diffusion coefficient of **C1** in the presence of NEt_4I was checked in the same conditions. The DOSY spectra showed that the diffusion coefficient of **C1**, 4.00×10^{-10} m^2/s, was similar to the one obtained in the absence of NEt_4I, but the diffusion coefficient of NEt_4I in the presence of **C1** was found to be 5.98×10^{-10} m^2/s, which was much smaller than the one of free NEt_4I. Since DOSY NMR showed only two species in solution, there was a fast exchange between **C1**@NEt_4I and free NEt_4I. These observations were in agreement with the ^{1}H NMR titration experiment.

In the case of **C4**, a few successive aliquots of host solution NEt_4I were added into a solution of **C4** in $CDCl_3$; the chemical shift changes were recorded after each addition and the spectra are shown in **Figure 58**. Clear signal broadening of the protons of NEt_4I were observed, and the methylene and methyl ammonium protons shifted upfield by about 0.33 and 0.22 ppm respectively, the values of which are smaller by comparison

with the changes observed in the case of **C1**. As the ^{1}H NMR spectra show, only slight chemical shift changes ($\Delta\delta$) of NEt_4I were observed upon changing the concentration of the guest. In addition, the chemical shifts of the protons of **C4** did not change at all, but the signals of the phosphine ligands became broader upon addition of NEt_4I. Assuming a 1 : 1 stoichiometry, the binding constant (K_a) was calculated to be 5972 ± 525 M^{-1} by the software BindFit.[133]

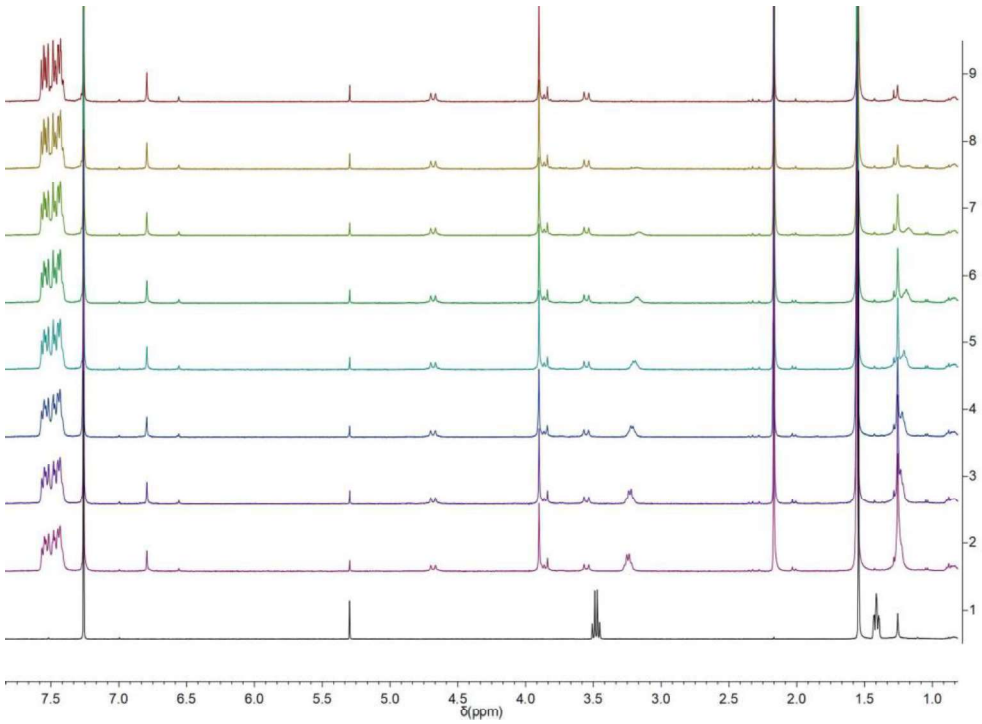


Figure 58. ^{1}H NMR spectra (400 MHz, 298 K, $CDCl_3$) of **C4** upon addition of NEt_4I (from top to bottom), 1: pure NEt_4I; 9: pure **C4**.

According to the ^{1}H NMR titration and DOSY experiments, Et_4N^+ could interact with the cavities of **C1** or **C4**, and a fast host–guest exchange on the NMR time scale was observed in both cases. Complex formation might be due to C-H···π interactions between the methyl group of Et_4N^+ and the proximal aromatic rings.[58,134] The binding constants were determined to be ~ 8900 and ~6000 M^{-1} for **C1** and **C4** respectively in $CHCl_3$, which were similar to the binding abilities of cryptophanes.[52] As a consequence of these preliminary studies, the gold CTB complexes could be interesting receptors for the recognization of ammonium salts.

5. Basic Photochemistry and Photophysics of the Gold CTBs

5.1 Electronic Absorption Spectroscopy

The absorption and emission spectra of **CTB(H,C$_2$H)**, **CTB(OMe,C$_2$H)** and the complexes **C1 – C9** (**C8** excepted) were investigated using 10^{-5} M solutions in $CHCl_3$. The ECD and corresponding absorption spectra of the enantiomers of **CTB(H,C$_2$H)** and **C1**, on the one hand, **CTB(OMe,C$_2$H)** and **C5**, in the other hand, were recorded in CH_2Cl_2 and acetonitrile, respectively. The numeric data are collected in **Table 6** (**Page 83**). The absorbance of the gold(I) acetylide complexes **C1 – C9** in the lowest-energy region of their electronic absorption spectra in $CHCl_3$ (*i.e.* at 325 nm for **C1 – C3, C7**, and **C9**, and at 365 nm for **C4 – C6**), shows a linear relationship with concentration, in agreement with the Beer-Lambert's law.

Figure 59 gathers the electronic absorption spectra of the series **CTB(H,C$_2$AuPR')**, including the CTB ligand precursor, **CTB(H,C$_2$H)**. This latter CTB shows strong absorptions in the UV region with maxima at 248 and 258 nm and a molar extinction coefficient of 39300 $M^{-1}cm^{-1}$ at this wavelength, and a much weaker absorption with maxima at 282 and 293 nm ($\varepsilon \approx 2000$ $M^{-1}cm^{-1}$). In their absorption spectra the gold complexes of **CTB(H,C$_2$H)** show similar UV-vis absorption patterns with intense high-energy, vibronically structured absorption bands at *ca* 250 – 300 nm, their maximum being centered at *ca* 283 nm, and exhibiting high molar extinction coefficients ($\varepsilon \approx$ 70000 ~ 87000 $M^{-1}cm^{-1}$). A slightly less intense band at ~ 295 nm, which is separated from the maximum by vibrational spacings of ~1500 – 1600 cm^{-1}, is also observed. These spacings correspond to the stretching frequencies of the aromatic carbon-carbon bonds. Finally, low-energy band tails can be seen between 310 – 375 nm ($\varepsilon \approx 2000$ $M^{-1}cm^{-1}$). With reference to literature studies on related alkynylgold(I) complexes [129,135,136], the intense higher-energy bands at about 250 − 300 nm could be assigned to [$\pi \rightarrow \pi^*$] intraligand transitions of the alkynyl ligands and the phenylene groups of the CTB. The lower-energy absorption bands at 310 − 375 nm could be possibly assigned to the d_π(Au)-π^*(C≡CAr) MLCT transition. In the case of complexes **C1 – C3**, the

bands below 260 nm were assigned to the intra-ligand (IL) transitions of the PPh_3 ligand, since their intensity decreased gradually as the number of phenyl groups decreased. By comparison with the corresponding absorptions of free **CTB(H,C₂H)**, shifts of the absorption bands to lower energies upon alkynyl metalation have been noted in the literature and have been attributed to enhanced conjugation in the metal acetylide due to metal-to-ligand back donation to π*(C≡CAr).[137,138]

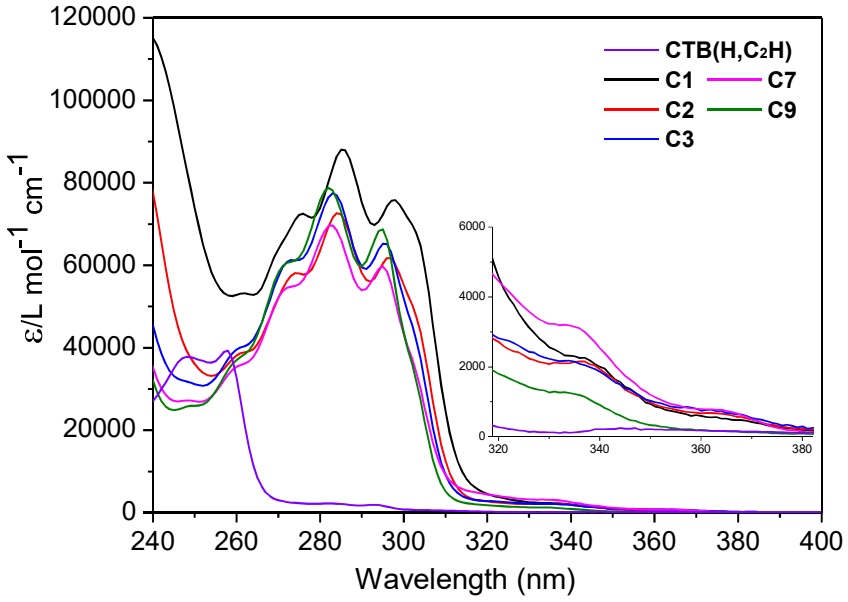


Figure 59. Electronic absorption spectra of 10^{-5} M solutions of **CTB(H,C₂H)** and complexes **C1**, **C2**, **C3**, **C7** and **C9** in $CHCl_3$.

The electronic absorption spectra of the complexes of the series **CTB(OMe,C₂AuPR')** and their CTB precursor are shown in **Figure 60**. **CTB(OMe,C₂H)** shows strong absorptions in the UV region with maxima at 249 and 258 nm ($\varepsilon \approx 30000\ M^{-1}cm^{-1}$), and a weaker absorption with maxima at 302 and 312 nm ($\varepsilon \approx 10000\ M^{-1}cm^{-1}$). The complexes **C4**, **C5**, and **C6** show a very similar UV-vis absorption pattern: Intense higher-energy bands at about 250 − 300 nm ($\varepsilon \approx 47000 \sim 51000\ M^{-1}cm^{-1}$), which are separated by vibrational spacings of ~2100 cm^{-1} corresponding to the stretching frequencies of the C≡C bond; lower energy absorption bands of similar intensity ranging between 300 – 340 nm ($\varepsilon \approx 37000 \sim 51000\ M^{-1}cm^{-1}$), and a residual absorption tail extending between 340 and 380 nm ($\varepsilon \approx 2100 \sim 2700$

$M^{-1}cm^{-1}$). Of the latter two bands, the first, which is not found in the series of unsubstituted CTB ligand and complexes, could be rationalized by the occurence of [n → π*] intraligand transitions from the OMe groups to the CTB and alkynyl ligands[104]; the second could be possibly assigned to the d_{π}(Au)-π*(C≡CAr), as in the case of the unsubstituted complexes. Their red shift by comparison with CTB(H,C_2AuPR_3) could be explained by the fact that the OMe group is electron-donating, which may reduce the energy of d_{π}(Au)-π*(C≡CAr) MLCT transition.[102] Finally, the band below 260 nm was also assigned to the IL transitions of the PPh_3 ligand, since its intensity decreased gradually as the number of phenyl group decreased.

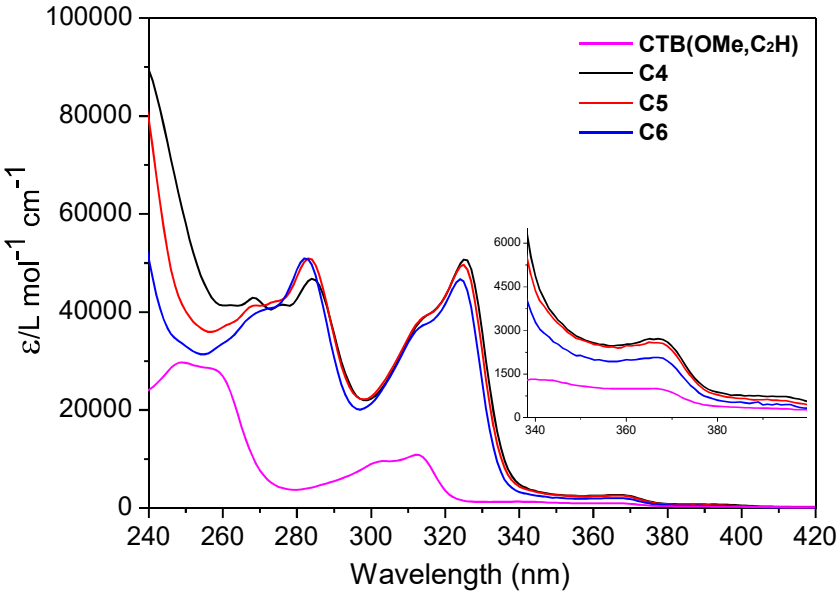


Figure 60. Electronic absorption spectra of 10^{-5} M solutions of **CTB(OMe,C_2H)** and complexes **C4**, **C5**, and **C6** in $CHCl_3$.

The ECD spectrum of (–)-**CTB(H,C_2H)** showed a sequence of negative-positive-negative bands with maxima at λ = 237, 255, 285, and 294 nm, the sign inversion occurring at 258 and 266 nm, and is mirror-image of the spectrum of (+)-**CTB(H,C_2H)** (**Figure 61**). The ECD spectra of the enantiomers of **CTB(H,C_2H)** were tentatively analyzed as follows. First, the unsymmetrical couplet extending between 225 nm and 266 nm was assigned to the B_{1u} transition of the benzene rings; the singly signed band extending between 266 and *ca* 300 nm was assigned to the B_{2u} transition. In the same

region, the ECD spectra of **C1** showed the same sequence of bands with maxima (or minima) at 242, 270, 288, and 304 nm with sign inversion at 264 and 274 nm (**Figure 61**). The sequence of signs for (–)-**C1** and (+)-**C1** was the same as for (–)-**CTB(H,C_2H)** and (+)-**CTB(H,C_2H)**, respectively. However, the ECD spectra of complex **C1** were shifted bathochromically by comparison with those of **CTB(H,C_2H)** by 6 - 8 nm if referring to the respective positions of the sign inversion wavelengths, 10 nm if referring to the low energy maximum of the B_{2u} band. In addition, the intensity of this low energy band was considerably enhanced by comparison with the corresponding band in the spectra of **CTB(H,C_2H)**, while the maximal $|\Delta\varepsilon|$ values of the high energy bisignate band of the B_{1u} transition were similar for **CTB(H,C_2H)** and **C1**, suggesting that the former was more perturbed by the organometallic substituent than the latter. Comparison of the ECD spectra of (–)/(+)-**C8** and (–)/(+)-**C1** showed that complex **C8** displayed similar and distinctive features. The band corresponding to the B_{1u} transition was singly signed, the position of its maximum was unchanged, and its intensity a little weaker, whereas the band corresponding to the B_{2u} transition had the same shape and maxima, but its intensity had decreased significantly, by more than a factor of two. The significant decrease of the intensity of the B_{2u} band of **C8**, which is due to the loss of a single $[Ph_3PAu]^+$ substituent, indicates that this substituent has a strong hyperchromic effect.

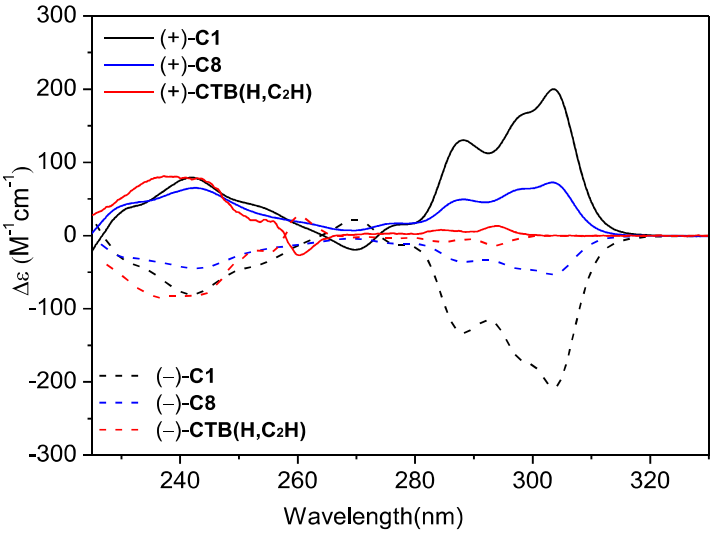


Figure 61. Superposition of the ECD spectra of the enantiomers of **CTB(H,C$_2$H)** and of their complexes **C1** and **C8** in CH_2Cl_2. Concentrations: (–)-**CTB(H,C$_2$H)**: 26.1×10^{-5} M; (+)-**CTB(H,C$_2$H)**: 27.0×10^{-5} M; (–)-**C1**: 9.0×10^{-5} M; (+)-**C1**: 9.7×10^{-5} M; (–)-**C8**: 13.6×10^{-5} M; (+)-**C8**: 13.2×10^{-5} M.

The ECD spectrum of (–)-**CTB(OMe,C$_2$H)** and its mirror-image spectrum of (+)-**CTB(OMe,C$_2$H)** are shown in **Figure 62**. They exhibited a sequence of negative-positive-positive-negative bands with maxima at λ_{max} = 244, 263, 294, and 312 nm, the sign inversion occurring at 258, 276 and 302 nm. The bisigned couplet in the region extending between 225 nm and 276 nm was tentatively assigned to the B_{1u} transition of the benzene rings. The doubly signed band extending between 276 and *ca* 320 nm could be assigned to the B_{2u} transition. Between 230 and 340 nm (–)-**C5** showed a sequence of negative-positive-negative bands with maxima at λ_{max} = 285, 304, and 326 nm and sign inversion at 294 and 312 nm. By comparison with (–)-**CTB(OMe,C$_2$H)**, the higher energy band between 225 and 294 nm, corresponding to the B_{1u} transition, was singly signed. The disappearance of the CD couplet could be connected to vibronic effects, affecting the two transitions in different ways.[10] The bisigned band extending between 294 and 340 nm, which corresponds to the B_{2u} transition, also underwent a relatively strong hyperchromic shift. Overall, compared to those of **CTB(OMe,C$_2$H)**, the B_{2u} bisigned band of complex **C5** was shifted bathochromically, by 10 nm if referring to the respective positions of the sign inversion wavelengths, by 14 nm if referring to its

low energy maximum/minimum. In addition, the ellipticity of the B_{2u} transition was considerably enhanced by comparison with the corresponding band in the spectra of **CTB(OMe,C$_2$H)**, showing again that it was more perturbed by the organometallic substituent than the higher energy B_{1u} transition.

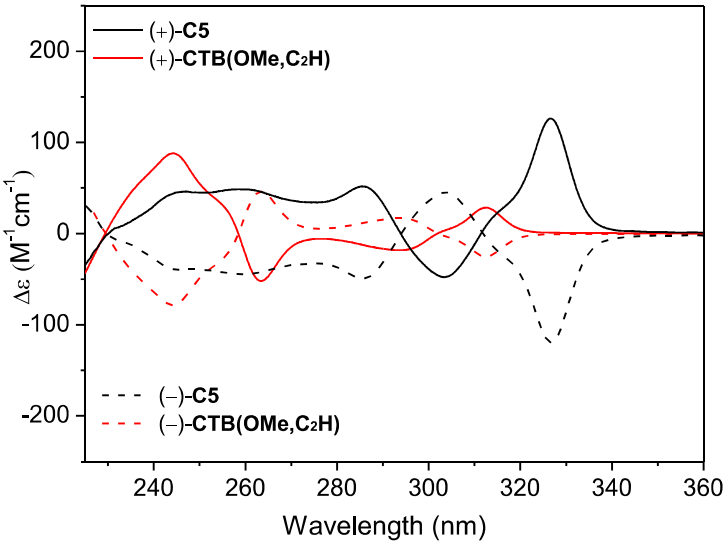


Figure 62. Superposition of the ECD spectra of the enantiomers of **CTB(OMe,C$_2$H)** and of complex **C5** in CH_2Cl_2. Concentrations: **(–)-CTB(OMe,C$_2$H)**: 23.8×10^{-5} M; **(+)-CTB(OMe,C$_2$H)**: 25.1×10^{-5} M; **(–)-C5**: 15.6×10^{-5} M; **(+)-C5**: 17.5×10^{-5} M.

5.2 Electronic Emission Spectroscopy

The luminescent properties of gold(I) complexes have been extensively studied. Some features, such as emission bands occuring over 500 nm in certain cases have been suggested to be related to aurophilic interactions.[97,99,104,139] According to the features observed in the absorption spectra, the excitation wavelengths were selected at $\lambda \approx 330$ nm and 280 nm. The electronic emission properties of the CTBs in $CHCl_3$ were first investigated in deoxygenated (Ar) conditions. Upon excitation of 10^{-5} M solutions in the strongest absorption band at 280 nm, **C1 – C3**, **C7** and **C9** all emitted blue light with a sharp maximum at 428 nm appended with a broad band exhibiting a maximum at 454 nm and shoulders at *ca* 465 nm. In addition, low intensity emission bands between 340 and 400 nm were observed. The emission quantum yields of the complexes at $\lambda_{em} > 400$ nm were determined by comparison with PhC_2AuPPh_3, which has a known quantum yield of 0.10 in $CHCl_3$ [105], and the corresponding lifetimes were all

around 30 μs for **C1**, **C7**, and **C9**, and 21 μs for **C2** and **C3**. The lifetimes of the unquenched emission at $\lambda_{em} < 400$ nm were much shorter, *ca* 1 ns for **C1**, **C7** and **C9**. The high intensity sharp luminescence with a maximum around 428 nm was sensitive to the nature of the phosphine ligands. It had been assigned to a $T_1 \rightarrow S_0$ $\nu_{0\text{-}0}$ emission in related compounds.[97] The broad band at 454 nm with shoulders at lower energy corresponds to the envelope of the transitions to the higher order vibrational ground state levels (ν_1, ν_2, etc.), which were well resolved in the case of the model complex PhC_2AuPPh_3.[136] The vibrational spacings of ~1500 cm^{-1} have been assigned to ground state phenyl ring deformation and symmetric phenyl ring stretch, the vibrational spacings of ~2100 cm^{-1} corresponding to the stretching frequencies of the C≡C bond. This emission corresponds to a phosphorescence, because it is quenched by oxygen, it is associated with a relatively large Stokes shift (*ca.* 10^3 cm^{-1}), and it shows quite a long lifetime of *ca.* 20−30 μs. Noticeably, this magnitude lies in the upper range of those of literature gold(I) acetylide complexes.[97,140]

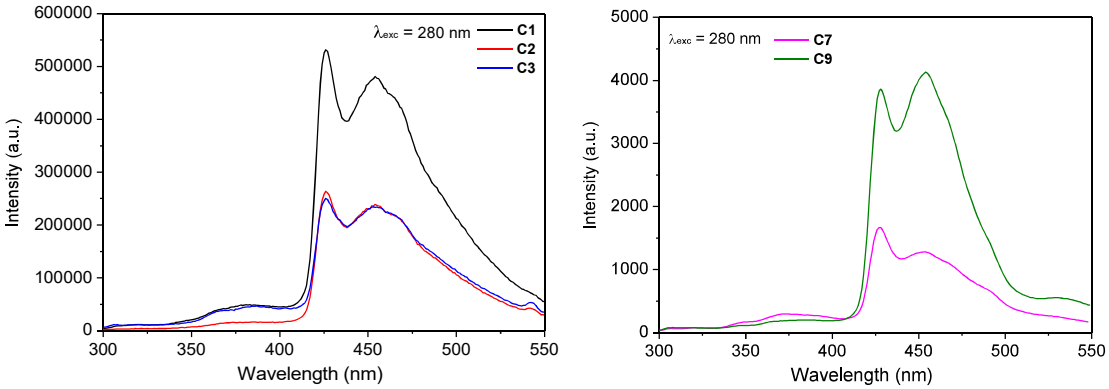


Figure 63. Emission spectra of 10^{-5} M solutions of the complexes **C1 – C3** (left), **C7** and **C9** in deoxygenated $CHCl_3$ at room temperature. Left: λ_{exc} = 280 nm.

The phosphorescence of complexes **C1 – C3** was no longer observed upon excitation at longer wavelength (330 nm) (**Figure 64**), while the fluorescence between 340 and 400 nm remained unchanged. The excitation wavelength dependence of the ratio between the phosphorescence and the fluorescence has been observed and investigated in the case of binuclear Au(I) alkynyl complexes of phenylene and

alkynyl/phenylene-bridged diphosphine ligands.[141,142] By analogy with earlier observations on Os(II) complexes [143], these observations were rationalized by invoking high lying S_n states with MLCT character, which transferred the excitation to T_1 via T_n states more efficiently than S_1 would do.

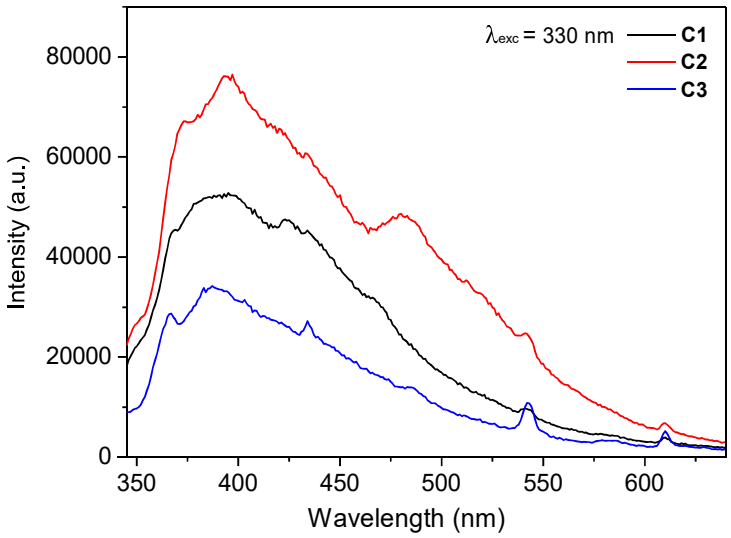


Figure 64. Emission spectra of 10^{-5} M solutions of the complexes **C1 – C3** in deoxygenated $CHCl_3$ at room temperature (λ_{exc}=330 nm).

Complexes **C1 – C3** were found to be luminescent in $CHCl_3$ also in aerated solutions (**Figure 65**). They exhibited emission features that were very similar to those observed in deoxygenated conditions when λ_{exc} was 330 nm. They exhibited broad emission bands between 350 and 400 nm with two maxima separated by ca. 1500 cm^{-1}, corresponding to the C=C vibrational modes of the aromatic rings, which indicates that the latter are involved in the emissive state. Upon excitation at shorter wavelength (280 nm), residual emission bands of phosphorescence are superposed to the higher energy fluorescence around 380 nm.

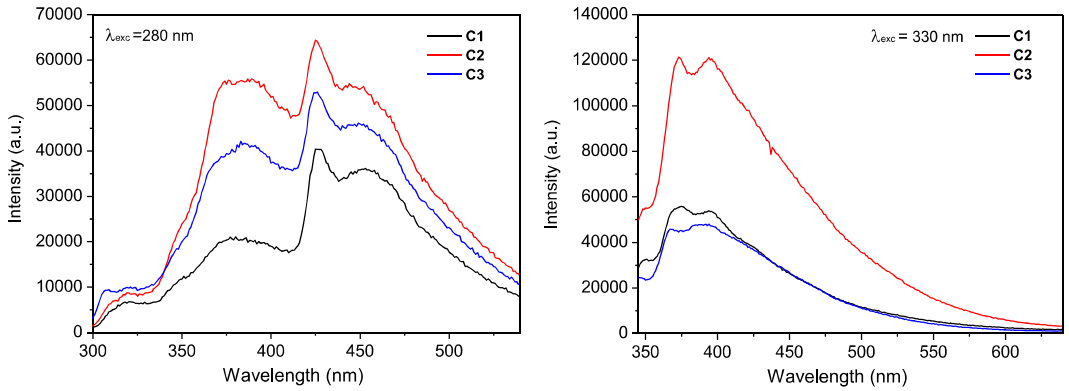


Figure 65. Emission spectra of 10^{-5} M solutions of the complexes **C1 – C3** in non deaerated $CHCl_3$ at room temperature. Left: λ_{exc} = 280 nm; right: λ_{exc} = 330 nm.

The electronic emission properties of **C4 – C6** in $CHCl_3$ were also investigated in deoxygenated (Ar) conditions. Upon excitation of 10^{-5} M solutions in the strongest absorption band at 330 nm, **C4 – C6** showed emission spectra that differed from each other, as illustrated in **Figure 66**. The spectrum of **C4** showed that the relative intensities of the fluorescence and the phosphorescence were very similar. The spectrum of **C5** displayed mainly phosphorescence-like emission, but to a lower extent than **C1 – C3**. By contrast, the spectrum of **C6** showed the opposite, as only fluorescence-like emission could be detected. We measured vibrational spacings of ca. ~ 1400 cm^{-1}, which have been assigned to ground state phenyl ring deformation and symmetric phenyl ring stretch[97], and of ca. ~ 2300 cm^{-1}, corresponding to the C≡C stretch[144], as shown in **Table 7** (**Page 84**). A possible interpretation is that these three complexes have triplet excited states lying at different energies. Upon excitation at 360 nm, the complexes **C4 – C6** showed only higher energy emission with similar profiles and λ_{max}, which meant that their S_1 states had similar energies. The emission quantum yields of the complexes were determined by comparison with PhC_2AuPPh_3 as well. Very long lifetimes were measured for **C4** (126 μs) and **C5** (80 μs). In addition, these three complexes all showed a shorter lifetime around 2 μs for **C4** and **C6**, 1 μs for **C5**, which would correspond to delayed fluorescence. The phosphorescence of **C4 – C6** was no longer observed in oxygenated (Ar) conditions, no matter what excitation wavelength was used. Only higher energy emission bands at 400 nm were observed; the small

Stockes shift, and occurrence in oxygenated solutions indicated that the emission bands between 380 and 450 nm do correspond to fluorescence.

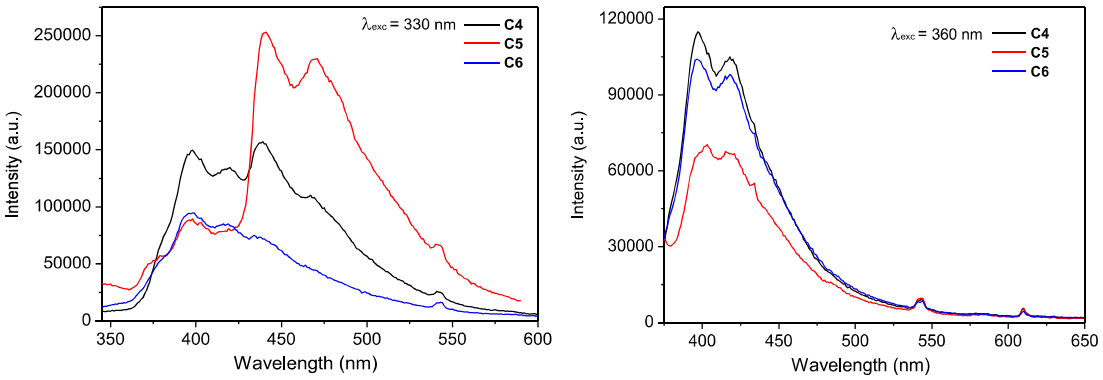


Figure 66. Emission spectra of 10^{-5} M solutions of the complexes **C4 – C6** in deoxygenated $CHCl_3$ at room temperature. Left: λ_{exc} = 330 nm; right: λ_{exc} = 360 nm.

The emission of non-degassed chloroform solutions containing various concentrations (10^{-6} – 10^{-2} M) of complex **C1** was also investigated by examining the solutions under a UV lamp (irradiation at 365 nm) with the naked eye (**Figure 67**). Whereas no emission at all could be detected from 10^{-6} M solutions, a blue emission from solutions at concentrations between 10^{-5} and 10^{-3} M progressively developed. Interestingly, the color of the emission switched to green at 10^{-2} M concentration.

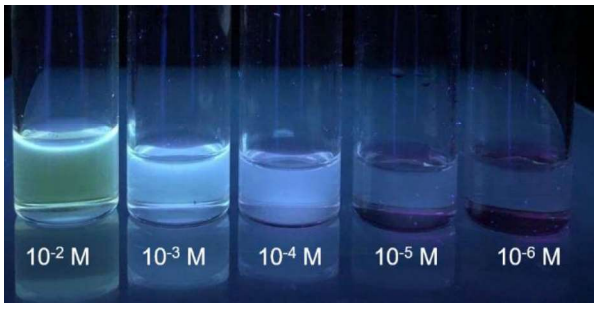


Figure 67. Photograph of vials containing solutions of complex **C1** in $CHCl_3$ at different concentrations under 365 nm irradiation.

The emission of powdered/ground samples of the complexes **C1 – C9** was recorded with excitation wavelength at 330 nm for **C1 – C3**, **C7**, and **C9**, and 365 nm for **C4 – C6**. Lower-energy emission bands were observed for all the complexes in the

solid state at room temperature. This emission was red shifted by comparison with the emission observed for the corresponding complexes in non-deoxygenated solutions. The solid state emission could be tentatively assigned to σ(Au-P) ← π* transitions, or to a metal-perturbed IL π ← π* transition with MLCT character. In most other gold(I) compounds studied, the phosphine ligands contain aryl substituents and the π* orbital involved is thought to be localized on the arylphosphine.[99] But since **C7** and **C9** contain PEt_3 and PCy_3 ligands, the π* orbital, in these cases at least, must be associated with the arylacetylide ligand subunits of the CTBs. Vibronic-structured emission bands with vibrational progressional spacings of ca. 1300 ~ 1700 cm^{-1}, corresponding to the C=C vibrational modes of the aromatic rings, vibrational progressional spacings of ca. 1920 cm^{-1}, corresponding to the C≡C stretch, were observed in the solid state emission spectrum of **C9**. In the case of **C7**, the intensities of the lower energy (510 nm) and the higher energy (around 400 nm) emissions were similar. However, for **C1 – C6**, the solid state emission spectra all show a single broad band, no vibrational fine structure being observed. Their maxima are all red shifted by comparison with the solution emissions in the following orders: **C1** (*ca.* 120 nm) < **C2** (*ca.* 133 nm) < **C3** (*ca.* 157 nm), and **C4** (*ca.* 70 nm) < **C5** (*ca.* 82 nm) < **C6** (*ca.* 120 nm) (**Figure 68**). Similar bathochromic shifts have been observed in other gold(I) complexes having short Au···Au contacts in the solid state, and the emission has usually been assigned to arise from a $^3(d_\delta^*\text{-}p_\sigma)$ or $^3(d_\sigma^*\text{-}p_\sigma)$ excited state.[105,145,146] According to our observations, the complexes **C3** and **C6**, which show the strongest bathochromic shifts, are also those containing $PPhMe_2$ as terminal phosphine ligand, which are the most electron-rich in the series PPh_3 < PPh_2Me < $PPhMe_2$. Therefore, this phosphine should favor the formation of Au···Au interactions to a lesser extent than the others. We have seen that aurophilic interactions in gold complexes with ancillary phosphine ligands are the result of a delicate balance between electronic and steric effects. In the present systems, the release of steric strain by using less sterically hindering phosphine ligands may be more determining than the electronic effect in the control of Au···Au interactions, which could explain the lower energy emission of the complexes containing the $PPhMe_2$ ligand. The

slight red shifts in emission energy on going from PPh_3 in **C1** and **C4** to $PPhMe_2$ in **C3** and **C6** are also consistent with an assignment of the emissive state as deriving from a $^3(\sigma \leftarrow \pi^*)$ transition associated with the [Au(C≡CR)] groups. $PPhMe_2$, being a better electron donor than PPh_3, would render the gold(I) center more electron rich, making the $^3[\sigma(\text{Au-P}) \rightarrow \pi^* (C\equiv C)]$ or metal-perturbed ^{3}IL $[\pi \rightarrow \pi^* (C\equiv C)]$/^{3}MLCT excited state low-lying in energy.[102,104]

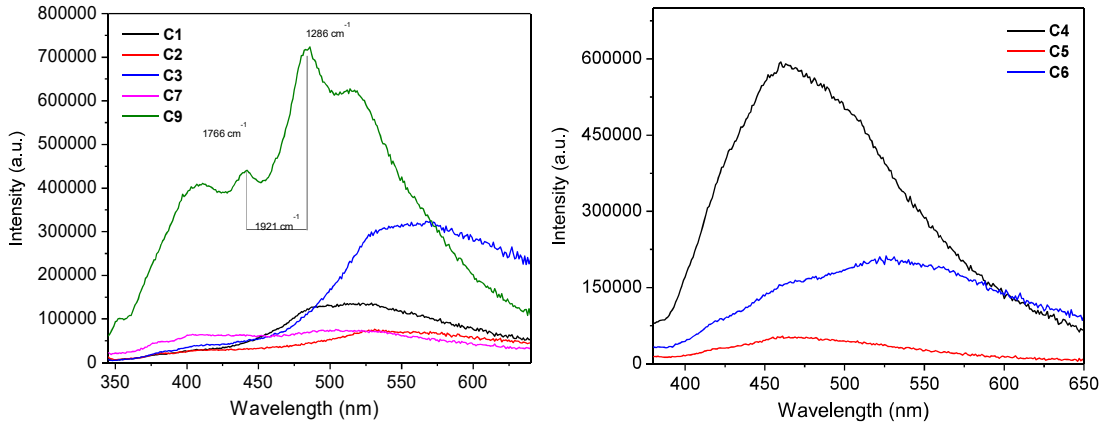


Figure 68. Solid state room temperature emission spectra of the complexes **C1 – C3**, **C7** and **C9** (left, λ_{exc} = 330 nm) and **C4 – C6** (right, λ_{exc} = 360 nm).

We also examined the solid state emission of the complexes by adsorption on alumina. Solutions of the complexes **C1**, **C3**, **C7**, and **C9** at different concentrations ($10^{-6} - 10^{-2}$ M) in chloroform were deposited on alumina TLC plates, and the spots examined under a UV lamp by irradiation at 365 nm (**Figure 69**). Spots from solutions at concentrations lower than 10^{-4} M were hardly seen, but all the complexes from 10^{-2} M solutions showed colored spots. Whereas 10^{-2} M solutions of **C1** and **C3** left bright yellow spots, 10^{-3} and 10^{-4} M solutions of **C1** produced a faint purple spot. The colors of the spots left by 10^{-2} M solutions of **C7** and **C9** were blue green, with an intensity similar to the intensity of the purple spot obtained from a 10^{-3} M solution of **C1**.

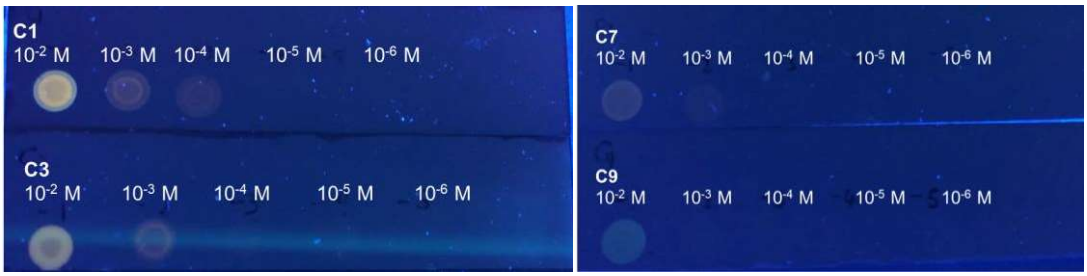


Figure 69. Photograph of a TLC plate coated with alumina onto which have been spotted solutions of CTBs **C1**, **C3**, **C7** and **C9** at different concentrations.

Table 6. Photophysical data of the complexes and the reference compounds in chloroform.

Compound	$\lambda_{max/sh}$ [nm] (ε_{max} [Lmol^{-1}cm^{-1}])	Cond.	$\lambda_{max/sh}$ [nm] (I_r [%])	Φ[a]	τ/μs
CTB(H,C$_2$H)	248 (37780), 258 (39250), 282 (2280), 293 (1920)				
CTB(OMe,C$_2$H)	249 (29730), 258 (28230), 302 (950), 312 (1086)				
C1	240 (113700), 262 (52350), 276 (71250), 285 (86600), 298 (74500), 336 (2200)^{sh}	Ar Air Solid	383, 426, 454, 467^{sh} 353^{sh}, 376, 395 515	0.0246	29.5
C2	238 (83622), 261 (38725), 274 (58089), 284 (72671), 296 (61750), 336 (2200)^{sh}	Ar Air Solid	373, 388, 426, 454, 467^{sh}, 374, 399 409, 532	0.0165	21.6
C3	238 (53776), 260 (39581), 273 (61265), 283 (77465), 295 (65234), 330 (2226)^{sh}	Ar Air Solid	369, 386, 426, 454, 467^{sh}, 375, 393 550	0.0103	21.5
C4	238 (91370), 268 (42926), 284 (46802), 313(37956), 325 (50687), 367 (2708)^{sh}	Ar Air Solid	398, 419, 439, 467^{sh}, 396^{sh}, 407 476	0.00638	1.74(8%) 126(92%)
C5	238 (85353), 268 (41273), 283 (50928), 313(38256), 325 (49659), 367 (2577)^{sh}	Ar Air Solid	391, 440, 470, 400 482	0.0103	0.88(2%) 80.4(98%)
C6	238 (59760), 270 (40145), 282 (50923), 313 (36836), 324 (46729), 366 (2074)^{sh}	Ar Air Solid	396, 419, 437^{sh}, 405 525	0.00365	1.80(10%) 38.4(90%)
C7	229 (49900), 234 (52000), 248 (25400)^{sh}, 261 (34600)^{sh}, 273 (55000)^{sh},283 (69800), 295 (59600), 333 (2380)	Ar Air Solid	373, 428, 453 372, 390 380, 402, 510	0.0246	31.8
C9	234 (56200), 250 (25900), 261 (37700)^{sh}, 273 (60800)^{sh}, 282 (78700), 295 (68700), 332 (1200)	Ar Air Solid	383, 428, 454, 368, 380 412, 443, 475, 515	0.0636	36.8

[a] Determined using PhC$_2$AuPPh$_3$ as reference.

Table 7. Progressional vibrational spacings identified in the emission spectra of complexes **C1 – C6**, **C7** and **C9** in deoxygenated $CHCl_3$ at room temperature.

Complex	Em. max. N° (λ_{exc} = 280 nm)	λ_{em} (nm) (λ_{exc} = 280 / 330 nm)	$\nu^{[a]}$ (cm^{-1})	$\nu_1 - \nu_2$ (cm^{-1})	$\nu_1 - \nu_3$ (cm^{-1})	$\nu_2 - \nu_3$ (cm^{-1})	Attribution	λ_{em} (nm) (λ_{exc} = 330/ 360 nm)	$\nu^{[a]}$ (cm^{-1})	$\nu_1 - \nu_2$ (cm^{-1})	Attribution
C1	1	383	26109	2580	/	/	?	373	26809	1492	Ar(C=C)
	2	425	23529	/	/	1307	Ar(C=C)	395	25316	/	/
	3	450(sh)	22222	/	3887	/	?	/	/	/	/
C2	1	383	26109	2580	/	/	?	369	27100	1654	Ar(C=C)
	2	425	23529	/	/	1307	Ar(C=C)	393	25445	/	/
	3	450(sh)	22222	/	3887	/	?	/	/	/	/
C3	1	383	26109	2580	/	/	?	368	27173	1446	Ar(C=C)
	2	425	23529	/	/	1307	Ar(C=C)	389	25706		
	3	450(sh)	22222	/	3887	/	?	/	/	/	/
C4	1	398	25125	1202	/	/	C-O(OMe)	397	25188	1265	Ar(C=C)
	2	418	23923	/	/	1143	C-O(OMe)	418	23923	/	/
	3	439	22779	/	2346	/	C≡C	/	/	/	/
C5	1	397	25188	2461	/	/	?	397	25188	1265	Ar(C=C)
	2	440	22727	/	/	1314	Ar(C=C)	418	23923	/	/
	3	467	21413	/	3775	/	?	/	/	/	/
C6	1	396	25252	1386	/	/	Ar(C=C)	397	25188	1265	Ar(C=C)
	2	419	23866	/	/	878	?	418	23923	/	/
	3	435	22988	/	2264	/	C≡C	/	/	/	/
C7	1	428	23364	1337	/	/	Ar(C=C)				
	2	454	22026	/	/	/	/				
C9	1	428	23364	1337	/	/	Ar(C=C)				
	2	454	22026	/	/	/	/				

6. Solvent-induced Supramolecular Assembly

6.1 Electronic Spectroscopy (Absorption, Emission and ECD) Studies in Solvent Mixtures

The Au(I) CTB complexes are not soluble at millimolar concentration in polar and/or hydrophilic solvents such as acetonitrile and methanol. Therefore, electronic absorption and emission spectroscopies were used to investigate the effect of the progressive change of the solvent properties, working with non-deoxygenated 10^{-5} M solutions. First, the effect of increasing the $CH_3CN/CHCl_3$ ratio from 0:100 to 99:1 v/v on the UV-vis absorption and emission spectra of **C1** and **C4** were studied. In the case of **C1** (**Figure 70**) a significant hyperchromism of all three major bands at 276, 285, and 298 nm (e.g., $\Delta\varepsilon/\varepsilon$ = + 15% for the 285 nm band), and a concomitant noticeable hypsochromic shift (*ca* 2 nm) of the absorption bands at 276 and 298 nm were observed. By contrast, both residual absorbance between 312 and 350 nm and intensity of the weak emission at 530 nm observed by excitation at 330 nm decreased.

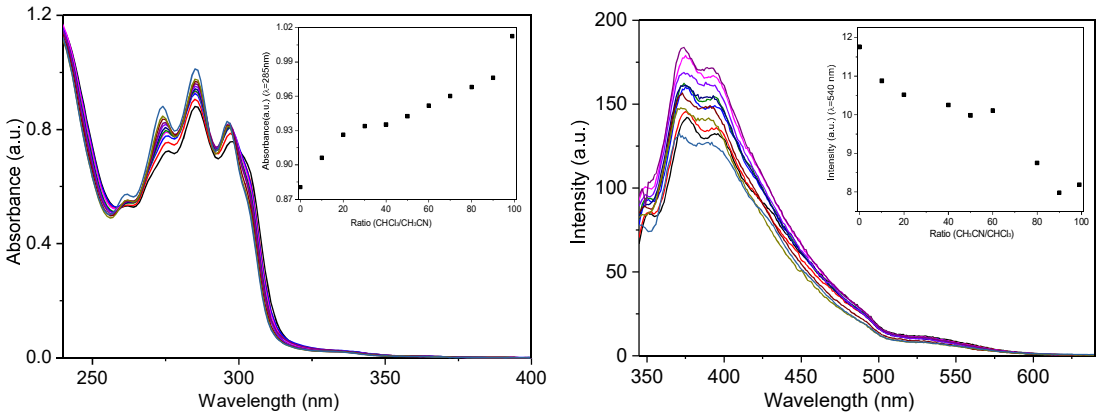


Figure 70. Absorption (left) and emission (right) spectra of freshly prepared 10^{-5} M solutions of **C1** in $CHCl_3/CH_3CN$ (λ_{exc} = 330 nm). Insets: Absorbance as a function of the solvent ratio 285 nm. Emission intensity in function of the solvent ratio at 540 nm.

In the case of **C4**, upon the increase of the proportion of CH_3CN, the absorbance of the higher energy bands at 284 nm increased by 20%, but the absorbance of the lower energy bands at 330 nm and the absorbance tails decreased. The intensity of the fluorescence band at 400 nm increased first; then, when the content of CH_3CN was

above 70%, it decreased, and a small blue shift of *ca*. 2 nm was observed. The emission bands at 540 nm decreased with the increase of MeCN content.

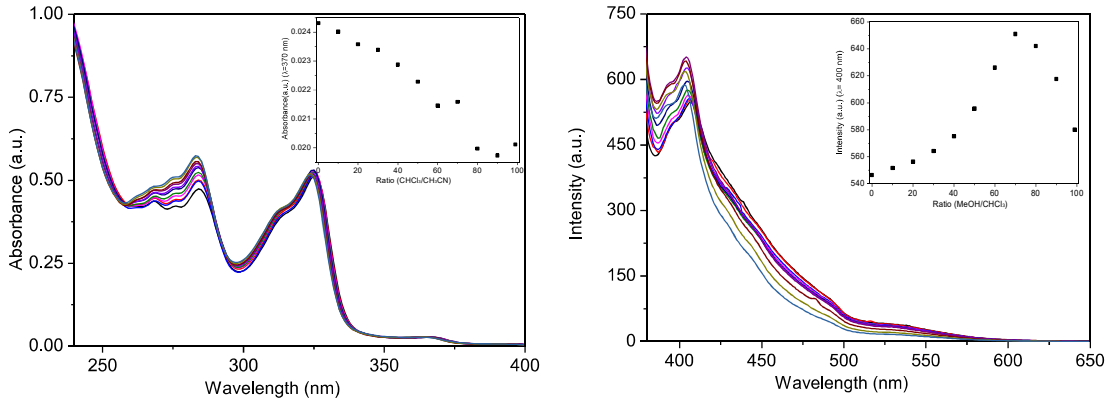


Figure 71. Absorption (left) and emission (right) spectra of freshly prepared 10^{-5} M solutions of **C4** in $CHCl_3/CH_3CN$ (λ_{exc} = 360 nm). Insets: Absorbance as a function of the solvent ratio at 370 nm. Emission intensity in function of the solvent ratio at 400 nm.

Next, we studied the effect of the gradual addition of methanol to chloroform solutions of the Au(I) CTB complexes on their electronic absorption and emission spectra. As shown in **Figure 72**, increasing the $CH_3OH/CHCl_3$ ratio from 0:100 to 99:1 v/v produced first a slight hyperchromism between 0 and 30% MeOH of the absorption bands of **C1**. Then the absorbance significantly decreased with band broadening and a significant red shift happened when MeOH exceed 60%. In general, between 0 and 99% MeOH, an overall 27% decrease happened to the maximum absorbance, and the corresponding wavelength shifted from 285 nm to 288 nm. It is worth noting that the absorbance of the low-energy tailing band (330 nm) increased in three stages: There were no changes from 0 to 30% methanol and a small blue shift was observed, then it increased slowly between 40 and 70% methanol, while the maximum was red-shifted to its original wavelength. Finally, a higher change rate was observed between 70 and 90% methanol, while a further red shift and absorbance broading were observed. Overall, the absorbance at 330 nm increased by a factor of nearly 3.5 between 0 and 90% methanol. This increase of absorbance is likely to be due to the combined Tyndall scattering and absorption of light by small size particles, a phenomenon that has been formalized by Mie.[147] Remarkable changes in the emission of **C1** collected upon

excitation at 330 nm in aerobic conditions were observed when increasing the MeOH/$CHCl_3$ ratio (**Figure 71**). This excitation wavelength was chosen because it is located in the MeOH content-dependent band tail of the absorption spectrum. The intensity of the fluorescence band with maxima at 376 and 395 nm decreased linearly while a new band with maxima at a much lower energy, in the visible range of the spectrum (494 and 539 nm), grew up progressively. The plot of the emission intensity at 540 nm versus the methanol/chloroform ratio showed features that were reminiscent of those previously noted for the variations of absorbance at 330 nm: No intensity change between 0 and 40% of methanol followed by a steady increase from 50 to 70%. A jump was then observed between 70 and 80%. The lowest energy emission maximum shifted significantly (13 nm) to shorter wavelengths from 550 nm for 50% MeOH to 537 nm for 99% MeOH. The shift was more pronounced above 70% MeOH. The evolution of the absorbance of the band tail at 330 nm was the same as the evolution of the intensity of the emission at 540 nm upon excitation at 330 nm. The same experiments run several hours after the preparation of the solutions showed that the absorbance of the solutions containing 80 – 99% MeOH had decreased by comparison with those measured for the fresh solutions. The variations of the emission intensity around 545 nm were similar to those observed with solutions examined immediately after preparation. Monitoring excitation spectra while observing the rise of the low energy emission (540 nm) showed the growth of bands at 288 and 308 nm, which coincide with the lower energy maxima of the absorption spectrum. In summary, the examination by electronic absorption and emission spectroscopies of dilute solutions of **C1** in chloroform/methanol mixtures containing increasing proportions of methanol showed that these solutions displayed a two-phase behavior: The regular solution phase for methanol contents < 50%, and a new phase for methanol contents ≥ 60%.

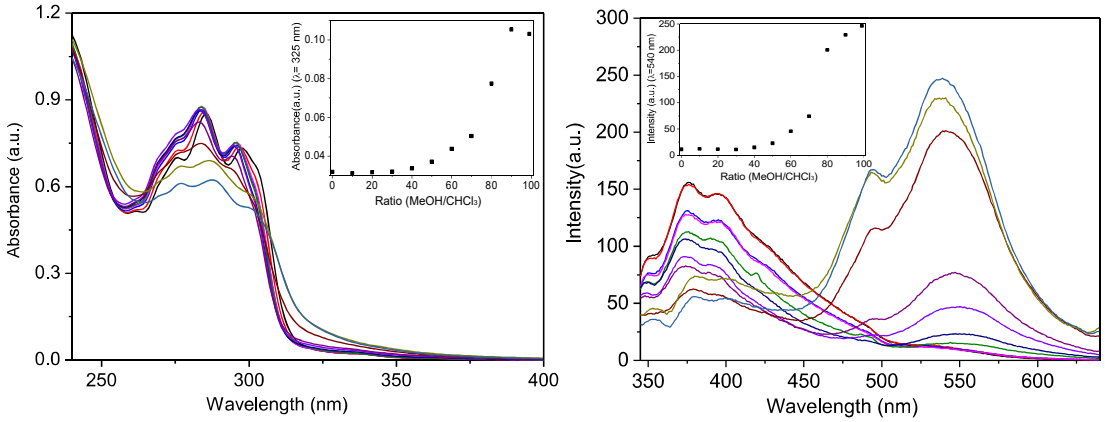


Figure 72. Absorption (left) and emission (right) spectra of freshly prepared 10^{-5} M solutions of **C1** in $CHCl_3$/MeOH. Insets: Absorbance as a function of the solvent ratio at 325 nm. Emission intensity in function of the solvent ratio at 540 nm.

$CHCl_3$/MeOH solutions of **C7** prepared in aerobic conditions showed more marked time-dependent features. The electronic absorption spectra recorded immediately after preparation of the solutions did broaden and the maximum of absorption underwent a hypsochromic shift from 283 to 279 nm, but the corresponding absorbance did not change significantly. The evolution of the emission spectra of the fresh $CHCl_3$/MeOH solutions also differed from what was observed in the case of **C1**. Upon increase of the MeOH content from 10 to 90% and finally 99%, the emission maximum at 371 nm shifted to the blue (365 nm at 99% MeOH), but its intensity did not decrease significantly, while the band at *ca* 540 nm was very weak (I_r = 0.03 at 99% MeOH). Nevertheless, the evolutions of the absorption and emission spectra after two days ripening in $CHCl_3$/MeOH mixtures resembled those observed for fresh solutions of **C1**. Plotting the absorbance at 325 nm *vs.* the MeOH/$CHCl_3$ ratio showed that it started to increase at 40% MeOH, the slope being then steeper between 60% and 90% MeOH. The emission spectra showed a steady decrease of the maximum at 372 nm, with a red shift to 379 nm at high methanol content, to *ca* 10% of its initial value, while a new band centered around 550 nm developed. The plot of the emission intensity at 553 nm *vs* the MeOH/$CHCl_3$ ratio showed also a two-step increase: At first between 40% and 60% MeOH, then, at a higher rate, between 60 and 90%. Noticeably, the solution containing 99% MeOH did not seem to strictly follow the absorption and emission

trends as the absorbance and emission intensity were slightly lower than those measured for 90% MeOH solutions.

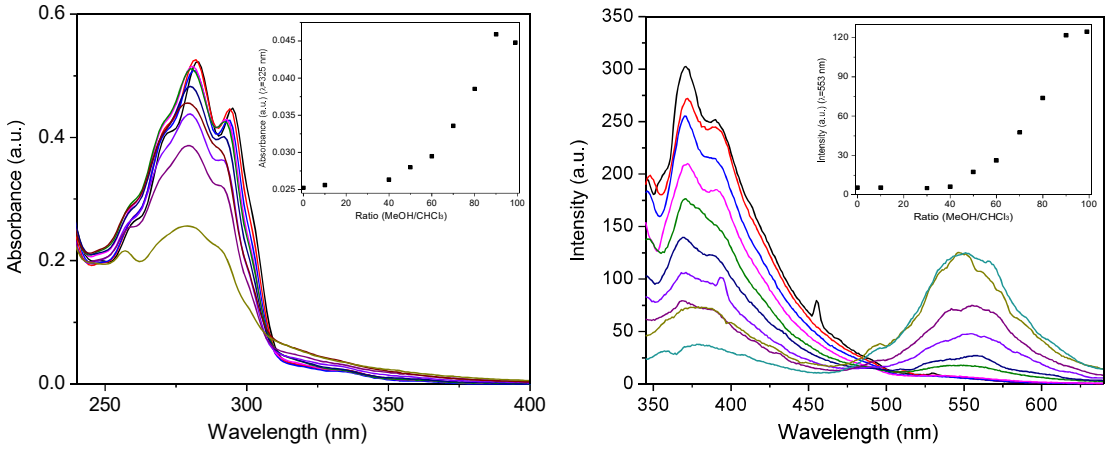


Figure 73. Absorption (left) and emission (right) spectra of aged 10^{-5} M solutions of **C7** in $CHCl_3$/MeOH. Insets: Absorbance as a function of the solvent ratio at 325 nm. Emission intensity in function of the solvent ratio at 540 nm.

The absorbance changes of solutions of **C9** in $CHCl_3$/MeOH mixtures were examined two days after their preparation. Increasing the methanol content up to 80% v/v shifted the maximum at 282 nm to 279 nm, while the other maximum (295 nm) also underwent a hypsochromic shift, with concomitant absorbance decrease as long as the content of MeOH was below 80%. When MeOH was 90% or 99%, a significant band broadening happened. The optical density at 330 nm started to increase at 20% MeOH, at an earlier stage than for complexes **C1** and **C7**. The evolution of the emission spectra of 10^{-5} M solutions of **C9** in $CHCl_3$/MeOH mixtures in aerobic conditions showed that the weak emission at 368 nm originally observed in $CHCl_3$ decreased upon gradual addition of MeOH, while a shoulder at lower energy emerged as a maximum at *ca* 381 nm for 30% of methanol. We did not observe any red shift whatever the MeOH content. Contrary to **C1** and **C7**, the decrease of this emission band was not accompanied with the progressive growth of a new low energy band between 500 and 600 nm, but ultimately (at 99% MeOH) led to the sudden apparition of bands at 485 and 529 nm, the shape of which differed from the bands observed in this region for **C1** and **C7**. Interestingly, the shape of these emission bands was reminiscent of the characteristics

of the emission band observed for the same complex in the solid state. By contrast, the maxima of the solid state emissions of complexes **C1** and **C7** were shifted to higher energies by comparison with the maxima recorded in 1:99 $CHCl_3$/MeOH (respectively 540 and 550 nm).

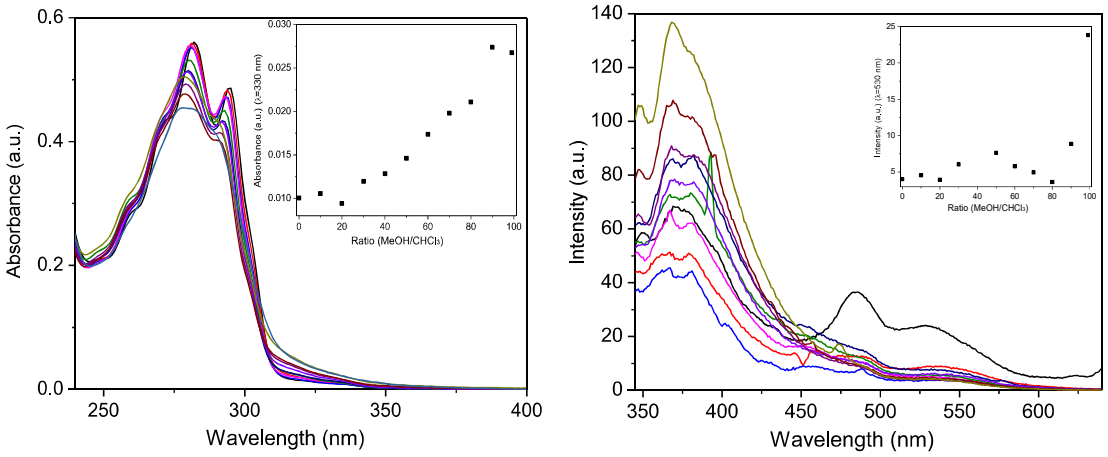


Figure 74. Absorption (left) and emission (right) spectra of aged 10^{-5} M solutions of **C9** in $CHCl_3$/MeOH. Insets: Absorbance as a function of the solvent ratio at 330 nm. Emission intensity in function of the solvent ratio at 540 nm.

$CHCl_3$/MeOH solutions of **C2** and **C3** prepared in aerobic conditions also showed time-dependent features. The electronic absorption spectra recorded immediately after preparation of the solutions did slightly broaden and the maximum of absorption underwent a small hypsochromic shift (2 nm) below 80%, but the corresponding optical densities did not change significantly. However, when the proportion of MeOH was above 80%, band broadening happened, and the corresponding optical densities decreased drastically. Changes in the absorbance of the band tail at lower energy could be observed only when the MeOH content was above 80%. Upon increase of the MeOH content from 10 to 90% and finally 99%, the intensity of emission maximum at 371 nm decreased gradually, while the emission band tail decreased first. However, when the MeOH content was increased, new lower energy emission bands appeared (at 70% MeOH for **C2**, 80% MeOH for **C3**). Nevertheless, the evolutions of the absorption and emission spectra after ripening of the $CHCl_3$/MeOH solutions resembled those

observed for fresh solutions of **C2** and **C3**, except that the new emission bands of aged solutions appeared at lower MeOH content. The intensity of the emission maximum at 372 nm showed a steady decrease, while a new band centered around 550 nm developed. The plot of the emission intensity at about 550 nm *vs* the MeOH/$CHCl_3$ ratio showed that this low energy emission band appeared at different MeOH content, 50% for **C2** and 60% for **C3**. Moreover, in both cases the aggregation phenomena were time-dependent. The changes in the emission intensity of **C2** in $CHCl_3$/MeOH observed at 540 nm at different ripening times are shown in **Figure 75**.

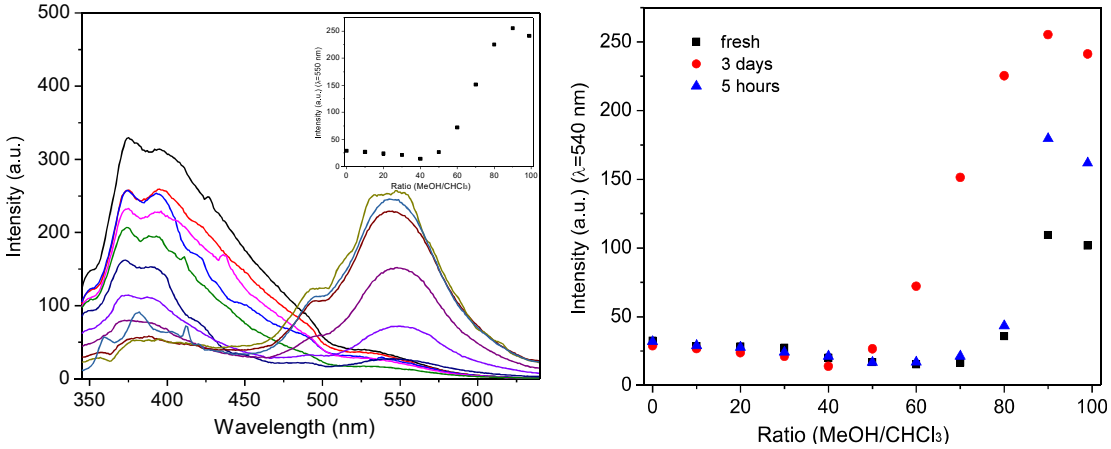


Figure 75. Emission spectrum of 10^{-5} M aged solutions of **C2** for 3 days in $CHCl_3$/MeOH (exc.: 330 nm) observed at 540 nm (left), Changes in the emission intensity at different ripening times (right): Black: Freshly prepared solutions; blue: five hours; red: aged solutions.

Now, comparing all five complexes together, the less electron-rich the phosphine ligands, the faster the formation of the new emission bands. The onset wavelengths of these new emission bands are collected in **Table 8**. For **C1**, the new lower energy bands appeared as soon as 40% MeOH in fresh solutions, which was much earlier than **C2** (70%), even more than **C3** (80%). Noticeably, neither **C7** nor **C9** showed such an emission. Ripened solutions of **C1** in $CHCl_3$/MeOH mixtures showed stronger emission than fresh solutions. However, the onset for the apparition of the new emission band did not change. Ripened solutions of **C2** and **C3** both showed also stronger emission than fresh solutions, but the onset of this emission appeared at lower MeOH content than before. Ripened solutions of **C7** showed the new emission band at 550 nm when

the MeOH content was 40%. As the low energy emission does not show up in $CHCl_3$/MeCN, even at high MeCN content, it is likely that it results from solvophobic interactions, rather than from changes in polarity. The CTB complexes are highly lipophilic, because of the CTB itself and the phosphine terminal ligands. Therefore, they form compacted supramolecular assemblies in order to minimize their exposition to the hydrophilic methanol solvent. At the same time, the aurophilic interactions could be established. In the cases of **C1 – C3**, which featured PPh_3-incorporating terminal ligands, lipophilic interactions were stronger than in the case of **C7** and **C9**. As a consequence, **C1 – C3** formed aggregates more readily. In addition, the enhanced electron deficiency of PPh_3-containing ligands favored the building up of Au···Au interactions. Within the series **C1 – C3**, the onset of emission at 540 nm followed the order of phosphine electron acceptor character: PPh_3 >PPh_2Me > $PPhMe_2$. By comparison with **C1**, **C7**, containing the more electron rich and the smallest phosphine ligands, and **C9**, containing more electron-rich, but biggest phosphine ligands, shows weaker emission at 550 nm. This indicates that unfavorable electronic effects predominate in the case of **C7**, whereas both unfavorable electronic and steric effects come into play in the case of **C9**.

We next consider the series **C4 – C6**. The electronic absorption spectra of **C4** (**Figure 76**) recorded immediately after preparation of the solutions slightly broadened, the maximum of absorption at 325 nm underwent a small hypsochromic shift (−2 nm) and the absorbance slightly decreased upon addition of MeOH. However, when the proportion of MeOH was above 80%, a significant band broadening happened, the corresponding optical densities decreased drastically, and a small red shift (+2 nm) was observed. The low energy absorbance above 350 nm increased when the MeOH content was 60% until it reached its maximum value for 99% MeOH. The corresponding emission spectra showed that the higher energy emission bands at 400 nm decreased gradually and a lower emission band at 545 nm appeared and increased when MeOH ≥ 60%. **C5** showed similar changes except that the new emission band appeared when the MeOH was above 80%.

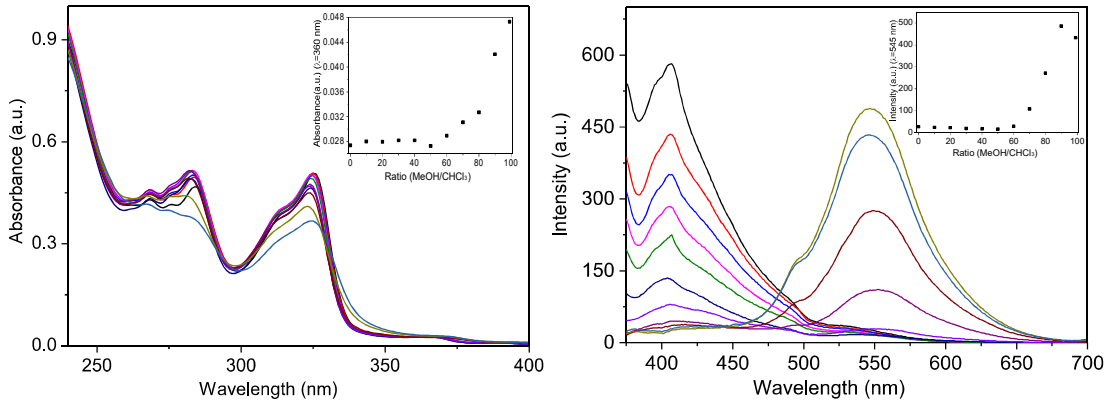


Figure 76. Fresh absorption spectra of 10^{-5} M solutions of **C4** in $CHCl_3$/MeOH, inset: Absorbance in function of the solvent ratio at 360 nm. Fresh emission spectra of 10^{-5} M solutions of **C4** in $CHCl_3$/MeOH (exc.: 330 nm), inset: Emission in function of the solvent ratio at 545 nm.

In the case of **C6**, increasing the $CH_3OH/CHCl_3$ ratio from 0:100 to 99:1 v/v produced a slight hypsochromic shift of ca. 2 nm between 0 and 80% MeOH at 282 nm. The absorbance at 282 nm increased gradually, while the absorbance at 324 nm decreased. However, as methanol continued to increase to 90% and 99%, the absorbance of both maxima at 282 nm and 324 nm decreased significantly. The corresponding bands broadened, while the low energy absorbance at 350 nm increased. In the case of fresh solutions, the intensity of the fluorescence band with a maximum at 406 nm decreased while a new band with a maximum at a longer wavelength (545 nm) grew up progressively after the percentage of MeOH was over 80%. The intensity ratios I_{545}^{99}/I_{406}^{0}, $I_{545}^{99}/I_{406}^{99}$, and I_{545}^{0}/I_{406}^{0} were 0.19, 4.40, and 0.048, respectively. The evolution of the emission spectra after two days ripening in $CHCl_3$/MeOH mixtures showed that the intensity of the fluorescence band at 406 nm decreased gradually between 0% and 70% MeOH. There was hardly any change after 80%. However, the new emission bands at 548 nm appeared when the MeOH content was 60%, therefore at an earlier stage than in the case of fresh solutions. Furthermore, they showed a much stronger emission at 90% MeOH than the corresponding fresh solutions. The intensity ratios I_{545}^{99}/I_{406}^{0}, $I_{545}^{99}/I_{406}^{99}$, and I_{545}^{0}/I_{406}^{0}, respectively 0.45, 9.31, and 0.048 were higher than those calculated for the fresh solutions, I_{545}^{0}/I_{406}^{0} excepted. However, upon going from 90 to 99% MeOH, a dramastic decrease of the emission band at 548 nm was

observed in the case of the aged solution.

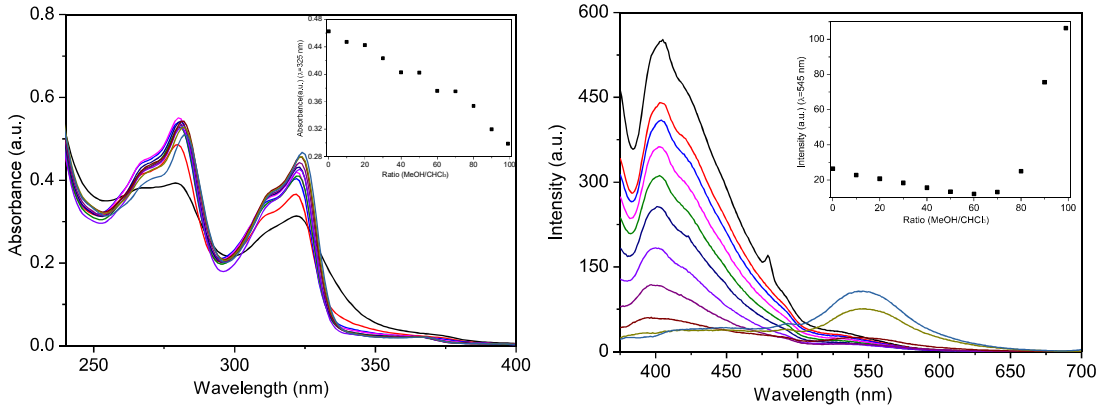


Figure 77. Absorption spectra of fresh 10^{-5} M solutions of **C6** in $CHCl_3$/MeOH. Inset: Evolution of the absorbance in function of the solvent ratio at 325 nm. Emission spectra of fresh 10^{-5} M solutions of **C6** in $CHCl_3$/MeOH (exc.: 360 nm). Inset: Evolution of the emission intensity in function of the solvent ratio at 545 nm.

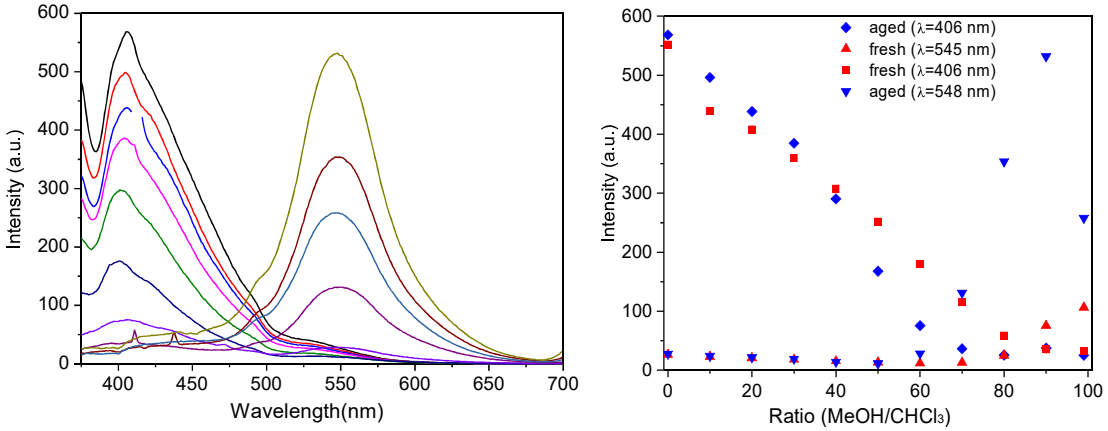


Figure 78. Left: Emission spectra of 10^{-5} M solutions of **C6** aged for two days in $CHCl_3$/MeOH (exc.: 360 nm). Right: Evolution of the emission intensities at 406 and 548 nm in function of the solvent ratio at different ripening times.

Table 8: The intensity ratios of the different complexes at *ca* 540 and 380 nm and the percentage of MeOH at the onset of the emission at 540 nm.

Compound	solution age	I_{540}^{99}/I_{380}^{0}	$I_{540}^{99}/I_{380}^{99}$	I_{540}^{0}/I_{380}^{0}	MeOH% at the onset of emission at 540 nm
C1	fresh	1.57	4.73	0.07	40%
	aged	1.96	5.88	0.064	40%
C2	fresh	0.38	2.37	0.16	70%
	aged	0.54	3.17	0.12	50%
C3	fresh	0.53	4.15	0.13	80%
	aged	0.72	9.65	0.067	60%

Table 8 (continued)

Compound	solution age	I_{540}^{99}/I_{380}^{0}	$I_{540}^{99}/I_{380}^{99}$	I_{540}^{0}/I_{380}^{0}	MeOH% at the onset of emission at 540 nm
C4	fresh	0.75	16.03	0.046	60%
C5	fresh	0.27	3.09	0.088	80%
	aged	0.38	6.23	0.086	60%
C6	fresh	0.19	4.0	0.048	80%
	aged	0.45	9.31	0.048	60%
C7	fresh	0.040	0.049	0.027	-
	aged	0.41	3.54	0.018	40%
C9	aged	0.018	5.95	0.029	**C9**

In the series **C1 – C6**, comparison of the pairs of complexes **C1**/**C4**, **C2**/**C5** and **C3**/**C6**-indicated that the ratio I_{540}^{99}/I_{380}^{0} between the emission band at 540 nm and the emission band at 380 nm was higher for the complexes deriving from **CTB(H,C$_2$H)**. Moreover, the onset of the emission at 540 nm appears at lower methanol contents in this first series, if we discard **C3** and **C6**, which show the new emission band at the same MeOH contents, the solution being fresh or not. These observations could be interpretated by the higher propensity of **C1 – C3** to form emissive aggregates than **C4 –C6**. Noticeably, the solutions containing 99% MeOH did not seem to strictly follow the absorption and emission trends. Their absorbance and emission intensities were lower than those measured for 90% MeOH solutions. In particular, the intensities of the emission bands of **C3** and **C6**, at about 540 nm, decreased significantly. Monitoring the excitation spectra of **C1 – C3** while observing the rise of the low energy emission (~540 nm) showed the growth of bands at 288 and 308 nm, which coincide with the lower energy maxima of the absorption spectrum. In addition, the excitation spectra in the series **CTB(OMe,C$_2$AuPR')** showed identical features, that is, a shoulder at 306 nm and a maximum at 320 nm, and a very broad band of weak intensity tailing from 350 to 400 nm. Remarkably, the shape and the maxima of the excitation spectra matched perfectly those of the absorption spectra.

Fresh and 3 days old 10^{-5} M solutions of the complexes **C1**, **C3**, **C7** and **C9**

containing different proportions of MeOH were prepared in vials. The solutions were examined under a UV lamp by irradiation at 365 nm. In the case of **C1**, fresh solutions in 40% MeOH were not emissive compared to solutions in 50% MeOH, which emitted very weakly. The emission intensity increased with the increase of MeOH content. After 3 days, no significant changes were observed. In the case of fresh **C3** solutions, a clear yellow emission was observed only when the proportion of MeOH was as high as 70%. By contrast with **C1**, **C3** showed after 3 days a yellow emission starting from 50% MeOH, which increased gradually as the MeOH content increased. In summary, 70% MeOH fresh solutions of **C3** and 50% MeOH aged solutions of **C3** both showed a very weak yellow emission. The onset of this emission appears at the MeOH proportions that were determined by fluorimetry. The photographs of **Figure 79** also clearly show that the emissive mixtures are turbid, which corresponds to the apparition of the aggregates. In the cases of fresh solutions of **C7** and **C9** no emission was observed, which also coincided with the observations by fluorimetry. For aged **C7** solution, similar observation was also found except the emission of **C7** was much weaker than **C1** and **C3**. 3 days-aged solutions of **C9** were not emissive at the naked eye, in agreement with the observations by fluorimetry.

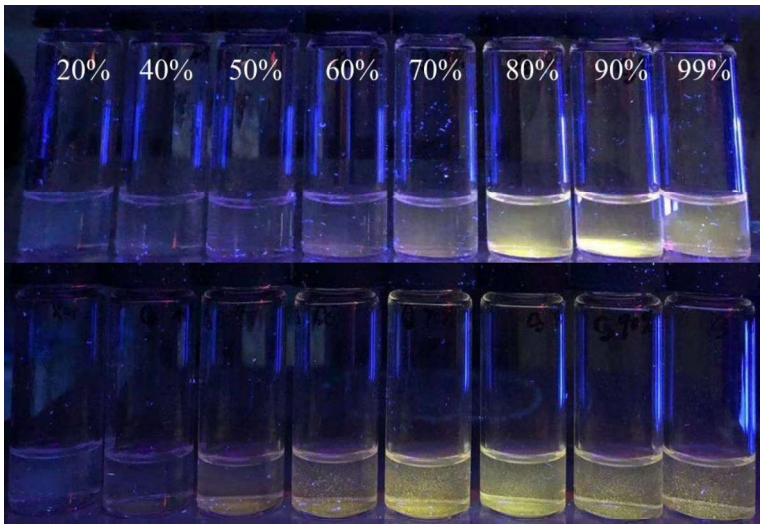


Figure 79. Photographs of vials containing 10^{-5} M solutions of complex **C3** in different proportions of MeOH in $CHCl_3$ under 365 nm irradiation. Top row: fresh solutions; bottom row: aged solutions.

The behaviors of solutions of enantiomerically pure gold(I) CTBs (**C1**, **C3**, **C5** and **C6**) in $CHCl_3$/MeOH mixtures of various compositions were studied by emission and ECD spectroscopies, **C8** was studied by absorption emission and ECD spectroscopies. Both enantiomers of **C1** were examined. The evolution of the emission spectra of (–)-**C1** with the MeOH/$CHCl_3$ ratio is reproduced in **Figure 80**. Upon addition of increasing amounts of MeOH the emission at 377 nm decreased, while the new emission band at low energy appeared clearly for 60% MeOH at 545 nm. It then grew up abruptly between 70 and 80 % MeOH, while its maximum was shifted to 537 nm, as shown in **Figure 80**. Similar observations were done in the case of (+)-**C1**. As a reminder, the emission at 545 nm of the racemic solution of **C1** showed up for 50% MeOH, then it increased with a significant gap for 70% ≤ MeOH ≤ 80%, followed by an increase between 80 and 99% MeOH at the same rate as between 50 and 70% MeOH. By comparison, the onset of the emission of enantiopure (–)-**C1** appeared for 10% more MeOH, but the emission intensity showed an increased gap also for 70% ≤ MeOH ≤ 80%. From this latter MeOH content, the emission intensity slowly evolved to its maximum value for 99% MeOH.

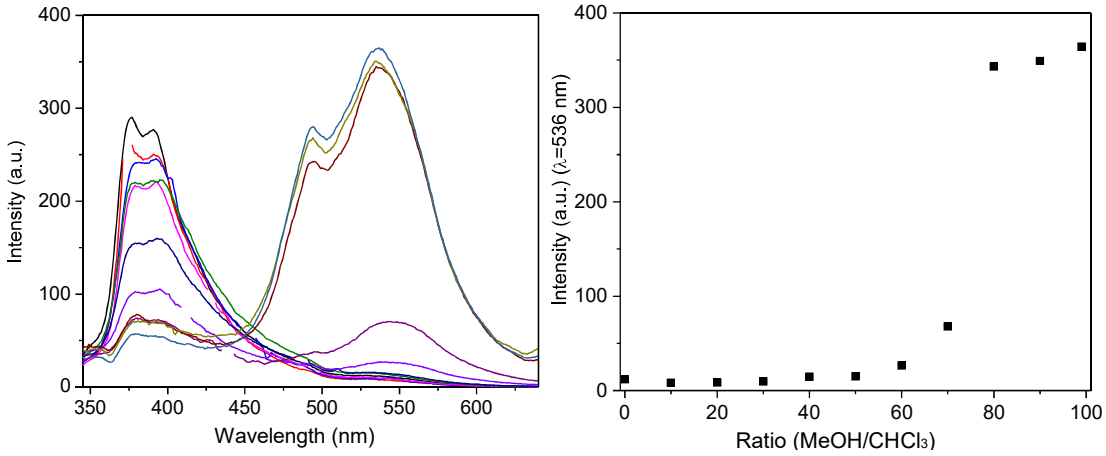


Figure 80. (Left) Evolution of the emission spectra of 10^{-5} M solutions of (–)-**C1** in $CHCl_3$/MeOH (exc.: 330 nm) and (right) plots of the emission intensities at 536 nm vs. the MeOH/$CHCl_3$ ratio.

In the case of (–)-**C8**, the evolution of the electronic absorption spectra in $CHCl_3$/MeOH mixtures was very similar to that observed for the C_3-symmetric

homologue **C1**: Slight hypsochromic shift of the main absorption band, decrease of its optical density at 280 nm, broadening and rise of an absorption tail around 320 – 330 nm. Monitoring the intensity of this absorption against the solvent composition showed that it started to increase significantly for ≥ 80% MeOH. The evolution of the emission spectra in aerobic conditions upon excitation at 330 nm was reminiscent of that observed in the case of **C1**, except the emission at 538 nm was weaker. In short, the evolution of the absorbance at 320 nm showed a sudden increase at MeOH > 70%, concomitantly with the variation of the emission intensity monitored at *ca.* 540 nm.

In the case of (–)-**C3**, upon increase of the MeOH content from 10 to 99%, the intensity of the emission maximum at 372 nm decreased gradually, while the emission band tail at 530 nm decreasing first. When the proportion of MeOH was 60%, a new lower energy emission band at 545 nm appeared, the intensity of which steadily increased until it reached its maximum at 99% MeOH. By comparison, in the case of racemic **C3**, the onset of the growth of the emission band at 545 nm required a slightly lower proportion of MeOH (60% vs. 70%), and the maximum of intensity of this emission band was reached for 90% MeOH. It then decreased to a lower value for 99% MeOH.

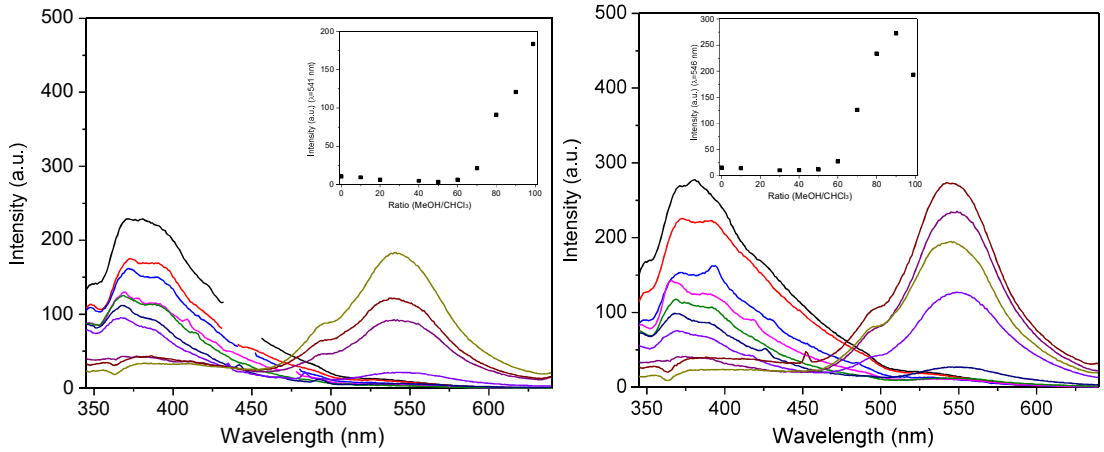


Figure 81. Aged emission spectra of 10^{-5} M solutions of (–)-**C3** (left) and **C3** (right) in $CHCl_3$/MeOH (exc.: 330 nm), inset: emission in function of the solvent ratio at about 546 nm.

In the case of **C5**, similar observations were done upon comparison of the emission

behaviors of the separated enantiomers vs. the racemate (**Figure 82**). The intensity of the higher energy emission band of both (−)-**C5** and *rac*-**C5** at 403 nm decreased while the lower energy new emission band at 545 nm appeared with the increase of the MeOH content. However, in the case of **C5**, the increase of the intensity of the lower energy emission band was steeper between 70 and 80% MeOH, and reached its maximum for 90% MeOH, whereas in the case of (−)-**C5**, the increase of the intensity of the same band was monotoneous between 70 and 99%, proportion of MeOH at which it reached its maxium, as observed in the case of **C3**.

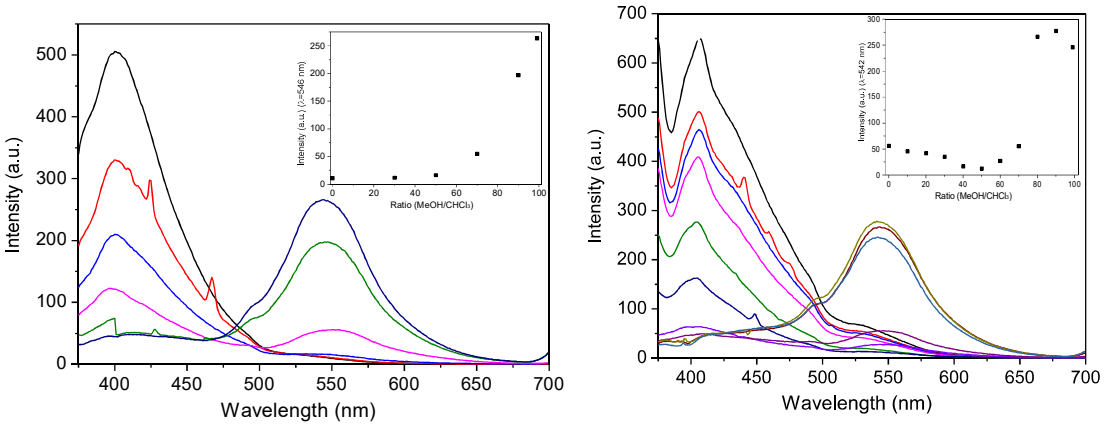


Figure 82. Emission spectra of 10^{-5} M solutions of (–)-**C5** (left) and *rac*-**C5** (right) in $CHCl_3$/MeOH (exc.: 360 nm), insets: plots of the emission intensities at around 540 nm vs. the MeOH/$CHCl_3$ ratio.

The ECD spectra of the optically active versions of **C1** showed approximatively mirror-image evolutions, which were roughly reminiscent of the changes observed in the absorption spectra of the racemate (**Figure 83**). For example, in the case of (+)-**C1**, the main absorption at 304 nm decreased in intensity and was progressively shifted to shorter wavelength (302 nm) until the MeOH content was < 80%. Considerable band broadening was already apparent at this latter concentration, but at 90% MeOH secondary maxima had completely disappeared and the main maximum had shifted to a longer wavelength (308 nm).

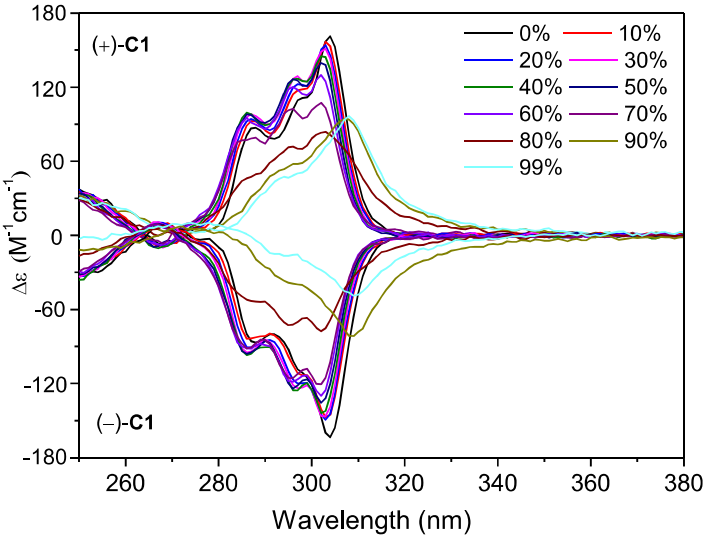


Figure 83. Evolutions of the ECD spectra of 10^{-5} M solutions of the enantiomers of complex **C1** in $CHCl_3$/MeOH mixtures at room temperature.

The ECD spectra of the optically active (–)-**C8** showed that the band with a maximum at 303 nm decreased in intensity below 40% MeOH, as well as a shoulder at 297 nm. However, with the increase of MeOH content, the absorption shoulder at 297 nm became dominant, no band broadening being observed, whatever the proportion of MeOH. Since the band broadening was related to nanoparticle formation, our observations indicated that (–)-**C8** did not form nanoparticles or that the nanoparticles were too small, which was also consistent with the emission results because (–)-**C8** showed much weaker luminescence.

The evolution of the ECD spectra of the optically pure complexes (–)-**C2** and (–)-**C3** (**Figure 84**) in $CHCl_3$/MeOH mixtures was similar to what was observed for (–)-**C8** when the MeOH content was < 80%: The main absorption at 304 nm decreased in intensity and was progressively shifted to shorter wavelength (302 nm) until the MeOH content was < 80%, but the shoulder at 297 nm became more and more dominant with the increase of MeOH. When the MeOH proportion was 80%, a drastic decrease was observed, at 90% MeOH secondary maxima had completely disappeared and the main maximum had shifted to longer wavelength (308 nm), which was similar to chiral **C1**

at 99% MeOH, the main maximum of which being shifted to 312 nm.

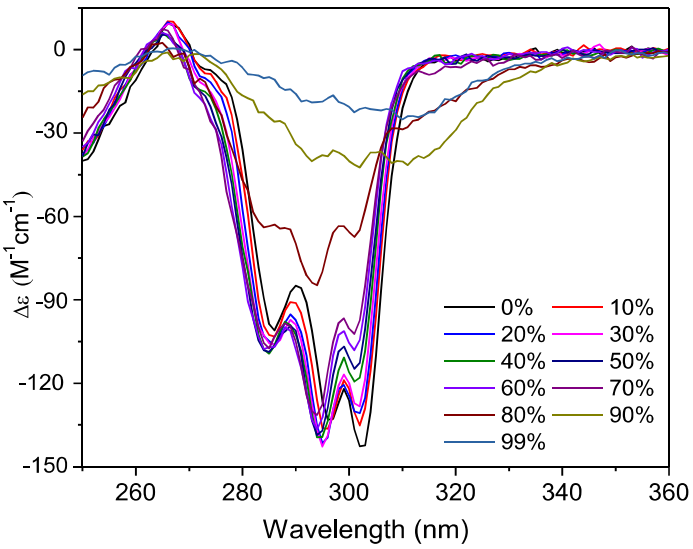


Figure 84. Evolution of the ECD spectra of 10^{-5} M solutions of the enantiomers of complex (–)-**C3** in $CHCl_3$/MeOH mixtures at room temperature.

The ECD spectra of the optically active versions of **C5** showed approximatively mirror-image evolutions. In the case of (+)-**C5**, the main absorption (at 326 nm) was in the positive region. It decreased in intensity, while being progressively shifted to shorter wavelength (324 nm) until the MeOH content was < 80%. The other main absorption (at 304 nm) was in the negative region. It decreased in intensity and shifted to 301 nm. Noteworthy also was the fact that the intensity of the low energy band of the B_{1u} couplet at 284 nm decreased gradually and disappeared at 99% MeOH/$CHCl_3$. A drastic decrease of the intensities of the bands at 324 and 304 nm was observed at 90% MeOH, but the maxima of these two bands shifted back to their original wavelength (304 nm and 326 nm). Concomitantly, a considerable band broadening was observed, producing band tailing down to 370 nm. At 99% MeOH, a significant red shift of about 8 nm was observed compared to 90% MeOH. In addition, the points of sign inversion at 293 and 310 nm shifted to lower energy, by 3 nm and 6 nm respectively. Noteworthy, the enantiomerically pure (–)-**C5** and (–)-**C6** showed exactly the same changes.

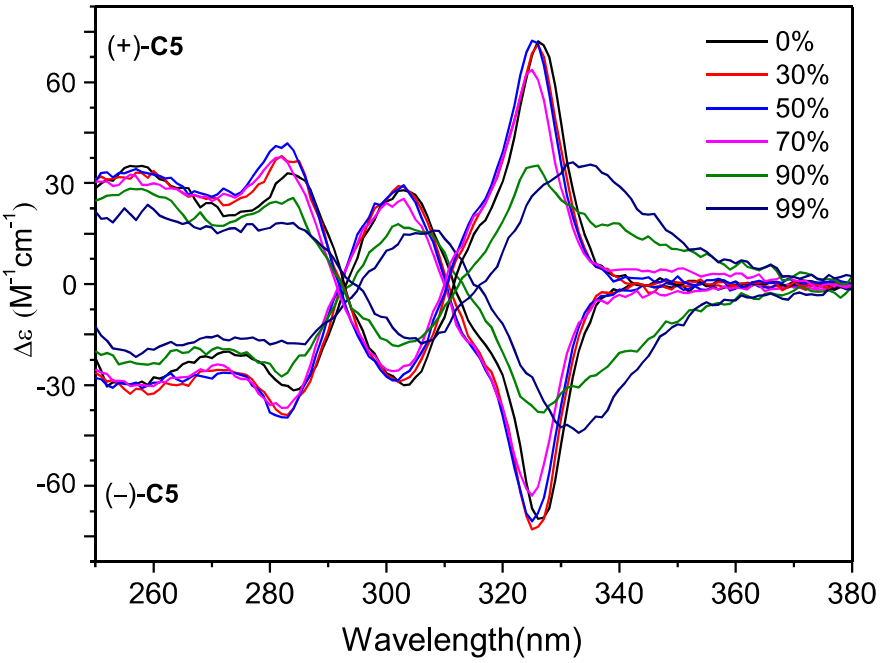


Figure 85. Evolutions of the ECD spectra of 10^{-5} M solutions of the enantiomers of complex **C5** in $CHCl_3$/MeOH mixtures at room temperature.

Rare are reports on optically-active nanoparticles.[148,149] Calculations, in the frame of the Mie theory, of the ECD spectra of hypothetical solutions of spherical nanoparticles of optically-active poly-*L*-glutamic acid (PGA) were reported, and compared to the experimental ECD spectrum of a PGA solution. They indicated that the broadening of the spectrum and red shift of wavelength maxima were both related to the formation of nanoparticles.[150] This study had shown that, as the radius of the spheres increased from 30 to 100 nm, the peak maxima and the cross-over points of the bisignate signal of the PGA solution observed experimentally shifted bathochromically, while the overall shape of the ECD signal was increasingly distorted.

6.2 Dynamic Light Scattering (DLS) and Scanning Tunneling Electron Microscopy (STEM)

The spectroscopic studies of solutions of the gold(I) CTBs in $CHCl_3$/MeOH of increasing MeOH proportion have shown absorption band broadening and tailing in the electronic absorption and circular dichroism spectra, the switch of the emission from the UV to the visible, and, at the naked eye, the detection of turbidity. These

observations were all consistent with the formation of (nano)particles as the medium became richer in MeOH. Therefore, we undertook the characterization of these nanoparticles by using two different techniques, dynamic light scattering (DLS) and scanning tunneling electron microscopy (STEM).

Firstly, solutions of **C1** at the concentration used for the electronic absorption and emission studies (10^{-5} M) were examined by dynamic light scattering (DLS). The selected MeOH/$CHCl_3$ ratios were 20:80, 50:50, 80:20 and 99:1, v/v. These experiments showed that the solutions contained nanoparticles, the size of which depended on the MeOH/$CHCl_3$ ratios. The corresponding distribution diagrams are shown in **Figure 86**.

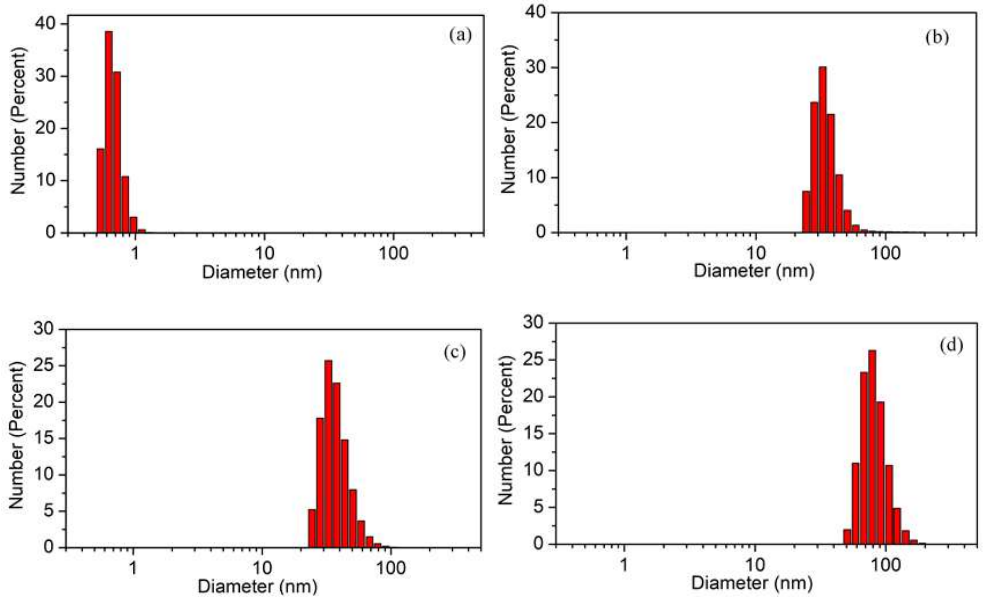


Figure 86. Nanoparticle size distribution diagrams for 10^{-5} M solutions of **C1** in $CHCl_3$/MeOH mixtures: (a) 80:20, (b) 50:50, (c) 20:80, and (d) 1:99.

Whereas the 20:80 composition hardly showed any nanoparticle, nanoparticles were detected for the 50:50 ratio. The distribution diagram showed that the size of the nanoparticles ranged between 25 and *ca* 80 nm, with a maximum of population for sizes of 30 – 35 nm. A similar distribution was observed in the case of the 80:20 composition, except that the proportion of nanoparticles ranging from 35 to 40 nm was higher than in the case of the 50:50 composition. Finally, the 99:1 composition contained a broader distribution of nanoparticles, with sizes ranging from 50 to 200 nm, the maximum of

population concerning sizes centered around 80 nm. These observations indicate that the DLS changes are in agreement with the changes in the electronic absorption and emission at 325 nm and 540 nm, respectively, which occurred when the methanol content was ≥ 50%.

DLS experiments have shown that, as the methanol content in chloroform/methanol solutions increased, molecular aggregates were formed. In order to identify the morphologies of the aggregate species, that is, observe precisely the shape of the discrete nanoparticles and determine their sizes, STEM images of **C1** were recorded using three different MeOH/$CHCl_3$ solvent mixtures (99:1, 80:20, 50:50 v/v). The results are shown in **Figure 87**. Spherical nanoparticles were observed, either in isolated or in aggregated forms, depending on the MeOH/$CHCl_3$ ratio. In the case of **C1**, at a ratio of 99:1 nanoparticles with diameters ranging from 25 to 70 nm were counted, including tiny aggregates of a few nanoparticles (**Figure 87**, left); at a ratio of 80:20, long necklaces of over 500 nm length made of aggregates of nanoparticles with diameters of 25 nm were found (**Figure 87**, right). Upon decreasing the MeOH/$CHCl_3$ ratio to 50:50, larger nanoparticles appeared in the microscope field either in isolated, dimer, or polynuclear forms. Spherical nanoparticles were also observed in the case of **C7** at 50% MeOH and 99% MeOH. The diameters of spherical nanoparticles ranged from 45 to 70 nm. Only few spherical nanoparticles of **C9** in 99% MeOH showed up.

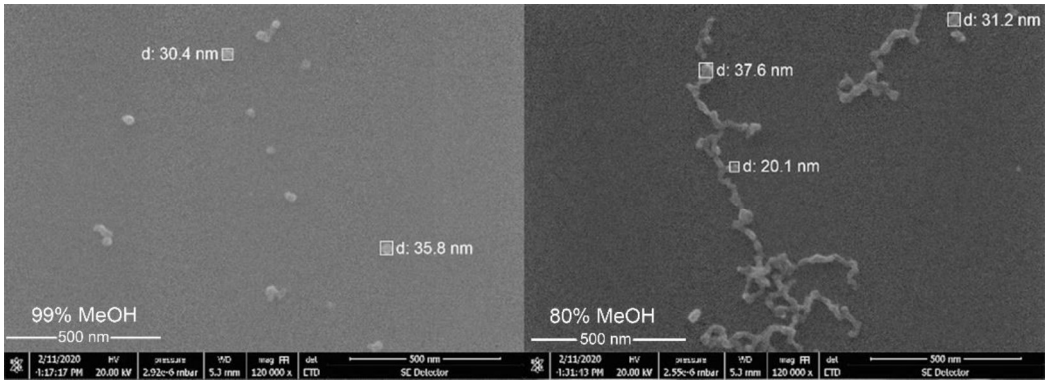


Figure 87. STEM images of **C1** in 99% MeOH (left) and 80% MeOH (right).

For **C4** (**Figure 88**), the formation of nanosphere particles was also found to have a clear relationship with the proportion of MeOH in $CHCl_3$. Isolated spheres with a

diameter from 25 nm to 70 nm were observed at a ratio of 99:1. When the ratio of methanol was 80%, isolated spheres or aggregates of spheres were harder to find compared to 99% MeOH. At a ratio of 50:50, only one square with one sphere with a diameter 56 nm was found. When the proportion of MeOH was 20%, no more spheres could be discovered. Instead, undefined structures were observed.

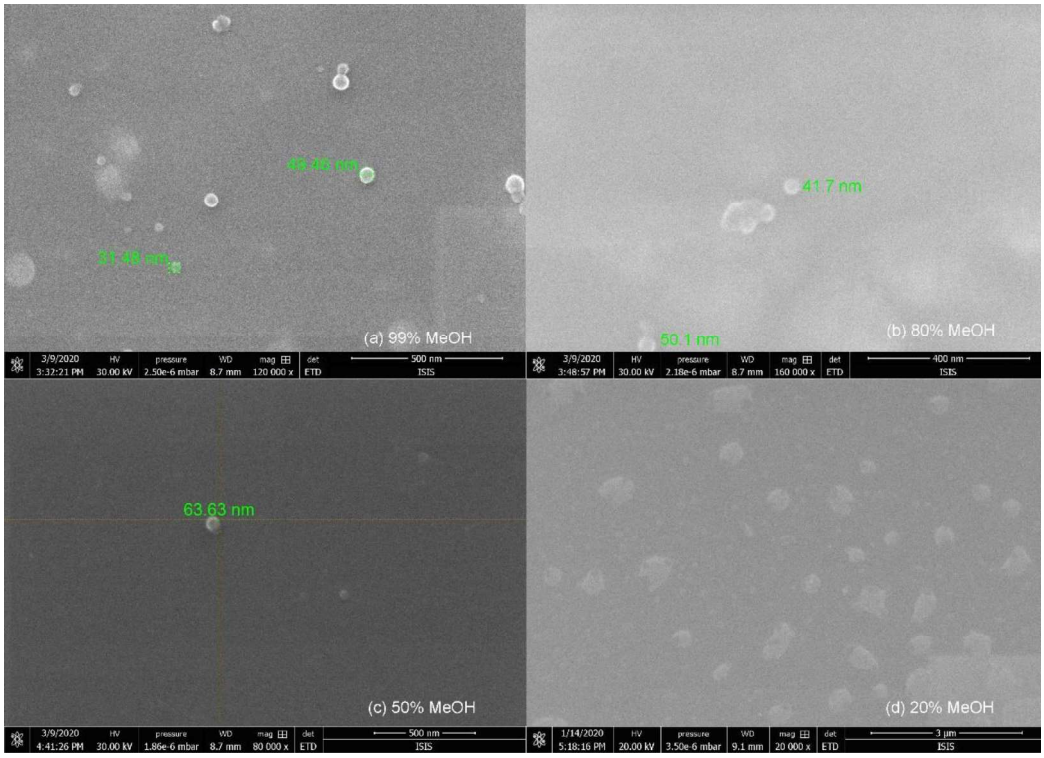


Figure 88. STEM images of **C4** in 99% MeOH (a), 80% MeOH (b), 50% MeOH (c), 20% MeOH (d).

6.3 Discussion

Electronic spectroscopy studies of the complexes **C1 – C9** in $CHCl_3$/MeOH mixtures and complementary DLS experiments for **C1**, STEM experiments for **C1**, **C4**, and **C7**, indicated that the formation of new, low energy, emission bands at the expense of higher energy emission bands was due to the formation of aggregates. The characteristics (λ_{max} and dependence of the intensity on the MeOH/$CHCl_3$ ratio) of this emission in the visible is related to the nature and the properties of the Au(I) ligands (CTB and phosphine). According to the electronic spectroscopy studies, it seems that the less electron-rich phosphines promoted more easily the formation of aggregates than the

more electron-rich phosphines in the following order: PPh_3 > PPh_2Me > $PPhMe_2$ > PEt_3 > PCy_3. In addition, the steric hindrance played a significant role as well, PEt_3 and PCy_3 are both electron-rich phosphine ligands, but no lower energy emission bands were observed upon increase MeOH content for **C9** excepted at 99% MeOH, because the Cy subunit was too large, and prevented the aggregation of **C9** at < 99% MeOH. For example, in the case of complex **C1**, the variations of the absorbance and emission intensities at fixed wavelengths indicated that the aggregates were already formed at MeOH ratios as low as 50%, v/v. In addition, the progression of the aggregation was not linear: It increased more rapidly for MeOH ratios > 60%, v/v. As aggregate formation did not occur in $CHCl_3$/MeCN, even at high MeCN content, it is likely that it resulted from solvophobic interactions rather than changes in the polarity of the medium. As a consequence of the proximity of the chromophores, strong hypochromic shifts of both the absorption and differential absorption (in the case of the optically-active complexes), are observed.[151] The most interesting electronic consequence of the aggregation is the development of a yellow-green emission ($\lambda_{max} \approx 540 - 550$ nm). Aggregation-induced emission of gold(I) acetylides was observed in several cases, in particular in water[129], water/solvent mixtures[152,153], and in mixed organic solvent systems[129], in the form of a low energy band in the visible part of the spectrum at wavelengths ranging from 550 to 650 nm. In the solid state, strong bathochromic shifts (e.g. from 420 to 550 nm) of the solution room temperature triplet emission of dinuclear complexes with short Au···Au distances around 3.136 - 3.153 Å, as determined by X-ray diffraction analysis, have been noted.[5] In other cases, the red shift was clearly the consequence of π-π stacking interactions.[99] Such low energy emission was also observed in multinuclear gold(I) acetylide complexes in which the gold atoms could be brought closer together by an external stimulus, such as the complexation of cations.[129,152,126] The red-shifted emission was assigned as arising from a d_σ*–p_σ excited state.[99]

The green emission observed in the case of solutions of complexes **C1** – **C7** in $CHCl_3$/MeOH mixtures of varying compositions is tentatively assigned to aggregation-

induced Au···Au interactions. The case of complex **C9** is particular, as it shows a weak emission between 500 and 600 nm for < 99% MeOH ratios, and a sudden change of the shape of the emission band above 450 nm for MeOH/$CHCl_3$ 99:1, which shows the same features as the emission band collected in the solid state.

A unique property of compounds **C1 – C9** among existing gold(I) acetylide complexes is their chirality, if we exclude the case of trinuclear derivatives of $[Fe(bipy)_3]^{2+}$.[132] As shown by the electronic spectroscopy studies, the aggregates of **C1** were formed either from the racemate (±)-**C1** or the separate optically-active forms (+)-**C1** and (–)-**C1**. Whereas the aggregates made from the latter forms are homochiral, the aggregates made from (±)-**C1** can be either heterochiral or homochiral. If the aggregates are homochiral, they can be considered as precursors of conglomerates, which are enantiomerically pure single crystals. The variations of the emission intensities of the band at ~ 539 nm of (+)-**C1** and (–)-**C1** in $CHCl_3$/MeOH mixtures are comparable with each other, with an onset at 60% MeOH (**Figure 80**, **Page 97**), whereas in the case of the racemate, this emission is clearly detectable at lower methanol contents (*i.e.* between 40 and 50%). This means that the composition of the aggregates made from (±)-**C1** differs qualitatively from the compositions of the aggregates made from the optically pure complexes: Whereas the latter are necessarily homochiral, the former are probably heterochiral. Therefore, they are related to racemates, which are single crystals made from both enantiomers of the same molecule.

The trends dentified in the evolution of the low energy intensity emission with the MeOH content upon comparison of solutions of optically pure **C1** and racemic **C1**, were also observed in the case of **C3** and **C5**: The onset of the emission at 545 nm always required ca. 10% more MeOH in the case of the optically pure CTBs by comparison with the corresponding racemates. However, unlike **C1**, for which the maximum of intensity was always observed at 99% MeOH, whether it was in optically pure or in racemic form, in the case of **C3** and **C5**, the maximum of emission intensity was observed at 99% MeOH for the optically pure compounds, and at 90% MeOH for the corresponding racemates. Taken together, these experiments indicated that the

structures of the aggregates obtained from the optically active gold CTBs differed from those of the aggregates obtained from the racemic mixtures of the complexes, and depended also on the nature of the CTBs. As the emission characteristics of the aggregates obtained from the racemic Au(I) CTBs differed from those of the aggregates formed from the optically pure CTBs, it is likely that the former are true racemates (each aggregate is made from an equal number of (+) and (−) CTB), rather than conglomerate (each aggregate is made from only one enantiomer).

7. Conclusion

A series of chiral trinuclear phosphine gold(I) alkynyl complexes derived from cyclotribenzylene have been synthesized and characterized. The complexes were found mainly in monomeric forms, as suggested by ^{1}H NMR spectroscopy, diffusion-ordered spectroscopy ruling out the formation of molecular cages by aurophilic interactions. Electrospray ionisation mass spectrometry and the scrambling experiment studies showed that doubly-charged homo-dimers could be formed in the gas phase, hetero-dimers as well. In addition, scrambling experiments indicated that there was an exchange between two different phosphine ligands which could form asymmetric gold CTB complexes. The ^{1}H NMR titration experiments of **C1** and **C4** with NEt_4I provided their binding abilities were close to cryptophanes, and that these organometallic CTBs could be used as hosts to recognize ammonium cations. The enantiomers of the ligand precursor as well as their gold complexes **C1** and **C5** have been separated by chiral HPLC. The complexes of the series **CTB(H,C_2AuPR')** had a long-lived phosphorescence, as well as those of the series **CTB(OMe,C_2AuPR')**, especially **C4** and **C5**. but compared to **CTB(H,C_2AuPR')**, these three complexes also displayed a delayed fluorescence in chlorinated solvents. The spectra recorded with deoxygenated solutions showed vibronic-structured emission bands, whereas a weak fluorescence in non-degassed solutions was observed upon excitation at higher energy. The luminescence properties of these complexes in the solid state were investigated as well. By comparison with the emission in solution, dramatic red shifts to ca 550 nm were observed, especially for **C3** and **C6**. These emission bands were assigned to Au···Au interactions. The spectroscopic properties of **C1** and **C4** were studied also in solvent mixtures ($CHCl_3$/MeCN and $CHCl_3$/MeOH). In the former case, they did not change significantly as the MeCN content was increased. In the latter case, the gradual addition of methanol produced different effects. A green emission band centered around 540 nm developed with the increase of the MeOH content. We found that this luminescence switch was due to the formation of aggregates, which we investigated by dynamic light scattering and scanning tunneling electron microscopy. We proposed that aggregate

formation originated from the solvophobic response of the complexes in the presence of methanol, and that the aggregation-induced emission (AIE) observed was likely to arise from electronic excited states involving contributions from Au···Au bonds, due to the constrained proximity of the complexes in the aggregates. In addition, the aggregates showed marked time-dependent properties, such as ripening, as detected by the differences between the emission intensities of freshly prepared solutions and aged solutions. All the investigated properties depended on the nature of the phosphine ligands and the alkynyl CTBs as well. Investigations on the optically-active versions of the gold CTB complexes indicated that the spectroscopic responses of these molecules showed an additional dependence on their enantiomeric purity, suggesting that the structures of the aggregates built from racemic mixtures (ee = 0%) differed from the structure of those formed from optically pure (ee = 100%) complexes.

Part II: Towards Organometallic/Coordination Hybrid Cryptophanes

1. Introduction and Objectives of Part II

In the past few decades, the research on metallo-supramolecular assembly involved the use of metal-ligand bonds for the construction of metallacycles, metallacages, metal coordination polymers, metal−organic frameworks (MOFs), and so on. The interest in these compounds arose from their potential applications in materials for optical sensing, as biological probes, as luminescent materials for light-emitting diodes, nonlinear optical materials, and liquid crystalline materials.[151,154–157] Generally speaking, transition metal centers are necessary in the construction of supramolecular coordination complexes, not only because of their regular and predictable geometry, but also because of their rich photophysical and photochemical properties. The latter are characterized by various excited states, which are associated with the metals and their ligands. The research on the luminescence of transition metal complexes has attracted a lot of attention, especially the luminescence arising from their triplet excited states, called phosphorescence. It is due to the large spin-orbit coupling induced by the heavy metal centers. Among the various transition metal complex systems, the square-planar d^8 platinum(II) complexes are considered to be important candidates for extensive exploration due to their rich photophysical properties. More specifically, platinum(II) alkynyl complexes have attracted a lot of attention in supramolecular chemistry because of their unique light emission properties and their ability to form Pt(II)···Pt(II) bonds. The electronic energy transitions involved are intraligand (IL) π→π* transitions within the alkynyl ligands (Ar–C≡C), [dπ(Pt)→π*(C≡CAr)] metal-to-ligand charge transfer (MLCT) transitions, π→π* intraligand charge transfer transitions (ILCT), and MMLCT (metal-metal-bond-to-ligand charge transfer) [d_σ*→p_σ/π*] transitions in the case of dinuclear complexes.[158–163]

A series of alkynylplatinum(II) terpyridine complexes like **R42** have been synthesized and employed by Yam and her group (**Figure 89**). For example, the dipicolylamine alkynylplatinum(II) complex **R42** was found to be weakly emissive. This low emission was mainly due to the quenching of the emission of the ^{3}MLCT

excited state by intramolecular electron transfer from the electron-rich amino substituents of the DPA part. The metal cation-binding capability of the complex was examined using both electronic absorption and emission spectroscopy. The results showed special recognition for Zn^{2+}. Titration by absorption spectroscopy indicated that the binding stoichiometry was 1:1 and the binding constant (log *K*) was determined to be 6.2 (±0.08). In addition, emission spectroscopy showed that the emission band at 600 nm increased by a factor of ten with the addition of 1 equiv of Zn^{2+}.[164]

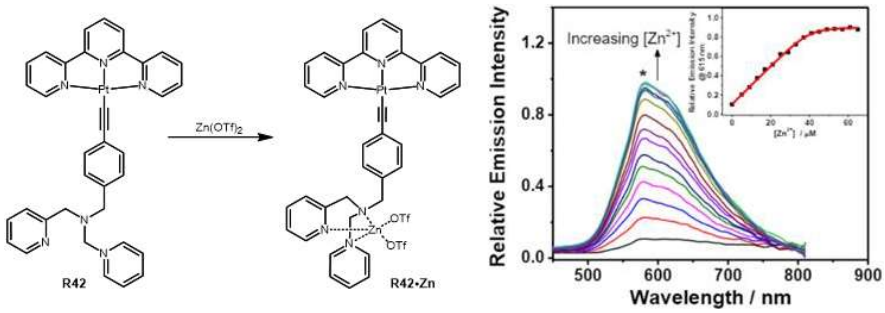


Figure 89. Host–guest association of the dipicolylamine-substituted alkynylplatinum(II) terpyridine complex with Zn^{2+}, and the corresponding luminescence change (Reproduced from Ref [164]).

Phosphorescent alkynylplatinum(II) terpyridine tweezers synthesized in Yam's group were used to study host–guest interactions with cationic, neutral and anionic platinum(II), palladium(II), gold(I), and gold(III) complexes. Due to extensive Pt(II)···Pt(II) interactions, the host-guest assembly process resulted in significant color changes and the turn-on of near-infrared (NIR) emission. This work has shown that the organometallic-tweezers can selectively recognize the π surface of π-conjugated organic and organometallic guests.[165]

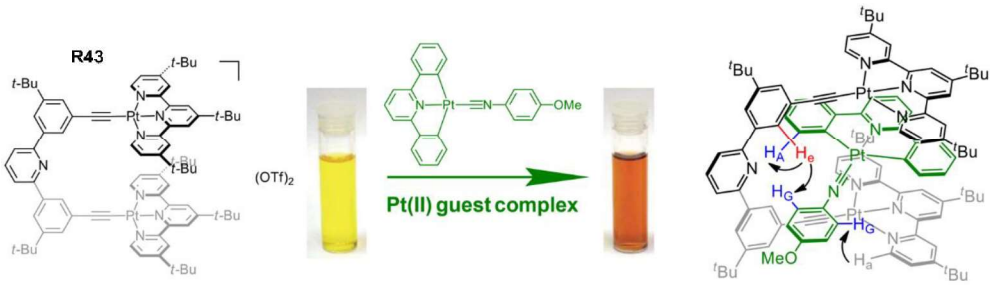


Figure 90. The host–guest association of the alkynylplatinum(II) terpyridine molecular tweezers with the platinum complex [Pt(C^N^C)(C≡N–C_6H_4–OMe-*p*)] produces a drastic color change (Reproduced from Ref [165]).

Wang and his coworkers developed a triarylboron-functionalized platinum(II) alkynyl complex, which was used to detect volatile organic compounds (VOC) in the solid state or neat films. The response of the molecular sensor was fast, *i.e.* a few seconds. By applying a vacuum or by dissolving and recasting the film, these luminescence changes were reversible and permanent in the presence of the detected VOC. Putting it in the air for a long time or heating it gently to remove solvent vapor could also restore the original color of the sample. Polar solvents, such as CH_2Cl_2, $CHCl_3$, CH_3CN, acetone, THF, and EtOH, induced an emission color shift from yellow to green; by contrast, the application of benzene, cyclohexane, or 1,4-dioxane switched the emission color to red, and the exposure to linear hydrocarbons or methanol completely quenched the emission of the sensor.[166]

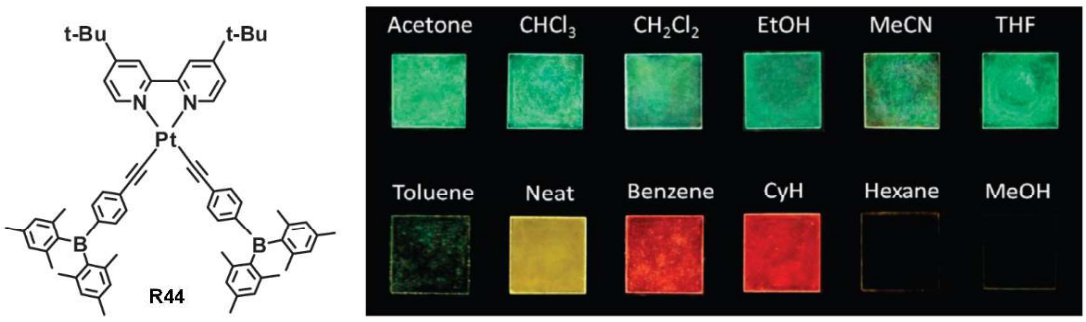


Figure 91. Luminescence response of films of platinum(II) alkynyl **R44** under UV irradiation to various organic vapors (Reproduced from Ref [166]).

Álvarez's group developed a platinum(II) alkynyl tweezer based on coronene subunits bound in *cis* arrangement to platinum in a square planar complex **R45** containing a 1,2-bis(diphenylphosphinoethane) ancillary ligand (dppe). It was expected that the angle between the two coronene fragments, close to 90°, would provide an appropriate distance to complex fullerenes. The studies showed that the receptor had a marked difference in recognizing C_{60} and C_{70}. The binding constants were determined by ^{1}H NMR titrations as 4600 ± 100 M^{-1} for C_{60}, and 20700 ± 600 M^{-1} for C_{70}. The flexibility of the molecular tweezers arms and the complementarity between the host

concave and the guests convex surfaces were demonstrated to be key factors for supramolecular complex formation.[167]

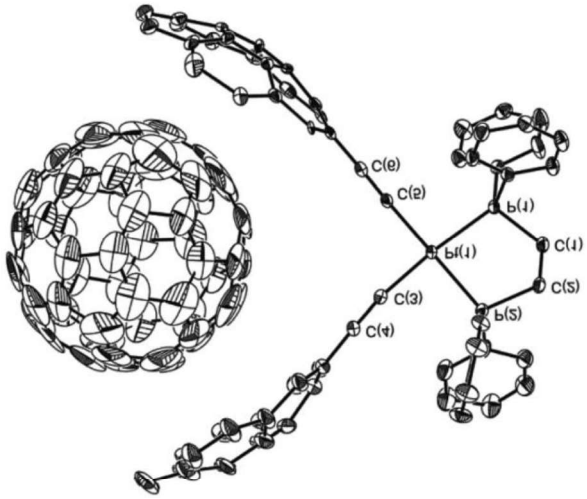


Figure 92. X-ray crystal structure of the supramolecular complex between C_{60} and the platinum(II) alkynyl tweezer **R45** based on coronene recognition motif (Reproduced from Ref [167]).

A family of metallacyclophanes based on the Pt-acetylide linkage and incorporating binaphthyl chiral subunits were synthesized and characterized by Lin's group. Due to the naphthyl π→π* transition, the ECD spectra of the metallacyclophanes showed a strong bisignate band at ~265-268 nm. In addition, an intense band at 330-333 nm was attributed to the acetylene π→π* transition. Then these metallacyclophanes and $Ti(O^iPr)_4$ were combined to form Ti-binolate complexes, which were used as catalyst in the enantioselective diethylzinc additions to aromatic aldehydes. The results showed that it was not possible for metallacyclophane **R46** to form a Ti-binolate complex because of its steric congestion. On the contrary, the more flexible unclosed metallacyclophane **R47** could react with $Ti(O^iPr)_4$ to form a Ti-binolate complex in which Ti(IV) is surrounded by a chiral coordination environment. This complex proved to be an effective catalyst for the enantioselective catalytic diethylzinc addition to aromatic aldehydes.[168,169]

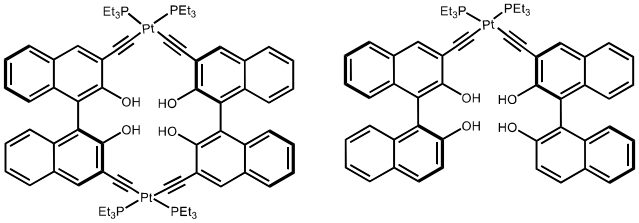


Figure 93. The structures of chiral metallacyclophanes **R46** and **R47**.

Metal−organic macrocycles have been attracted a lot attention in recent years. For example, Sun's group synthesized a metal−organic hexagon **R48** from dianthracene-based dipyridyl and platinum(II) alkynyl complexes based on coordination-driven self-assembly. The trinuclear complex emitted yellow light in the solid state. Remarkably, after the solid was slightly ground the color of the emission changed to yellow-green, and with further grinding, it changed to brownish yellow. Interestingly, the brownish-yellow luminescence could be switched back to its original yellow color after the complex was treated with dichloromethane vapor for 1 min. This reversible conversion could be repeated several times by the grinding/exposure-to-solvent process. These results indicated that Pt (II)-acetylides can be used in the manufacture of smart materials, the functions of which are easily controlled by the stoichiometry and the geometry of the building blocks.[170]

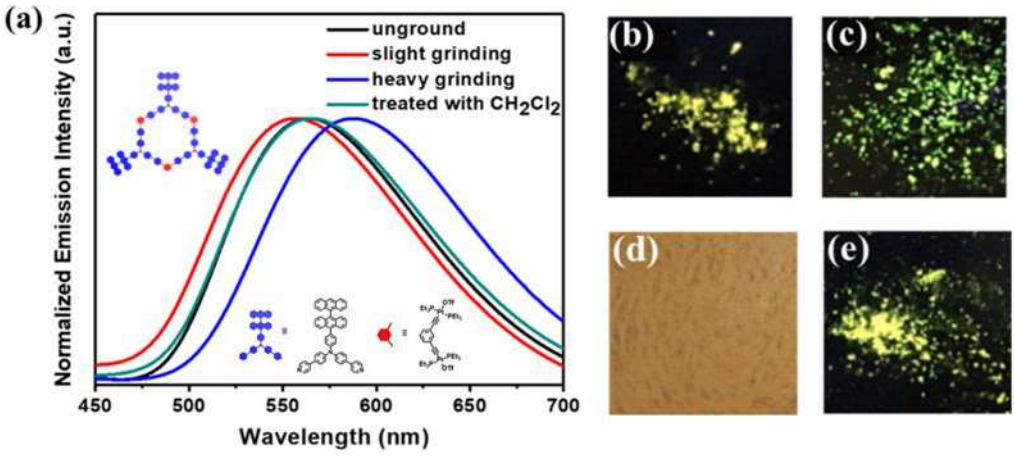


Figure 94. (a) Photoluminescence spectra of hexagon complex **R48** in different states; photographs of hexagon powder under irradiation by UV light at 365 nm: (b) unground hexagon; (c) slightly ground solid hexagon; (d) heavily ground solid hexagon; (e) hexagon after treatment with dichloromethane solvent vapor (Reproduced from Ref [170]).

A series of homonuclear and heteronuclear metallacycles were synthesized by Stang's group. These molecular squares, based on Pt-acetylide complex moieties, contain pyridyl or nitrile ligand subunits, which were used to coordinate with Pt(II)/Pd(II) by self-assembly (**Figure 95**). These molecular squares/rectangles were used to study the binding characteristics of the alkynyl groups to metals cations such as Ag^+, Cu^+, and Au^+ via π-interaction of the bound alkynyl group to the open coordination sites of the metal guest. Once the molecular squares were functionalized with silver successfully, they were used for the complexation of neutral monodentate and bidentate ligands, such as pyrazine.[171,172]

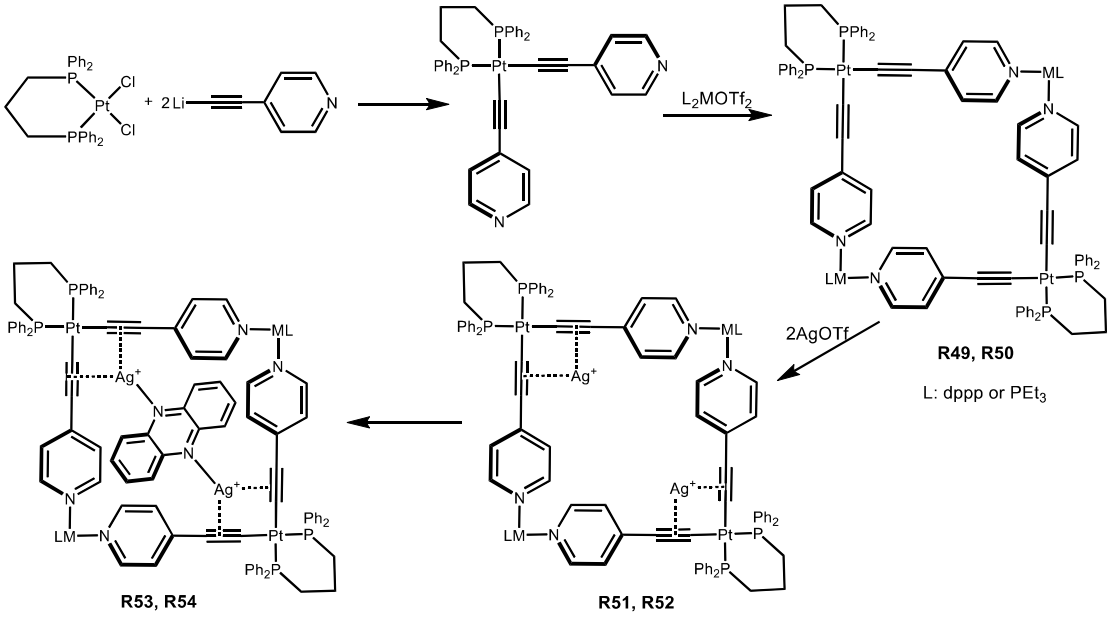


Figure 95. The recognition mechanism of neutral guests via Lewis acid/base molecular square receptors.

Although several examples of metallo-cryptophanes were reported, their application in the detection of neutral guests was rarely investigated. Until now, there was only one report on the optical properties of metallo-cryptophanes[93], but the application in the detection through changes in photophysical and chemical properties was not studied. As discussed above, Pt-acetylide complexes have rich luminescence properties and could also be used as building blocks to construct metal-based macrocyclic and macropolycyclic, cage-like molecules. Our aim, in this part, was to

synthesize a series of luminescent metallo-cryptophanes incorporating both metal-carbon bonds and coordination bonds. The metallo-organic cryptophanes will be constructed from asymmetric CTBs containing two identical monodentate metal binding sites forming weak coordination bonds (carbonitrile function (RCN)) and a monodentate binding site capable of establishing strong organometallic bonds (terminal alkyne function (RCCH)). First the CTBs will be *cis*-coordinated through the alkynyl groups to a square-planar platinum(II) center bearing phosphine auxiliary ligands (e.g. either two monodentate triethylphosphine PEt_3 or a bidentate 1,3-bis(diphenylphosphino)propane (dppp) chelate). The mononuclear platinum complexes thus obtained will be called "precryptophanes", because they should readily afford the target organometallic cryptophanes by simple coordination of $[ML']^{2+}$ = $[Pd(dppp)]^{2+}$ or $[Pt(dppp)]^{2+}$ metal complex fragments to two carbonitrile groups from each CTB (**Figure 96**).

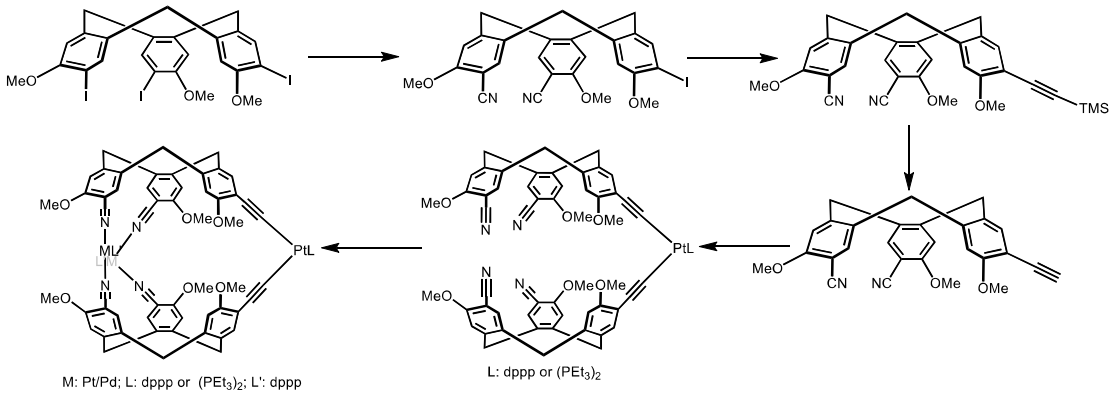


Figure 96. The synthesis route of targeted organometallic cryptophanes.

Once the organometallic cryptophanes are synthesized, they will be used as complexes-as-ligands for the intracavity coordination of soft metal cations like M' = Ag^+, Cu^+ and Au^+, which will bind the platinum alkynyl fragment *via* the "π-tweezer effect". Finally, the tetranuclear organometallic cryptophanes will be used as receptors for the molecular recognition of Lewis bases (S), including anions, a kind of guests that have been widely ignored so far by the classical cryptophanes. The targeted guests include inorganic anions (e.g., cyanide, nitrate, thiolate) and chiral natural nitrogen

bases (e.g., alkaloids including nicotine and those of the amphetamine family). All of these substrates have an environmental or toxicological interest. Such a recognition mechanism is shown in **Figure 97**. It is assumed that the sequential binding of M' followed by S will change the emission properties of the organometallic cryptophane.

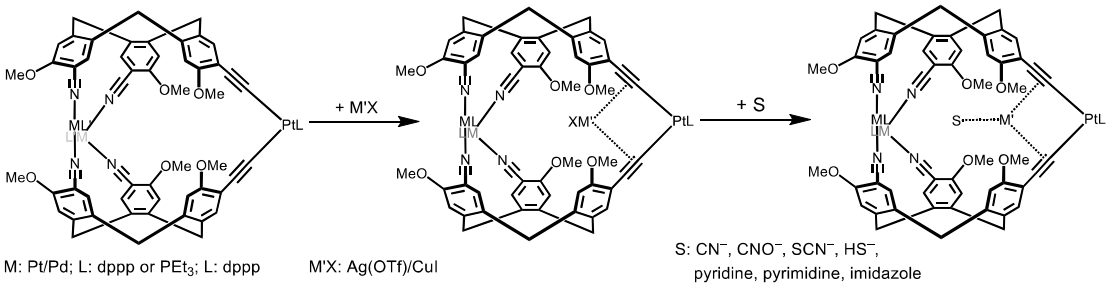
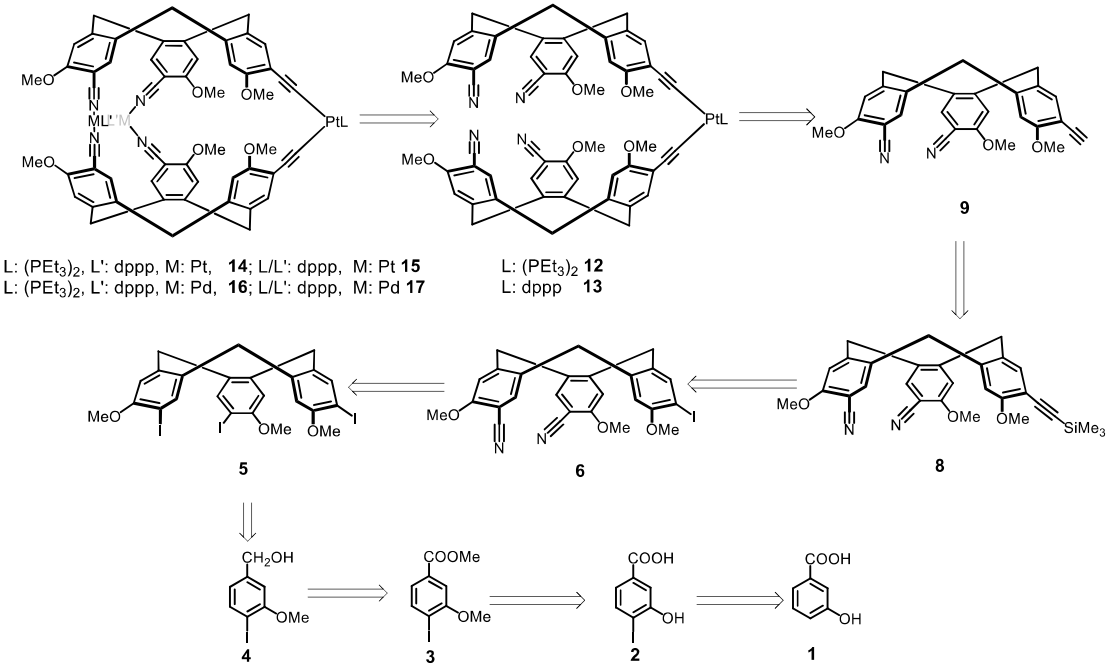


Figure 97. The recognition mechanism based on light-emissive organometallic cryptophanes.

2. Synthesis, Characterization and Resolution of an Asymmetric CTB Alkynyl Ligand Precursor

The targeted organometallic/coordination hybrid cryptophanes presented in part II of this manuscript incorporate two types of bridges, those made from platinum(II)-carbon bonds with alkynyl ligand subunits and those made from palladium(II) or platinum(II) coordination bonds with carbonitrile ligand subunits. The metallo-cryptophanes **14-17** should be obtained from the so-called precryptophane intermediates by a simple coordination of $[PdL]^{2+}$ or $[PtL]^{2+}$ metal complex fragments to the carbonitrile binding subunits.



Scheme 1. Retrosynthesis of the targeted metallo-cryptophanes **14-17**.

The precryptophanes are bis-alkynyl complexes of platinum(II) in which the alkynyl ligands derive from the asymmetric CTB **9**. The square planar coordination sphere of the Pt^{2+} cation is completed by the bidentate dppp or two PEt_3 ancillary ligands. So the crucial step was to make the asymmetric CTB **9**, which could be prepared from the known symmetric CTB **5** by the sequence of steps shown in **Figure**

98.

The CTB **5** was synthesized in 4 steps, based on a known procedure starting from the commercially available 3-hydroxybenzoic acid **1**.[31] Benzoic acid was first reacted with KI under basic conditions (NaOH). Protonation with HCl gave 3-hydroxy-4-iodobenzoic acid **2** in 46% yield. Compound **2** was next reacted with MeI in acetone under basic conditions (K_2CO_3) to produce methyl 3-methoxy-4-iodobenzoate **3** in 97% yield. This methyl ester intermediate was efficiently reduced using DIBAL-H to benzyl alcohol **4**. The next step was the trimerization of compound **4** in the presence of P_2O_5 in refluxing diethyl ether. The intermediate CTB **5** was obtained in 46% yield after purification by precipitation.

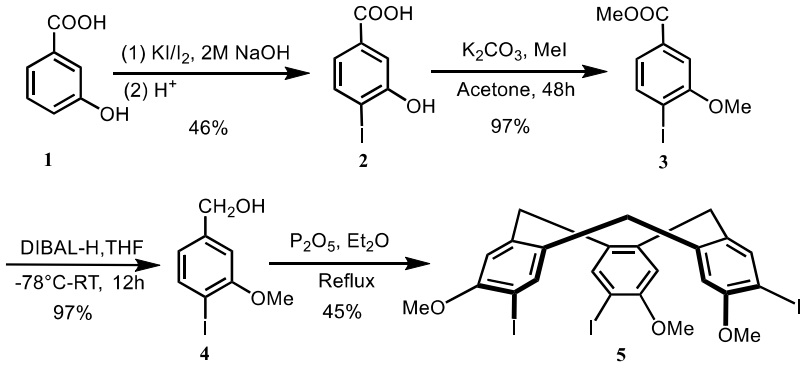


Figure 98. The synthesis route of precursor CTB **5**.

The most important step was the substitution of two of the iodine atoms out of three by the nitrile group. Accordingly, **5** was treated with 0.5 equiv. of zinc cyanide in the presence of a catalytic amount of [$Pd(PPh_3)_4$] in DMF at 120 °C for about 2 hours.[173] The solvent was removed and the residue was purified by column chromatography. Two main products were isolated: the target asymmetric CTB **6**, in 34% yield, and CTB **7**, which resulted from a single substitution, in 21% yield. Then, the TMS-protected alkynyl substituents were introduced by reacting separately compounds **6** and **7** with trimethylsilylacetylene through the cross coupling Sonogashira reaction.[114] The intermediate products **8** and **10** were obtained in 70% and 60% yields, respectively. Then they were reacted with TBAF in THF, which afforded the desired CTB ligand

precursor in 70% yield and the doubly alkyne-substituted CTB **11** in 55% yield after purification by column chromatography.

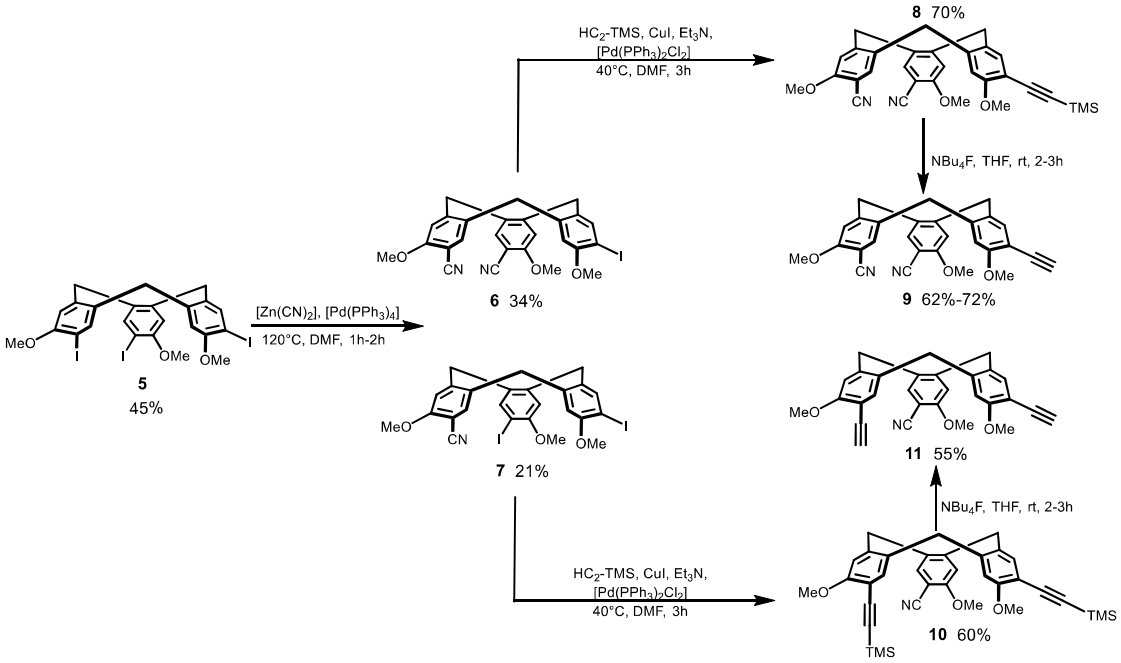


Figure 99. The synthesis of asymmetric CTB **9** and CTB **11**.

The ligand precursor CTB **9** is asymmetric (C_1-symmetry) and was obtained as a racemic mixture. Its asymmetry was clearly revealed by its ^{1}H NMR spectrum (**Figure 100**) that displayed six singlets in the aromatic region corresponding to the three α and the three α' protons for each aromatic ring. Due to the influence of the acetylene bond, α3' moved towards the upfield chemical shift region compared to α1' and α 2', which are both close to the nitrile groups. In addition, the three methoxy groups appeared as three singlets, at 3.942, 3.934 and 3.912 ppm for OMe1, OMe2, and OMe3, respectively. The two former showed similar chemical shifts because both are *ortho* to the nitrile groups. The signal of OMe3, which is in the shielding field of the acetylene bond, is upfield shifted by comparison with those of the other methoxy substituents. As expected, the axial and equatorial protons all showed three doublets. Finally, the signal of the alkynyl proton appeared as a singlet at 3.272 ppm. The doubly alkyne-substituted CTB **11** is also asymmetric (**Figure 101**). As a consequence, its ^{1}H NMR spectrum also displayed six singlets in the aromatic region corresponding to the three α and the three

α’ protons for each aromatic ring. The three methoxy groups also appeared as three singlets, and the axial and equatorial protons all showed three doublets each. Finally, the two alkyne protons showed up as two singlets, which were close to each other, but were distinct. The spectrum of CTB **11** (**Figure 101**) showed also three singlets in the region of the OMe substituents, but the most shielded had close chemical shifts because they were from OMe2 and OMe3, which are both ortho to the alkyne substituents. The less shielded singlet was due to OMe1, ortho to the carbonitrile group. Because of the shielding effect of the acetylene bond, α3’ for CTB **9,** α3’ and α 2’ for CTB **11** showed similar chemical shifts.

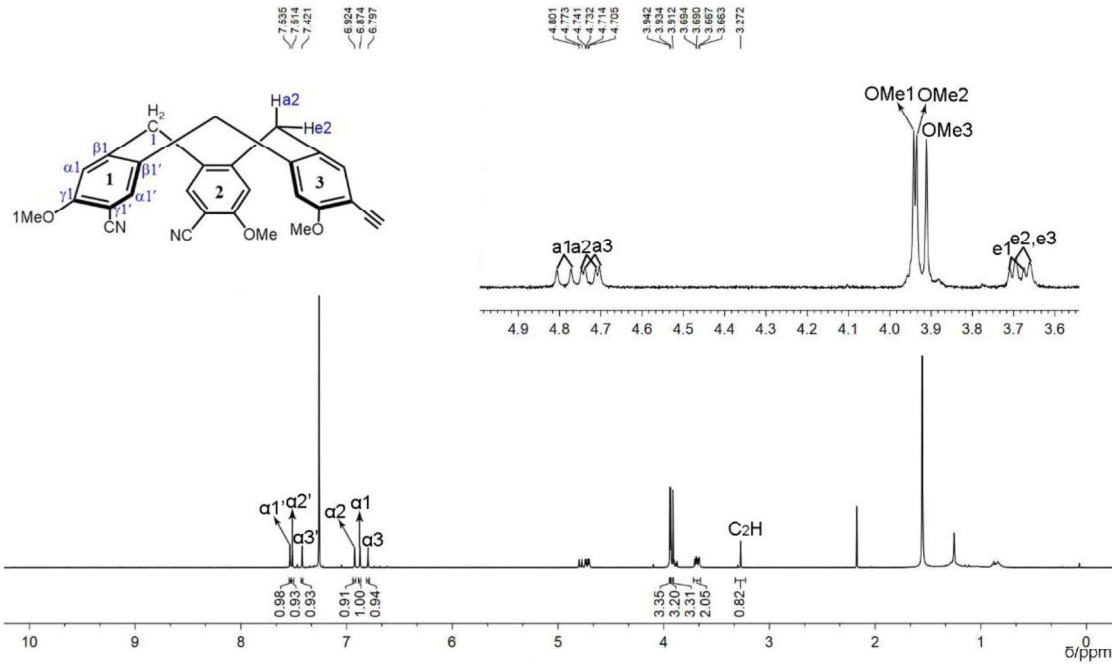


Figure 100. The ^{1}H NMR spectrum of CTB **9** in $CDCl_3$ at 298 K.

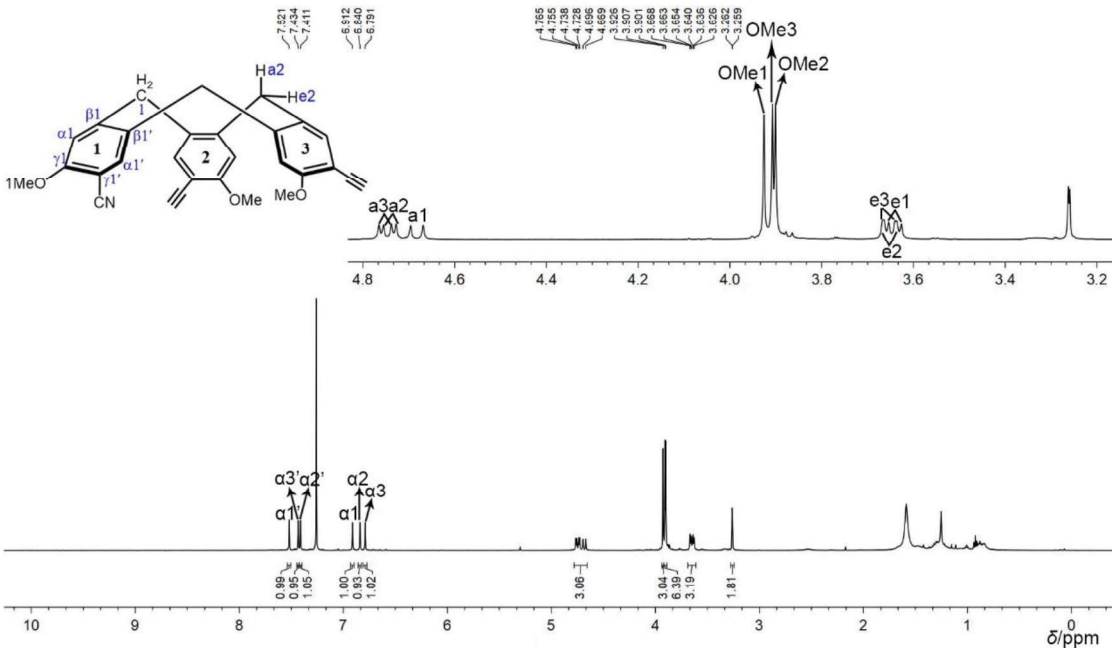


Figure 101. The ^{1}H NMR spectrum of CTB **11** in $CDCl_3$ at 298 K.

As explained in the introduction, the CTB derivatives are chiral when the two substituents R_1 and R_2 on each benzene ring are different, and the racemic mixtures can be often resolved by using chiral HPLC. So the optically pure enantiomers of CTB **9** could also be obtained by column chromatography of the racemate on a chiral phase, that is, (*S,S*)-Whelk-O1, using heptane/ethanol/dichloromethane as eluent. The polarimetry data indicated that the first eluted enantiomer of CTB was (+)-**9**, and that the second eluted enantiomer was (–)-**9**. The chiroptical properties of **9** are collected in **Table 9** (polarimetry) and illustrated in **Figure 102** (ECD spectra). The ECD spectra of (–)-**9** and (+)-**9** in dichloromethane show features that are perfect mirror images of each other. In the B_{1u} region, (+)-**9** and (–)-**9** show each two oppositely signed CD bands between ca. 230 and 280 nm, the sequence of signs being respectively positive-negative and negative-positive from high to low energy. In the B_{2u} region, (+)-**9** and (–)-**9**, display two oppositely signed bands each, with negative-positive and positive-negative sequences from high to low energy (ca. 280–325 nm), respectively. (+)/(–)-**9** both showed bands with maxima at λ = 240, 261, and 314 nm with sign inversion at 252 and 303 nm.

Table 9. Specific rotations of CTB **9** in CH_2Cl_2 at 298 K.

λ (nm)	first eluted enantiomer on (*S*,*S*)-Whelk-O1 $[\alpha]_\lambda^{25}$ (CH_2Cl_2, c = 0.07 g/mL)	second eluted enantiomer on (*S*,*S*)-Whelk-O1 $[\alpha]_\lambda^{25}$ (CH_2Cl_2, c = 0.06 g/mL)
589	+ 6	– 6
578	+ 7	– 7
546	+ 9	– 9
436	+ 36	– 35
405	+ 64	– 63
365	+ 241	– 238

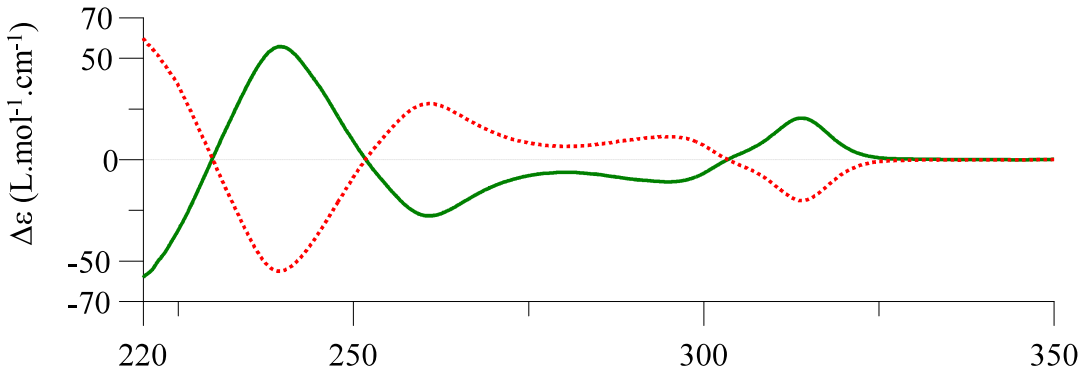


Figure 102. ECD spectra of optically pure CTB **9** in CH_2Cl_2. The green solid line is the spectrum of the first eluted enantiomer, the red dotted line, the one of the second eluted enantiomer.

3. Preparation of the Precryptophanes Based on [(-C_2)$_2$Pt(PEt_3)$_2$] (12) and [(-C_2)$_2$Pt(dppp)] (13) Hinges. First Attempts of Cryptophane Formation

Reaction of CTB **9** with either [Pt(PEt_3)$_2Cl_2$] or [Pt(dppp)Cl_2] in 2:1 ratio in the presence of base allowed us to obtain a Pt-bridged CTB dimer as a 1:1 mixture of diastereomers. We proposed to call this complex "precryptophane", because it should lead directly to the target organometallic cryptophane by reaction with two equivalents of Pd(II) or Pt(II) metal complex by coordination to a carbonitrile ligand subunit of each CTB.

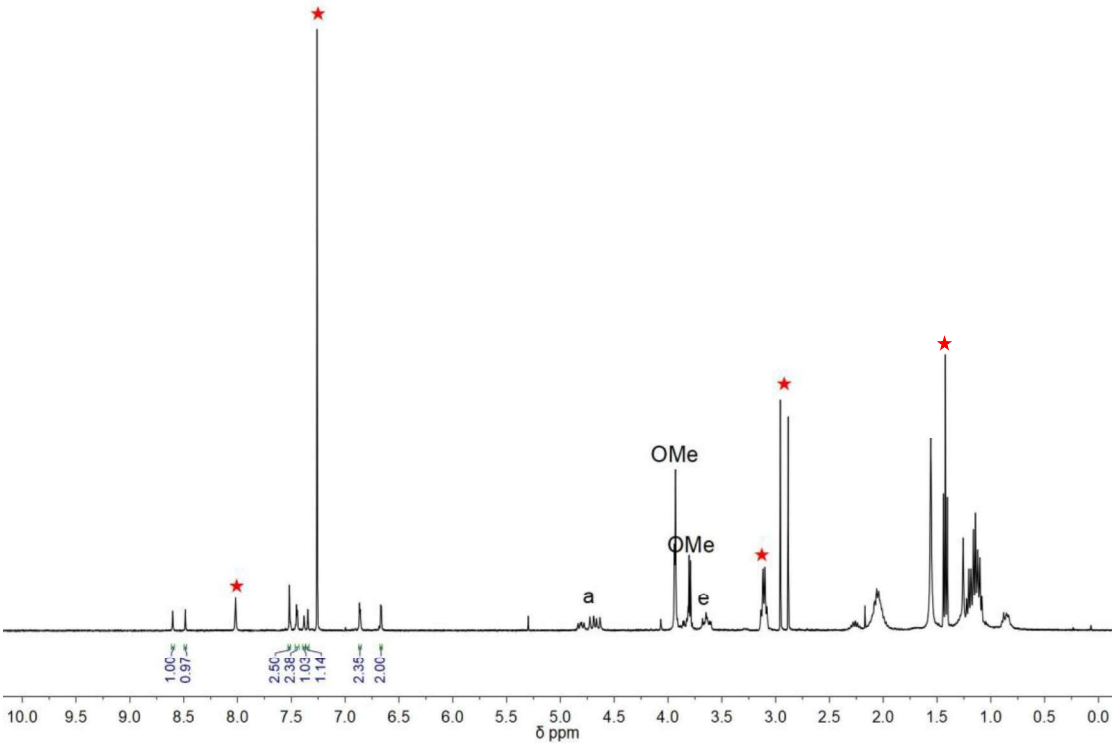


Figure 103. The ^{1}H NMR spectrum of crude product **12** in $CDCl_3$ at 298 K. (Stars stand for residual solvent signals)

First, a racemic mixture of CTB **9** reacted with *cis*-[Pt(PEt_3)$_2Cl_2$] and copper iodide as co-catalyst under basic conditions (Et_3N) in DMF at room temperature for 2 days. The crude product, obtained by evaporation of the solvent, was purified by column

chromatography on silica gel to give pale yellow powder (precryptophane **12)** which was characterized and studied in detail by NMR spectroscopy. Since the synthesis was carried out from a racemic mixture of **9**, the precryptophanes were generated as three stereoisomers, that is, two diastereomers, a *syn-meso* form, and two *anti*-chiral forms as illustrated in **Figure 104**. According to their structures, the *meso* form showed a C_s-symmetry, and the chiral forms had a C_2-symmetry. Since the diastereomers had very similar retention factors, they were not separated successfully. The mixture was enriched in one diastereomer, the major (M) one, and depleted in the other diastereomer, the minor (m) one, the ratio between M and m being 1.6 : 1.

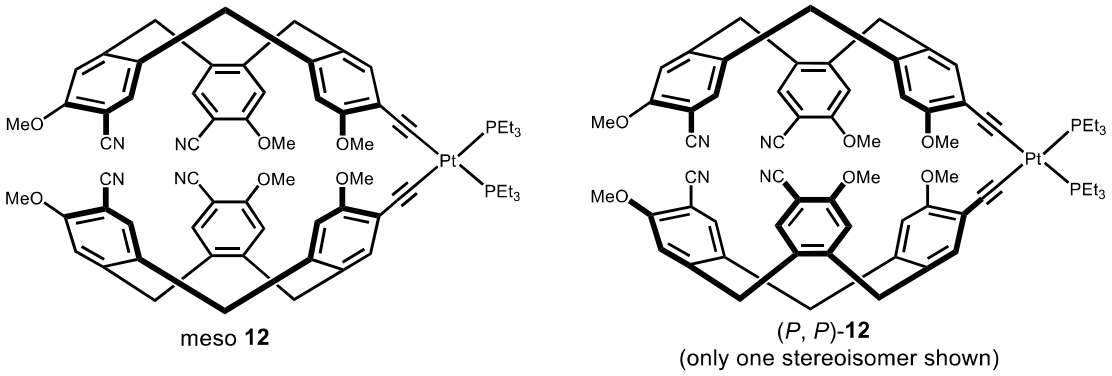


Figure 104. The structures of precryptophanes based on [(-C_2)$_2$Pt(PEt_3)$_2$] hinge.

Examination of the ^{1}H NMR spectrum (**Figure 105**) of the diastereomeric mixture of precryptophane **12** showed first that the singlet corresponding to the terminal alkyne proton was no longer present, which means that the metal and CTB **9** were successfully connected. Second, the NMR spectrum showed twelve singlets in the aromatic region, which corresponded to six aromatic protons for each diastereomer. In addition, the number of the signals of the methoxy protons and of the axial and equatorial protons of the methylene bridges were also multiplied by two. All these features are consistent with the presence of two diastereomers of C_s and C_2 symmetries, respectively. Incorporation of CTB **9** into precryptophanes **12** had noticeable effects on the chemical shifts of several of their protons. The singlets of the α3' (m, M) protons of the benzene ring bearing the alkyne group exhibited a very large downfield chemical shift change

by about 1.0-1.1 ppm, compared with the precursor **9**. Such shifts are probably due to the binding of [*cis*-Pt(PEt_3)$_2$]$^{2+}$. In addition, compared with those of the α3' (m, M) protons, the signals of the α2 (m, M) protons showed smaller downfield shifts, but compared with those of α2', they were downfield shifted by about 0.5 ppm. This might be related to the proximity of α2 protons to the α3' protons.

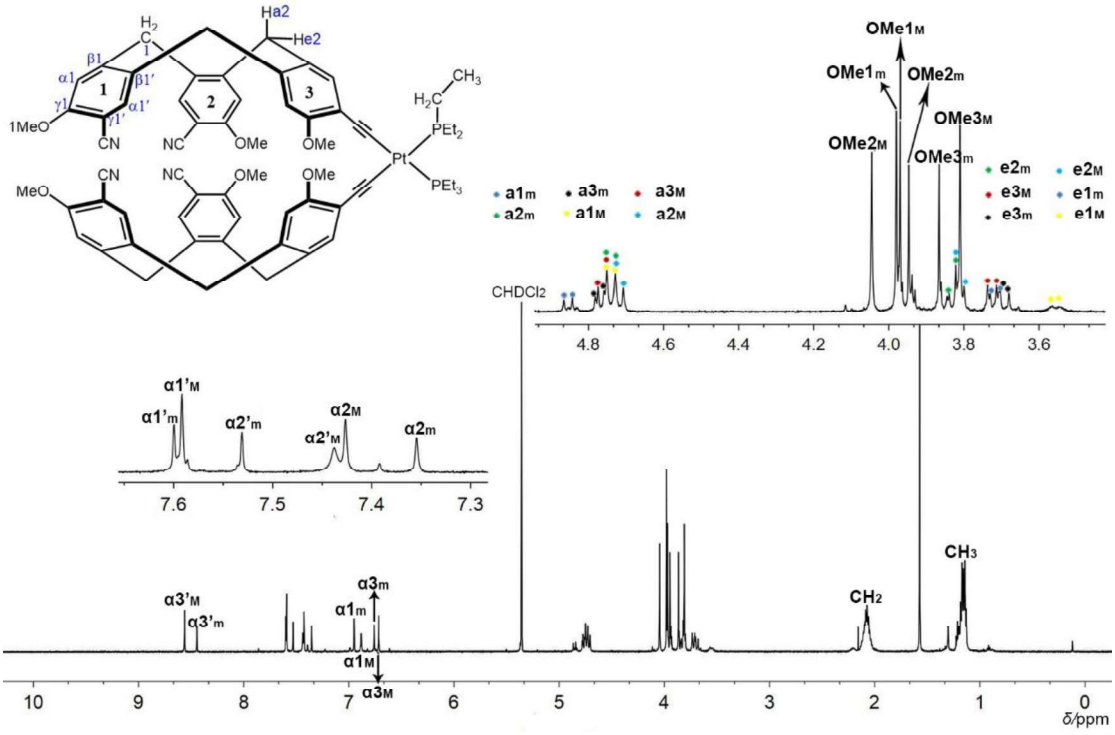


Figure 105. ^{1}H NMR spectrum of compound **12** in CD_2Cl_2 at 298 K

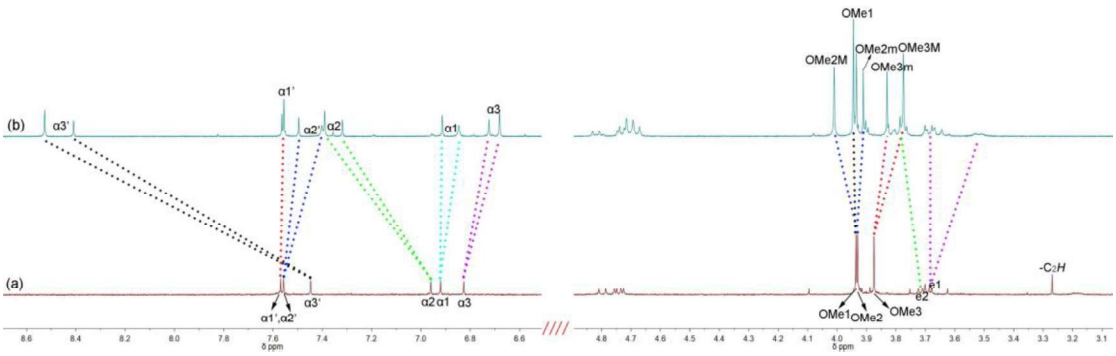


Figure 106. ^{1}H NMR partial spectra of compound **9** (a) and **12** (b) in CD_2Cl_2 at 298 K

The presence of the two diastereomers in the purified mixture was also attested by the ^{31}P NMR spectrum, which displayed two singlets at 4.18 (M) and 4.23 (m) ppm, the ratio between two diastereomers being 1.6:1. The coupling constant $J_{P,Pt}$ = 2495 MHz was consistent with the values that literature reported.[168,169] DOSY experiments (**Figure 107**) indicated that the diffusion coefficient of CTB **9** (9.74×10^{-10} m^2/s) was higher than the diffusion coefficient of **12** (6.10×10^{-10} m^2/s) by 60%, thus confirming that the precryptophanes are CTB dimers.

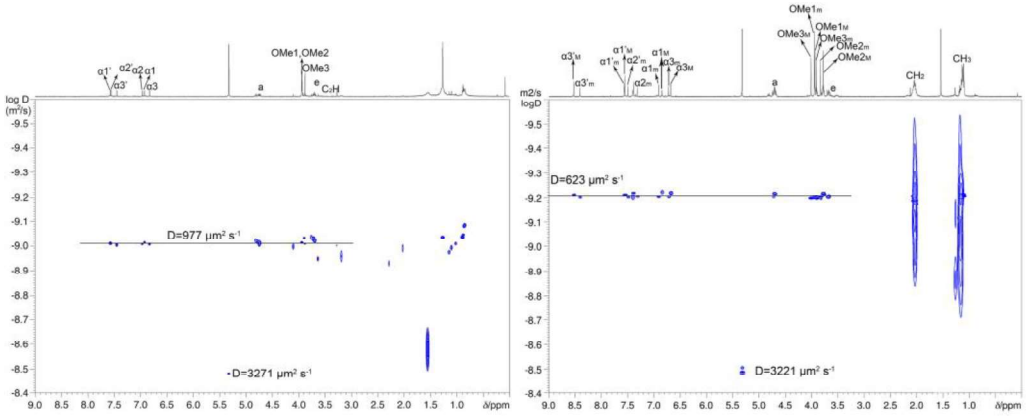


Figure 107. DOSY NMR spectra of **9** (left) and **12** (right) in CD_2Cl_2 at 298 K

The positive-ion ESI mass spectra of the diastereomeric mixture of precryptophanes **12** in acetone showed the expected isotopic distributions for the molecular peak, which appeared as a copper (Cu^+) adduct, at m/z = 1361.38 $[(C_{68}H_{72}N_4O_6P_2Pt)Cu]^+$, and a sodium ($Na^+$) adduct at m/z = 1321.44 $[(C_{68}H_{72}N_4O_6P_2Pt)Na]^+$ in **Figure 108**. We shall come back to the origin of these adducts.

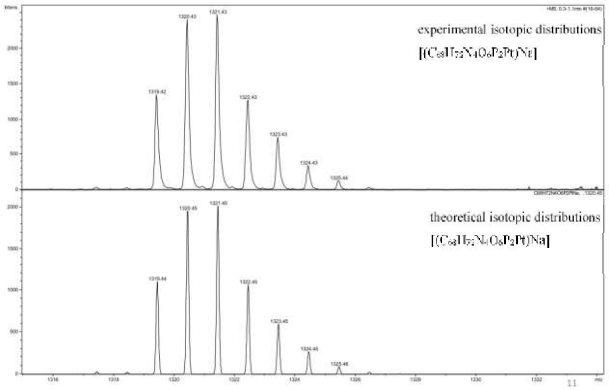


Figure 108. ESI-MS of compound **12**: Detail of the molecular peak.

In a second set of experiments, we used the optically pure CTB (+)-**9** in order to prepare the diastereomerically pure precrytophane **12** in an optically pure, chiral form. Accordingly, compound (+)-**9** was reacted with [Pt(dppp)Cl_2] and copper iodide in the presence of triethylamine in THF. The reaction mixture was stirred at room temperature for 6 hours, the solvent was removed in vacuo to give a solid residue, which was purified by column chromatography to give pale yellow solid powder of enantiopure precryptophane **13** in 80% yield. The complex was examined first by ^{1}H NMR spectroscopy. Compared to the spectrum of the starting CTB **9**, the spectrum of the precryptophane **13** (**Figure 109**) showed that the proton signal corresponding to the terminal alkyne group was no longer present, which indicated that the akynyl fragment of the CTB bas bound to platinum. As for each diastereomer of precryptophane **12**, there were six singlets for the protons in the aromatic region, which corresponded to α1, α2, α3, α1', α2', and α3' of each aromatic ring, respectively. Due to the strong deshielding effect analyzed previously, the signals of protons α3' and α2 shifted downfield by about 0.84 and 0.3 ppm respectively; in addition, the signal of proton α3 shifted upfield by about 0.4 ppm. In the aliphatic region of the spectrum, three different singlets were observed for the methoxy protons, and two groups of three doublets each were noted for the axial and equatorial diastereotopic protons of the methylene bridges. Most importantly, the protons of –OMe2 and –OMe1 showed very similar chemical shifts, because of their similar environment. By contrast, the singlet of –OMe3 was moved upfield, by about 0.6 ppm, which is quite significant, and could be due to the strong shielding effect of one of the phenyl substituents of the dppp ancillary ligand of the platinum bridge. The proximity of the –OMe3 group and such a phenyl ring was attested by the presence of correlation spots between the singlet of –OMe3 and the signals of the aromatic protons of this dppp substituent in the ^{1}H/^{1}H ROESY map (**Figure 109**). This observation was another proof that the CTB **9** had connected to the [Pt(dppp)]$^{2+}$ metal complex fragment successfully. The ^{31}P NMR spectrum displayed only one singlet, at –9.36 ppm, confirming the diastereomeric purity of the complex. The positive-ion ESI mass spectra of the precryptophane **13** dissolved in THF showed

the expected isotopic distributions for the molecular peak, which appeared as the sodium (Na^+) adduct at m/z = 1497.42 [$(C_{83}H_{68}N_4O_6P_2Pt)Na^+$] and, as in the case of precryptophane **12**, as the copper (Cu^+) adduct at m/z = 1537.38 [$(C_{83}H_{68}N_4O_6P_2Pt)Cu^+$] also.

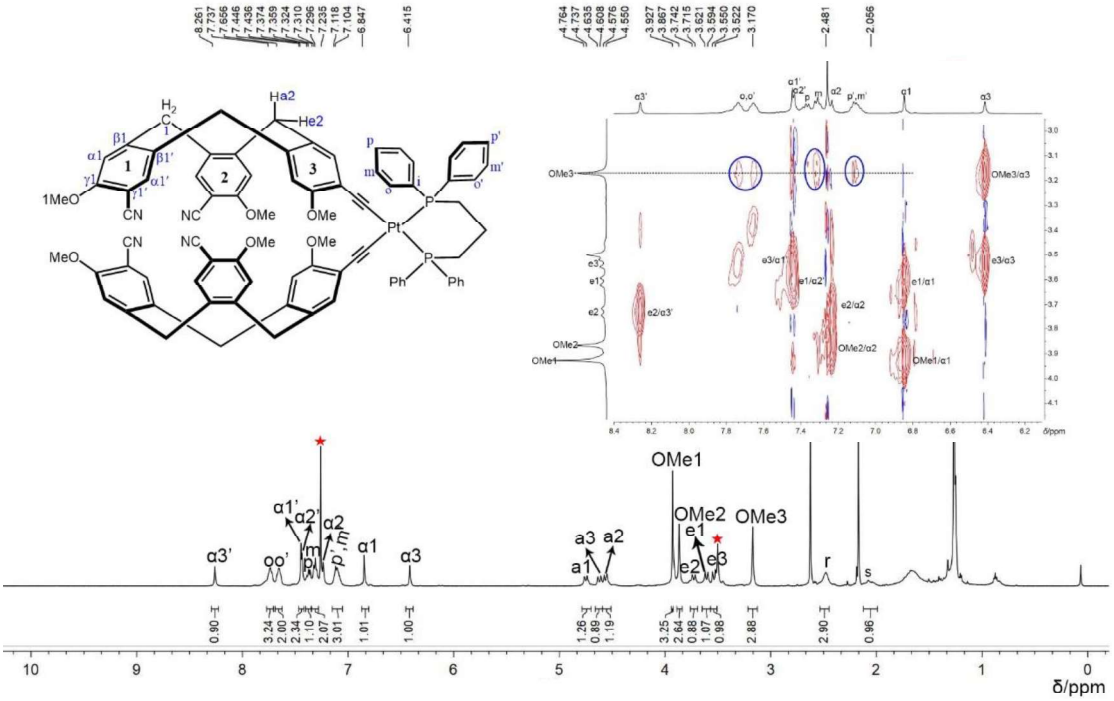


Figure 109. ^1H NMR spectrum of diastereomerically and enantiomerically pure precryptophane **13**. The inset shows a detailed region of the $^1H/^1H$ ROESY map in which correlations between the signal of the –OMe3 protons with a phenyl ring of dppp are highligted.

Once the precryptophanes **12** and **13** were prepared (**12**, as a diastereomeric mixture; **13** as in enantiopure form), they were used for the investigations of metallo-cryptophane formation. In a first series of experiments, in order to test the possible role of the solvent as template on self-assembly, as the literature reported[154,81], **12** and [Pd(dppp)][OTf]$_2$ in a 1:2 ratio were dissolved in either CD_2Cl_2, $CDCl_3$, or $C_2D_2Cl_4$ (0.6 mL). Then the reaction mixture was stirred for 1.5 - 2 hours at room temperature. Analysis of the resulting solution by ^1H NMR spectroscopy gave the spectra shown in **Figure 110**. Very broad signals are observed in the aromatic and aliphatic regions of the spectrum in which the signals of the aromatic protons on the one hand, and those of the,

–OMe and methylene protons (equatorial and axial), on the other hand, seem mixed together in both CD_2Cl_2 and $C_2D_2Cl_4$. But in $CDCl_3$, upon mixing the two components, a yellow precipitate appeared gradually. The ^1H NMR spectrum of the supernatant solution showed that it contained exclusively [Pd(dppp)][OTf]$_2$, as the signals of the protons of **12** had all disappeared. The broad signals observed in CD_2Cl_2 and $C_2D_2Cl_4$ solutions were assumed to be due to the exchange between the two coordinated $[Pd(dppp)]^{2+}$ fragments, on the one hand, or between bound and unbound $[Pd(dppp)]^{2+}$, on the other hand. In order to slow down and speed up the exchange rate, variable-temperature (VT) experiments in the low-temperature regime in CD_2Cl_2 and high-temperature regime in $C_2D_2Cl_4$, respectively, were undertaken (The corresponding figures are shown in the Experimental Part **Figure 56** and **57**, **Page 233**). Unfortunately, the VT experiments did not provide useful information, as the broad signals did not sharpen, neither at low temperature, nor at high temperature.

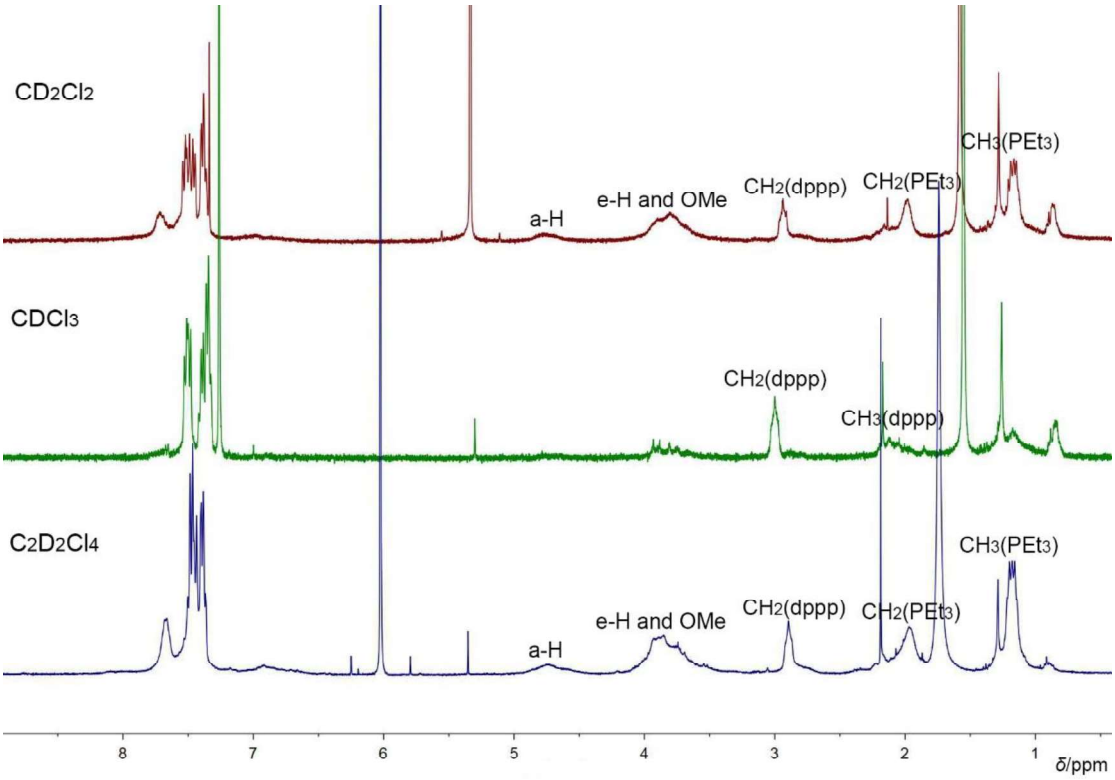


Figure 110. ^1H NMR spectra of precryptophane **12** with $[Pd(dppp)]^{2+}$ in different solvent at 298 K.

A complication could have arosen from the fact that precryptophane **12** was supplied in the form of a diastereomeric mixture. The broadness of the ^{1}H NMR signals could therefore result from exchange phenomena of the $[Pd(dppp)]^{2+}$ connectors between diastereomers. To exclude this possibility, attempts of metallo-cryptophane formation by closing the cavity of **13** with the $[Pd(dppp)]^{2+}$ metal complex fragment were carried out. Accordingly, (+)-**13** and $[Pd(dppp)][OTf]_2$ in *ca.* 2:1 ratio were mixed in CD_2Cl_2, and the resulting suspension was stirred for 1.5 h, after which it gave a clear yellow solution. The reaction mixture was directly investigated by using VT ^{1}H NMR experiments in the low-temperature regime (**Figure 111**). At 298 K, the spectrum again showed broad signals. However, with the decrease of temperature, the resolution got better, but it was still difficult to clearly identify the individual signals of metallo-cryptophane protons. Finally, another hypothesis was considered: The precryptophane may adopt two limiting conformations, one in which the cavities of the CTBs face each other, as in the desired metallo-cryptophane, or one in which the CTBs are rotated by 180° about the Pt–C(aryl) axis (**Figure 112**). Clearly, this last conformation would not lead to a metallo-cryptophane, but, rather, to a 1D and/or 2D-coordination polymer.

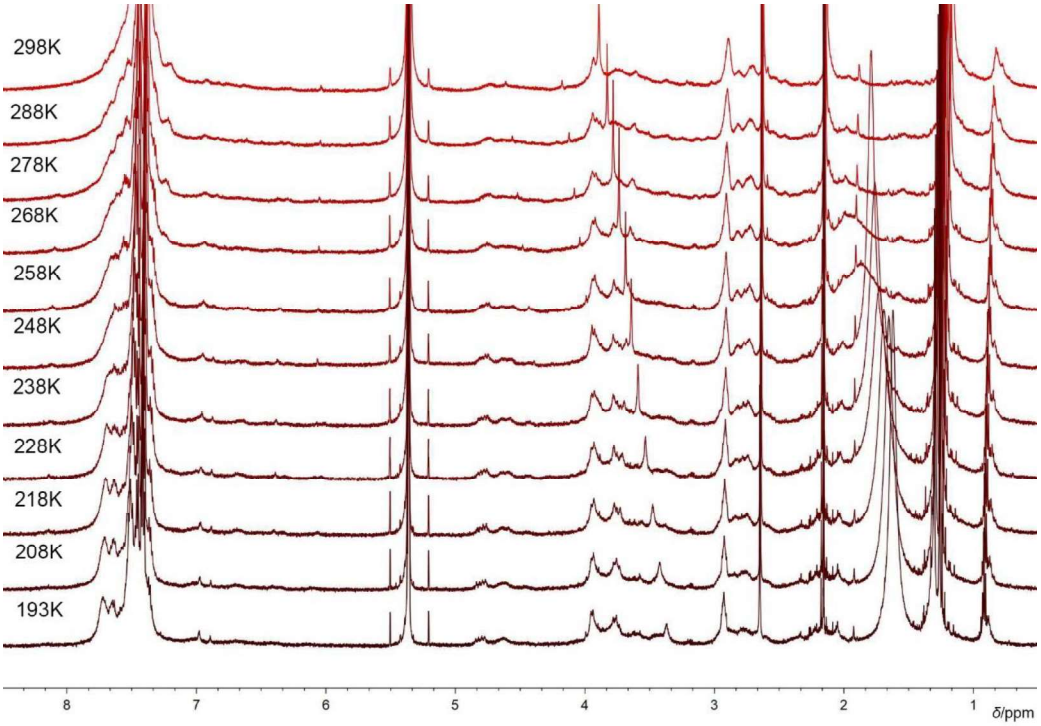


Figure 111. Variable temperature ^{1}H NMR (CD_2Cl_2, 600 MHz) of (+)-**13** with $[Pd(dppp)][OTf]_2$.

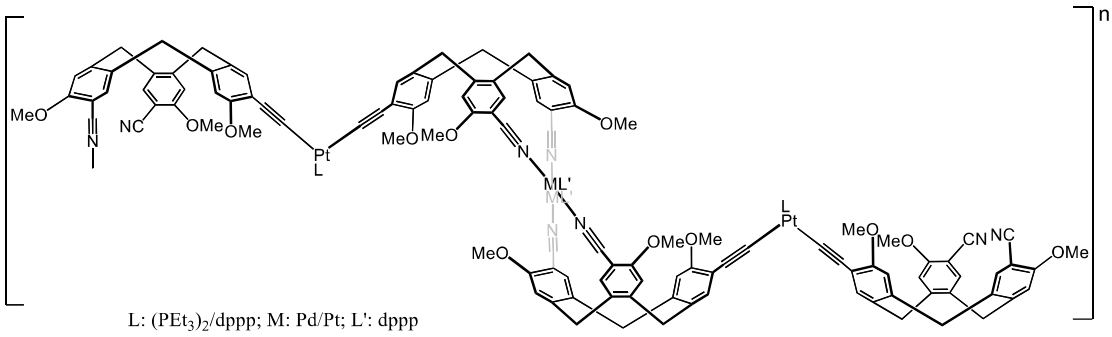


Figure 112. The limiting conformation of the precryptophane in which the CTBs adopt a side-to-side arrangement leads to a coordination polymer.

So, in order to obtain metallo-cryptophanes rather than coordination polymers, it was important to supply the precryptophanes in the correct conformation, i.e., the one in which the two Pt-bound CTB fragments were face to face. For that purpose, precryptophane **13** was prepared again, but in racemic form. Unlike the previous syntheses, it was purified by column chromatography using neutral alumina as stationary phase. Surprisingly, in addition to precryptophane **13**, another Pt-bridged CTB dimer (compound **18**) was isolated. The polarities of **13** and **18** were very similar, but their ^{1}H NMR spectra, compared in **Figure 113**, were completely different. According to the relative integrations of the signals of the CTB component and the $[Pt(dppp)]^{2+}$ metal complex fragment, compound **18** was indeed also a precryptophane dimer. In fact, the ^{1}H NMR spectrum of **18** showed two groups of six singlets in the aromatic region and two groups of three singlets for the -OMe groups. The relative integrations between the two groups were 1.3:1, which indicated that compound **18** was isolated in the form of two diastereomers, with a slight excess of one diastereomer over the other. Compared with the CTB precursor **9**, the chemical shifts of α1, α1’ and α2’ did not change, whatever the diastereomer considered. By contrast, the signals of the α3’ protons of the two diastereomers shifted upfield by about 0.573 ppm (for the major diastereomer M) and 0.666 ppm (for the minor diastereomer m). As for precryptophane **13**, these shifts could be due to the shielding effect of the phenyl moieties of the $[Pt(dppp)]^{2+}$ group. As for α protons, the signals of α2 (m) and α3 (m) shifted upfield

by about 0.289 ppm and 0.268 ppm, while those of α2 (M) and α3 (M) shifted upfield by approximately 0.257 ppm and 0.273 ppm, respectively. These changes were due to the fact that these two protons α2 (m, M) and α3 (m, M) are closer to dppp than protons α1, α1', and α2'. Compared with their homologues in CTB **9**, the chemical shifts of protons a1/e1, which are away from the $[Pt(dppp)]^{2+}$ bridge, did not change significantly, because of similar chemical environments. However, due to the relative proximity of $[Pt(dppp)]^{2+}$, the signals of a2 and a3 moved 0.19 and 0.15 ppm upfield, and those of e2 and e3 shifted upfield by 0.16 and 0.29 ppm, respectively. The singlets of the OMe3 substituents (m, M) also shifted upfield, by about 0.38 ppm. Again, this change could be due to the shielding effect of the phenyl substituents of the dppp chelate. Remarkably, the most affected methoxy protons were the OMe2 of both diastereomers, which showed the largest upfield chemical shift changes, by about 0.54 ppm (for M) and 0.35 ppm (for m). From this observation, we made the hypothesis that the OMe2 substituents of one of the CTBs in the major as well as the minor diastereomer were located in the cavity of the other CTB through rotation about the metal-carbon bond. This conformational change also made OMe3 closer to the phenyl group of dppp, which could be proved by 2D ROESY NMR. The stacked NMR spectra (**Figure 114**) clearly showed that α3' and α2 exhibited completely opposite chemical shift changes in compound **13** and **18**. Signals of α3 both shifted upfield and signals of other aromatic protons did not show significant change. Both the singlets of the OMe3 substituents in compound **13** and **18** shifted upfield, which could be due to the shielding effect of the phenyl substituents of the dppp chelate. Anyway, these differences indicated that compound **13** and **18** had completely different structures.

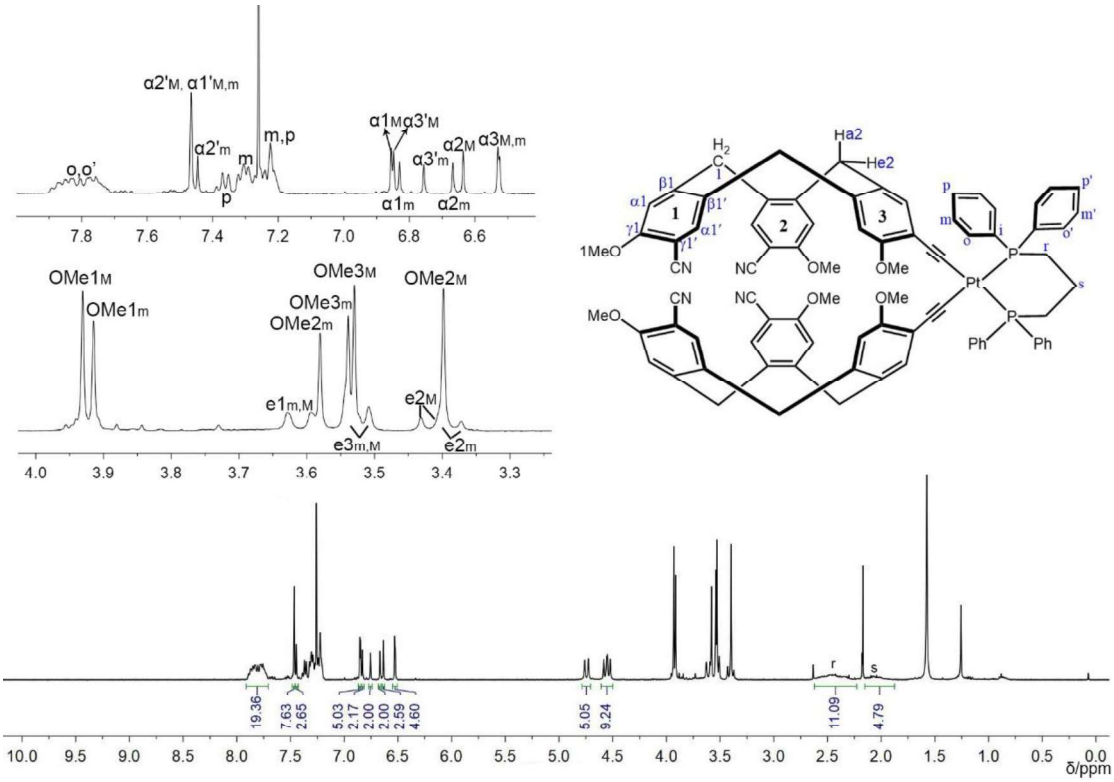


Figure 113. ^{1}H NMR spectrum of compound **18** in $CDCl_3$ at 298 K.

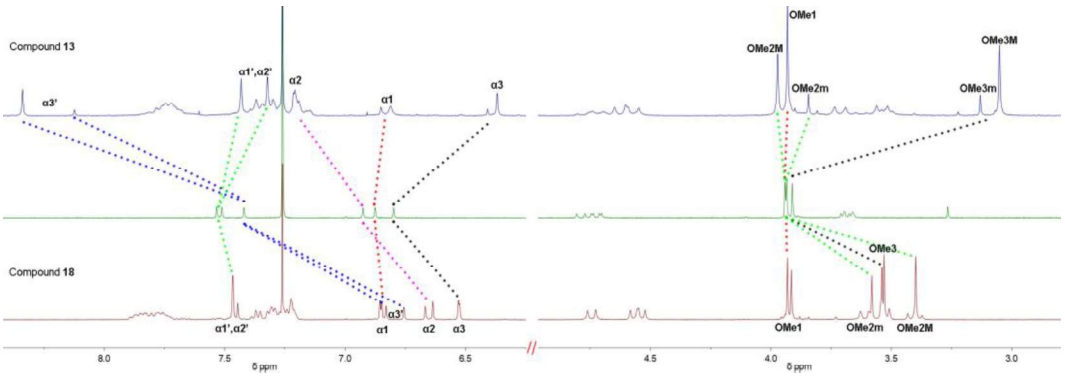


Figure 114. Stacked plots of selected regions of the ^{1}H NMR spectra of CTB **9**, precryptophane **13** and precryptophane **18**.

ESI-MS was used to further identify compound **18**. As seen previously, the molecular peak of enantiomerically pure precryptophane **13** (**Figure 115**) showed the expected isotopic distribution pattern at m/z = 1537.35 for the $[M + Cu]^+$ adduct. By contrast, the molecular peak of the diastereomers of compound **18** showed the expected isotopic distribution pattern at m/z = 1497.41, which corresponded to the $[M + Na]^+$ adduct, as shown in **Figure 116**. As, so far, the mass spectra of the precryptophanes

always showed at least a molecular peak corresponding to the copper adduct, we had thought that, as in the most common case of the sodium adducts, the molecule had captured a copper ion from the ionization chamber, due to the affinity of σ-donor nitrile ligands for Cu(I), and the possibility of the acetylene triple bond to interact with Cu(I) through metal-π interactions. However, the different ESI-MS results obtained for precryptophane **13** and precryptophane **18** led us to reconsider the actual chemical nature of these precryptophanes by making the following hypotheses: (i) Precryptophanes **12** and **13** were actually mononuclear copper(I) complexes of the precryptophanes; (ii) compound **18** did not complex copper(I). These hypotheses readily explained the differences observed between the ^{1}H NMR spectra of **13** and **18**.

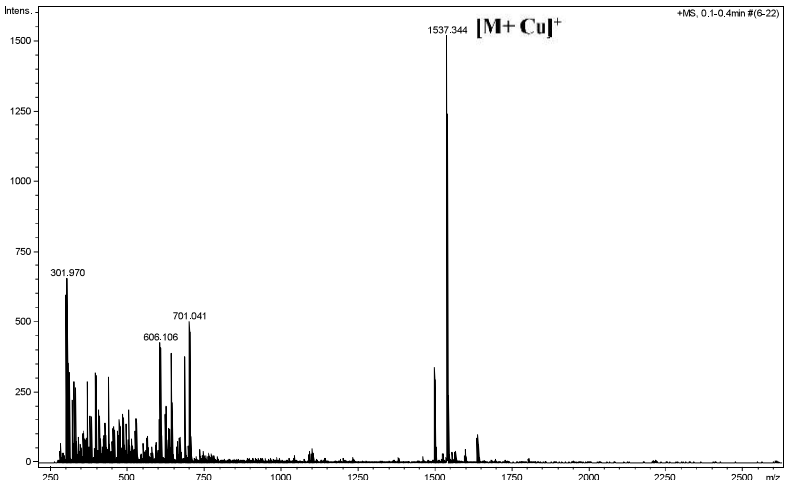


Figure 115. The mass spectrum of compound **13** in isopropanol with 1% HCOOH.

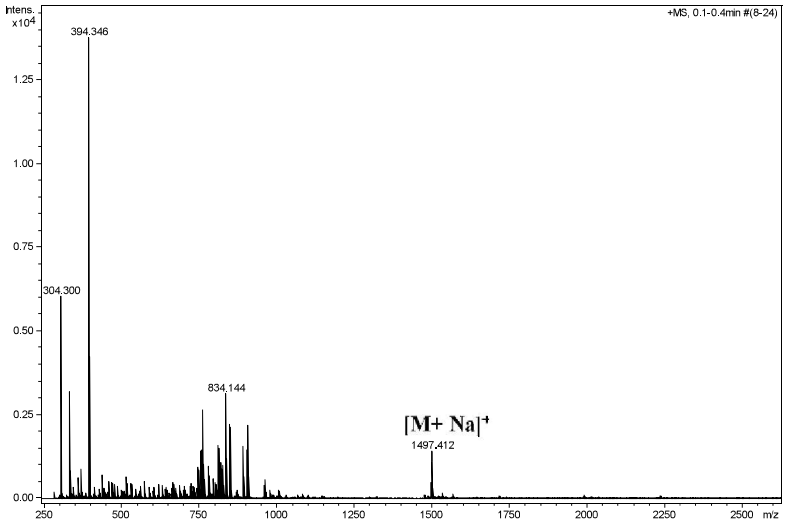


Figure 116. The mass spectrum of compound **18** in isopropanol with 1% HCOOH.

In order to confirm these hypotheses, precryptophane **18** was reacted with an excess of CuI. Examination of the crude product by ^{1}H NMR spectroscopy (**Figure 117**) clearly revealed that the addition of CuI, hence the complexation of Cu^{+} by precryptophane **18** induced strong downfield shifts of the signals of the α3 and α'3 aromatic protons and strong upfield shifts of the singlets of the –OMe2 and –OMe3 substituents. Comparison of their ^{1}H NMR spectra, although there were small differences of chemical shifts, clearly showed that compound **18** had transformed into **13** upon addition of Cu^{+} even in excess. This result was then confirmed by mass spectrometry. The ESI-MS showed the expected isotopic distribution patterns for the $[M + Cu]^{+}$ adduct at m/z = 1537.35, while the signal at m/z = 1497.41 corresponding to the $[M + Na]^{+}$ adduct had disappeared.

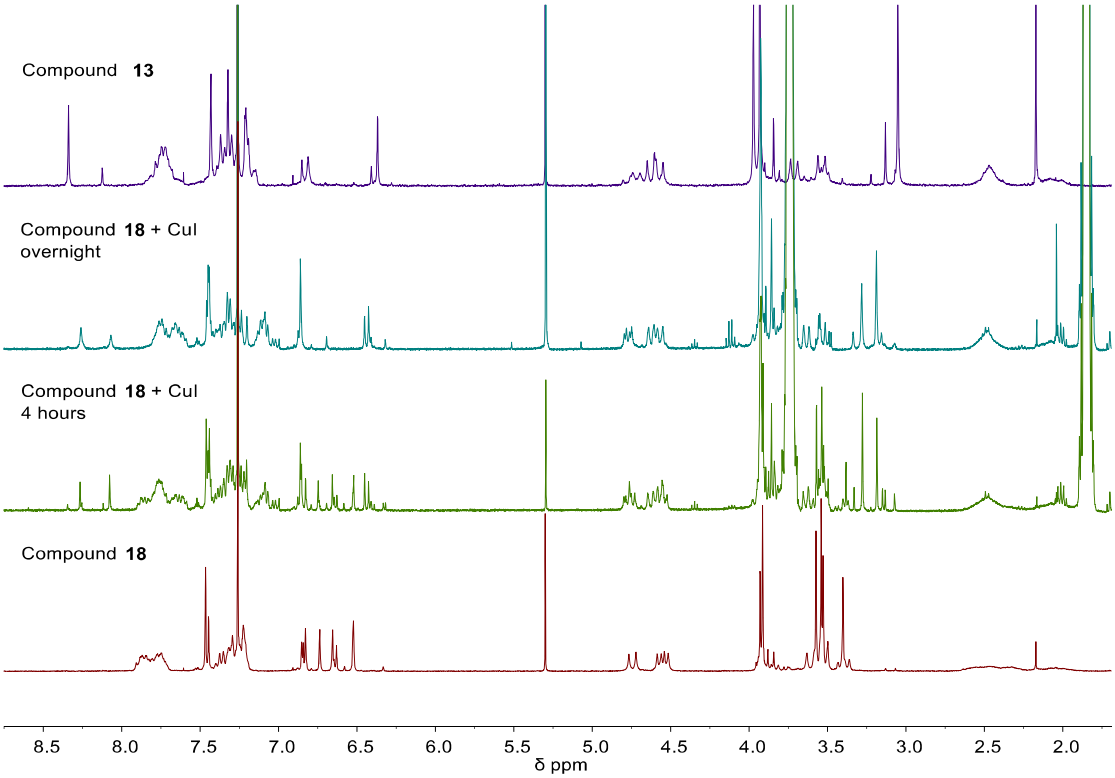


Figure 117. Stacked plot of ^{1}H NMR spectra showing the gradual conversion of compound **18** into precryptophane **13** by complexation of Cu^{+}.

Next, the controlled conversion of **13** back into **18** was carried out by addition of excess NaCN, in order to remove Cu^+ from **13** as the very stable $[Cu(CN)_4]^{3-}$ complex. As shown in **Figure 118**, upon the addition of NaCN, the signals of the protons belonging to **13** disappeared completely, while those of the protons of **18** appeared. The complete conversion of **13** into **18** was confirmed by ESI-MS, which showed that the signal corresponding to the $[M + Cu]^+$ adduct at m/z = 1537.35 was no longer present, and was replaced by the signal corresponding to the $[M + H]^+$ proton adduct at m/z = 1475.43.

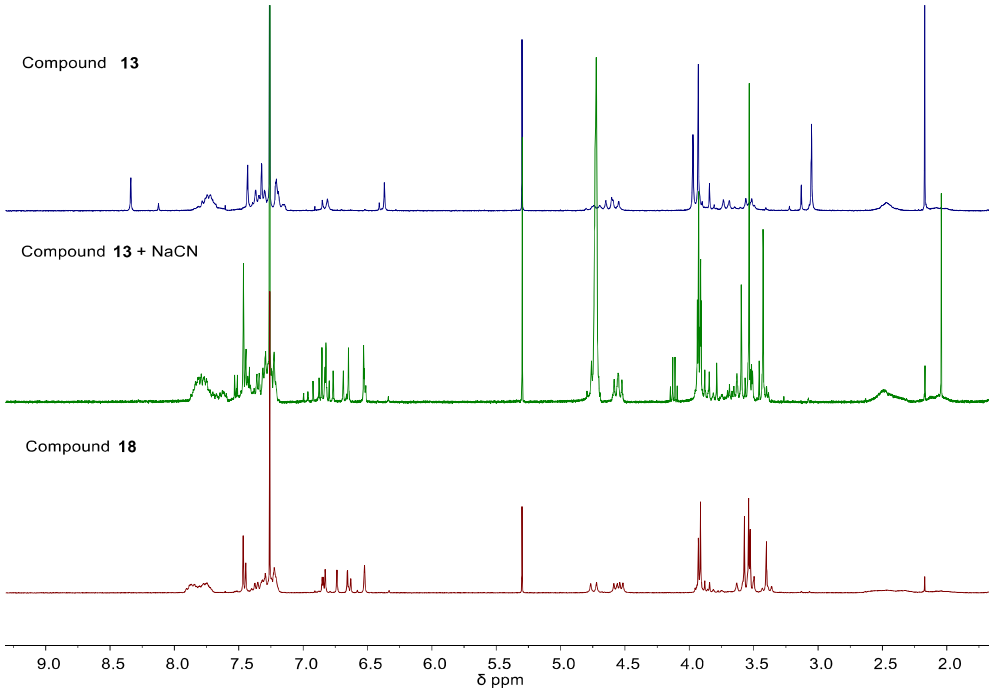


Figure 118. Stacked plot of ^{1}H NMR spectra showing the gradual conversion of compound **13** into precryptophane **18** by reaction with excess NaCN.

All these experiments have clearly demonstrated that compound **13** was actually a mononuclear Cu(I) complex of the precryptophane and corresponded to the formulation $\{[Pt(dppp)][(\mathbf{9}–H)]_2Cu\}^+$. Therefore its structure could differ from the structures of the limiting conformations that we have envisaged for the copper-free precryptophane, *i.e.*, compound **18**. Comparison of the ^{1}H NMR spectra of **13** and CTB **9** (**Figure 114**), showed that the signals of **9** that underwent the highest shifts in the precryptophane **13** were those of protons α3' and α2, both downfield shifted, and those of protons α3 and

OMe3, both upfield shifted. The signals of the other protons did not move significantly. The highest chemical shift change was observed for the α3' protons, which is closest to the triple bond. Therefore, we considered the hypothesis that the unique shift observed for protons α3' was induced by coordination of CuI in the proximity of this proton. The proximity is made possible by coordination of the Cu^{+} moiety to the ArC≡C- acetylenic bonds through π interactions. As shown in **Figure 119**, the Cu(I) bound I^{-} anion is close to the α3' protons, with which it can form CH···I^{-} bonds. The downfield shifts of the signals of the proximal α2 protons could also be explained by the CH···I^{-} bonds. The control of the conformation of the precryptophane by the coordination of CuI places OMe3 and α3 (to a lesser extent) in the shielding field of the dppp phenyls, which can explain why the signal of the OMe3 and α3 protons have moved upfield significantly.

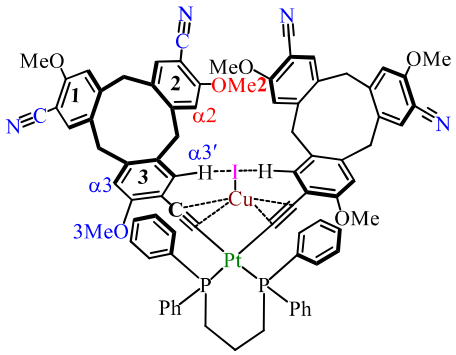


Figure 119. Proposed chemical structure of the precryptophane copper(I) complex **13**.

We assumed that agostic interaction also happened to compound **12**, as shown in **Figure 120**. The stacked plot of the ^{1}H NMR spectra of compounds **9**, **12** and **13** showed that the signals of protons α3', α2 and α3 of **12** and **13** displayed similar changes, that is, α3' and α2 showed significant downfield shift changes, α3, upfield shifts. In the aliphatic region of the spectra, the signals of protons –OMe1 and –OMe2 did not move. Those of –OMe3 shifted upfield, more in the case of **13**, which could be explained by the stronger shielding effect of the phenyl substituents of the dppp chelate than PEt_3 ligands. Actually, if the two CTB moieties were face to face in compound **12**, it would not be possible to observe any correlation between the protons of the PEt_3 ancillary ligands of the platinum bridge and the protons of the –OMe3 substituents of the CTB

ligands, since the ethyl groups cannot approach and affect the –OMe3. The effective presence of a correlation spot between the singlet of –OMe3 and the signal of the PEt_3 ligand in the $^1H/^1H$ ROESY map (**Figure 121**) confirms our hypothesis on the structure of precryptophane **12**.

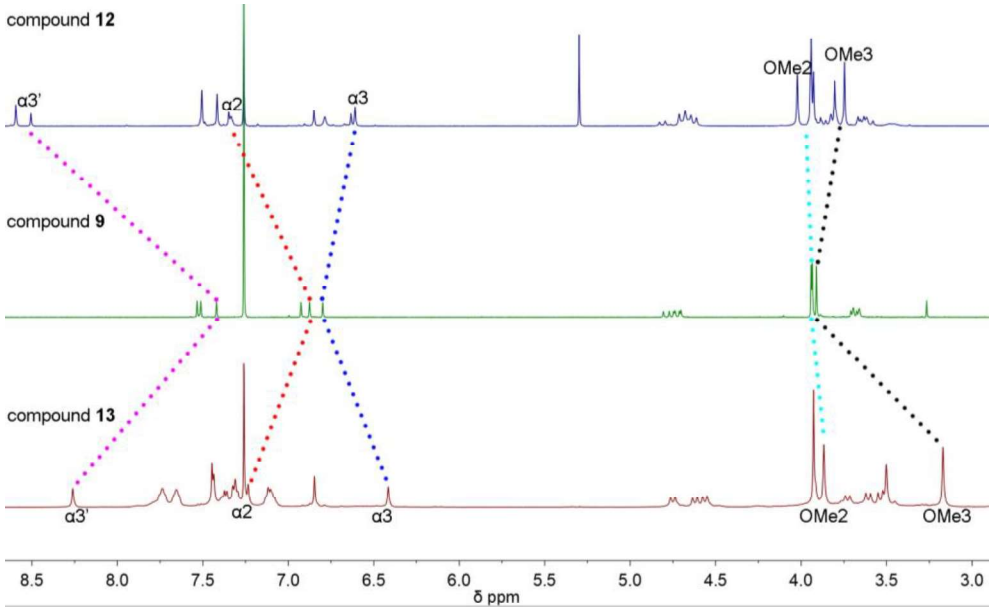


Figure 120. Stacked plots of selected regions of the ^1H NMR spectra of CTB **9**, precryptophane **12** and precryptophane **13**.

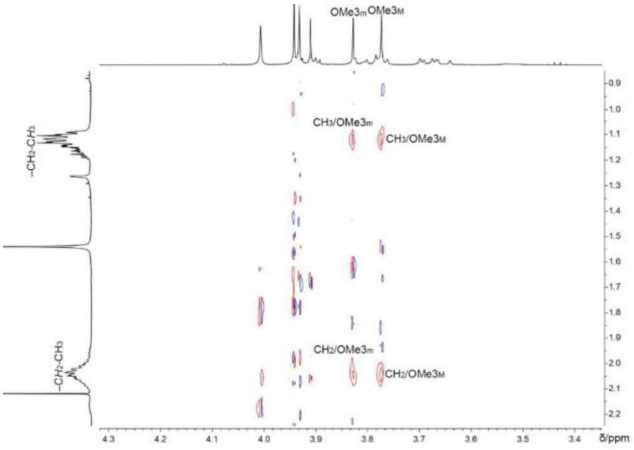


Figure 121. Detail of the ROESY map of compound **12**, showing the through space correlations between the protons of the PEt_3 ancillary ligands of the platinum bridge and the protons of the –OMe3 substituents of the CTB ligands.

4. Synthesis and Characterization of Cu-Free Precryptophanes

According to the findings reported in the preceding section, we reconsidered the procedure for the synthesis of copper(I)-free precryptophanes. Firstly, the conditions of reaction of CTB **9** with [Pt(dppp)Cl_2] and copper iodide in DMF were unchanged: heating at 45 °C for 2 days. However, the work-up included the treatment of the crude product, obtained after evaporation of the solvent and redissolution in $CHCl_3$, with an excess of an aqueous solution of NaCN for 4 hours. After separation of the phases, the product was purified by column chromatography on silica gel, which provided pure precryptophane **18** as a diastereomeric mixture. Then, compound **18** was studied by ^{1}H NMR spectroscopy in different solvents. The chemical shifts δ and corresponding $\Delta\delta$ of protons of **18** are collected in **Table 10** (**Page 150**). In $CDCl_3$, as shown before, the signal of –OMe2 was the most upfield shifted, whereas, in the case of the copper complex **13**, it was the signal of -OMe3 that underwent the strongest upfield shift. Since the CTB could rotate about the Pt-Ar(C) axis, it could be possible that the –OMe2 substituent of one CTB could be positioned in the shielding field of the cavity of the other CTB, as illustrated in **Figure 113** (**Page 137**). In addition, it is likely that the fit is different for the *meso* and chiral forms. As the shielding of the –OMe2 protons was stronger for the chiral form (0.536 ppm) than for the *meso* form (0.354 ppm), the –OMe2 group fitted better in the concavity of the other CTB in the chiral diastereomers than in the *meso* diastereomer. In addition, because the rotation of the metal-carbon bond moved α3’ of the other CTB in the shielding field of dppp, its signal was shifted upfield. Similar observations were done in CD_2Cl_2, although compound **18** seemed to decompose a little in this solvent. The –OMe2 group showed the most upfielded shifts by comparison with –OMe3, which indicated that the –OMe2 substituent went inside of the cavity of the other CTB as well, but the interaction between the cavity and –OMe2 was weaker than in $CDCl_3$. In $C_2D_2Cl_4$, the ^{1}H NMR spectrum (**Figure 122**) showed that it was the signal of the –OMe3 proton that underwent the highest upfield shift for the *meso* form. Moreover, the signals of the –OMe3 and –OMe2 groups of the chiral form were equally shifted. These observations could also be explained by the fact

that the interaction between the cavity and –OMe2 in $C_2D_2Cl_4$ was weaker than in $CDCl_3$ and that the –OMe2 group of the chiral diastereomer fitted better in the concavity of the other CTB than those of the *meso* diastereomer in $C_2D_2Cl_4$ as well as in $CDCl_3$. All the signals of the α3', α2 and α3 protons in different solvents showed upfield shifts, which were due to the shieding effect of the phenyl moieties of the $[Pt(dppp)]^{2+}$ group.

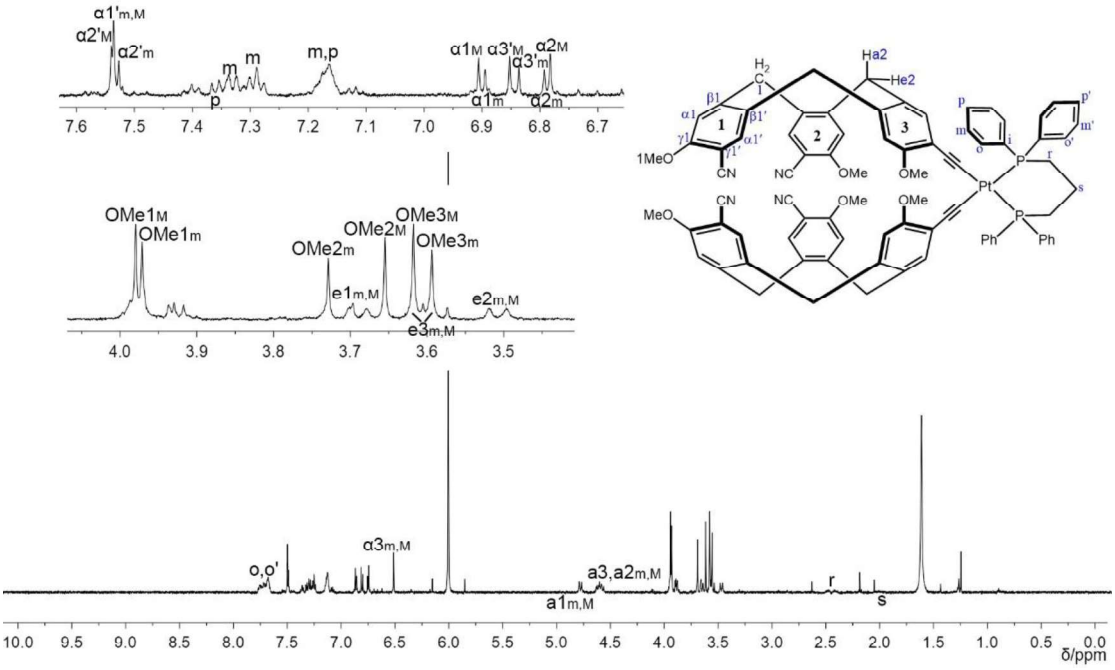


Figure 122. ^{1}H NMR spectrum of compound **18** in $C_2D_2Cl_4$ at 298 K.

Noticeably, another interesting finding was that along precryptophane **18**, a new compound (**19**) could be separated, the polarity of which was very close to the polarity of compound **18**. The yield of **19** was about 4%. Examination of this new compound by ^{1}H NMR spectroscopy (**Figure 123**) indicated that it contained two CTB components, as attested by the presence of six methoxy groups, twelve aromatic protons, six axial protons, and six equatorial protons. According to the integration of all the protons, **19** was a pure compound rather than a mixture of a pair of diastereomers. Therefore, compound **19** is a Pt-bridged CTBs dimer, and it is asymmetric. The composition of compound **19** was confirmed by ESI-MS, as its spectrum showed the expected isotopic distribution pattern for the $[M + H]^+$ adduct at m/z = 1475.43.

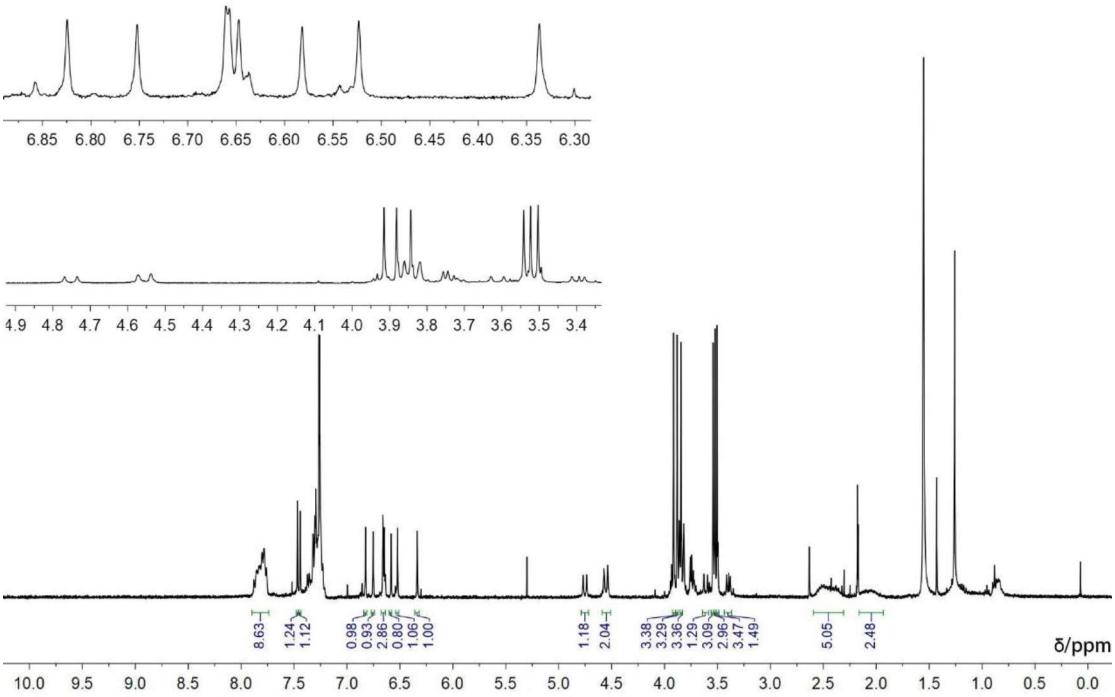


Figure 123. ^{1}H NMR spectrum of compound **19** in $CDCl_3$ at 298 K.

We discovered that precryptophane **19** converted gradually into precryptophane **18** in $C_2D_2Cl_4$ solution at room temperature, and that the conversion was accelerated by heating the solution to 45 °C. The conversion of **18** back into **19** was investigated starting from **18**. It was found that the rate of conversion of **18** into **19** was much slower than the rate of conversion of **19** into **18** at room temperature, and 45 °C as well, which meant **18** is a more stable compound. Then heating of these two solutions (starting from **19** and starting from **18**) was continued at 75 ˚C for 8 hours. The two solutions obtained the similar ultimate equilibrium, the ratio between **18** and **19** being about 3.5 : 1. As a matter of fact, we could not drive the interconversion to completion (**Figure 124**).

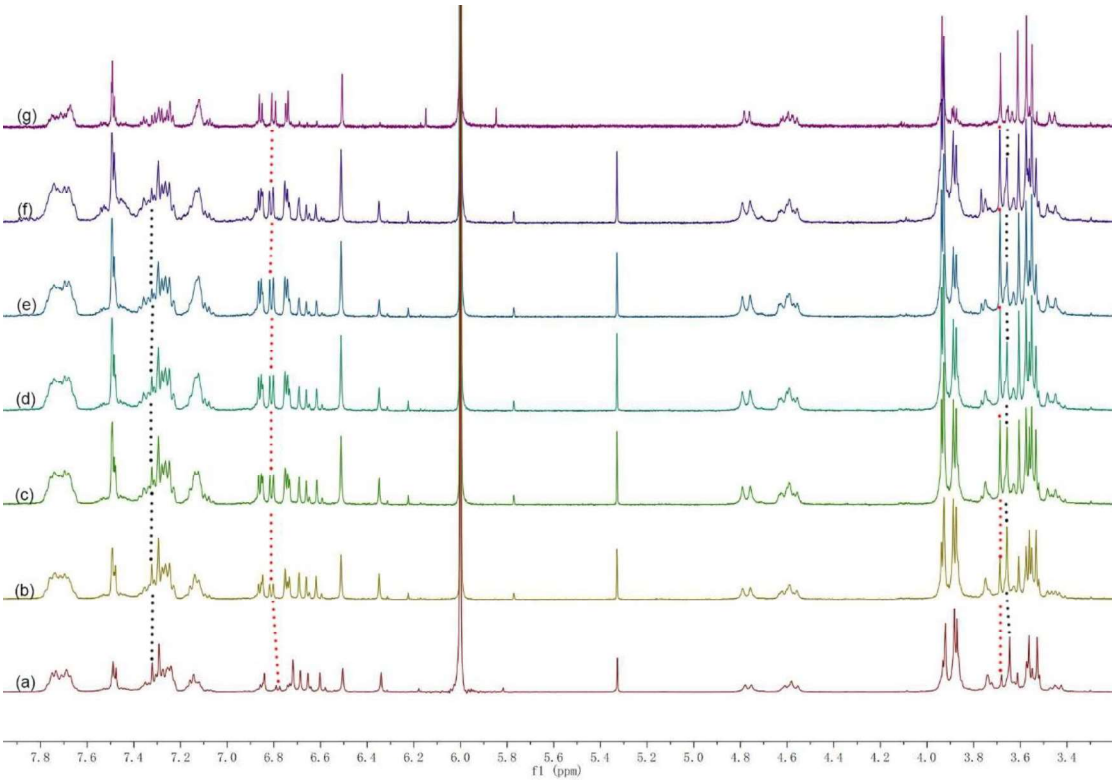


Figure 124. Stacked plot of the spectra obtained upon monitoring a solution of precryptophane **19** in $C_2D_2Cl_4$ by ^1H NMR spectroscopy. (a) pure **19** in $C_2D_2Cl_4$ for one day at room temperature; (b) after two days at room temperature; (c) after four days at room temperature; (d) after heating for six hours at 45˚C; (e) after heating for one day at 45˚C; (f) after heating for eight hours at 75˚C; (g): **18** after keeping in solid state for two days at room temperature.

Then, the reaction of compound **9** with $Pt(PEt_3)Cl_2$ and copper iodide as co-catalyst in THF at 55 ˚C for 8 hours was carried out. The product, after using NaCN to remove Cu^+, was purified by column chromatography on silica gel. The Cu-free precryptophane **20** was obtained as a mixture of diastereomers, which were studied in $CDCl_3$, CD_2Cl_2 and $C_2D_2Cl_4$. The chemical shifts δ and corresponding $\Delta\delta$ of protons of **20** are collected in **Table 11** (**Page 151**). Examination of the NMR spectrum showed that there was almost no changes for the aromatic protons and the bridging methylene protons, only the –OMe2 protons being effected. In $C_2D_2Cl_4$, the signals of protons –OMe2 of both diastereomers were shifted upfield equally, indicating that these groups interact similarly with the cavity of the other CTB through rotation about the metal-carbon bond. As the two CTBs are equivalent, there is a fast exchange between –OMe2 in the cavity and –OMe2 outside the cavity. In CD_2Cl_2, the –OMe2 protons of the minor

diastereomer underwent a stronger upfield shift than those of the major diastereomer. Finally, in $CDCl_3$, –OMe2 of the minor diastereomer showed a much higher upfield chemical shift (0.55 ppm) than in CD_2Cl_2 and $C_2D_2Cl_4$, and this upfield shift was stronger than for the major diasteromer (0.23 ppm). This difference results from the fact that the –OMe2 substituent in the minor diasteromer interacts better with the cavity of the other CTB, as suggested by comparison of the CPK models of the chiral vs the *meso* form. No significant chemical shifts were observed in the aromatic region, which confirms that it was the shielding effect of the phenyl moieties of dppp that were responsible of the upfield shifts of α3', α3 and α2 protons of precryptophane **18**.

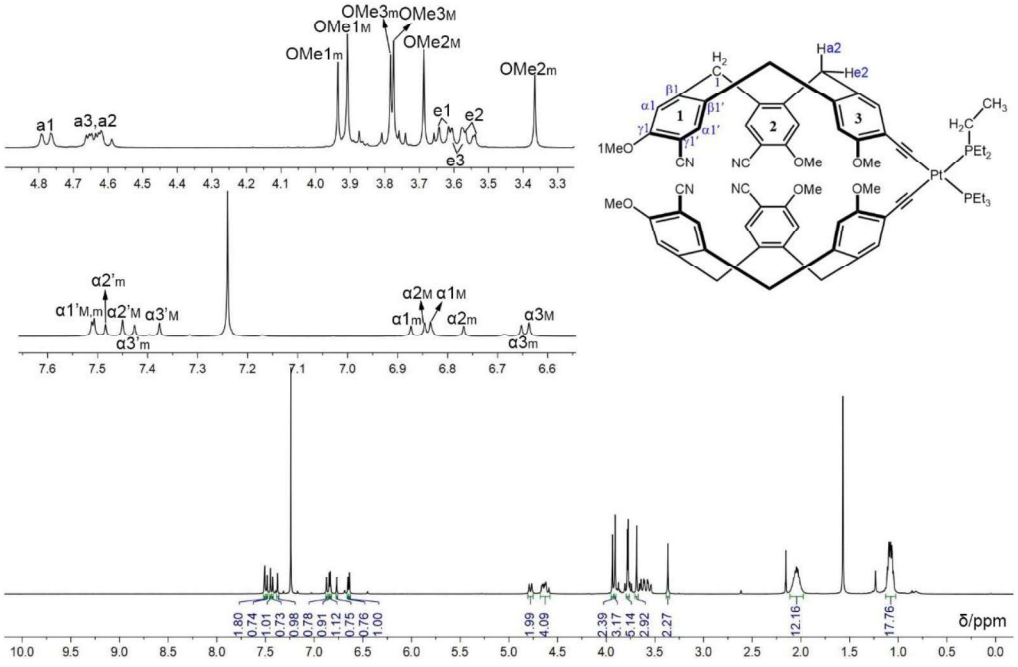


Figure 125. ^{1}H NMR spectrum of compound **20** in $CDCl_3$ at 298 K.

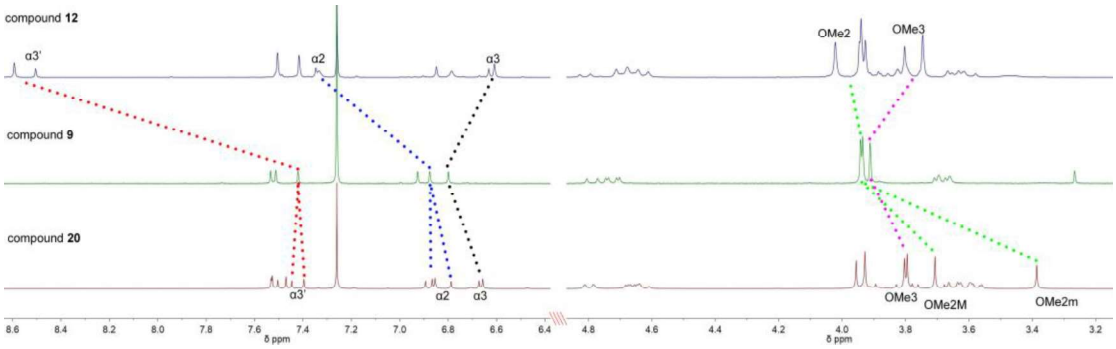


Figure 126. Stacked plots of selected regions of the ^{1}H NMR spectra of compound **9**, **12** and **20** in $CDCl_3$ at 298 K.

Besides, as shown in **Figure 125**, there were some tiny signals, the integration of which indicated that they originated from a single compound. According to the literature, they are likely to be due to the saddle form (compound **21**), but it was not possible for us to separate it from compound **20**. However, a mixture of compound **21** (major) and **20** (minor) was observed by ^{1}H NMR experiment. As shown in **Figure 127**, we discovered that no conversion of precryptophane **21** into **20** could be observed in $CDCl_3$ solution at room temperature, and that the conversion was accelerated by heating the solution to 45 °C. It seemed that the solution had already reached the ultimate equilibrium. Because no change was observed even when the solution was heated at 60 ˚C for another 1 day, as a matter of fact, we could not drive the interconversion to completion, the ultimate ratio between **21** and **20** being around 1:3.3.

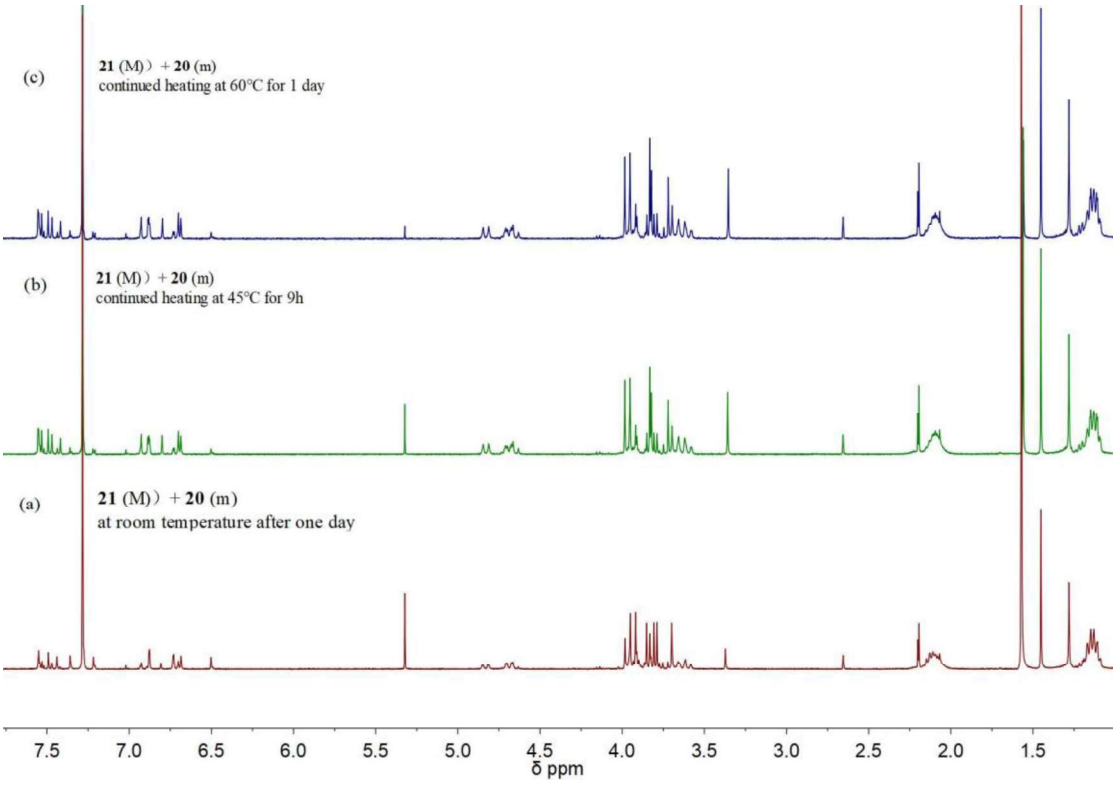


Figure 127. Stacked plot of the spectra obtained upon monitoring a solution of precryptophane **21** in $CDCl_3$ by ^{1}H NMR spectroscopy. (a) A mixture of **21** (major) and **20** (minor) at room temperature for one day; (b) after heating for nine hours at 45˚C; (c) after heating for one day at 60˚C.

The inclusion of the –OMe2 group of the chiral diastereomer of **18** inside of the cavity of the other CTB is shown in **Figure 128(a)** and is also illustrated by the CPK model shown in **Figure 128(b)**. They are also valid for compound **20** in which the phosphine ligand is PEt_3.

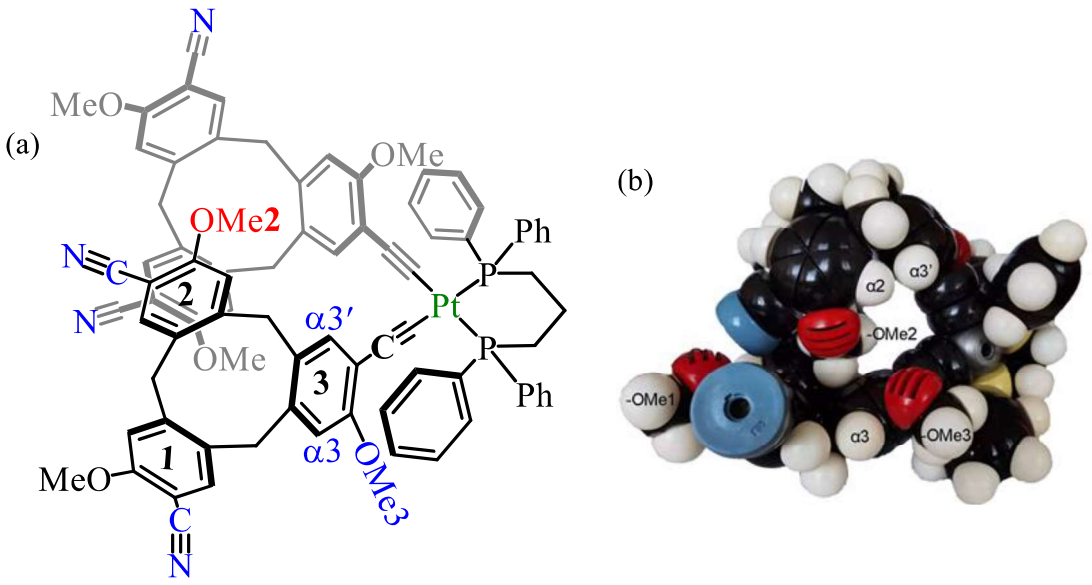


Figure 128. The structure and CPK model of the chiral precryptophane **18** showing how the –OMe2 substituent of one of the CTBs fits into the concavity of the other CTB.

Table 10. $^{1}H^{[a]}$ NMR data: Chemical shifts δ and CIS $\Delta\delta$ of protons of the compound **18** in different solvents.

		o	p,m	α1'	α2'	α1	α3'	α2	α3	a1	a3	a2	OMe1	OMe3	OMe2	e1	e3	e2	-CH_2-	-CH_3
CTB **9** ($CDCl_3$)				7.535	7.514	6.874	7.421	6.924	6.797	4.787	4.719	4.728	3.942	3.912	3.934	3.693	3.680	3.677		
18 $CDCl_3$ (500 MHz)	m	7.913-7.708	7.390-7.215	7.466	7.446	6.830	6.756	6.667	6.524	4.744	4.566	4.539	3.915	3.539	3.580	3.610	3.526	3.388	2.442	2.045
	M			7.466	7.466	6.856	6.848	6.636	6.530				3.931	3.530	3.398			3.418		
$\Delta\delta$ (δ_9-δ_{18})				0.069	0.068 0.048	0.044 0.018	0.665 0.573	0.257 0.288	0.273 0.267	0.043	0.153	0.189	0.027 0.011	0.373 0.382	0.354 0.536	0.083	0.154	0.289 0.259		
CTB **9** ($C_2D_2Cl_4$)				7.528	7.519	6.865	7.431	6.923	6.777	4.771	4.708	4.711	3.935	3.889	3.935	3.694	3.676	3.676		
18 $C_2D_2Cl_4$ (600 MHz)	m	7.765-7.674	7.366-7.278 7.122	7.492	7.483	6.851	6.792	6.749	6.507	4.772	4.606	4.567	3.927	3.550	3.686	4.646	3.562	4.464	2.473 2.414	2.004
	M			7.492	7.496	6.862	6.808	6.738	6.507				3.936	3.574	3.611					
$\Delta\delta$ (δ_9-δ_{18})				0.036	0.036 0.023	0.014 0.003	0.639 0.623	0.174 0.185	0.270	0.001	0.102	0.144	0.028 0.009	0.339 0.315	0.249 0.324	0.048	0.114	0.212		
CTB **9** (CD_2Cl_2)				7.569	7.557	6.920	7.447	6.960	6.826	4.798	4.737	4.746	3.936	3.875	3.930	3.713	3.699	3.690		
18 CD_2Cl_2 (500 MHz)	m	7.834-7.751	7.366-7.254	7.508	7.503	6.877	6.626	6.702	6.586	4.760	4.614	4.587	3.909	3.641	3.621	3.648	3.568	3.434	2.503 2.426	2.005
	M			7.508	7.512	6.889	6.675	6.709	6.586			4.594	3.918	3.636	3.571			3.458		
$\Delta\delta$ (δ_9-δ_{18})				0.061	0.054 0.045	0.043 0.031	0.821 0.772	0.258 0.251	0.24	0.038	0.123	0.159 0.152	0.027 0.018	0.234 0.239	0.309 0.359	0.065	0.131	0.256 0.232		

[a] δ, ppm *vs* residual solvents.

Table 11. $^{1}H^{[a]}$ NMR data: Chemical shifts δ and CIS $\Delta\delta$ of protons of the compound **20** in different solvents.

		α1'	α2'	α3'	α1	α2	α3	a1	a3	a2	OMe1	OMe3	OMe2	e1	e3	e2	-CH_2-	-CH_3
CTB **9** ($CDCl_3$)		7.535	7.514	7.421	6.874	6.924	6.797	4.787	4.719	4.728	3.942	3.912	3.934	3.693	3.680	3.677		
20 $CDCl_3$ (500 MHz)	m	7.532	7.504	7.446	6.893	6.788	6.673	4.799	4.660	4.654	3.956	3.803	3.386	3.651	3.613	3.577	2.059	1.100
	M	7.527	7.470	7.396	6.854	6.866	6.657	4.799	4.669	4.622	3.928	3.795	3.707	3.651	3.613	3.577	2.059	1.100
$\Delta\delta$ (δ_9-δ_{20})		0.003 0.008	0.010 0.044	-0.025 0.025	-0.019 0.020	0.136 0.083	0.124 0.140	-0.012	0.059 0.050	0.074 0.106	-0.006 0.014	0.109 0.117	0.548 0.227	0.043 0.043	0.068	0.10		
CTB **9** ($C_2D_2Cl_4$)		7.528	7.519	7.431	6.865	6.923	6.777	4.771	4.708	4.711	3.935	3.889	3.935	3.694	3.676	3.676		
20 $C_2D_2Cl_4$ (500 MHz)	m	7.561	7.511	7.496	6.890	6.917	6.701	4.817	4.694	4.667	3.956	3.858	3.733	3.679	3.654	3.630	2.016	1.084
	M	7.557	7.496	7.448	6.874	6.901	6.695	4.817	4.694	4.667	3.942	3.858	3.700	3.679	3.654	3.630	2.016	1.084
$\Delta\delta$ (δ_9-δ_{20})		-0.033 -0.028	0.008 0.023	-0.065 -0.017	-0.025 -0.009	0.006 0.022	0.076 0.082	-0.046 -0.046	0.014	0.044	-0.021 -0.007	0.031	0.202 0.235	0.015	0.022	0.046		
CTB **9** (CD_2Cl_2)		7.569	7.557	7.447	6.920	6.960	6.826	4.798	4.737	4.746	3.936	3.875	3.930	3.713	3.699	3.690		
20 CD_2Cl_2 (500 MHz)	m	7.568	7.547	7.386	6.926	6.928	6.732	4.804	4.702	4.684	3.943	3.834	3.623	3.682	3.648	3.642	2.016	1.084
	M	7.568	7.532	7.362	6.911	6.938	6.723	4.804	4.695	4.695	3.930	3.834	3.735	3.682	3.648	3.631	2.016	1.084
$\Delta\delta$ (δ_9-δ_{20})		-0.001 -0.001	0.010 0.025	0.061 0.085	-0.006 0.009	0.032 0.022	0.094 0.103	-0.006 -0.006	0.035 0.042	0.062 0.051	-0.007 -0.007	0.041	0.307 0.195	0.031	0.051	0.048 0.059		

[a] δ, ppm *vs* residual solvents.

5. Analytical Chiral HPLC Separation of Compound 18

The mixture of **18** (major compound) and **19** (minor compound) was examined by HPLC on a chiral stationary phase (Chiralpak IH) and eluted with the solvent mixture heptane/ethanol/dichloromethane 60/10/30, v/v. As shown by the chromatogram and the corresponding polarimetry (**Figure 129**), while the two enantiomers of **18** appeared at 7.22 and 9.62 min, respectively, its *meso* form appeared at 9.08 min (**Figure 129**). In addition, according to its relative integration, the signal at 7.22 min was due to two compounds, which gave opposite polarimetric responses, because the integration of the polarimetric signal at 7.23 min was smaller compared to the integration of the polarimetric signal at 9.68 min. Therefore, the compound giving the positive polarimetric signal at 7.22 min and the compound giving the negative polarimetric signal at 6.16 min should constitute a pair of enantiomers. As they are in lower amount than the enantiomeric pair of **18**, they correspond to compound **19**, which confirms that the signal of the –OMe2 of the chiral diastereomers of compound **18** was the most upfield shifted. Through ^{1}H NMR spectroscopy characterization, ESI-MS spectrometry, and the possibility of interconversion experiments between **18** and **19**, a hypothesis can be drawn that compound **19** might be the saddle-out form of precryptophane **18**.

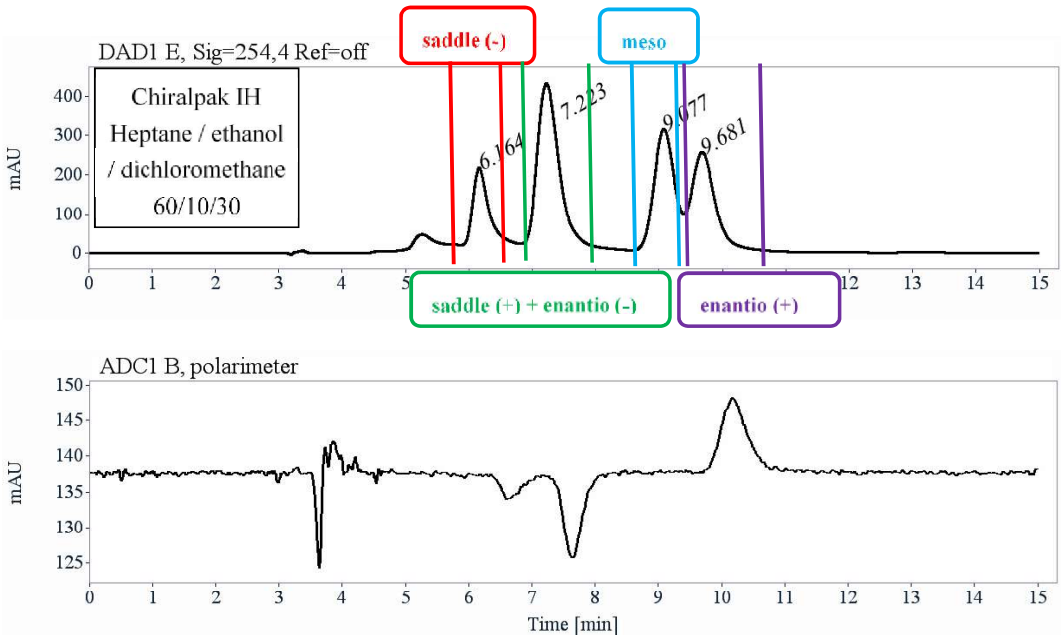


Figure 129. Chromatograms of the mixture of compound **18** and **19** preparative HPLC on Chirapak IH and polarimetry at 254 nm.

Table 12. Elution times of the different compounds on Chiralpak IH and their corresponding integration

RT [min]	Area	Area%	Capacity Factor
6.16	3603	13.09	1.09
7.22	10166	36.94	1.45
9.08	6993	25.41	2.08
9.68	6756	24.55	2.28
Sum	27519	100.00	

The mixture of **18** and **19** was first injected into a preparative Chiralpak IH HPLC column (250 × 10 mm). Elution was performed in the same conditions as for the analytical preparations, and provided pure (−)-**19**, a mixture of (−)-**18** and (+)-**19**, the pure *meso* form of **18** and a mixture of *meso* form of **18** and (+)-**18**. The fractions were collected in an ice bath and the solvent was removed below 20 °C. Then the mixture of (−)-**18** and (+)-**19** was injected in a Chiralpak IA HPLC column. Again the use of hexane/ethanol/dichloromethane (60/10/30) as mobile phase allowed us to separate the two components of the mixture successfully into pure (−)-**18** and (+)-**19**. Finally, the mixture of *meso* and (+)-**18** was purified by HPLC on Chiral Art Cellulose SJ, which provided the pure *meso* form of **18** and (+)-**18**. The ECD spectra of the optically active compounds thus isolated are shown in **Figure 130**. The green solid line and red dotted line correspond to (−)-**19** and (+)-**19** respectively. They are perfect mirror images of each other. The red-brown solid line and the orange solid line correspond to (−)-**18** and (+)-**18** respectively. The ECD spectra of optically active precryptophane **18** and saddle-out conformers **19** are similar, except that the intensities of the signals of (+)/(−)-**18** were more than twice as much as those corresponding to the enantiomers of **19**. The ECD spectra showed the absorption bands with maxima (or minima) at 220, 247, 300, 324 and 344 nm with sign inversion at 235, 283, 313 and 337 nm. The ECD spectra of **18** and **19** exhibit a strong bisignate band at 247 nm due to the phenyl $\pi \rightarrow \pi^*$ transitions and an intense band at 300 nm assignable to the acetylenic $\pi \rightarrow \pi^*$ transitions[168,169], along with two weaker bands between 310 − 350 nm that can be attributed to mixed transitions ^{1}LLCT [π(C≡C-**CTB**1) → π^*(**CTB**2)] through the Pt center and ^{1}MLCT

[dπ(Pt) → π*(C≡C-**CTB**)]. The band below 235 nm could be assigned to the chiral arrangement of the dppp groups on the Pt centers.

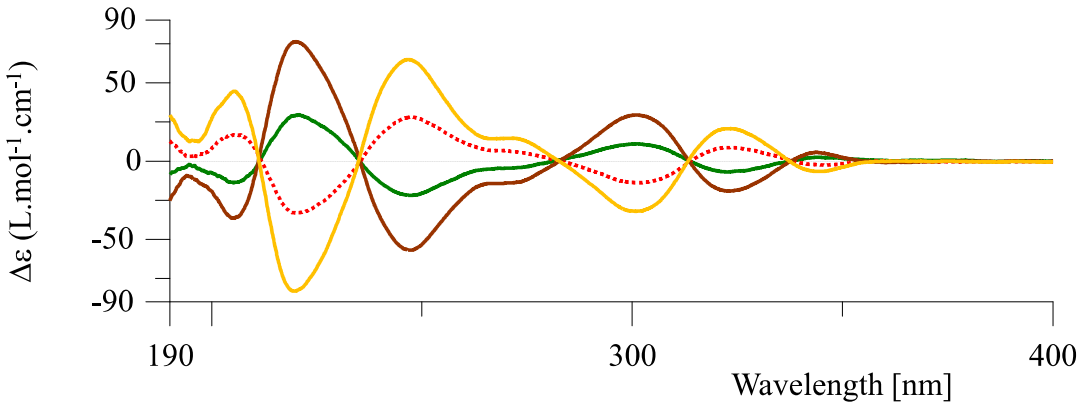


Figure 130. ECD spectra of optically pure compound **18** and saddle-out conformation **19** in acetonitrile. The red-brown and orange solid lines correspond to (−)-**18** and (+)-**18** respectively; the green solid line is the spectrum of (−)-**19**, the red dotted line, the spectrum of (+)-**19**.

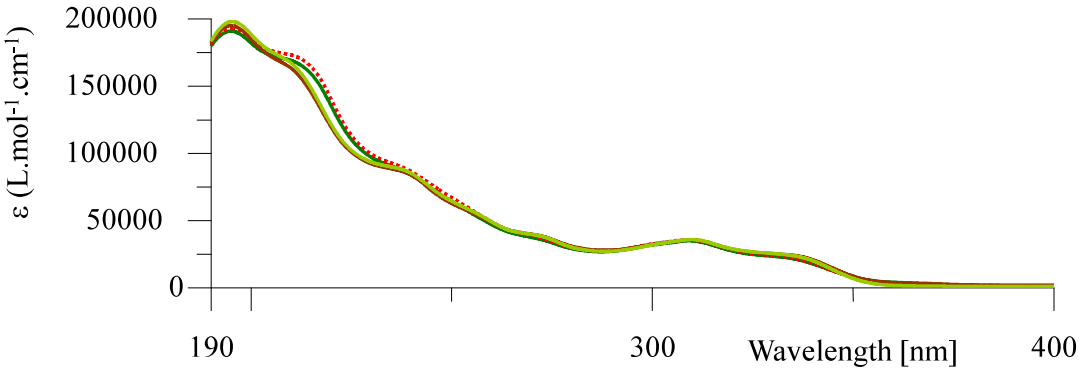


Figure 131. UV-vis absorbance spectra of optically pure compound **18** and saddle conformation **19** in acetonitrile. The red-brown and orange solid lines correspond to (−)-**18** and (+)-**18** respectively; the green solid line is the spectrum of (−)-**19**, the red dotted line, the spectrum of (+)-**19**.

The spontaneous conversion of **19** into **18** was repeated starting from pure (–)-**19**. The evolution of the ^{1}H NMR spectra is shown in **Figure 132**. After keeping the solution overnight at 298 K, it was observed that minute amounts of **18** had started to appear. After one week, the spectrum clearly showed that compound **18** was the major product, the signals belonging to compound **19** being very weak. There was no more changes after another week, which meant that the equilibrium between **18** and **19** had been achieved. In addition, the ratio between chiral **18** and *meso* **18** was 1:1. When starting from (–)-**18**, which contained a little of (+)-**19** (**Figure 133**), it was found that

the proportion of compound **19** decreased clearly after a night, which meant that the conversion of **19** into **18** was faster than **18** into **19**. In addition, after one week, the signals of **19** were very weak, and the equilibrium already achieved if the solution after one week was compared to the solution after two weeks.

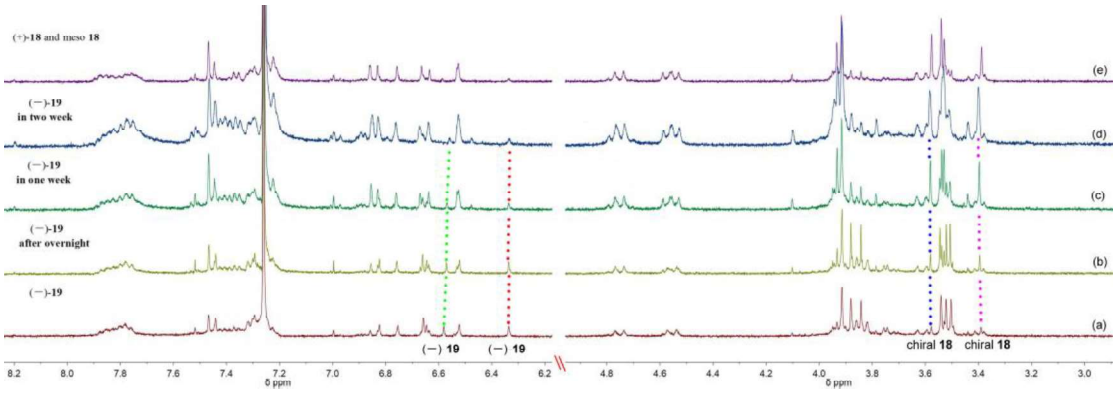


Figure 132. Evolution of the ^{1}H NMR spectrum of (–)-**19** in $CDCl_3$ at 298 K with time.

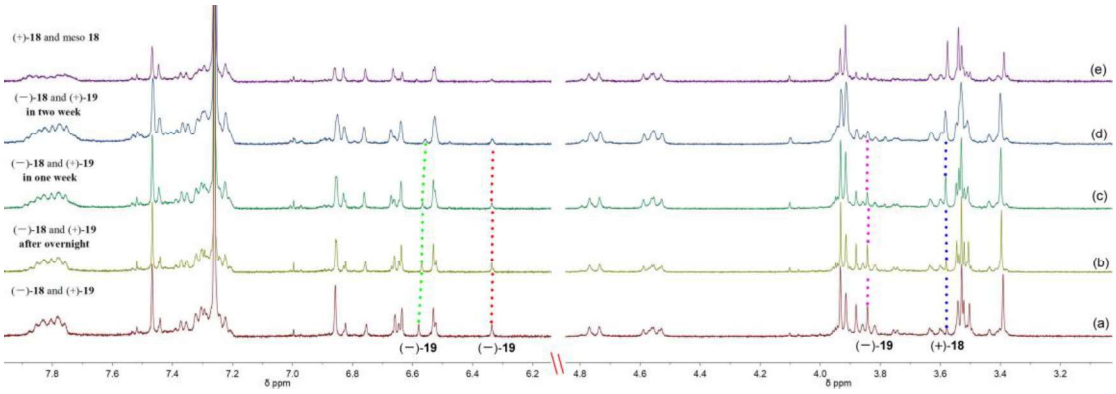


Figure 133. Evolution of the ^{1}H NMR spectrum of (–)-**18** with a small amount of (+)-**19** in $CDCl_3$ at 298 K with time.

6. Cryptophane Formation Starting from Cu-Free Precryptophanes

6.1 Photophysical Properties of 18 and 20 in $CHCl_3$, CH_2Cl_2 and $C_2H_2Cl_4$

The electronic spectra of compound **9** showed a major π→π* transition at ~250 nm due to phenyl groups and weaker absorptions at ~310 nm due to the acetylenic and cyano groups π → π* transitions that have been delocalized into the phenyl groups of **9**. Once metallo-precryptophanes **18** and **20** were formed, a new high energy band appeared at 230 nm, which could be assigned to the $[Pt(dppp)]^{2+}$ moiety. Compounds **18** and **20** displayed in CH_2Cl_2 intense high-energy absorptions at 310 nm, which were likely to result from mixed transitions, including intraligand (^{1}IL C≡CR), ligand to ligand (dppp → C≡CR) and metal to ligand (C≡CR or dppp) character. The lower energy absorption broad bands at about 340 nm were tentatively assigned to alkynyl substituents, which were attributed to mixed transitions ^{1}LLCT [π(C≡C-**CTB**1) → π*(**CTB**2)] through the Pt center and ^{1}MLCT [dπ(Pt) → π*(C≡C-**CTB**)]. In addition, **18** and **20** showed minor solvent effects, the spectra in $CHCl_3$, CH_2Cl_2 and $C_2H_2Cl_4$ having bands of similar shapes and energies.

From the emission spectra, it was found that compounds **18** and **20** are both emissive even in aerated solutions, and exhibit broad vibronic-structured emission bands between 380 and 450 nm ($\lambda_{exc} \approx 360$ nm). However, compound **20** showed much weaker emission compared to **18** in $C_2H_2Cl_4$, which suggested that the emissive state in the latter probably derived from ligand-to-ligand charge transfer (LLCT) transitions [π(C≡C-**CTB**) → π*(**dppp**)]. As discussed before, $CHCl_3$ and $C_2H_2Cl_4$ could enter the cavities of compound **18**, but there was an exchange between captured and free solvent in $CHCl_3$, which meant that the conformation of **18** was not as stable as in $C_2H_2Cl_4$. This difference might be the reason why the emission intensity of **18** was stronger in $C_2H_2Cl_4$ than in $CHCl_3$.

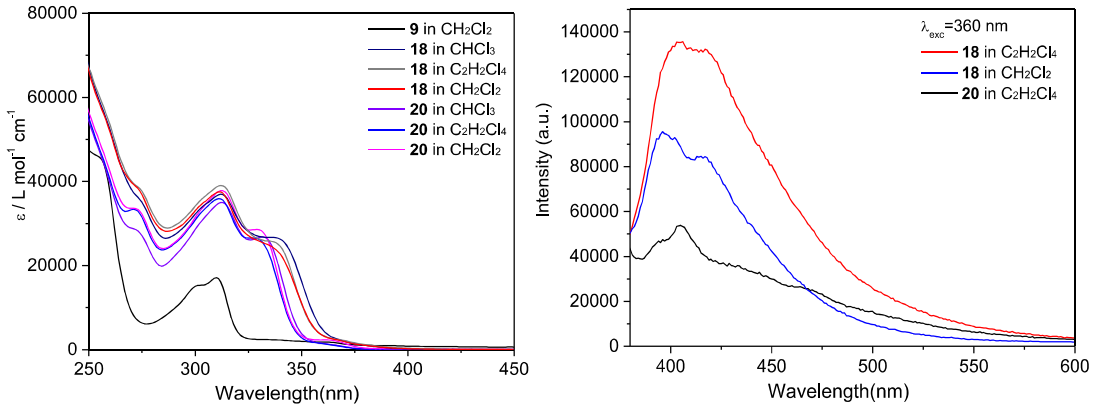


Figure 134. Electronic absorption (left) and emission (right) spectral traces of complexes **18** and **20** in different solvents at room temperature.

6.2 Photophysical Properties of 18 Coordinated with Pt(dppp)(OTf)$_2$

The coordination properties of **18** with Pt(dppp)(OTf)$_2$ were investigated in CH_2Cl_2 by UV−vis and emission titration experiments. The room temperature UV−vis spectral changes of **18** upon addition of Pt(dppp)(OTf)$_2$ were shown in **Figure 135**. The absorbance of the bands of **18** at 312 nm shifted to lower energy (*ca.* 315 nm) and the shoulder at 338 nm disappeared, while the lower energy absorption bands over 360 nm increased gradually upon the addition of Pt(dppp)(OTf)$_2$. Finally, a well-defined isosbestic point was observed at 350 nm, which meant that compound **18** was converted into another species during the titration experiments. The plot of the absorbance change at 375 nm as a function of the concentration of Pt(dppp)(OTf)$_2$ indicated that the stoichiometric binding ratio between Pt(dppp)(OTf)$_2$ and **18** was 2:1, which was consistent with our expectations. The increase of the absorption bands at 230 nm was due to the phenyl groups of $[Pt(dppp)]^{2+}$. Upon the addition of Pt(dppp)(OTf)$_2$ into the CH_2Cl_2 solution of **18**, the emission intensity at 400 and 420 nm decreased gradually, the quenching of fluorescence being probably due to the coordination of the $[Pt(dppp)]^{2+}$ complex fragments with the cyano groups, allowing for deactivation of the excited state through the dd states of the nitrile bound Pt^{2+} cations. The stoichiometric binding ratio was determined to be 2:1, the quenching of the emission for $[Pt(dppp)]^{2+}$/[**18**] ratios greater than two being due to intermolecular processes.

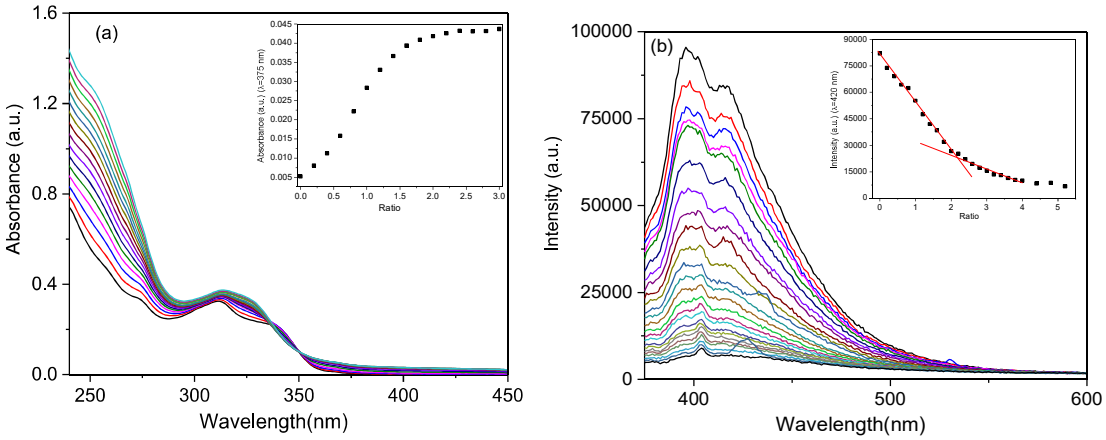
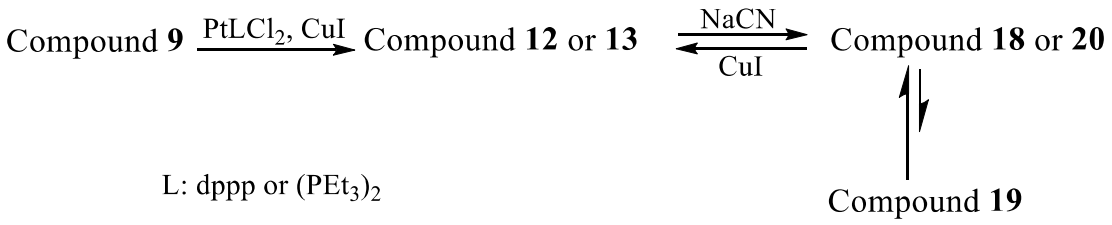


Figure 135. (a) UV−vis spectral changes of **18** (1.0×10^{-5} mol L^{-1}) in CH_2Cl_2 upon addition of $[Pt(dppp)]^{2+}$. (b): Emission spectral changes of **18** (1.0×10^{-5} mol L^{-1}) in CH_2Cl_2 upon addition of $[Pt(dppp)]^{2+}$. Inserts: plots of the absorbance and emission change at 375 nm and 420 nm as a function of the ratio $[Pt(dppp)]^{2+}$/[**18**]

7. Conclusion

The asymmetric cyclotribenzylene CTB **9** was synthesized and characterized, and it was resolved into a pair of enantiomers by using chiral HPLC. Then a series of chiral Pt-bridged CTB dimer precryptophane complexes derived from racemic CTB **9** have been synthesized and characterized by NMR and ESI-MS spectroscopy, the *meso* form showed a C_s-symmetry, and the chiral forms had a C_2-symmetry. We found that Copper iodide is pi-coordinated with alkynyl fragment, at the same time, H-bonds were formed between coordinated iodide and α3', and the α2 was closer to iodide as well, when these precryptophanes were synthesized by using CuI as co-catalyst. As a consequence, the chemical shifts of α3' and OMe3 underwent large changes. Attempts of metallo-cryptophane formation by closing the cavity of the precryptophanes **12** and **13** with the $[Pd(dppp)]^{2+}$ metal complex fragment led presumably to metallo-polymers instead of metallo-cryptophanes. Cu^+ could be removed by addition of excess NaCN. It was found that the –OMe2 substituent of one CTB was positioned in the shielding field of the cavity of the other CTB for the Cu-free precryptophanes **18** and **20**. However, the interaction between –OMe2 and the cavity of the other CTB was different in different solvents. In addition, the NMR spectra showed that these two complexes both contained a saddle form. The conversions of **19** into **18** and **18** into **19** were followed by ^{1}HNMR experiments. The reactions and exchanges among these compounds are displayed in **Scheme 2**.



Scheme 2. The studies of precryptophanes starting from compound **9**.

Experimental Part

Experimental Details:

Materials, methods and instrumentation.

Unless otherwise stated, all reactions were performed under argon, using the following solvents and liquid reagents, which were dried and distilled under argon: DMF (anhydrous magnesium sulfate), THF (Na/benzophenone), CH_2Cl_2 (P_2O_5), MeOH (Mg), Et_3N (KOH), acetone (K_2CO_3). Other solvents and reagents were used as received. The following compounds were synthesized according to the literature: CTB(OMe,C_2H)[118], CTB(H, OTf)[116], Au(PPh_3)Cl[173], Au(PPh_2Me)Cl[173], Au($PPhMe_2$)Cl[173], Au(SMe_2)Cl.[174] NMR spectra were recorded on Bruker Avance III 400 MHz, 500 MHz and 600 MHz spectrometers (the automatic acquisition was used for ^{13}C NMR, ROESY, HSQC and HMBC). Chemical shifts were reported using the residual solvent signal (7.26 and 77.16 for $CHCl_3$; 5.32 and 53.84 for $CDHCl_2$; 6.00 and 73.78 for C_2DHCl_4) as internal reference for ^{1}H NMR and for ^{13}C NMR and the signal of H_3PO_4 placed inside an insert for ^{31}P NMR, ^{13}C NMR spectra were acquired with proton decoipling. Column chromatographic separations were carried out over Merck silica gel 60 (0.040-0.063 mm) and Merck Al_2O_3 90 standardized. Analytical thin layer chromography (TLC) was performed on Merck silica gel TLC plates F-254. Electronic absorption spectra were recorded using a Cary 5000 double beam spectrophotometer from Agilent technologies and emission spectra were recorded using Jasco FP-8300 and HORIBA JobinYvon Fluorolog FL3-22 spectrofluorimeter for steady-state and lifetime measurements. Optical rotations were measured on a Jasco P-2000 polarimeter with a halogen lamp at wavelengths of 589, 578, 546, 436 and 405 nm, or on a 241 Perkin-Elmer polarimeter with a sodium lamp at 589 nm, a mercury lamp at 578, 546, 436 and 365 nm, and a double-jacketed 10 cm cell at 25°C. ECD and UV spectra were measured on a JASCO J-815 spectrophotometer equipped with a JASCO Peltier cell holder PTC-423 to maintain the temperature at 25.0 ± 0.2°C. ESI-MS spectra were acquired by electrospray mass spectrometry in the positive mode on an orthogonal time-of-flight micrOTOF-QII BRUKER. DLS experiments were performed by using a Malvern Zetasizer NanoZS instrument. STEM images were obtained with a Quanta250 FEG

electron microscope from Thermofischer company. Infrared spectra were reported in frequency of absorption using Alpha Bruker Optics spectrometer. Melting points were recorded with a SMP3 Stuart Scientific microscope in open capillary tubes and are uncorrected.

Part I:

^{1}H NMR Titration Experiments:

The guest solution $Et_4N^+I^-$ (10^{-4} M) in 0.5 mL $CDCl_3$, the host solution of CTBs (**C1** and **C4**) (around 5×10^{-3} M) in $CDCl_3$ were prepared in small vials. A few successive aliquots (range from 1μL to 20 μL) of host solution were added via a small syringe. The chemical shift changes were recorded after each addition.

ESI-MS Experiments:

The mass spectrometry data of the gold CTBs complexes dissolved in $CHCl_3$ (10^{-4} M), were obtained by ESI-TOF. The molecular peak $[M+H]^+$ could be observed only when the sample was injected in an acidic solvent mixture ($CHCl_3$/*i*PrOH/HCO_2H 1.00:0.99:0.01, v/v/v).

UV-vis absorption and Emission Experiment:

C1 (8.59 mg, 0.005 mmol), **C2** (7.65 mg, 0.005 mmol), **C3** (6.72 mg, 0.005 mmol), **C4** (9.03 mg, 0.005 mmol), **C5** (8.10 mg, 0.005 mmol), **C6** (7.17 mg, 0.005 mmol), **C7** (6.42 mg, 0.005 mmol), **C9** (8.85 mg, 0.005 mmol) were dissolved in 5 mL volumetric flasks to prepare the mother solutions ($1.0*10^{-3}$ M). 25, 125, 250 and 500 μL of mother solution of each complex were withdrawn and diluted in 5 mL volumetric flasks to prepare solutions at four different concentrations (5.0×10^{-6} M, 25×10^{-6} M, 50×10^{-6} M, 100×10^{-6} M), which were used to record the UV-vis absorption spectra in a cell of 0.2 cm.

For solution emission and excitation spectra, all samples (1.0×10^{-5} M in $CHCl_3$) were degassed on a high-vacuum line in a two-compartment cell consisting of a 10 ml round bulb equipped with a sidearm 1 cm fluorescence cuvette and sealed from the

atmosphere by a stopper. Solutions were rigorously degassed with at least four successive freeze–pump–thaw cycles.

Solid-state emission and excitation spectra at room temperature were recorded with ground solid samples loaded in a quartz tube inside a quartz-walled Dewar flask.

UV-vis absorption and emission experiment in non-deoxygenated mixture solvent $CHCl_3$/MeOH or $CHCl_3$/MeCN:

100 μL of **C1** mother solution in 10 mL volumetric flasks were withdrawn and were diluted to 1.0×10^{-5} M with different mixture solvent (the volume ratio of MeOH or MeCN ranged from 0 to 99%). The other complexes were prepared in the same way.

The emission spectra were recorded using Jasco FP-8300 with 5 nm slit. For **C1**, **C2**, **C3**, **C7**, **C9**, the emission spectra were obtained with exciting wavelength at 330 nm. For **C4**, **C5**, **C6**, the emission spectra were obtained with exciting wavelength at 365 nm.

ECD Experiment:

A cell of 1 mm of optical pathlength was used. The CD spectrometer was purged with nitrogen before recording each spectrum, which was baseline subtracted. The baseline was always measured for the same solvent and in the same cell as the samples. The spectra are presented without smoothing and further data processing. Acquisition parameters: 0.2 nm as intervals, scanning speed 50 nm/min, band width 2 nm, and 3 accumulations per sample except **CTB(H, C_2H)** (band width 1 nm, and 1 accumulation).

Preparative separation of compound CTB(OMe, C_2H):

About 35 mg of compound **CTB(OMe, C_2H)** dissolved in dichloromethane (10 mL) were separated by using Chiralpak ID (250 × 10 mm), hexane/ethanol/dichloromethane 40:30:30 v/v as mobile phase, at a flow-rate of 5 mL/min and a UV detection at 254 nm. Injections: 40 times 250 μL, every 6.2 minutes. 18.0 mg of the first eluted enantiomer with ee > 99.5%, 12.1 mg of the second eluted enantiomer with ee > 98.5% and 4.2 mg of the mixture of enantiomers were collected. Yield of first enantiomer: 51.4%; yield of

second enantiomer: 34.3%.

Preparative separation of compound CTB(H, C_2H):

About 10 mg of compound **CTB(H, C_2H)** dissolved in dichloromethane (7 mL) were separated by using Chiralpak IB (250 × 10 mm), hexane/ethanol/dichloromethane 70:10:20 v/v as mobile phase, at a flow-rate of 5 mL/min and a UV detection at 254 nm. Injections: 70 times 100 µL, every 3.0 minutes. 3.5 mg of the first eluted enantiomer with ee > 99.5%, 3.5 mg of the second eluted enantiomer with ee > 99.5% and 3.0 mg of the mixture of enantiomers were obtained. Yield of first enantiomer: 35%; yield of second enantiomer: 35%.

Preparative separation of compound C1:

About 46 mg of compound **C1** dissolved in 1.5 mL dichloromethane were separated by using Chiralpak IF (250 × 4.6 mm), hexane/ethanol/dichloromethane 20:40:40 v/v as mobile phase, at a flow-rate of 1 mL/min and a UV detection at 254 nm. Injections: 35 times 40 µL, every 8.0 minutes. Obtained 20.4 mg of first fraction (**FR1**, (−)-**C8** and (−)-**C1**) which was separated later; 2 mg of second fraction (**FR2**, (+)-**C8**, 4% yield); 12.4 mg of third fraction (**FR3**, (+)-**C1**, 27% yield) and 6.5 mg of intermediate.

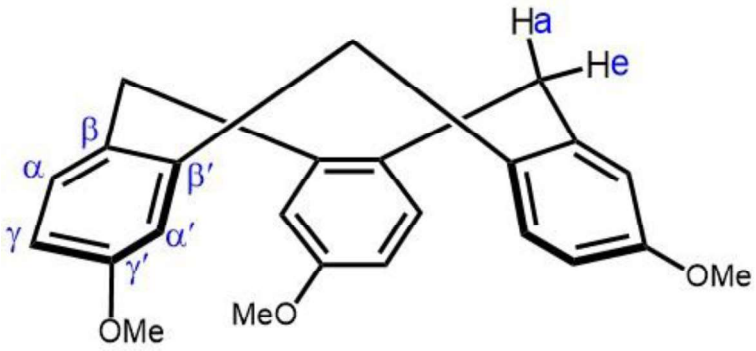
Then about 20 mg of compound **FR1** ((−)-**C8** and (−)-**C1**) dissolved in 0.75 mL of CH_2Cl_2 were separated by using (*S*,*S*)-Whelk-O1 (250 × 4.6 mm), hexane/ethanol/dichloromethane 40:30:30 v/v as mobile phase, at a flow-rate of 1 mL/min and a UV detection at 220 nm. Injections: 25 times 30 µL, every 10.0 minutes. 2.8 mg of first fraction (**FR1A**, (−)-**C8**, 6% yield) and 9.6 mg of second fraction (**FR1B**, (−)-**C1**, 21% yield) were obtained.

Preparative separation of compound C5:

About 4 mg of compound **C5** dissolved in a mixture of dichloromethane, ethanol and hexane (50:25:25 v/v; 1.2 mL) were separated by using Chiralpak IB (250 × 4.6 mm), hexane/ethanol/dichloromethane 40:40:20 v/v as mobile phase, at a flow-rate of 5 mL/min and a UV detection at 230 nm. Injections: 24 times 50 µL, every 10 minutes.

1.55 mg of the first eluted enantiomer, 1.4 mg of the second eluted enantiomer and 1 mg of the mixture of enantiomers were obtained. Yield of first enantiomer: 38.7%; yield of second enantiomer: 35%.

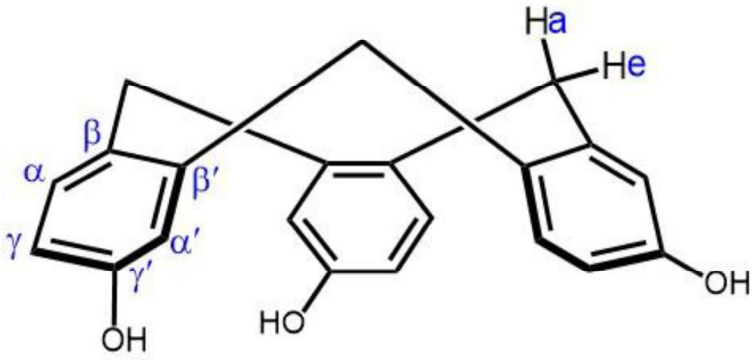
CTB(H,OMe)



A solution of 3-methoxybenzyl alcohol (21.1 g, 0.153 mol) in 60 mL CH_2Cl_2 was added into a suspension of phosphorus pentoxide P_2O_5 (11 g, 0.0775 mol, 0.5 equiv) in 30 mL CH_2Cl_2. The reaction mixture was warmed to reflux and the stirring stopped. After 4 hours, the solid product was separated from the liquid phase. It was washed with distilled water until neutrality of the aqueous phase, then the oily residue was extracted with CH_2Cl_2. The organic phases were combined, concentrated, and the residue purified by column chromatography on silica gel, using cyclohexane/dichloromethane (3:7) as eluent. Finally, crystallization from Et_2O, afforded the pure **CTB(H,OMe)** as a colorless solid (0.53 g, 2.9 % yield).

^{1}H NMR (400 MHz, $CDCl_3$, 298 K): δ = 7.278 (d, $^3J_{H,H}$ = 8.4 Hz, 3 H; α-H), 6.882 (d, 3 H, $^4J_{H,H}$ = 2.4 Hz, α'-H), 6.646 (dd $^3J_{H,H}$ = 8.4 Hz and $^4J_{H,H}$ = 2.4 Hz, 3 H; γ-H), 4.765 (d, $^2J_{H,H}$ = 14.0 Hz, 3 H; a-H), 3.739 (s, 9 H; OMe-H), 3.643 (d, $^2J_{H,H}$ = 14.0 Hz, 3 H; e-H) ppm, in agreement with literature data.[42]

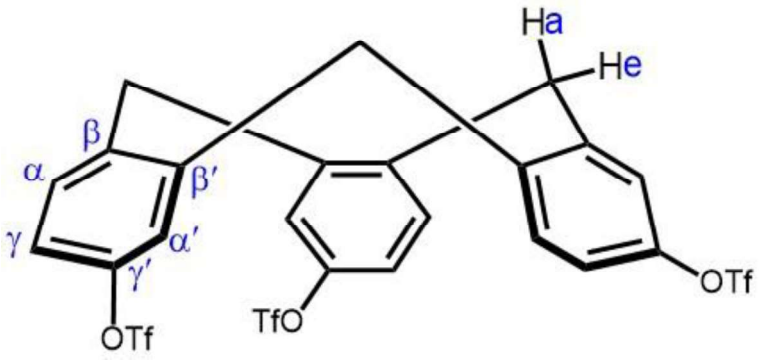
CTB(H,OH)



A solution of boron tribromide (0.79 mL, 8.3 mmol, 7.5 equiv) in 9 mL CH_2Cl_2 was slowly added to an ice-cooled solution of **CTB(H,OMe)** (0.4 g, 1.11 mmol) in 30 mL CH_2Cl_2. After completion of the addition, the reaction mixture was allowed to warm to room temperature and stirred overnight. Methanol was then added to quench the reaction until a clear solution was obtained. Evaporation of the solvent and washing with MeOH three times afforded an oil. The oily residue was not soluble in CH_2Cl_2, so the product was triturated into CH_2Cl_2 until it became a solid, which was then purified by column chromatography on silica gel, using cyclohexane / ethyl acetate (2:3) as eluent. **CTB(H,OH)** was obtained as a colorless solid (0.275 g, 78 % yield).

^{1}H NMR: (400 MHz, acetone-d6, 298 K): δ = 7.946 (s, 3 H; OH-H), 7.215 (d, $^3J_{H,H}$ = 8.4 Hz, 3 H; α-H), 6.886 (d, 3 H, $^4J_{H,H}$ = 2.4 Hz, α'-H), 6.561 (dd $^3J_{H,H}$ = 8.4 Hz and $^4J_{H,H}$ = 2.4 Hz, 3 H; γ-H), 4.779 (d, $^2J_{H,H}$ = 14.0 Hz, 3 H; a-H), 3.553 (s, 9 H; OMe-H), 3.643 (d, $^2J_{H,H}$ = 14.0 Hz, 3 H; e-H) ppm, in agreement with literature data.[42]

CTB(H,OTf)



A solution of triflic anhydride $(CF_3SO_2)_2O$ (1.34 g, 4.75 mmol, 3.8 equiv) in 20 mL CH_2Cl_2 was slowly added to an ice-cooled solution of **CTB(H,OH)** (0.395 g, 1.24 mmol) in a mixture of 20 mL pyridine and 20 mL CH_2Cl_2. After addition, the reaction mixture was allowed to warm to room temperature and stirred overnight. Water was then added, and the mixture was extracted three times with CH_2Cl_2. The combined organic layers were dried with anhydrous magnesium sulfate. Filtration and evaporation of the solvent afforded a residue, which was purified by column chromatography on silica gel, using cyclohexane / ethyl acetate (3:2) as eluent, to give a solid powder of **CTB(H,OTf)** (0.67 g, 76 % yield).

^{1}H NMR (400 MHz, $CDCl_3$, 298 K): δ = 7.429 (d, $^3J_{H,H}$ = 8.4 Hz, 3 H; α-H), 7.258 (d, 3 H, $^4J_{H,H}$ = 2.4 Hz, α'-H), 7.090 (dd $^3J_{H,H}$ = 8.4 Hz and $^4J_{H,H}$ = 2.4 Hz, 3 H; γ-H), 4.862 (d, $^2J_{H,H}$ = 13.6 Hz, 3 H; a-H), 3.821 (d, $^2J_{H,H}$ = 13.6 Hz, 3 H; e-H) ppm, in agreement with literature data.[116]

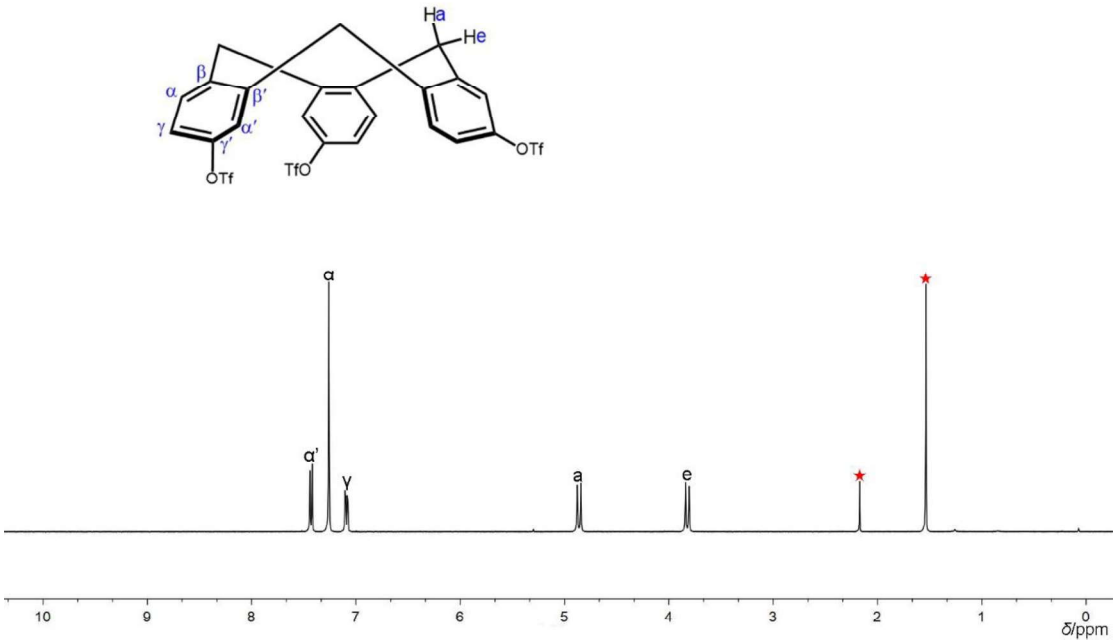
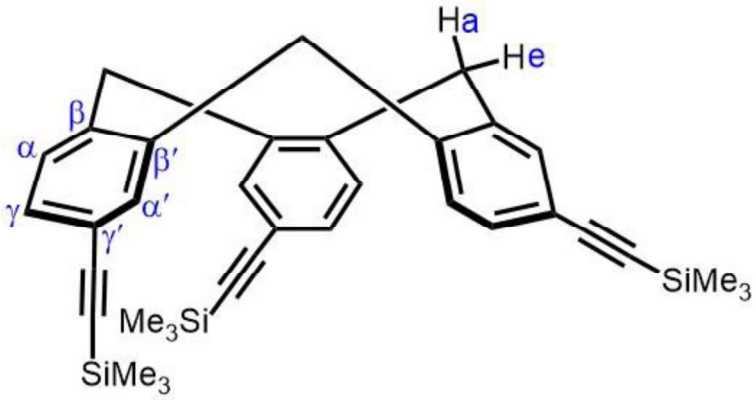


Figure 1. ^{1}H NMR spectrum of compound **CTB(H,OTf)**

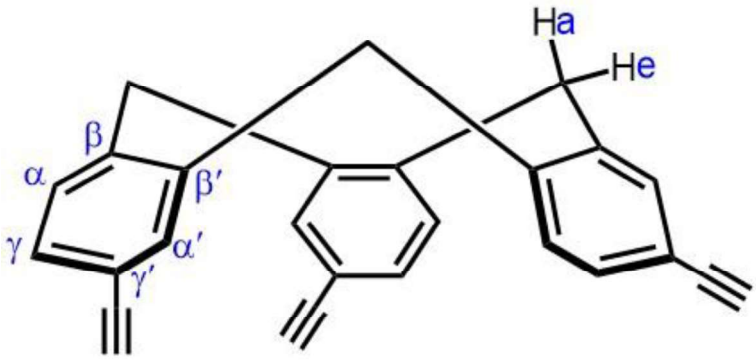
CTB(H,C$_2$TMS)



CTB(H,OTf) (0.36 g, 0.504 mmol) and $PdCl_2(PPh_3)_2$ (0.07 g, 0.10 mmol, 0.2 equiv) were dissolved in 30 mL of dimethylformamide, (trimethylsilyl) acetylene (0.045 g, 0.65 mL, 4.5 mmol, 9 equiv) and dried triethylamine 1.5 mL were added, and the solution was heated to 70 °C. After overnight stirring, the solution was cooled to room temperature, the solvent was evaporated to dryness and the residue dried under vacuum to give a dark brown solid, which was purified by column chromatography on silica gel, using cyclohexane / dichloromethane (7:2) as eluent, to give a yellow solid powder of **CTB(H,C$_2$TMS)** (0.197 g, 70% yield)

^{1}H NMR (400 MHz, $CDCl_3$, 298 K): δ = 7.429 (d, $^4J_{H,H}$ = 1.6 Hz, 3 H; α'-H), 7.322 (d, 3 H, $^3J_{H,H}$ = 8.0 Hz, α-H), 7.222 (dd $^3J_{H,H}$ = 8.0 Hz and $^4J_{H,H}$ = 1.6 Hz, 3 H; γ-H), 4.773 (d, $^2J_{H,H}$ = 13.6 Hz, 3 H; a-H), 3.676 (d, $^2J_{H,H}$ = 13.6 Hz, 3 H; e-H), 0.234 (s, 3 H; $SiMe_3$-H) ppm.

CTB(H,C$_2$H)



The intermediate **CTB(H,C$_2$TMS)** (0.197 g, 0.358 mmol) was dissolved in 10 mL of THF. Tetrabutylammonium fluoride (4.0 mL of a 1 M solution in THF, 4.0 mmol, 11 equiv) was added, and the solution was allowed to react at room temperature overnight. The THF was evaporated under vacuum, and distilled water (50 mL) was added. The resulting mixture was extracted three times (120 mL) with dichloromethane. The organic phases were washed with water, dried with anhydrous magnesium sulfate, and concentrated by rotary evaporation to give a brown yellow solid, which was purified by column chromatography on silica gel, using cyclohexane / dichloromethane (7:2) as eluent, to give a yellowish solid powder of **CTB(H,C$_2$H)** (0.1 g, 83.2% yield).

mp: 218.9 °C.

^{1}H NMR (400 MHz, $CDCl_3$, 298 K): δ = 7.484 (d, $^4J_{H,H}$ = 1.6 Hz, 3 H; α'-H), 7.338 (d, 3 H, $^3J_{H,H}$ = 8.0 Hz, α-H), 7.248 (dd $^3J_{H,H}$ = 8.0 Hz and $^4J_{H,H}$ = 1.6 Hz, 3 H; γ-H), 4.815 (d, $^2J_{H,H}$ = 13.6 Hz, 3 H; a-H), 3.717 (d, $^2J_{H,H}$ = 13.6 Hz, 3 H; e-H), 3.020 (s, 3 H; C_2H-H) ppm.

^{13}C NMR (125 MHz, $CDCl_3$, 298 K): δ = 140.0 (β-C), 139.1 (β'-C), 133.9 (α'-C), 131.1 (γ-C), 130.4 (α-C), 121.1 (γ'-C), 83.5 (C≡C), 36.9 (CH_2) ppm.

Elemental analysis: $C_{27}H_{18}$·2/3H_2O, C 91.49, H 5.50, found, C 91.48, H 5.41.

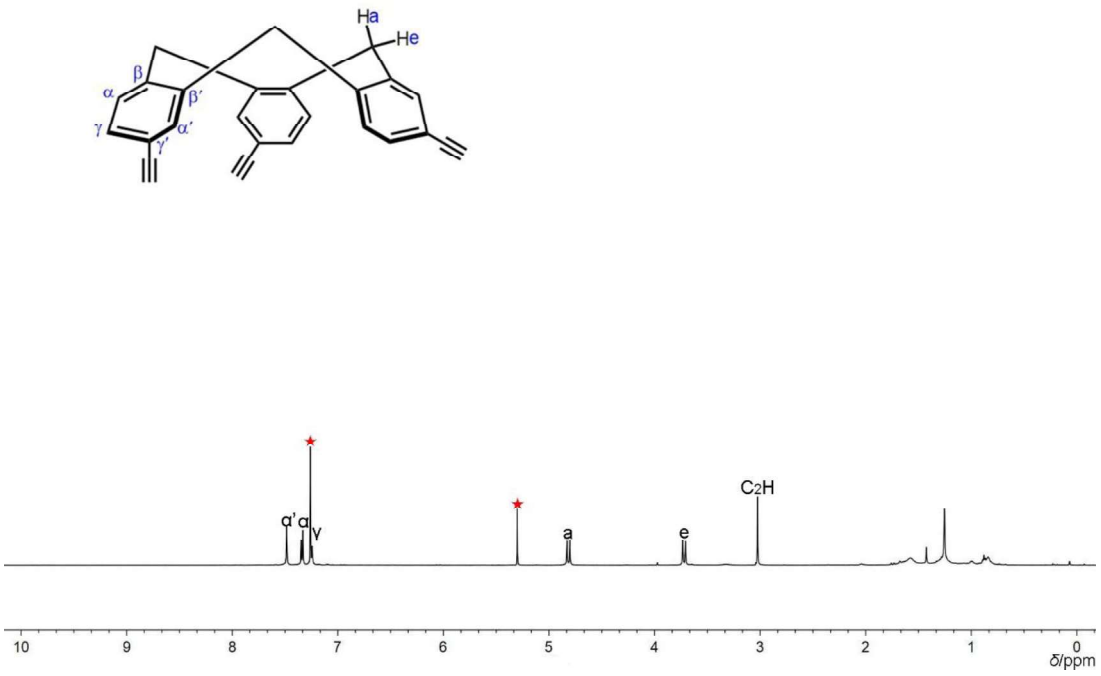
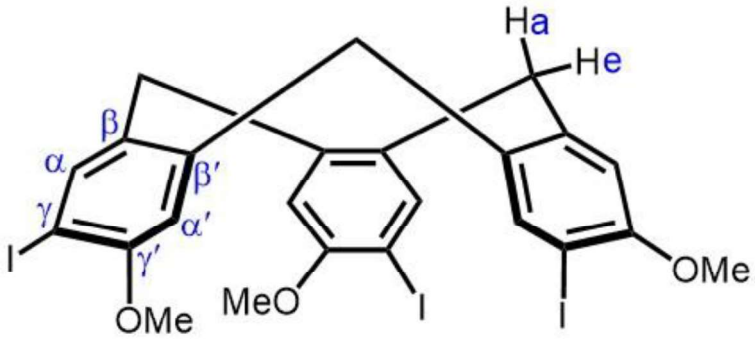


Figure 2. ^{1}H NMR spectrum of compound **CTB(H,C$_2$H)**

CTB(OMe,I)



3-Hydroxybenzoic acid (20.8 g, 0.15 mol) was dissolved in 2 M NaOH (0.4 mol, 200 mL, 2.67 equiv) and a solution of iodine (35.1 g, 0.138 mol, 0.92 equiv) and of KI (27.5 g, 0.165 mol, 1.1 equiv) in H_2O (150 mL) was added dropwise. Stirring was continued for 20 min, concentrated 12 M HCl was added gradually until the pH of solution was 1 and, with the addition of HCl, more and more solid appeared. Then the precipitate was filtered off and rinsed with water, finally, re-crystallized from EtOH–H_2O (1:5) and dried under vacuum to afford 3-hydroxy-4-iodobenzoic acid (14 g, 35% Yield).

3-Hydroxy-4-iodobenzoic acid (9 g, 0.034 mol) was dissolved in 400 mL acetone and potassium carbonate (19.4 g, 0.137 mol) was added. The reaction mixture became white and cloudy. 12 mL of iodomethane were added slowly and the reaction mixture was warmed to 35°C with overnight stirring. Then, acetone was evaporated by rotary evaporation. The crude product was dissolved in CH_2Cl_2 and washed with distilled water until neutrality of the aqueous phase. The organic phase was dried with anhydrous magnesium sulfate and concentrated by rotary evaporation, then dried under vacuum. The 4-iodo-3-methoxybenzoic acid methyl ester was obtained as a yellowish solid (8.43 g, 93.5% Yield).

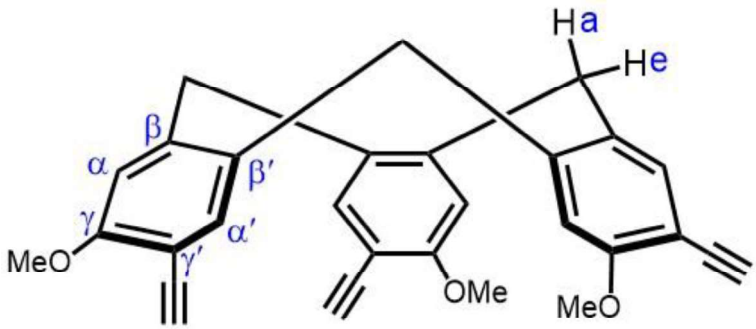
The 4-iodo-3-methoxybenzoic acid methyl ester (5 g, 0.017 mol) was dissolved in 83 mL of tetrahydrofuran. The mixture was cooled to –78 °C, 70 mL diisobutylaluminium hydride (Dibal-H) was transferred into a dropping funnel and added dropwise. The mixture was stirred at room temperature overnight and then quenched at 0 °C by addition of 1 M HCl solution until the pH of the solution was 6. The product was

extracted with dichloromethane (200 mL × 3). All the combined organic phases were washed with distilled water until neutrality of the aqueous phase and then anhydrous magnesium sulfate was added. After filtration and concentration under vacuum, the 4-iodo-3-methoxybenzyl alcohol was obtained as a bright-yellow oil (4.4 g, 97.5% Yield).

A solution of 4-iodo-3- methoxybenzyl alcohol (4.4 g, 0.17 mol) in 50 mL diethyl ether was added into a suspension of phosphorus pentoxide P_2O_5 (11 g, 0.77 mol, 4.5 equiv) in 180 mL of diethyl ether. The reaction mixture was heated to reflux then stirring was stopped. After 3 days, the diethyl ether was evaporated. The crude product was filtered and washed with distilled water until neutrality of the aqueous phase. The obtained crude product was purified by trituration in dichloromethane to give **CTB (OMe, I)** as a white solid (3.49 g, 45% Yield).

^{1}H NMR (400 MHz, $CDCl_3$, 298 K): δ = 7.723 (s, 3 H; α'-H), 6.738 (s, 3 H; α-H), 4.652 (d, $^2J_{H,H}$ = 13.6 Hz, 3 H; a-H), 3.863 (s, 9 H; OCH_3-H), 3.582 (d, $^2J_{H,H}$ = 13.6 Hz, 3 H; e-H) ppm in agreement with literature data.[31]

CTB(OMe,C$_2$H)



CTB(OMe,I) (0.2 g, 0.271 mmol), copper iodide (0.010 g, 0.054, 0.2 equiv) and $PdCl_2(PPh_3)_2$ (0.038 g, 0.054 mmol, 0.2 equiv) were dissolved in 7 mL of dimethylformamide. (Trimethylsilyl) acetylene (0.069 g, 1.0 mL, 6.9 mmol, 25 equiv) and dried triethylamine 1.0 mL were added, and the solution was heated to 40 °C. After overnight stirring the solution was cooled to room temperature, the solvent was evaporated under vacuum and the solid residue dried under vacuum to give dark brown solid. This compound was used directly in the next step without purification.

The crude intermediate **CTB(OMe,C$_2$TMS)** (0.28 g) was dissolved in 30 mL of THF. Tetrabutylammonium fluoride (4.0 mL of a 1 M solution in THF, 4.0 mmol) was added, and the solution was allowed to react at room temperature for 4h. The THF was evaporated under vacuum, and distilled water (50 mL) was added. The resulting mixture was extracted three times (120 mL) with dichloromethane. The organic phases were washed with water, dried with anhydrous magnesium sulfate, and concentrated under vacuum to give a brown yellow solid, which was purified by column chromatography on silica gel, using dichloromethane as eluent, to give a light brown solid powder of **CTB(OMe,C$_2$H)** (0.052 g, 44 % yield).

^{1}H NMR (400 MHz, $CDCl_3$, 298 K): δ = 7.424 (s, 3 H; α'-H), 6.836 (s, 3 H; α-H), 4.720 (d, $^2J_{H,H}$ = 13.6 Hz, 3 H; a-H), 3.896 (s, 9 H; OCH_3-H), 3.546 (d, $^2J_{H,H}$ = 13.6 Hz, 3 H; e-H), 3.242 (s, 3 H; C_2H-H) ppm, in agreement with literature data.[118]

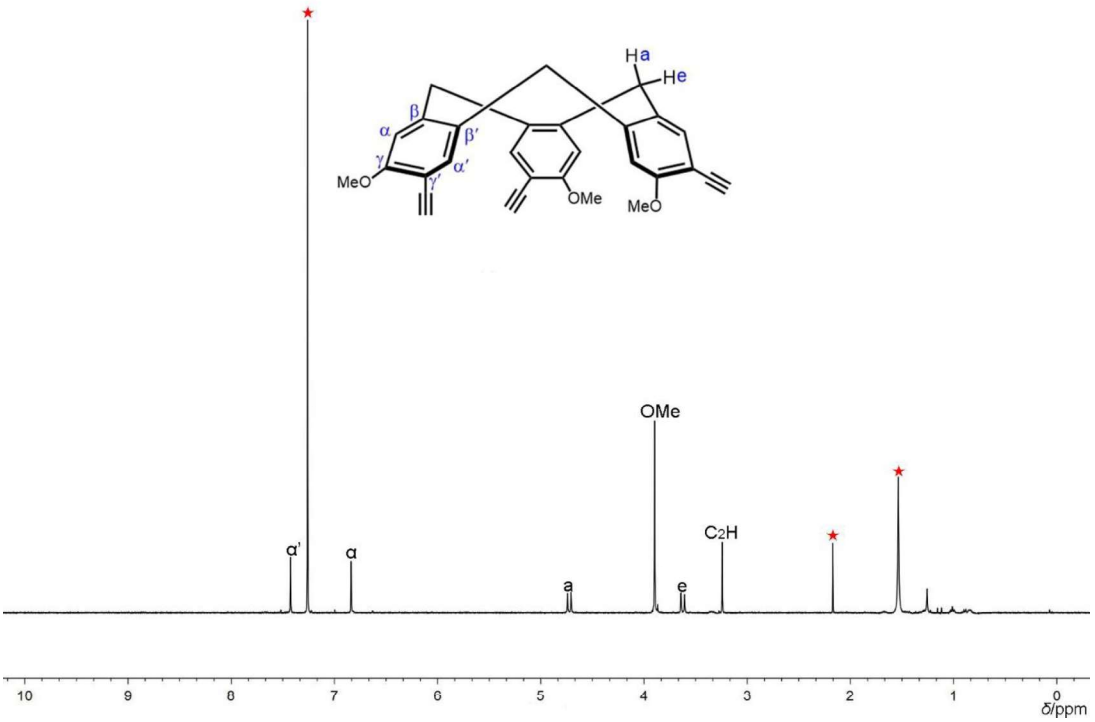


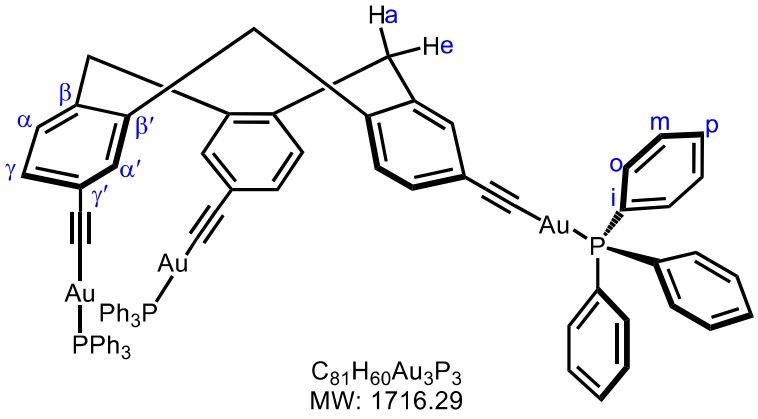
Figure 3. ^{1}H NMR spectrum of compound **CTB(OMe,C_2H)**

CTB(R,C_2AuPR'$_3$)

CTB(H,C_2Au)$_n$: A solution of sodium acetate (0.0753 g, 0.918 mmol) in a mixture of THF (0.5 mL) and methanol (3 mL) was added to a solution of **CTB(H,C_2H)** (0.0349 g, 0.102 mmol) and [AuCl(SMe_2)] (0.090 g, 0.306 mmol, 3 equiv) in a mixture of THF (12 mL) and methanol (3 mL). The resulting reaction mixture was stirred overnight at room temperature to produce a black green precipitate. The solid was collected by filtration, washed with THF, methanol, water, methanol again, and diethylether, and dried. It was used for the next steps without further purification.

CTB(H,C_2AuPPh$_3$) C1

((10,15-dihydro-5*H*-tribenzo[a,d,g]cyclononenyl) 2,7,12-triethynyl)(triphenyl-phosphaneyl)gold(I)



CTB(H,C_2AuPPh$_3$): Method A. **CTB(H,C_2H)** (0.01 g, 0.0292 mmol), [AuCl(PPh_3)] (0.058 g, 0.117 mmol, 4 equiv), and sodium methoxide (0.024 g, 0.438 mmol, 15 equiv) were mixed in methanol/THF (1:1, v/v, 10 mL) at 40 °C. After stirring of the reaction mixture for 3 days, the solvents were removed by rotary evaporation. The residue was taken into dichloromethane, then filtered to remove NaCl and the excess of sodium methoxide, which afforded a clear yellow solution. The latter was concentrated to a volume of about 1 mL, and treated by dropwise addition of cyclohexane (1.5 mL) until precipitation of the product. The precipitate was stored at 0 °C overnight, filtered, and dried under vacuum, affording a yellow solid powder. Yield: 0.030 g, 60%.

Method B. A solution of PPh_3 (0.0321 g, 0.122 mmol, 3 equiv) in THF (1.5 mL) was added to a suspension of **CTB(H,C_2Au)$_n$** (0.038 mg, 0.041 mmol) in dichloromethane (4 mL) and the reaction mixture stirred overnight. It was subsequently filtered by using a sintered glass funnel (porosity 4) to give a clear light yellow solution, which was evaporated to dryness. The solid residue was washed with methanol, affording a light yellow crystalline solid. Yield: 0.055 g, 78%.

mp: 198 °C.

^{1}H NMR (500 MHz, $CDCl_3$, 298 K): δ = 7.508 (d, $^4J_{H,H}$ = 1.5 Hz, 3 H; α'-H), 7.258 (d, 3 H, $^3J_{H,H}$ = 8.0 Hz, α-H), 7.207 (dd $^3J_{H,H}$ = 8.0 Hz and $^4J_{H,H}$ = 1.5 Hz, 3 H; γ-H), 4.750 (d, $^2J_{H,H}$ = 13.2 Hz, 3 H; a-H), 3.633 (d, $^2J_{H,H}$ = 13.2 Hz, 3 H; e-H) ppm.

^{13}C NMR (125 MHz, $CDCl_3$, 298 K): δ = 138.8 (β'-C), 138.1 (β-C), 134.5 (*o*-C), 134.2 (α'-C), 131.6 (*p*-C), 131.1 (γ-C), 130.3 (α-C), 129.7 (*i*-C), 129.3 (*m*-C), 123.4 (γ'-C), 104.5 and 104.3 (C≡C), 37.1 (CH_2) ppm.

^{31}P NMR (162 MHz, $CDCl_3$, 298 K) δ = 42.97 ppm.

Elemental analysis: Calcd for calcd for $C_{81}H_{60}Au_3P_3 \cdot 2CH_2Cl_2$, C 52.83, H 3.42, found, C 52.47, H 3.46.

ESI-MS: Calcd. for $C_{81}H_{60}Au_3P_3$, 1716.29; found 1717.28 $[M + H]^+$

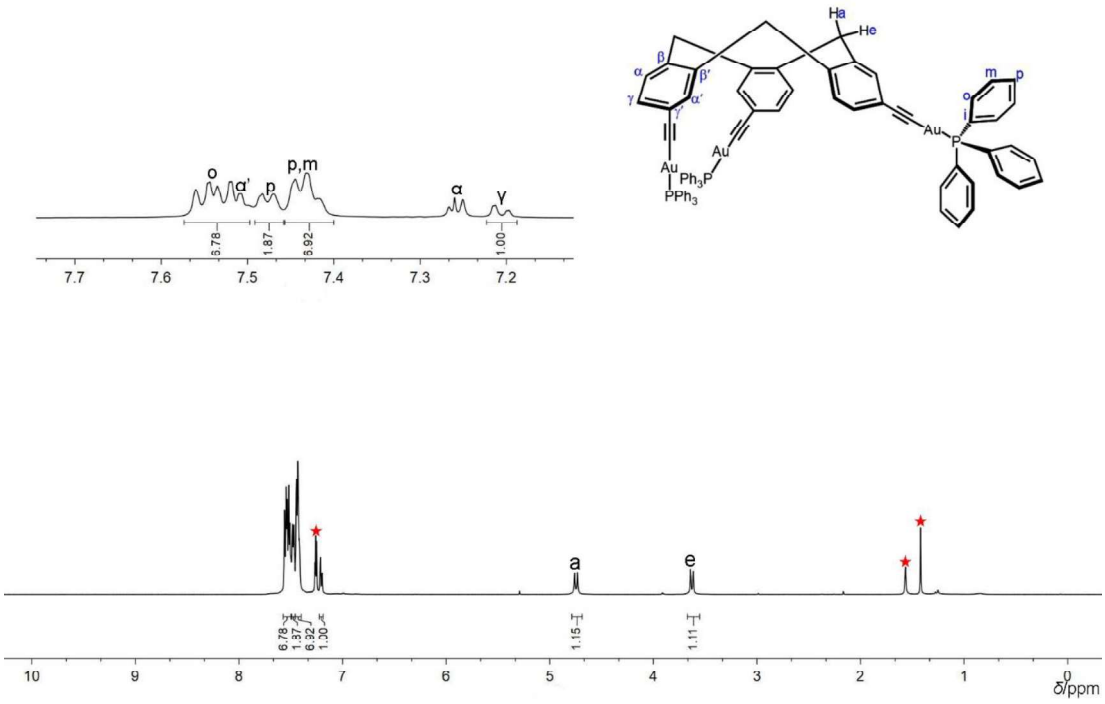
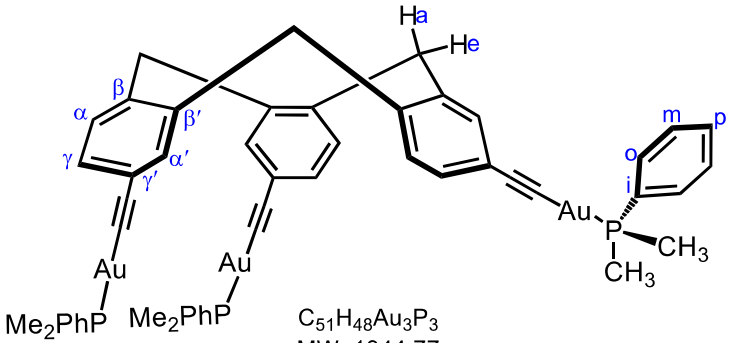


Figure 4. ^{1}H NMR spectrum of compound **CTB(H,C$_2$AuPPh$_3$) C1**

CTB(H,C_2AuPPh_2Me) C2

((10,15-dihydro-5*H*-tribenzo[a,d,g]cyclononenyl)2,7,12-triethynyl)(methyldiphenyl-phosphaneyl)gold(I)



$C_{51}H_{48}Au_3P_3$
MW: 1344.77

CTB(H,C_2AuPPh_2Me): Method A. **CTB(H,C_2H)** (0.01 g, 0.0292 mmol), [AuCl(PPh_2Me)] (0.050 g, 0.117 mmol, 4 equiv), and sodium methoxide (0.024 g, 0.438 mmol, 15 equiv) were mixed in methanol/THF (1:1, v/v, 10 mL) at 40 °C. After stirring of the reaction mixture for 3 days, the solvents were removed by rotary evaporation. The residue was taken into dichloromethane, then filtered to remove NaCl and the excess of sodium methoxide, which afforded a clear yellow solution. The latter was concentrated to a volume of about 1 mL, and treated by dropwise addition of cyclohexane (1.5 mL) until precipitation of the product. The precipitate was stored at 0 °C overnight, filtered, and dried under vacuum, affording a yellow powder. Yield: 0.019 g, 43%.

Method B. A solution of PPh_2Me (0.017 g, 0.084 mmol, 3 equiv) in THF (1.0 mL) was added to a suspension of **CTB(H,C_2Au)$_n$** (0.026 g, 0.028 mmol) in dichloromethane (3 mL) and the reaction mixture stirred overnight. It was subsequently filtered by using a sintered glass funnel (porosity 4) to give a light yellow clear solution, which was evaporated to dryness. The solid residue was washed with methanol, affording a light yellow crystalline solid. Yield: 0.036 g, 80%.

mp: 195 °C.

^{1}H NMR (500 MHz, $CDCl_3$, 298 K): δ = 7.490 (d, $^4J_{H,H}$ = 1.5 Hz, 3 H; α'-H), 7.249 (d,

3 H, $^{3}J_{H,H}$ = 8.5 Hz, α-H), 7.186 (dd $^{3}J_{H,H}$ = 8.5 Hz and $^{4}J_{H,H}$ = 1.5 Hz, 3 H; γ-H), 4.743 (d, $^{2}J_{H,H}$ = 13.5 Hz, 3 H; a-H), 3.625 (d, $^{2}J_{H,H}$ = 13.5 Hz, 3 H; e-H), 2.053 (d, $^{2}J_{H,P}$ = 9.0 Hz, 3 H; CH_3-H) ppm.

^{13}C NMR (125 MHz, $CDCl_3$, 298 K): δ = 138.8 (β'-C), 138.1 (β-C), 134.1 (α'-C), 133.0 (*o*-C), 131.9 (*i*-C), 131.6 (*p*-C), 131.0 (γ-C), 130.2 (α-C), 129.3 (*m*-C), 123.4 (γ'-C), 104.7 and 104.5 (C≡C), 37.1 (CH_2), 14.2($^{1}J_{C,P}$ = 35.0 Hz, CH_3) ppm.

^{31}P NMR (162 MHz, $CDCl_3$, 298 K): δ = 27.21 ppm.

Elemental analysis: Calcd for $C_{66}H_{54}Au_3P_3 \cdot 0.5H_2O$, C 51.48, H 3.60, found, C 51.45, H 3.66.

ESI-MS: Calcd. for $C_{66}H_{54}Au_3P_3$, 1530.24; found 1531.24 $[M + H]^+$.

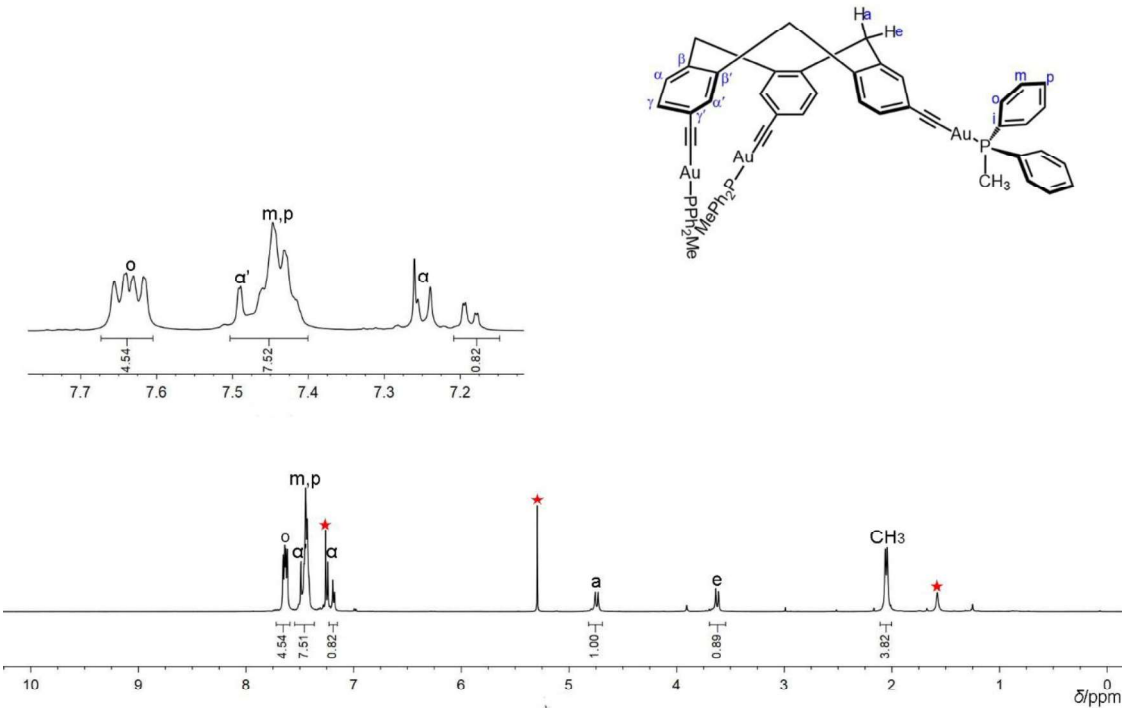
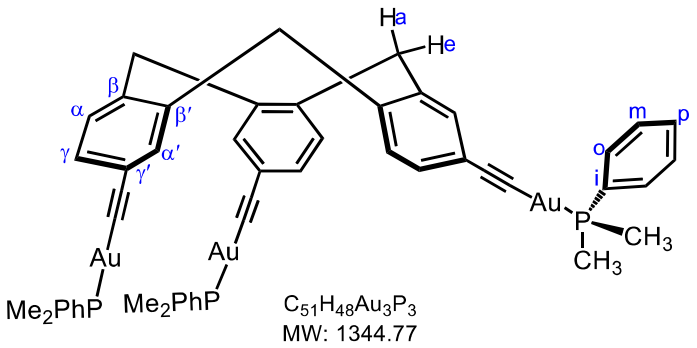


Figure 5. ^{1}H NMR spectrum of compound **CTB(H,C_2AuPPh_2Me) C2**

CTB(H,C_2AuPPhMe$_2$) C3

((10,15-dihydro-5*H*-tribenzo[a,d,g]cyclononenyl)2,7,12-triethynyl)(dimethylphenyl-phosphaneyl)gold(I)



CTB(H,C_2AuPPhMe$_2$): Method A. Not used, as AuCl(PPhMe$_2$) could not be made.

Method B. A solution of PPhMe$_2$ (0.013 g, 0.097 mmol, 3 equiv) in THF (1.0 mL) was added to a suspension of **CTB(H,C_2Au)$_n$** (0.030 g, 0.032 mmol) in dichloromethane (3 mL) and the reaction mixture stirred overnight. It was subsequently filtered by using a sintered glass funnel (porosity 4) to give a light yellow clear solution, which was evaporated to dryness. The solid residue was washed with methanol, affording a light yellow crystalline solid. Yield: 0.023 g, 53%.

mp: 187.5 °C.

^{1}H NMR (500 MHz, $CDCl_3$, 298 K): δ = 7.481 (d, $^4J_{H,H}$ = 1.5 Hz, 3 H; α'-H), 7.244 (d, 3 H, $^3J_{H,H}$ = 8.0 Hz, α-H), 7.177 (dd $^3J_{H,H}$ = 8.0 Hz and $^4J_{H,H}$ = 1.5 Hz, 3 H; γ-H), 4.742 (d, $^2J_{H,H}$ = 13.3 Hz, 3 H; a-H), 3.623 (d, $^2J_{H,H}$ = 13.3 Hz, 3 H; e-H), 1.747 (d, $^2J_{H,P}$ = 9.5 Hz, 6 H; CH_3-H) ppm.

^{13}C NMR (125 MHz, $CDCl_3$, 298 K): δ = 138.8 (β'-C), 138.1 (β-C), 134.2 (α'-C), 132.8 (*i*-C), 132.1 (*o*-C), 131.7 (*p*-C), 131.0 (γ-C), 130.2 (α-C), 129.3 (*m*-C), 123.5 (γ'-C), 104.9 and 104.6 (C≡C), 37.0 (CH_2), 15.7 ($^1J_{C,P}$ = 35.0 Hz, CH_3) ppm.

^{31}P NMR (162 MHz, $CDCl_3$, 298 K) δ = 14.24 ppm.

Elemental analysis: Calcd for $C_{51}H_{48}Au_3P_3 \cdot 0.5H_2O$, C 45.25, H 3.65, found, C 45.23,

H 3.74.

ESI-MS: Calcd. for $C_{51}H_{48}Au_3P_3$, 1344.20; found 1345.20 $[M + H]^+$.

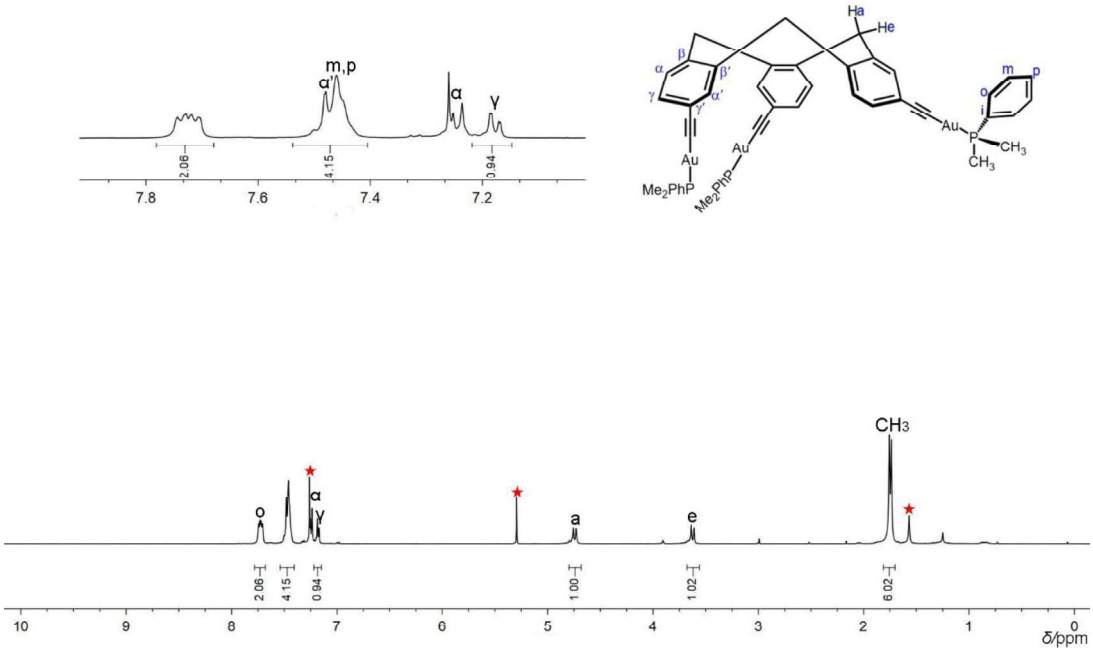
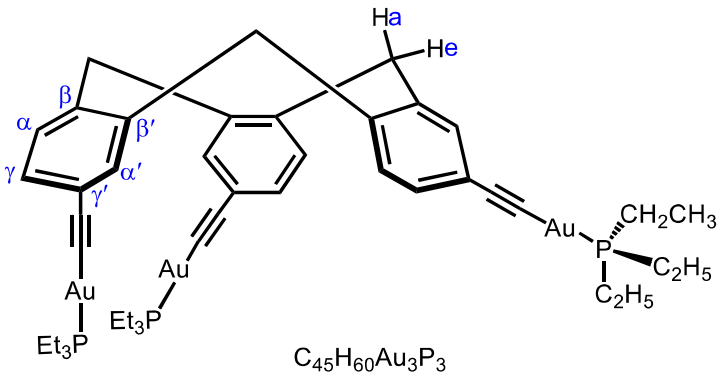


Figure 6. ^{1}H NMR spectrum of compound **CTB(H,C_2AuPPhMe_2) C3**

CTB(H,C_2AuPEt$_3$) C7

(10,15-dihydro-5*H*-tribenzo[a,d,g]cyclononenyl) 2,7,12-triethynyl)(triethyl-phosphaneyl)gold(I)



$C_{45}H_{60}Au_3P_3$
MW: 1284.80

CTB(H,C_2AuPEt$_3$): Method A. **CTB(H,C_2H)** (0.02 g, 0.0585 mmol), [AuCl(PEt$_3$)] (0.063 g, 0.181 mmol, 3.1 equiv), and sodium methoxide (0.047 g, 0.877 mmol, 15 equiv) were mixed in methanol/THF (1:1, v/v, 16 mL) at 40 °C. After stirring of the reaction mixture for 4 days, the solvents were removed by rotary evaporation. The residue was taken into dichloromethane, then filtered to remove NaCl and the excess of sodium methoxide, which afforded a clear yellow solution. The latter was concentrated (about 1 mL CH_2Cl_2) and treated by dropwise addition of cyclohexane (about 1.5 mL) until precipitation of the product. The precipitate was filtered and dried under vacuum, affording a yellow solid powder. Yield: 0.050 g, 68%.

^{1}H NMR (500 MHz, $CDCl_3$, 298 K): δ = 7.460 (d, $^4J_{H,H}$ = 1.4 Hz, 3 H; α'-H), 7.215 (d, 3 H, $^3J_{H,H}$ = 8.0 Hz, α-H), 7.163 (dd $^3J_{H,H}$ = 8.0 Hz and $^4J_{H,H}$ = 1.4 Hz, 3 H; γ-H), 4.716 (d, $^2J_{H,H}$ = 13.3 Hz, 3 H; a-H), 3.594 (d, $^2J_{H,H}$ = 13.3 Hz, 3 H; e-H), 1.775 (quint, 18 H; CH_2-H), 1.176 (2t, 27 H; CH_3-H) ppm.

^{13}C NMR (125 MHz, $CDCl_3$, 298 K): δ = 138.8 (β'-C), 138.0 (β-C), 134.1 (α'-C), 130.9 (γ-C), 130.2 (α-C), 123.5 (γ'-C), 104.3 and 104.1 (C≡C), 37.0 (CH_2), 18.1 and 17.9 ($^1J_{C,P}$ = 35.0 Hz, CH_2CH_3), 9.0 (CH_2CH_3) ppm.

^{31}P NMR (162 MHz, $CDCl_3$, 298 K) δ = 38.50 ppm.

Elemental analysis: calcd for $C_{45}H_{61}Au_3P_3 \cdot 4/3C_6H_{12}$, C 45.57, H 5.48, found, C 45.61, H 5.43.

ESI-MS: Calcd. for $C_{51}H_{48}Au_3P_3$, 1284.29; found 1285.14 $[M + H]^+$.

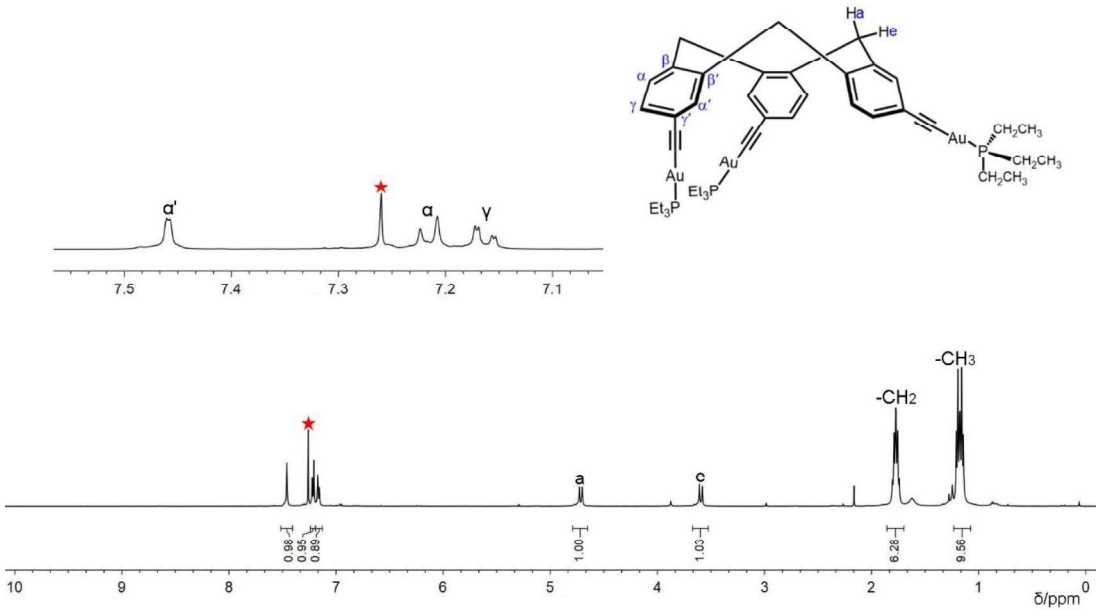
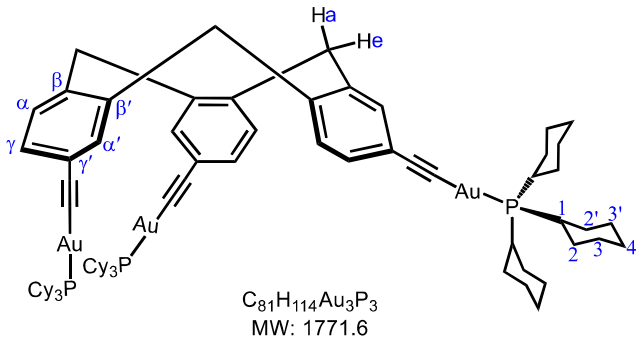


Figure 7. ^{1}H NMR spectrum of compound **CTB(H,C_2AuPEt_3) C7**

CTB(H,C_2AuPCy$_3$) C9

((10,15-dihydro-5*H*-tribenzo[a,d,g]cyclononenyl) 2,7,12-triethynyl)(tricyclohexyl-phosphaneyl)gold(I)



CTB(H,C_2AuPCy$_3$): PCy_3·HBF_4 (0.15 g, 0.407 mmol) was dissolved in 5 mL of MeOH. Et_3N (0.12 g, 3 equiv, 0.17 mL) was added dropwise slowly at −50 - −30 °C. After completion of the addition, the reaction mixture was heated until it became a solution, then the solution was cooled down and a white precipitate appeared. The solid was filtered with exclusion of O_2 and H_2O and the product dried under vacuum, which provided PCy_3.

(Cy_3P)AuCl: To a solution of Au(SMe_2)Cl (0.034 mg, 0.116 mmol) dissolved in CH_2Cl_2(5 mL), PCy_3 (0.032 mg, 0.114 mmol, 1 equiv) was added. The clear solution was stirred at room temperature overnight. The solution was concentrated, then the product was precipitated and washed with MeOH. Yield: 30 mg (55.0%).

CTB(H,C_2H) (0.008 g, 0.0234 mmol), [AuCl(PCy_3)] (0.042 g, 0.082 mmol, 3.5 equiv), and sodium methoxide (0.019 g, 0.351 mmol, 15 equiv) were mixed in methanol/THF (1:1, v/v, 10 mL) at 40 °C. After stirring the reaction mixture for 1 day, the solvents were removed by rotary evaporation. The residue was taken into dichloromethane, then filtered to remove NaCl and the excess of sodium methoxide, which afforded a clear yellow solution. The latter was concentrated to a volume of about 1 mL, and treated by dropwise addition of MeOH (1.5 mL) until precipitation of the product. The precipitate was stored at 0 °C overnight, filtered, and dried under vacuum, affording a yellow solid powder. Yield: 0.030 g, 72%.

^{1}H NMR (500 MHz, $CDCl_3$, 298 K): δ = 7.473 (d, $^{3}J_{H,H}$ = 1.0 Hz, 3 H; α'-H), 7.195 (AB, $^{3}J_{AB}$ = 8.0 Hz, $\Delta\nu$ = 11.2 Hz, $^{4}J_{H,H}$ = 1.5 Hz, 6 H; α-H, γ-H), 4.704 (d, $^{2}J_{H,H}$ = 13.0 Hz, 3 H; a-H), 3.584 (d, $^{2}J_{H,H}$ = 13.0 Hz, 3 H; e-H), 1.982 (m, 27 H; 1-H, 3,3'-H), 1.840 (br s, 18 H; 2,2'-H), 1.716 (br s, 9 H; 4-H), 1.466 (br s, 18 H; 3,3'-H), 1.257 (br m, 27 H; 4 H, 2,2'-H) ppm.

^{13}C NMR (125 MHz, $CDCl_3$, 298 K): δ = 138.7 (β'-C), 137.9 (β-C), 134.2 (α'-C), 131.0 (γ-C), 130.2 (α-C), 123.6 (γ'-C), 103.9 and 103.7 (C≡C), 37.1 (CH_2), 33.3 (1-C), 30.8 (3,3'-C), 27.3 (2,2'-C), 26.0 (4-C) ppm.

^{31}P NMR (162 MHz, $CDCl_3$, 298 K) δ = 56.77 ppm.

Elemental analysis: calcd for $C_{81}H_{114}Au_3P_3{\cdot}2CH_2Cl_2$, C 51.35, H 6.13, found, C 51.41, H 6.18

ESI-MS: Calcd. for $C_{81}H_{114}Au_3P_3$, 1770.71; found 1771.72 $[M + H]^+$.

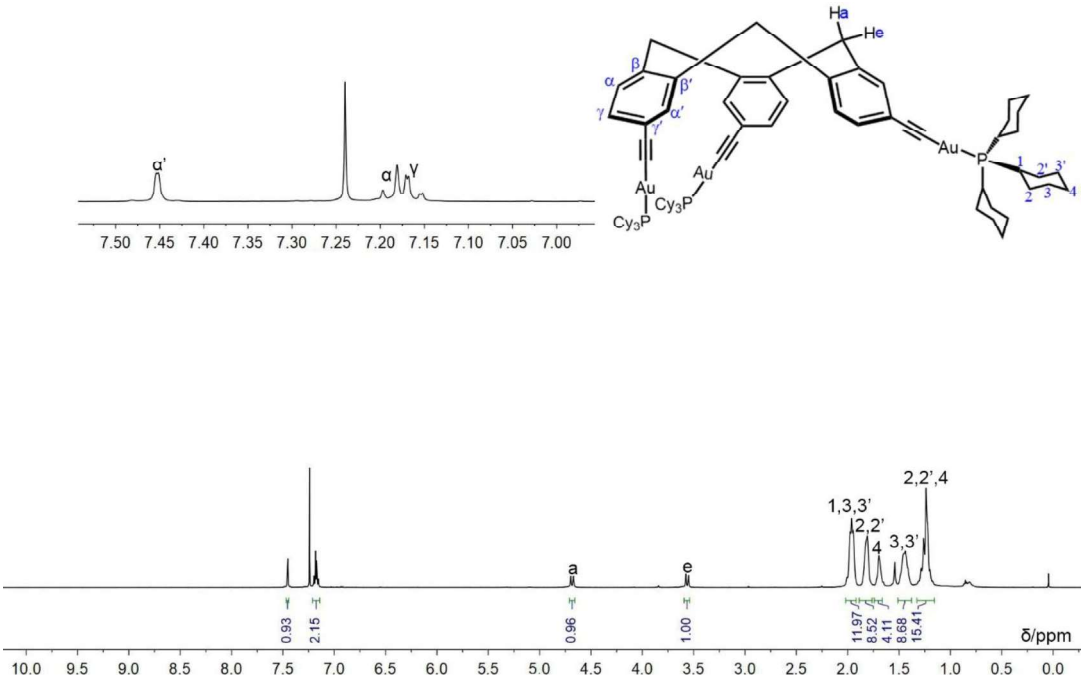
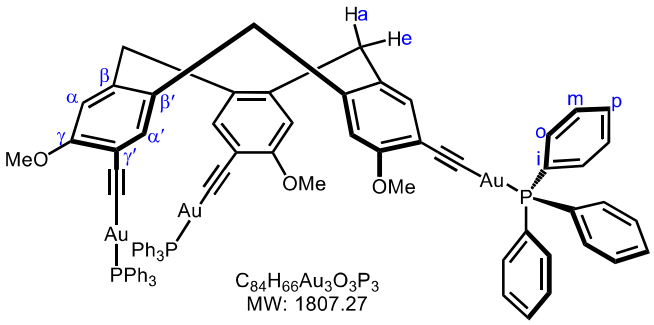


Figure 8. ^{1}H NMR spectrum of compound **CTB(H,C_2AuPCy_3) C9**

CTB(OMe,C_2Au)$_n$: A solution of sodium acetate (0.038 g, 0.468 mmol) in a mixture of THF (0.5 mL) and methanol (3 mL) was added to a solution of **CTB(OMe,C_2H)** (0.023 g, 0.052 mmol) and [AuCl(SMe_2)] (0.046 g, 0.156 mmol, 3 equiv) in a mixture of THF (12 mL) and methanol (3 mL). The resulting reaction mixture was stirred overnight at room temperature to produce a black green precipitate. The solid was collected by filtration, washed with THF, methanol, water, methanol again, and diethylether, and dried. There were some impurities (normally, the color of polymers is yellow, but this product was more like brown), but as they did not affect the next step, this reagent was used without further purification.

CTB(OMe,C_2AuPPh$_3$) C4

((3,8,13-trimethoxy-10,15-dihydro-5*H*-tribenzo[a,d,g]cyclononenyl)2,7,12-triethynyl)(triphenyl-phosphaneyl)gold(I)



CTB(OMe,C_2AuPPh$_3$): Method A. **CTB(OMe,C_2H)** (0.008 g, 0.0185 mmol), [AuCl(PPh$_3$)] (0.030 g, 0.061 mmol, 3.3 equiv), and sodium methoxide (0.025 g, 0.463 mmol, 15 equiv) were mixed in methanol/THF (1:1, v/v, 10 mL) at 40 °C. After stirring of the reaction mixture for 4 hours, the solvents were removed by rotary evaporation. The residue was taken into dichloromethane, then filtered to remove NaCl and the excess of sodium methoxide, which afforded a clear yellow solution. The latter was concentrated to a volume of about 1 mL and treated by dropwise addition of cyclohexane (1.5 mL) until precipitation of the product. The precipitate was stored at 0 °C overnight, filtered, and dried under vacuum, affording a yellow solid powder. Yield: 0.025 g, 76%.

mp: 181 °C.

^{1}H NMR (500 MHz, $CDCl_3$, 298 K): δ = 7.555 (d, $^3J_{H,H}$ = 8.0 Hz, $^4J_{H,H}$ = 1.5 Hz, 9 H; o-H), 7.528 (dd, $^3J_{H,H}$ = 8.0 Hz, $^4J_{H,H}$ = 1.5 Hz, 9 H; o'-H), 7.486 (s, 3 H; α'-H), 7.475 (d, $^3J_{H,H}$ = 8.0 Hz, $^4J_{H,H}$ = 1.5 Hz, 9 H; p-H), 7.434 (2 d, $^3J_{H,H}$ = 8.0 Hz, 18 H; m-H, m'-H), 6.790 (s, 3 H; α-H), 4.680 (d, $^2J_{H,H}$ = 14.0 Hz, 3 H; a-H), 3.898 (s, 9 H; OCH_3-H), 3.551 (d, $^2J_{H,H}$ = 14.0 Hz, 3 H; e-H) ppm.

^{13}C NMR (125 MHz, $CDCl_3$, 298 K): δ = 159.4 (γ-C), 139.8 (β-C), 135.8 (α'-C), 134.5 (*o*-C), 131.6 (*p*-C), 130.6 (β'-C), 129.8 (*i*-C), 129.2 (*m*-C), 112.7 (γ'-C), 111.9 (α-C), 99.9 and 99.7 (C≡C), 56.3 (OCH_3), 37.1 (CH_2) ppm.

^{31}P NMR (162 MHz, $CDCl_3$, 298 K) δ = 42.97 ppm.

Elemental analysis: Calcd for $C_{84}H_{66}Au_3P_3O_3 \cdot 3/2CH_2Cl_2$, C 53.08, H 3.60, found: C 52.96; H 3.74.

ESI-MS: Calcd. for $C_{84}H_{66}Au_3P_3O_3$, 1806.32; found 1807.33 $[M + H]^+$.

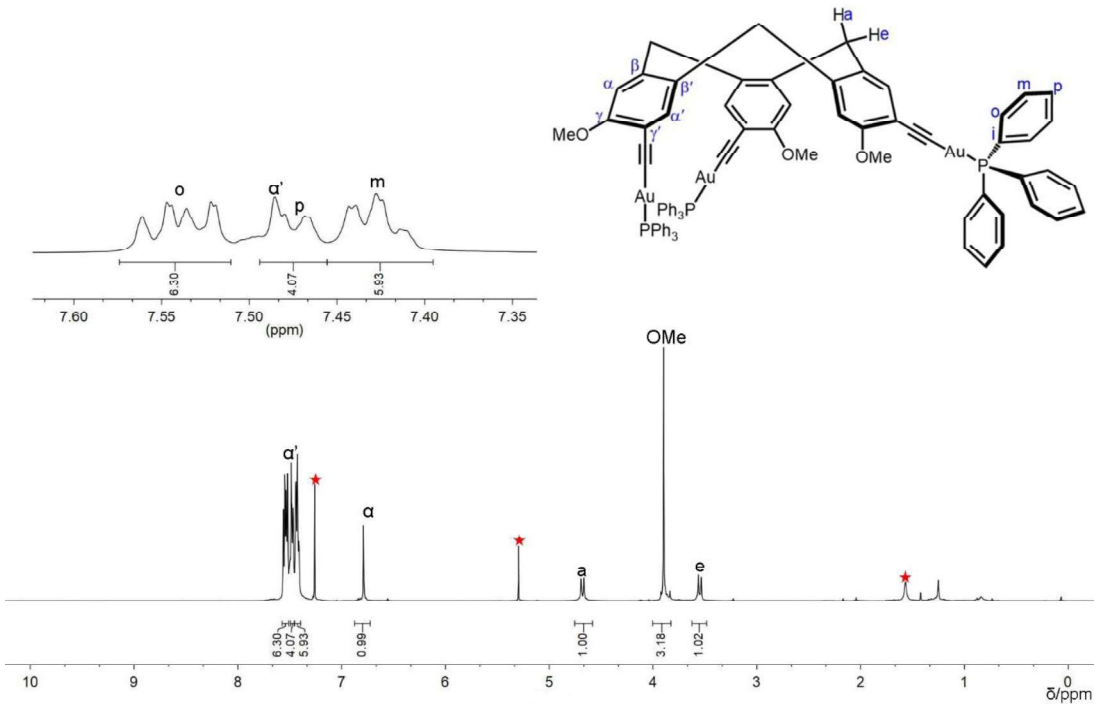
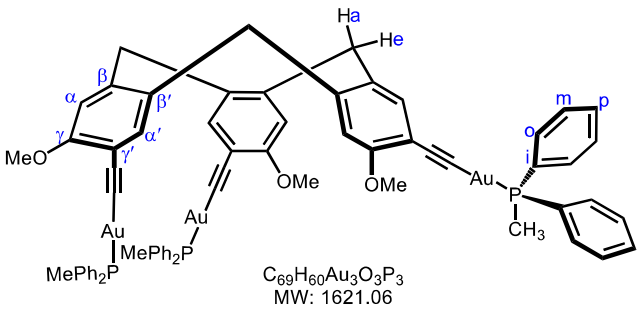


Figure 9. ^{1}H NMR spectrum of compound **CTB(OMe,C_2AuPPh$_3$) C4**

CTB(OMe,C$_2$AuPPh$_2$Me) C5

((3,8,13-trimethoxy-10,15-dihydro-5*H*-tribenzo[a,d,g]cyclononenyl)2,7,12-triethynyl)(methyldiphenyl-phosphaneyl)gold(I)



CTB(OMe,C$_2$AuPPh$_2$Me): Method A. **CTB(OMe, C$_2$H)** (0.013 g, 0.0298 mmol), [AuCl(PPh$_2$Me)] (0.040 g, 0.0926 mmol, 3.1 equiv), and sodium methoxide (0.032 g, 0.592 mmol, 20 equiv) were mixed in methanol/THF (1:1, v/v, 10 mL) at 40 °C. After stirring of the reaction mixture for 1 day, the solvents were removed by rotary evaporation. The residue was taken into dichloromethane, then filtered to remove NaCl and the excess of sodium methoxide, which afforded a clear yellow solution. The latter was concentrated to a volume of about 2 mL and treated by dropwise addition of cyclohexane (2 mL) until precipitation of the product. The precipitate was stored at 0 °C overnight, filtered, and dried under vacuum, affording a yellow solid powder. Yield: 0.038 g, 80%.

Method B. A solution of PPh$_2$Me (0.024 g, 0.118 mmol, 3 equiv) in THF (1.0 mL) was added to a suspension of **CTB(OMe,C$_2$Au)$_n$** (0.040 g, 0.039 mmol) in dichloromethane (4 mL) and the reaction mixture stirred overnight. It was subsequently filtered by using a sintered glass funnel (porosity 4) to give a light-yellow clear solution, which was evaporated to dryness. The solid residue was washed with methanol, affording a light yellow crystalline solid. Yield: 0.038 g, 60%.

mp: 177.2 °C.

^{1}H NMR (500 MHz, $CDCl_3$, 298 K): δ = 7.639 (d, $^3J_{H,H}$ = 7.2 Hz, $^4J_{H,H}$ = 1.5 Hz, 12 H; o-H), 7.468 (s, 3 H; α'-H), 7.451 (m, 18 H; m-H, p-H), 6.783 (s, 3 H; α-H), 4.679 (d,

$^{2}J_{H,H}$ = 13.2 Hz, 3 H; a-H), 3.888 (s, 9 H; OCH_3-H), 3.545 (d, $^{2}J_{H,H}$ = 13.2 Hz, 3 H; e-H) ppm, 2.032 (d, $^{2}J_{H,P}$ = 11.5 Hz, 3 H; CH_3-H) ppm.

^{13}C NMR (125 MHz, $CDCl_3$, 298 K): δ = 159.4 (γ-C), 139.9 (β-C), 135.7 (α'-C), 133.0 (*o*-C), 132.0 (*i*-C), 131.6 (*p*-C), 130.6 (β'-C), 129.2 (*m*-C), 112.7 (γ'-C), 111.9 (α-C), 100.2 and 99.9 (C≡C), 56.3 (OCH_3), 37.1 (CH_2), 14.3 ($^{1}J_{H,H}$ = 36.2 Hz,CH_3) ppm.

^{31}P NMR (162 MHz, $CDCl_3$, 298 K) δ = 27.11 ppm.

Elemental analysis: Calcd for $C_{69}H_{60}Au_3O_3P_3 \cdot 2CH_2Cl_2$, C 47.62, H 3.60, found: C 47.66, H 3.62.

ESI-MS: Calcd. for $C_{69}H_{60}Au_3O_3P_3$, 1620.28; found 1621.26 $[M + H]^+$.

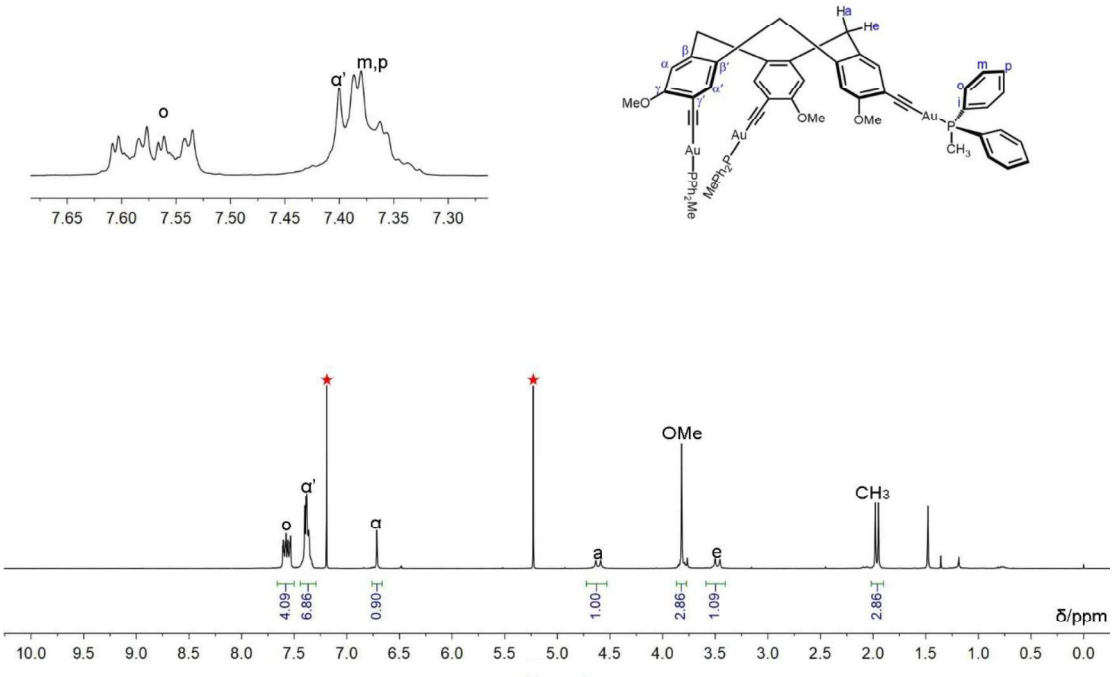
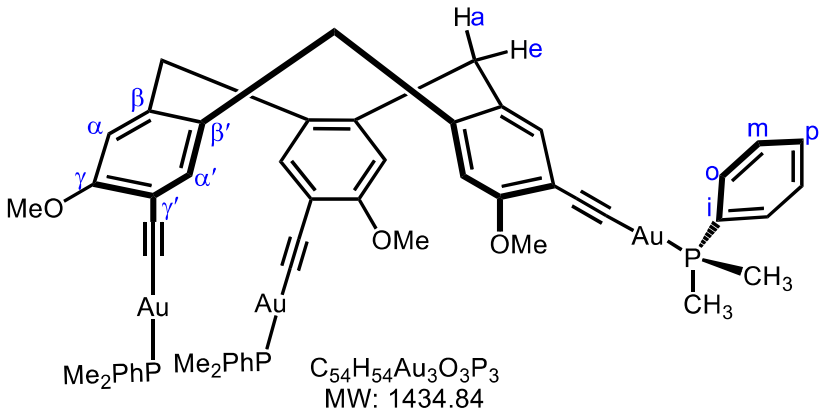


Figure 10. ^{1}H NMR spectrum of compound **CTB(OMe,C_2AuPPh_2Me) C5**

CTB(OMe,C$_2$AuPPhMe$_2$) C6

((3,8,13-trimethoxy-10,15-dihydro-5*H*-tribenzo[a,d,g]cyclononenyl)2,7,12-triethynyl)(dimethylphenyl-phosphaneyl)gold(I)



CTB(OMe,C$_2$AuPPhMe$_2$): Method A. **CTB(OMe,C$_2$H)** (0.010 g, 0.0231 mmol), [AuCl(PPhMe$_2$)] (0.035 g, 0.0946 mmol, 4.1 equiv), and sodium methoxide (0.030 g, 0.555 mmol, 24 equiv) were mixed in methanol/THF (1:1, v/v, 10 mL) at 40 °C. After stirring of the reaction mixture for 1 day, the solvents were removed by rotary evaporation. The residue was taken into dichloromethane, then filtered to remove NaCl and the excess of sodium methoxide, which afforded a clear yellow solution. The latter was concentrated to a volume of about 1 mL, and treated by dropwise addition of cyclohexane (1 mL) until precipitation of the product. The precipitate was stored at 0 °C overnight, filtered, and dried under vacuum, affording a yellow solid powder. Yield: 0.018 g, 60%.

Method B. A solution of PPhMe$_2$ (0.013 g, 0.097 mmol, 3 equiv) in THF (1.0 mL) was added to a suspension of **CTB(OMe,C$_2$Au)$_n$** (0.033 g, 0.032 mmol) in dichloromethane (3 mL) and the reaction mixture stirred overnight. It was subsequently filtered by using a sintered glass funnel (porosity 4) to give a light yellow clear solution, which was evaporated to dryness. The solid residue was washed with methanol, affording a light yellow crystalline solid. Yield: 0.023 g, 72%.

mp: 182.5 °C.

^{1}H NMR (500 MHz, $CDCl_3$, 298 K): δ = 7.737 (d, $^{3}J_{H,H}$ = 7.2 Hz, $^{4}J_{H,H}$ = 1.6 Hz, 6 H; o-H), 7.461 (s, 3 H; α'-H), 7.468 (m, 9 H; m-H, p-H), 6.786 (s, 3 H; α-H), 4.681 (d, $^{2}J_{H,H}$ = 13.2 Hz, 3 H; a-H), 3.890 (s, 9 H; OCH_3-H), 3.548 (d, $^{2}J_{H,H}$ = 13.2 Hz, 3 H; e-H) ppm, 1.737 (d, $^{2}J_{H,P}$ = 9.6 Hz, 3 H; CH_3-H) ppm.

^{13}C NMR (125 MHz, $CDCl_3$, 298 K): δ = 159.4 (γ-C), 139.9 (β-C), 135.7 (α'-C), 132.9 (*i*-C), 132.2 (*o*-C), 131.7 (*p*-C), 130.6 (β'-C), 129.2 (*m*-C), 112.8 (γ'-C), 111.9 (α-C), 100.3 and 100.1 (C≡C), 56.3 (OCH_3), 37.1 (CH_2), 15.7 ($^{1}J_{H,H}$ = 35.0 Hz, CH_3) ppm.

^{31}P NMR (162 MHz, $CDCl_3$, 298 K) δ = 14.16 ppm.

Elemental analysis: Calcd for $C_{54}H_{54}Au_3O_3P_3$·0.5CyH, C 46.35, H 4.09, found: C 46.19, H 4.04.

ESI-MS: Calcd. for $C_{54}H_{54}Au_3O_3P_3$, 1434.23; found 1435.20 $[M + H]^+$.

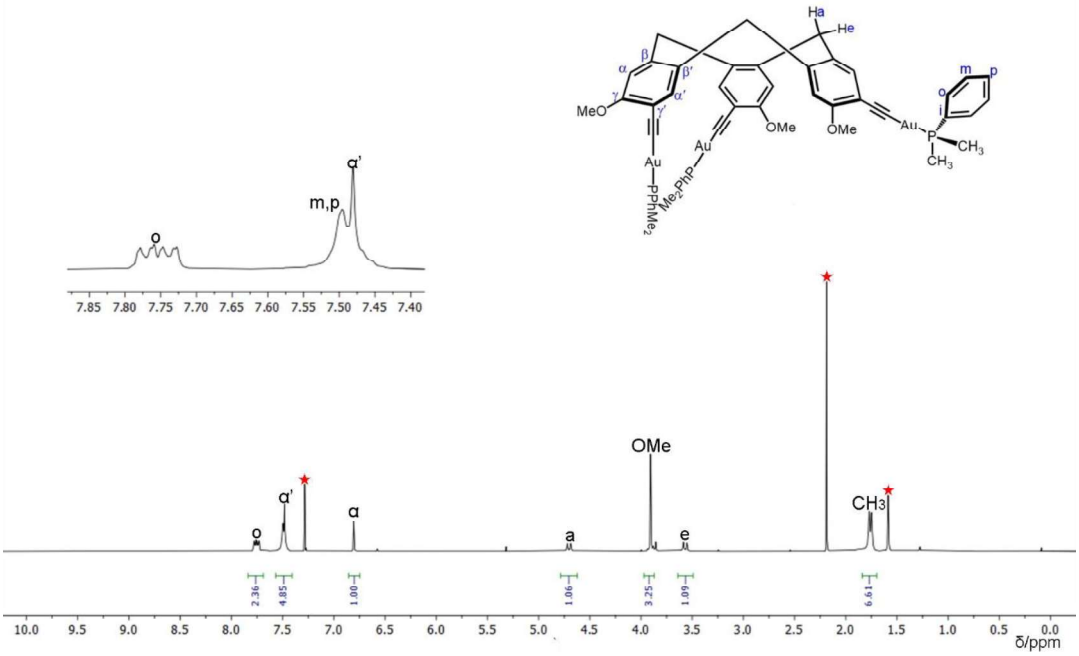


Figure 11. ^{1}H NMR spectrum of compound **CTB(OMe,C_2AuPPhMe_2) C6**

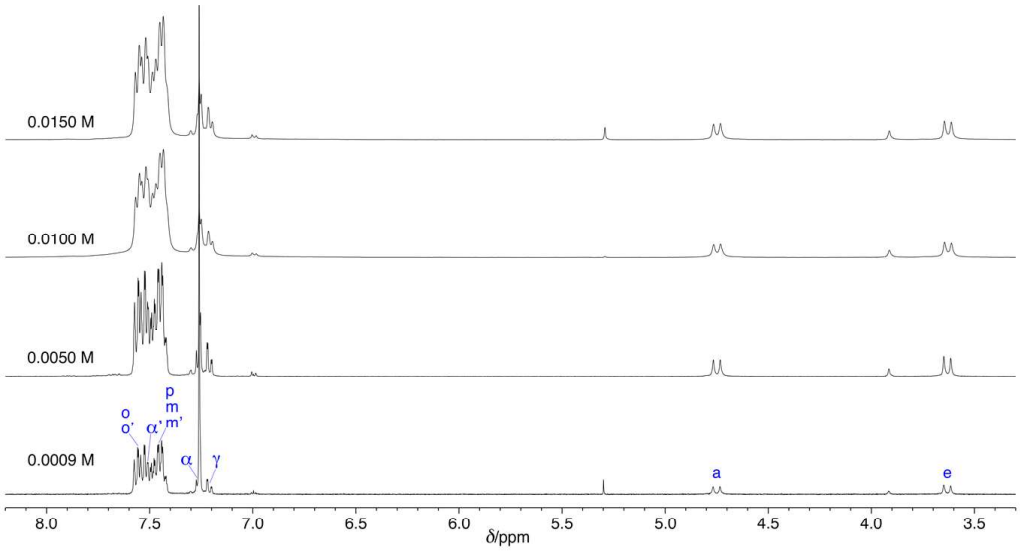


Figure 12. Variable concentration ^{1}H NMR ($CDCl_3$, 600 MHz) of **C1.**

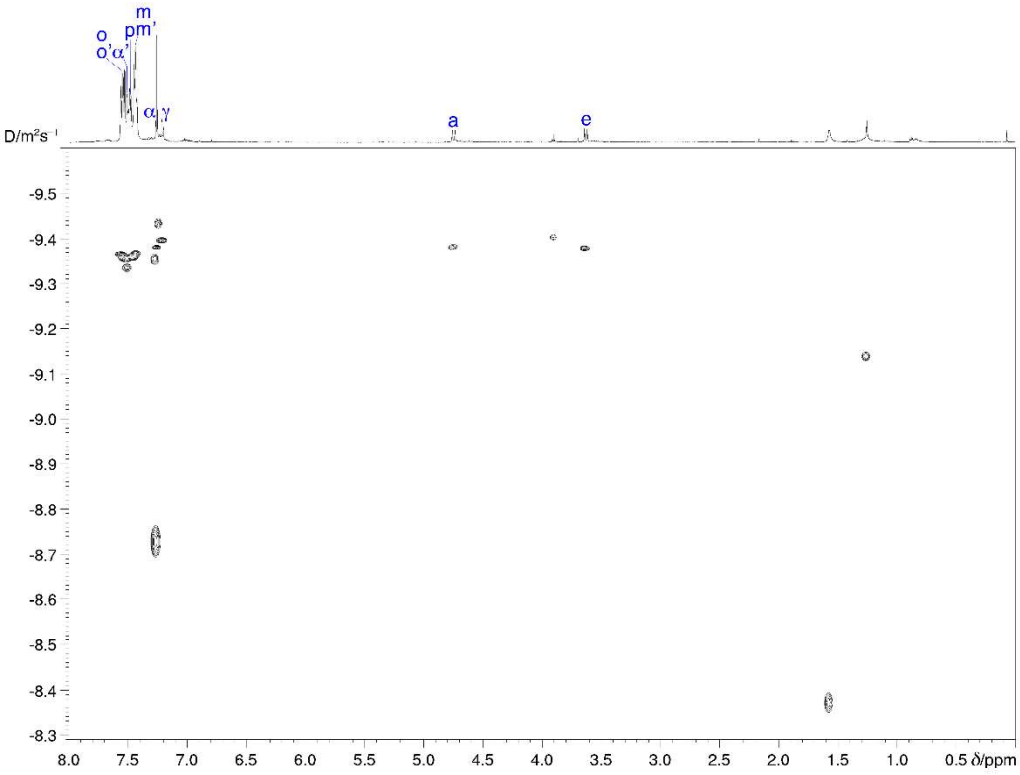


Figure 13. DOSY spectrum of **C1**

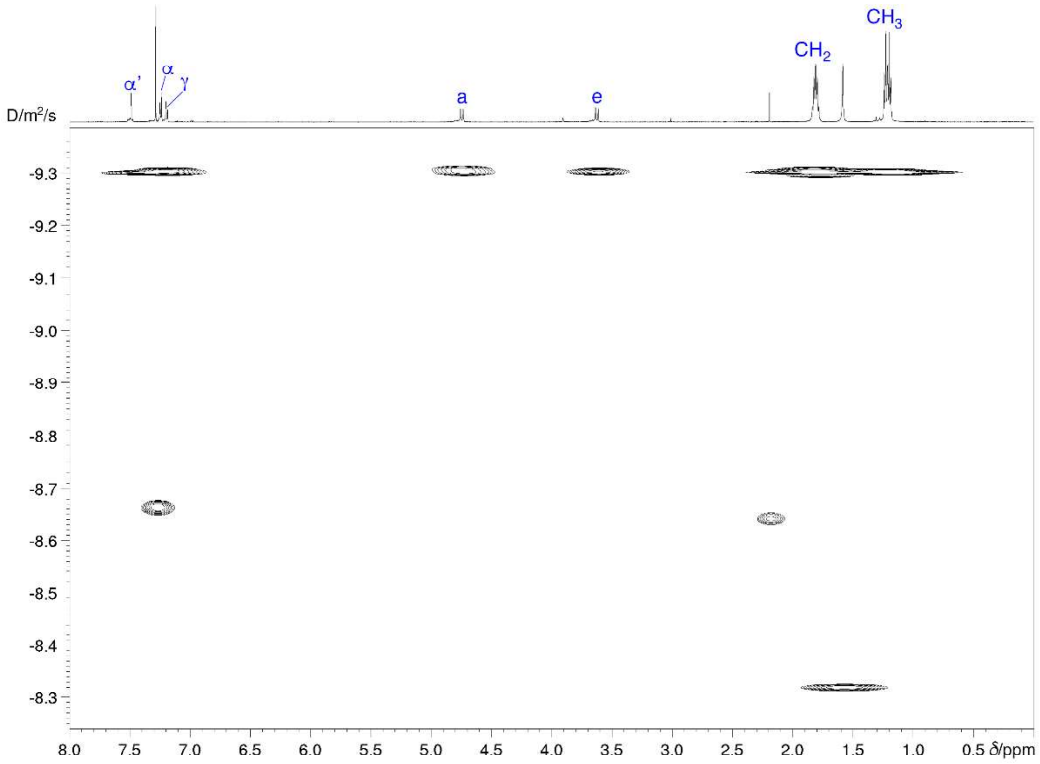


Figure 14. DOSY spectrum of **C7**

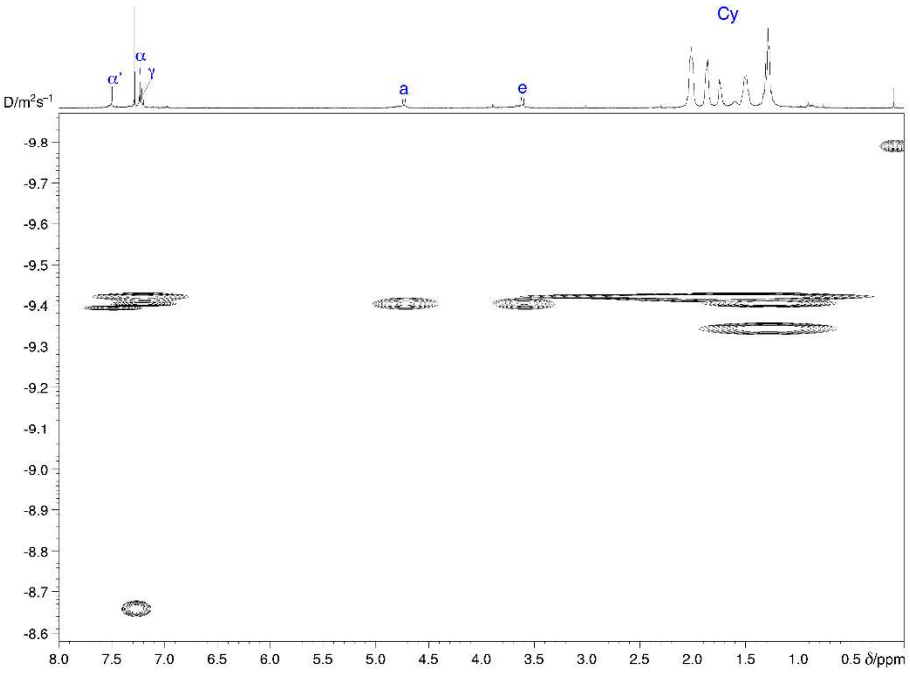


Figure 15. DOSY spectrum of **C9**

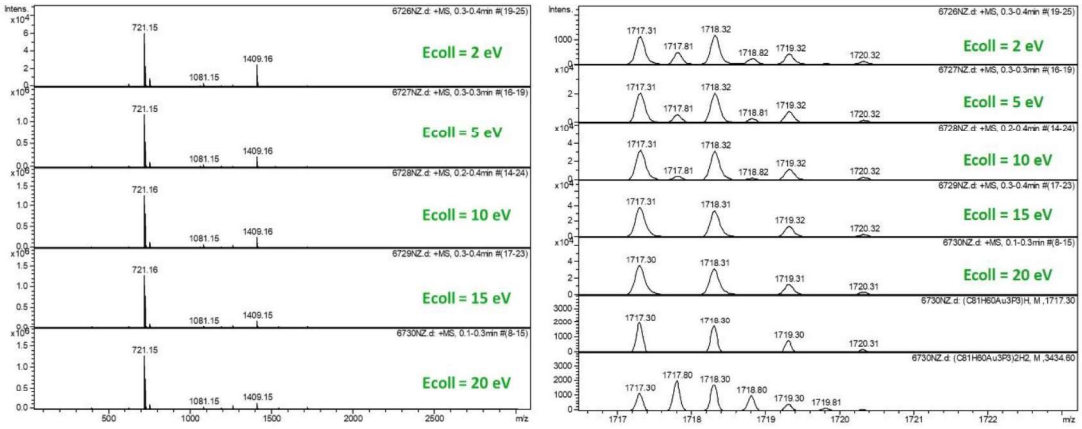


Figure 16. ESI-MS of **C1**, 2×10^{-5} M in *i*-PrOH/$CHCl_3$/HCO_2H 0.495:0.495:0.010 and detail of the molecular peak.

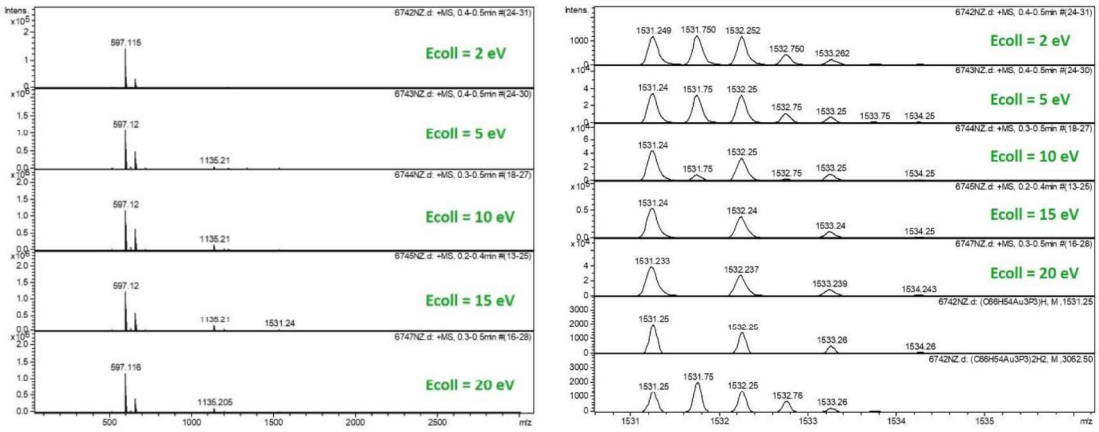


Figure 17. ESI-MS of **C2**, 2×10^{-5} M in *i*-PrOH/$CHCl_3$/HCO_2H 0.495:0.495:0.010 and detail of the molecular peak.

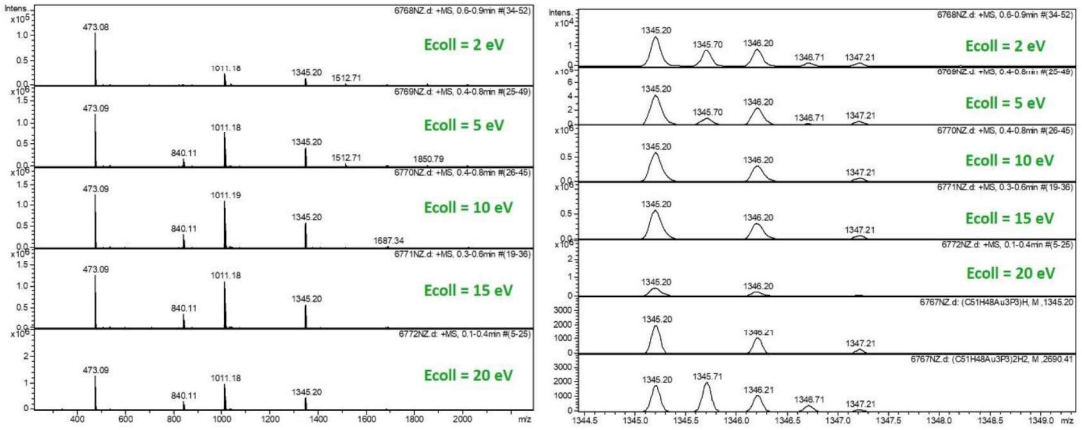


Figure 18. ESI-MS of **C3**, 2×10^{-5} M in *i*-PrOH/$CHCl_3$/HCO_2H 0.495:0.495:0.010 and detail of the molecular peak.

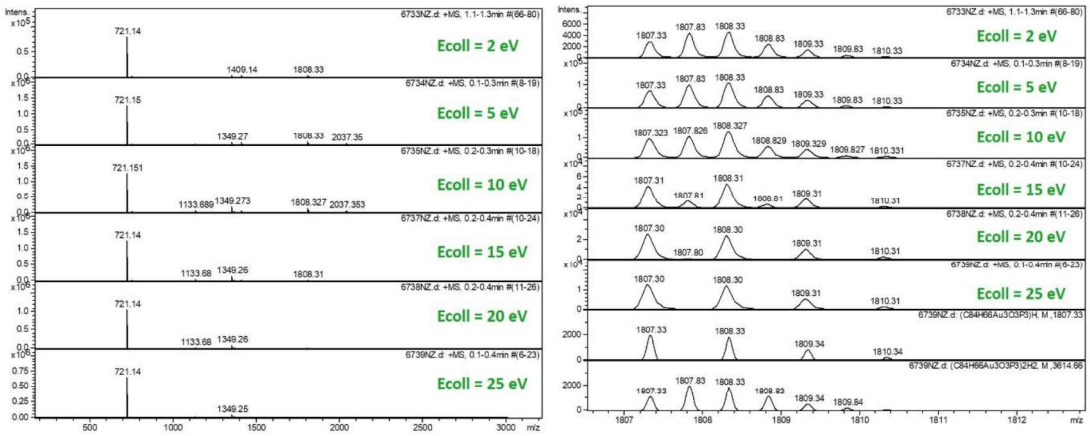


Figure 19. ESI-MS of **C4**, 2×10^{-5} M in *i*-PrOH/$CHCl_3$/HCO_2H 0.495:0.495:0.010 and detail of the molecular peak.

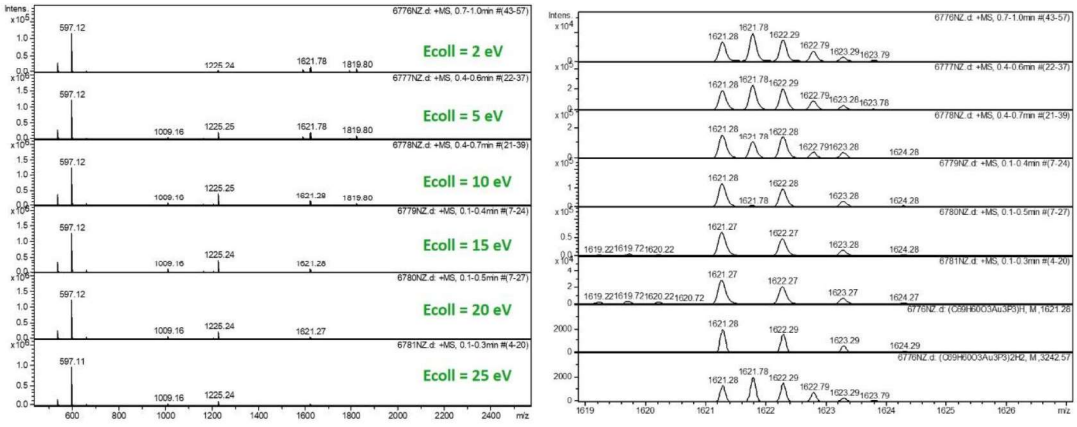


Figure 20. ESI-MS of **C5**, 2×10^{-5} M in *i*-PrOH/$CHCl_3$/HCO_2H 0.495:0.495:0.010 and detail of the molecular peak.

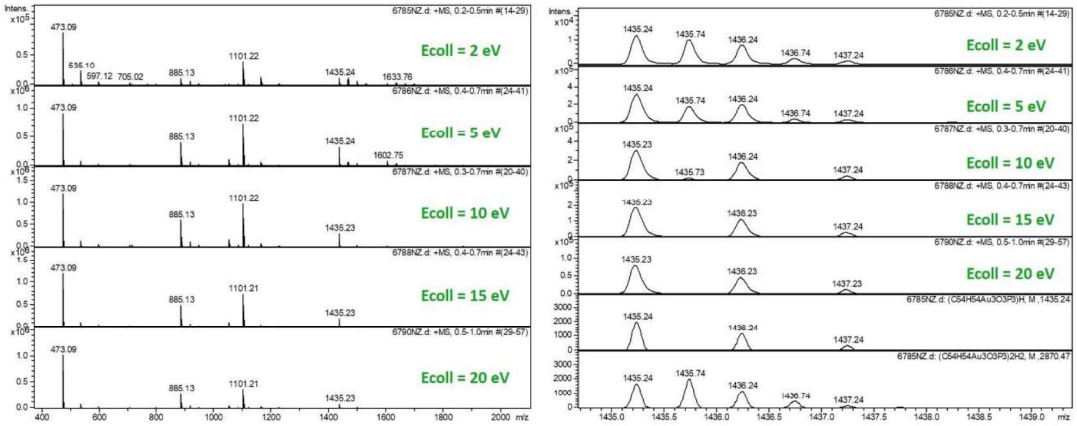


Figure 21. ESI-MS of **C6**, 2×10^{-5} M in *i*-PrOH/$CHCl_3$/HCO_2H 0.495:0.495:0.010 and detail of the molecular peak.

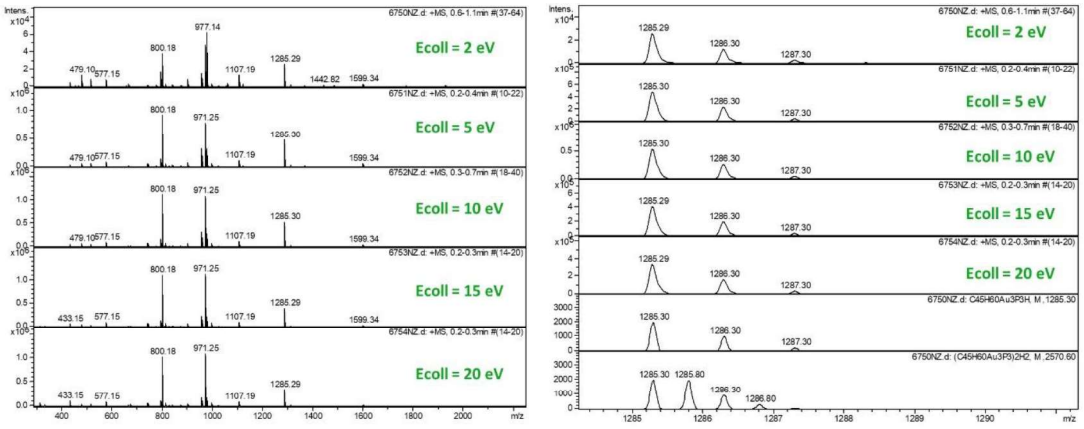


Figure 22. ESI-MS of **C7**, 2×10^{-5} M in *i*-PrOH/$CHCl_3$/HCO_2H 0.495:0.495:0.010 and detail of the molecular peak.

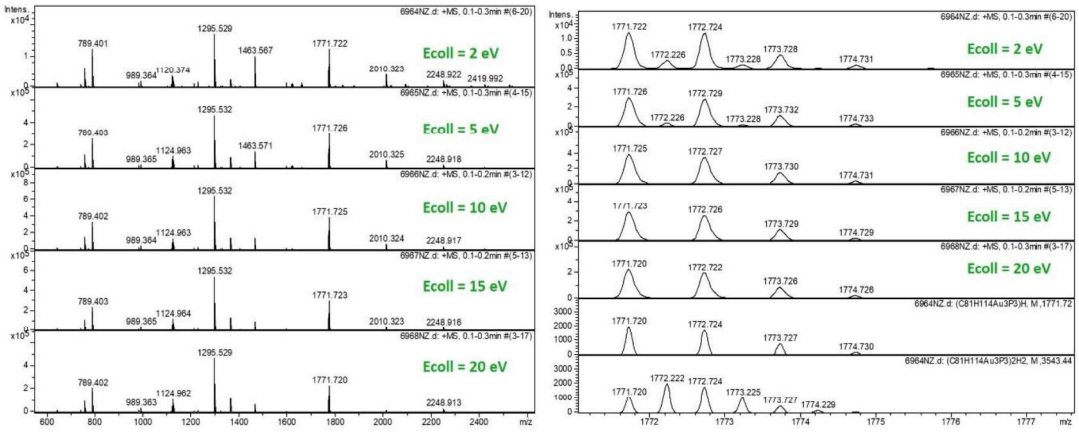


Figure 23. ESI-MS of **C9**, 2×10^{-5} M in *i*-PrOH/$CHCl_3$/HCO_2H 0.495:0.495:0.010 and detail of the molecular peak.

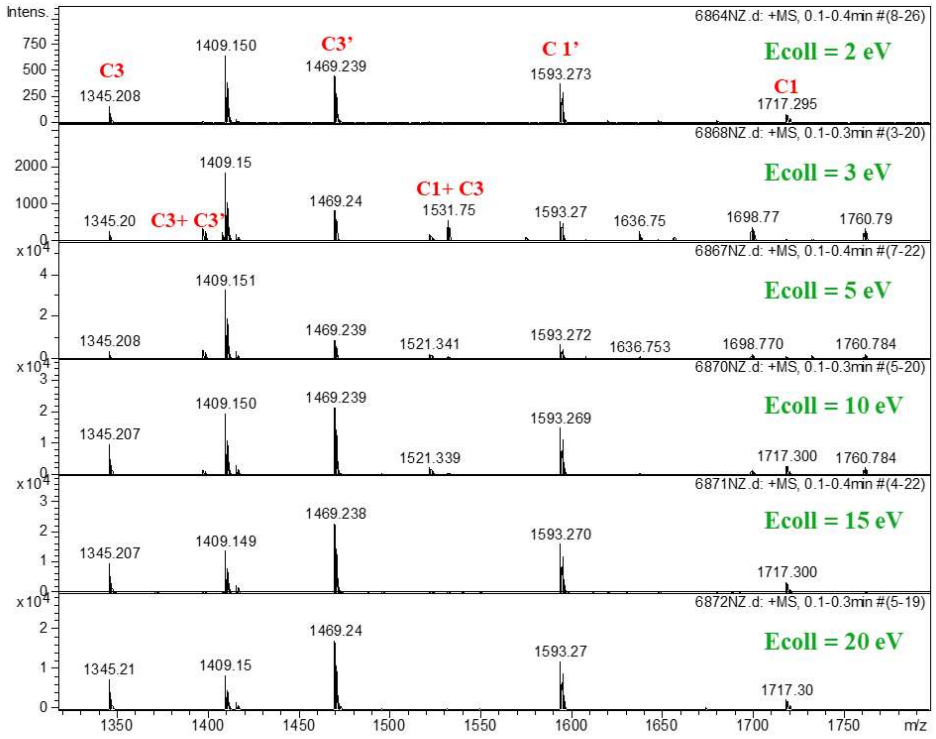


Figure 24. ESI-MS of **C1** with **C3**, detail of the evolution of the molecular peak as a function of E_{coll}.

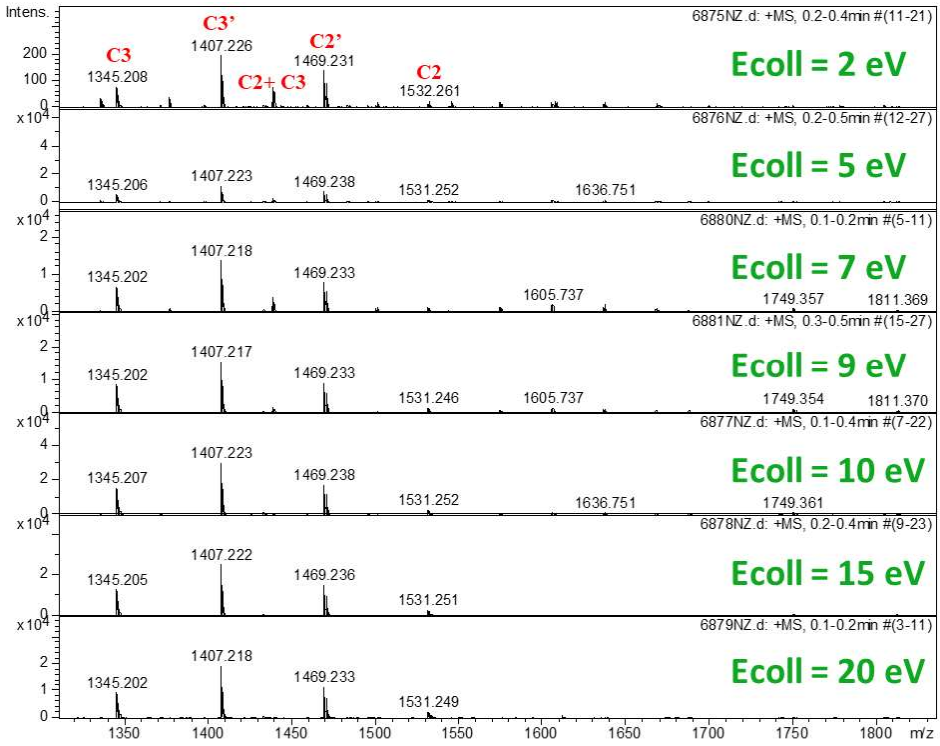


Figure 25. ESI-MS of **C2** with **C3**, detail of the evolution of the molecular peak as a function of E_{coll}.

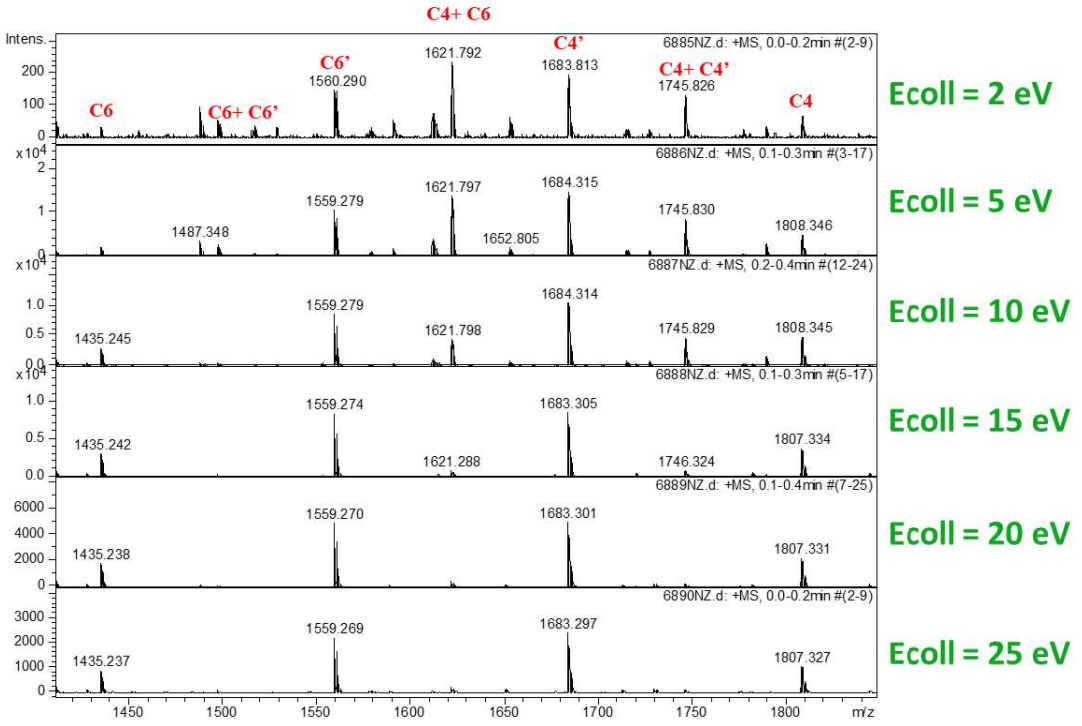


Figure 26. ESI-MS of **C4** with **C6**, detail of the evolution of the molecular peak as a function of E_{coll}.

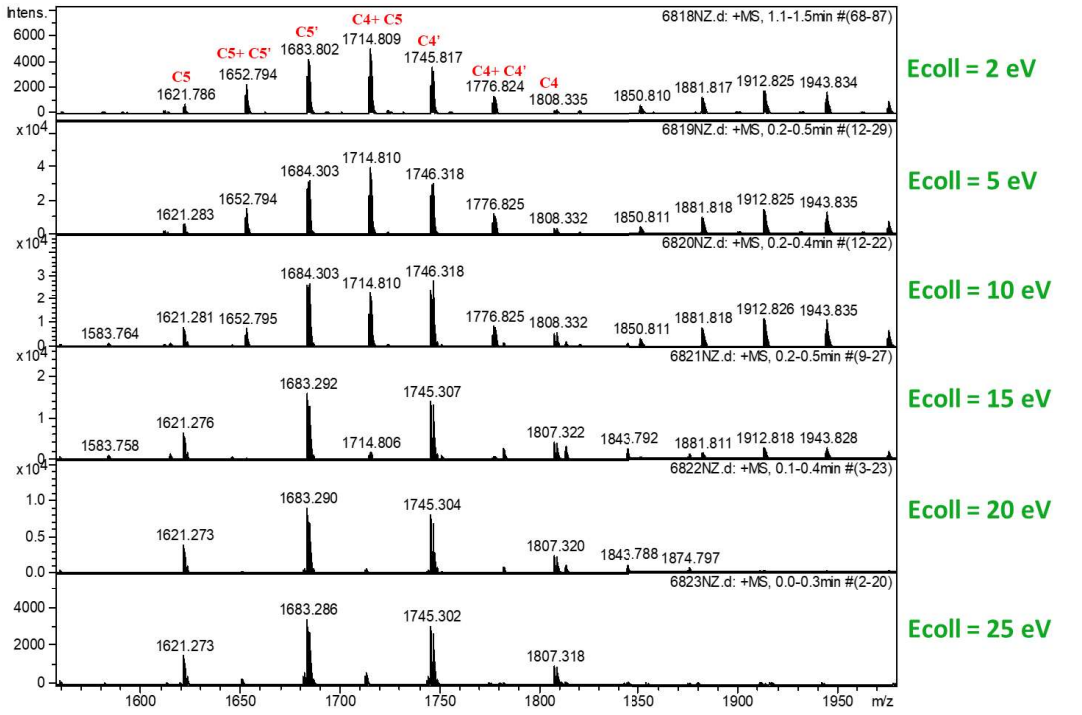


Figure 27. ESI-MS of **C4** with **C5**, detail of the evolution of the molecular peak as a function of E_{coll}.

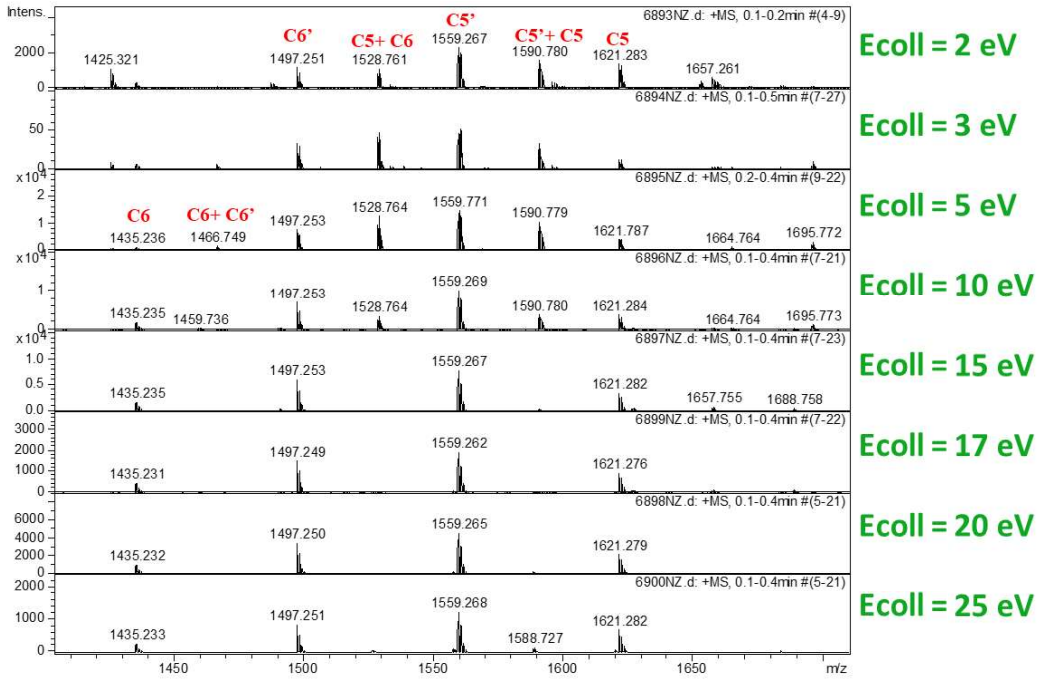


Figure 28. ESI-MS of **C5** with **C6**, detail of the evolution of the molecular peak as a function of E_{coll}.

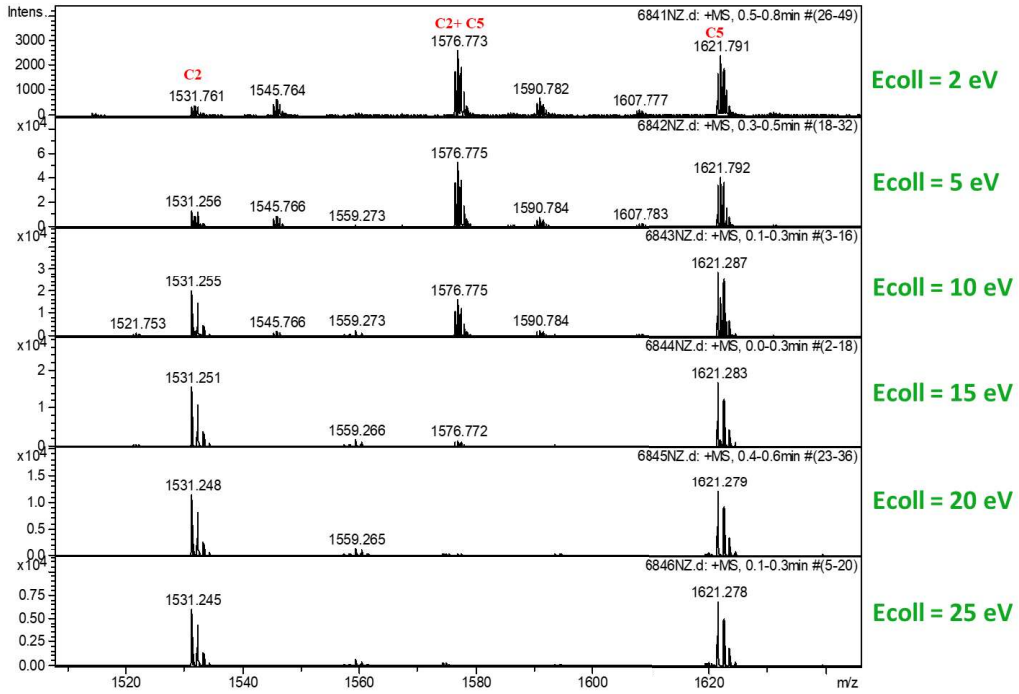


Figure 29. ESI-MS of **C2** with **C5**, detail of the evolution of the molecular peak as a function of E_{coll}.

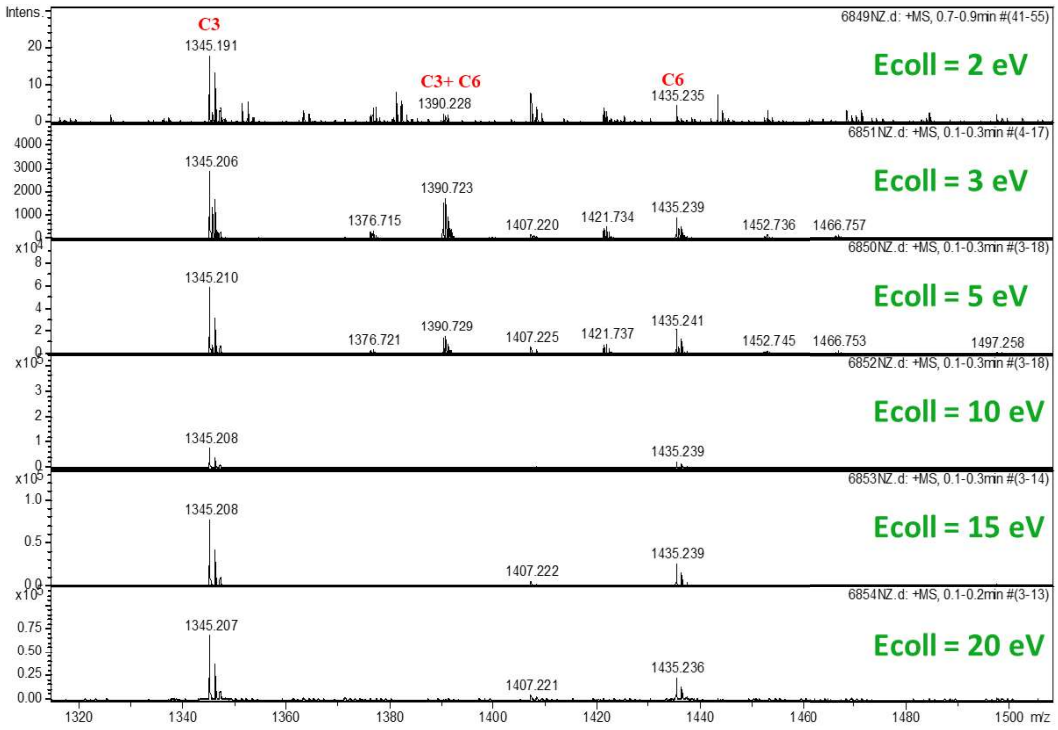


Figure 30. ESI-MS of **C3** with **C6**, detail of the evolution of the molecular peak as a function of E_{coll}.

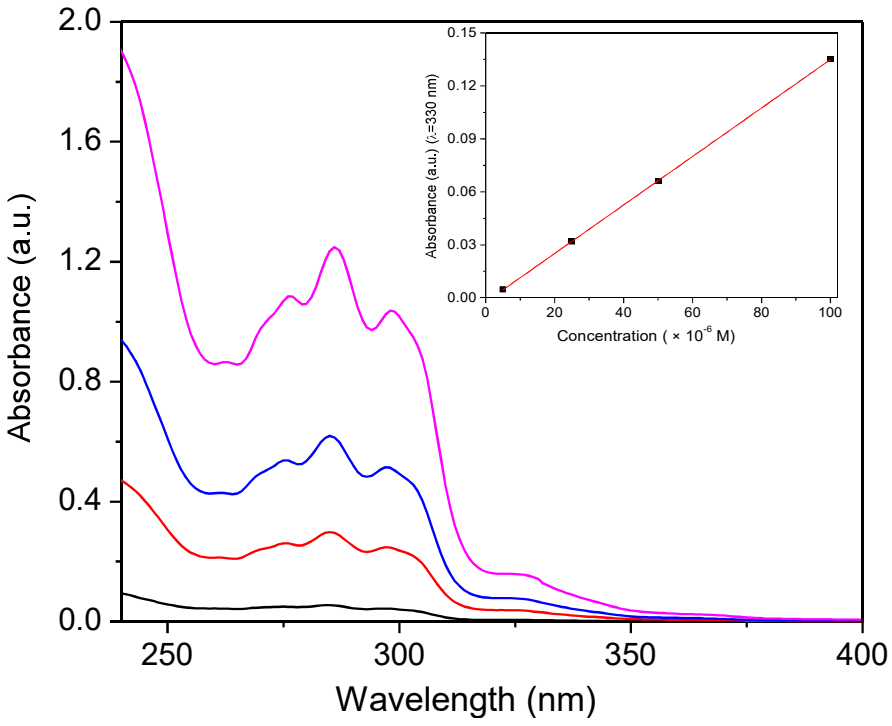


Figure 31. Electronic absorption spectra of **C1** in $CHCl_3$ at concentrations of 5.0 to 100 × 10^{-6} M. Inset: Absorbance at 330 nm *vs.* concentration.

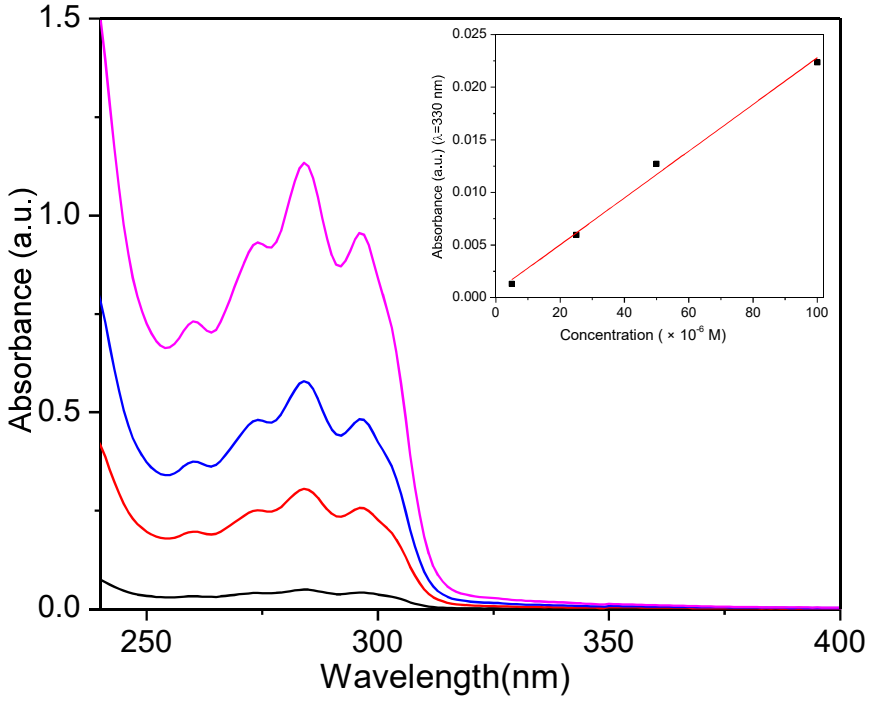


Figure 32. Electronic absorption spectra of **C2** in $CHCl_3$ at concentrations of 5.0 to 100 × 10^{-6} M. Inset: Absorbance at 330 nm *vs.* concentration.

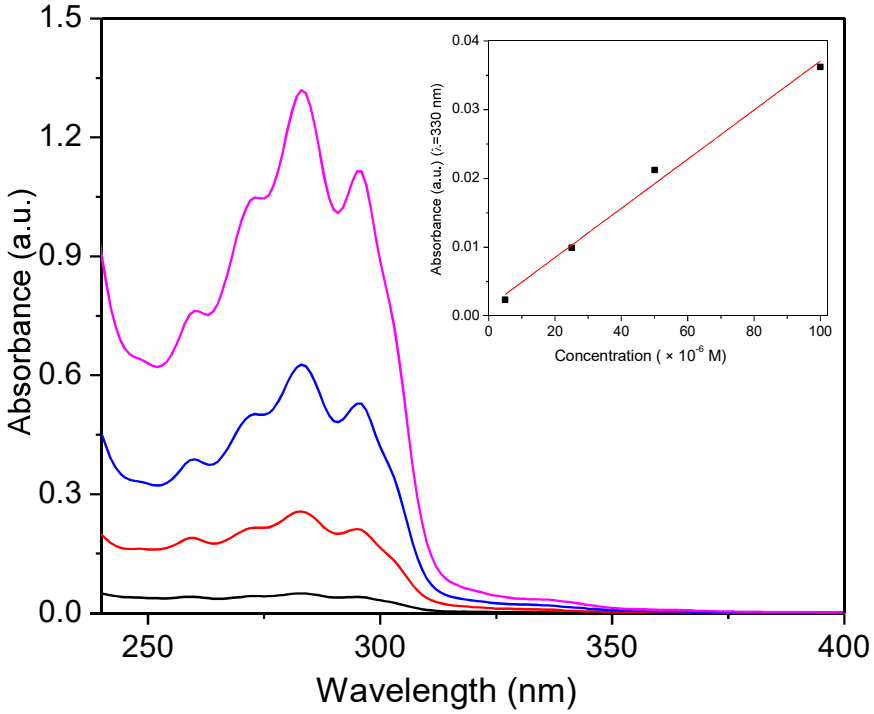


Figure 33. Electronic absorption spectra of **C3** in $CHCl_3$ at concentrations of 5.0 to 100 × 10^{-6} M. Inset: Absorbance at 330 nm *vs.* concentration.

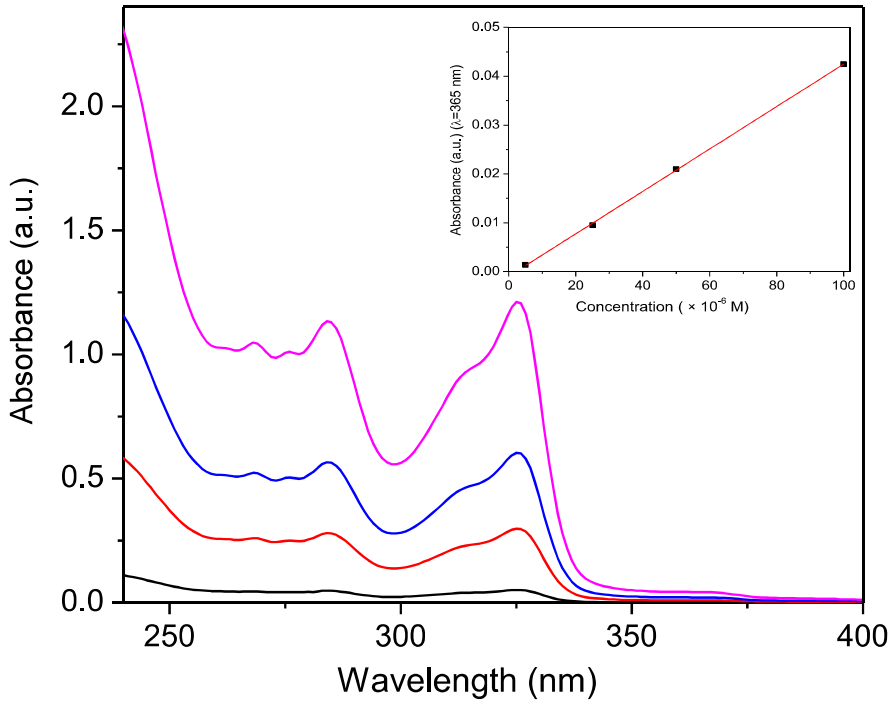


Figure 34. Electronic absorption spectra of **C4** in $CHCl_3$ at concentrations of 5.0 to 100 × 10^{-6} M. Inset: Absorbance at 365 nm *vs.* concentration.

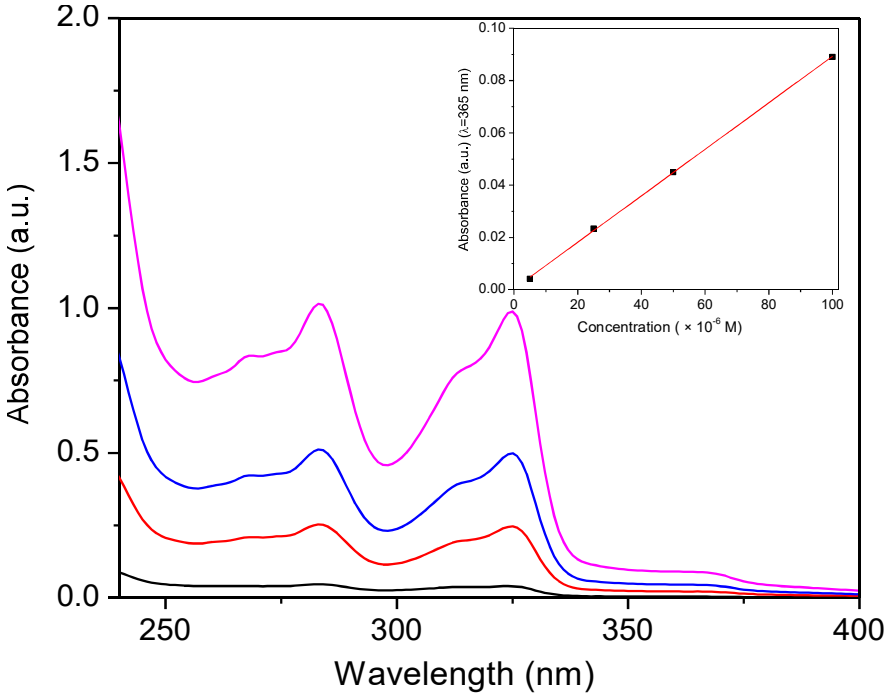


Figure 35. Electronic absorption spectra of **C5** in $CHCl_3$ at concentrations of 5.0 to 100 × 10^{-6} M. Inset: Absorbance at 365 nm *vs.* concentration.

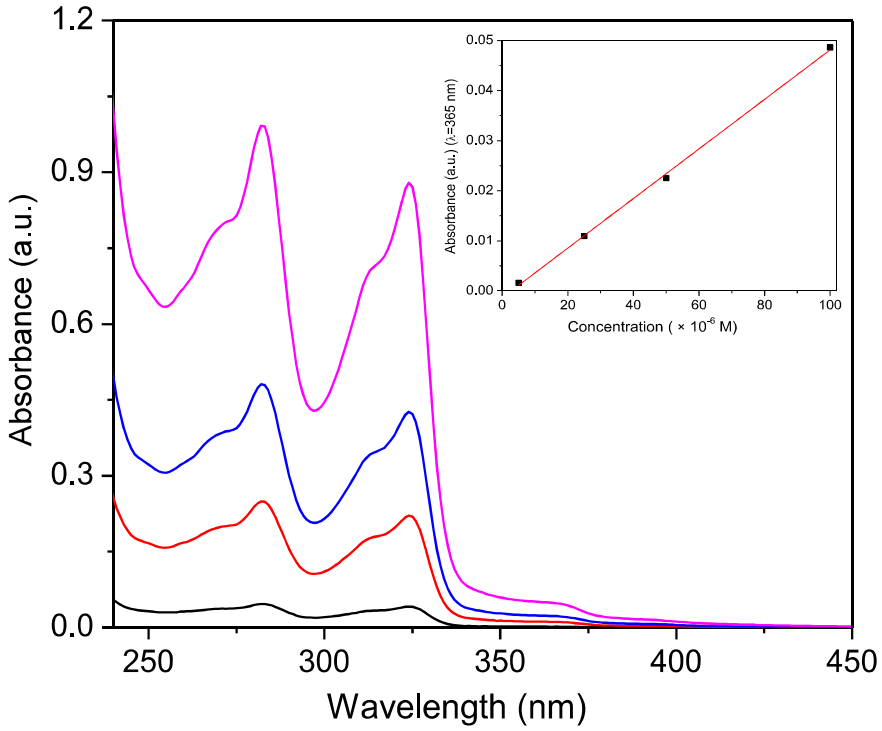


Figure 36. Electronic absorption spectra of **C6** in $CHCl_3$ at concentrations of 5.0 to 100 × 10^{-6} M. Inset: Absorbance at 365 nm *vs.* concentration.

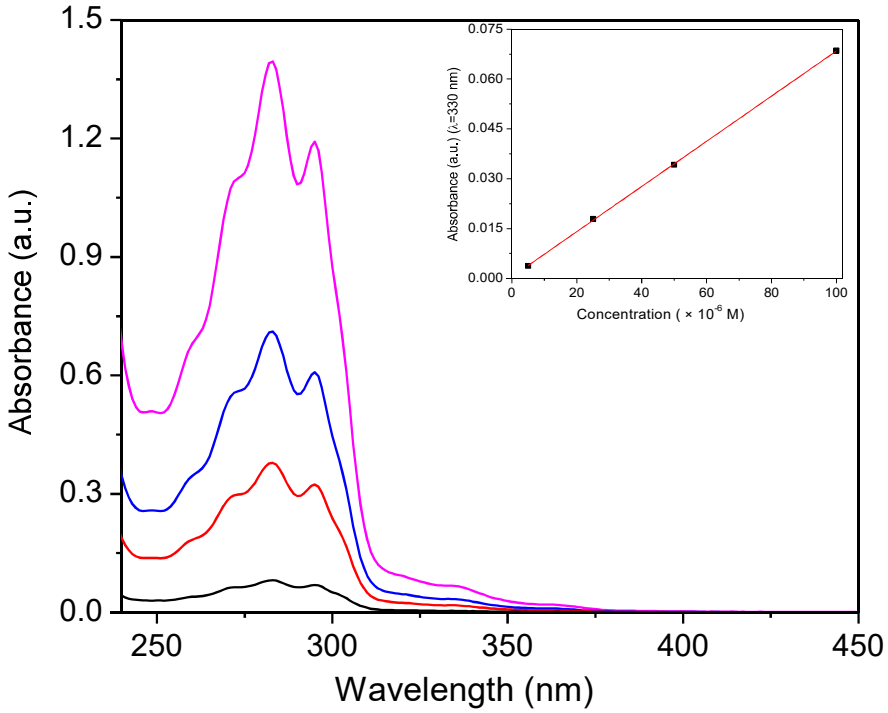


Figure 37. Electronic absorption spectra of **C7** in $CHCl_3$ at concentrations of 5.0 to 100 × 10^{-6} M. Inset: Absorbance at 330 nm *vs.* concentration.

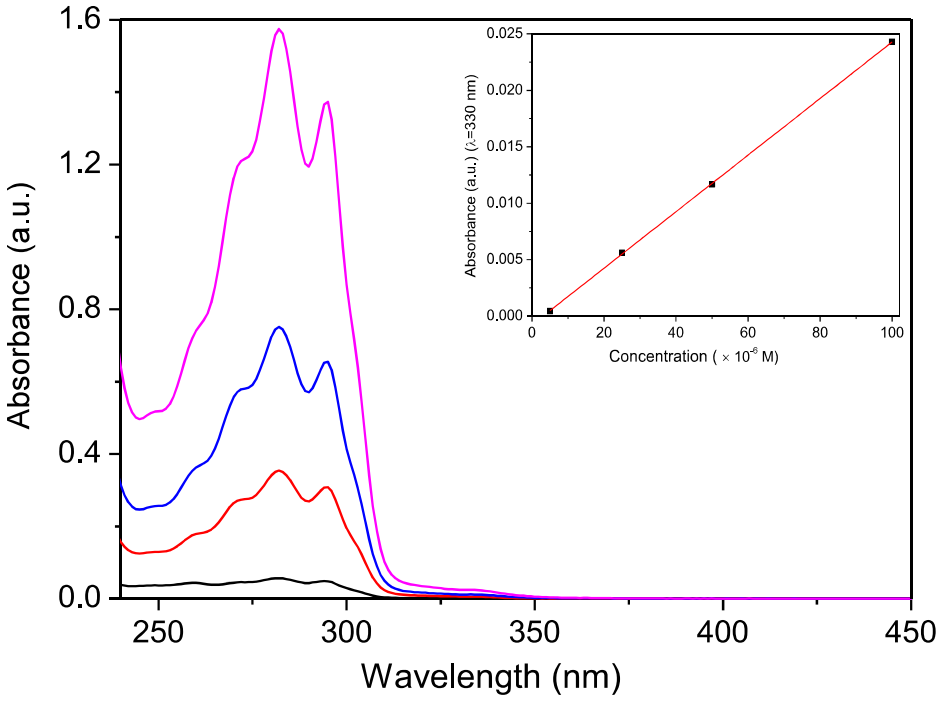


Figure 38. Electronic absorption spectra of **C9** in $CHCl_3$ at concentrations of 5.0 to 100 × 10^{-6} M. Inset: Absorbance at 330 nm *vs.* concentration.

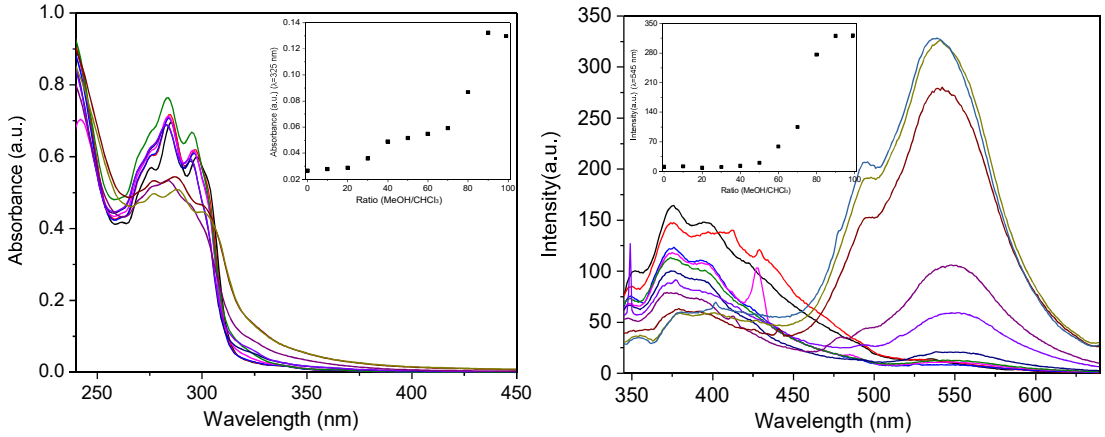


Figure 39. Absorption spectra of aged 10^{-5} M solutions of **C1** in $CHCl_3$/MeOH, inset: Absorbance in function of the solvent ratio at 325 nm. Emission spectra of aged 10^{-5} M solutions of **C1** in $CHCl_3$/MeOH (exc.: 330 nm), inset: Emission in function of the solvent ratio at 545 nm.

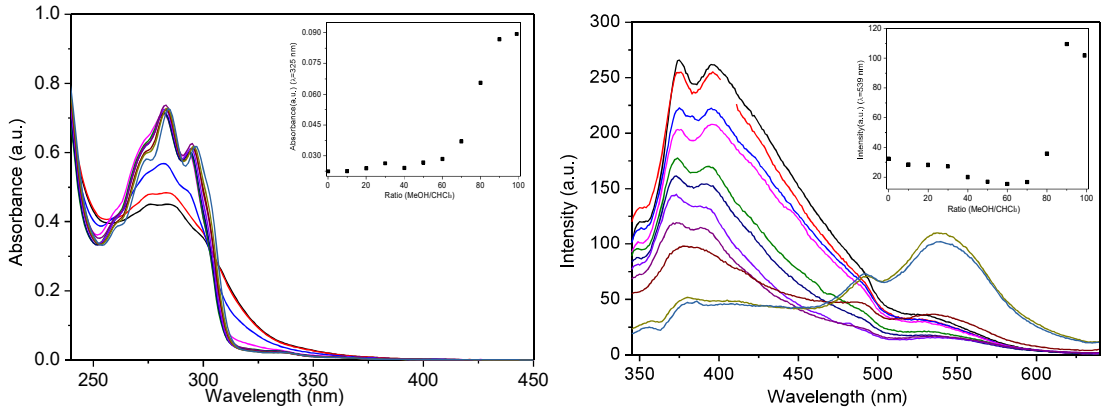


Figure 40. Absorption spectra of fresh 10^{-5} M solutions of **C2** in $CHCl_3$/MeOH, inset: Absorbance in function of the solvent ratio at 325 nm. Emission spectra of fresh 10^{-5} M solutions of **C2** in $CHCl_3$/MeOH (exc.: 330 nm), inset: Emission in function of the solvent ratio at 539 nm.

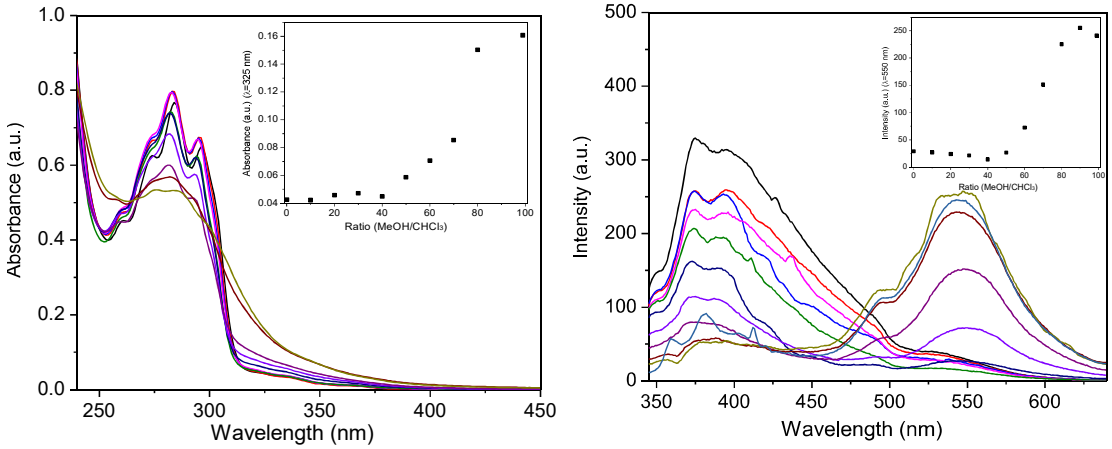


Figure 41. Absorption spectra of aged 10^{-5} M solutions of **C3** in $CHCl_3$/MeOH, inset: Absorbance in function of the solvent ratio at 325 nm. Emission spectra of aged 10^{-5} M solutions of **C3** in $CHCl_3$/MeOH (exc.: 330 nm), inset: Emission in function of the solvent ratio at 550 nm.

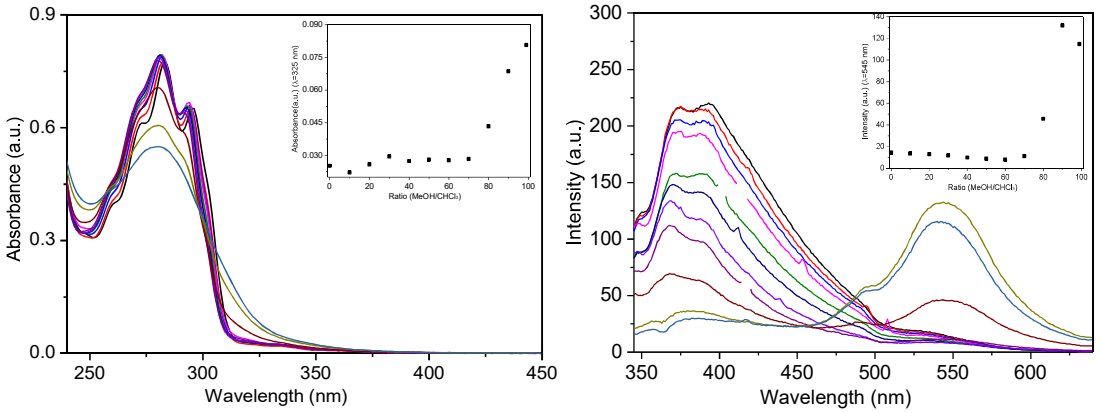


Figure 42. Absorption spectra of fresh 10^{-5} M solutions of **C3** in $CHCl_3$/MeOH, inset: Absorbance in function of the solvent ratio at 325 nm. Emission spectra of fresh 10^{-5} M solutions of **C3** in $CHCl_3$/MeOH (exc.: 330 nm), inset: Emission in function of the solvent ratio at 545 nm.

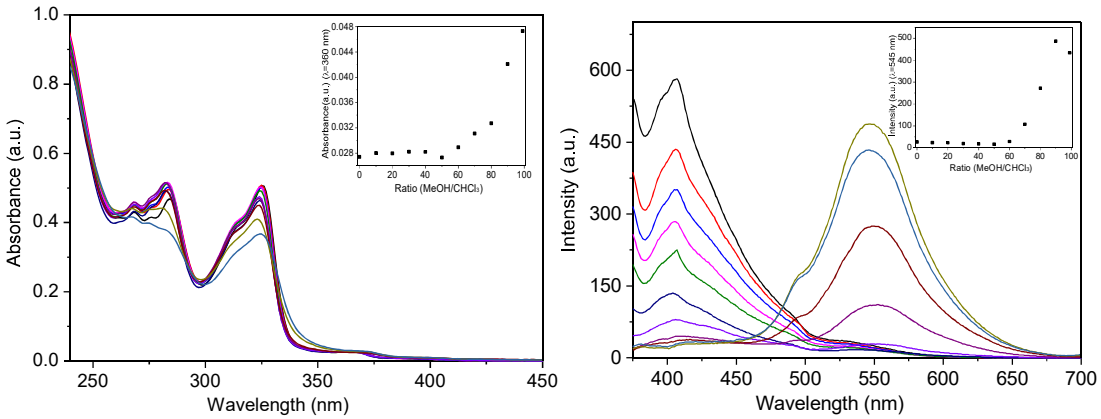


Figure 43. Absorption spectra of fresh 10^{-5} M solutions of **C4** in $CHCl_3$/MeOH, inset: Absorbance in function of the solvent ratio at 360 nm. Emission spectra of fresh 10^{-5} M solutions of **C4** in $CHCl_3$/MeOH (exc.: 330 nm), inset: Emission in function of the solvent ratio at 545 nm.

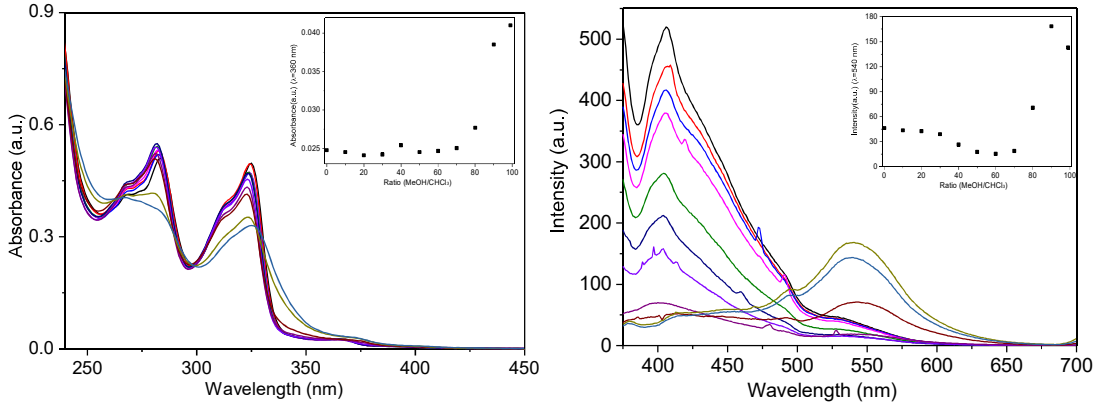


Figure 44. Absorption spectra of fresh 10^{-5} M solutions of **C5** in $CHCl_3$/MeOH, inset: Absorbance in function of the solvent ratio at 360 nm. Emission spectra of fresh 10^{-5} M solutions of **C5** in $CHCl_3$/MeOH (exc.: 330 nm), inset: Emission in function of the solvent ratio at 540 nm.

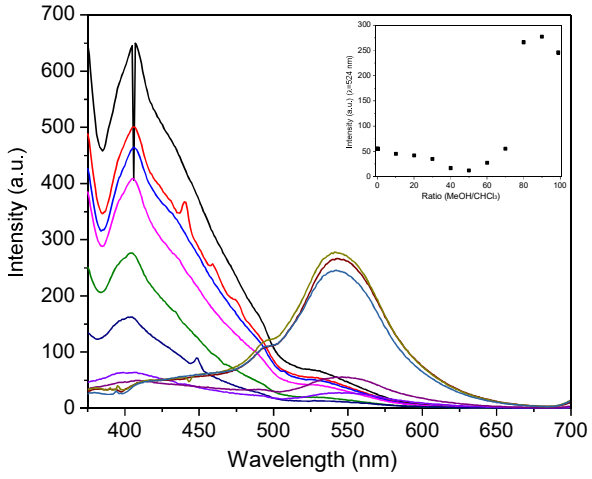


Figure 45. Emission spectra of aged 10^{-5} M solutions of **C5** in $CHCl_3$/MeOH (exc. 330 nm). Inset: Emission intensity in function of the solvent ratio at 524 nm.

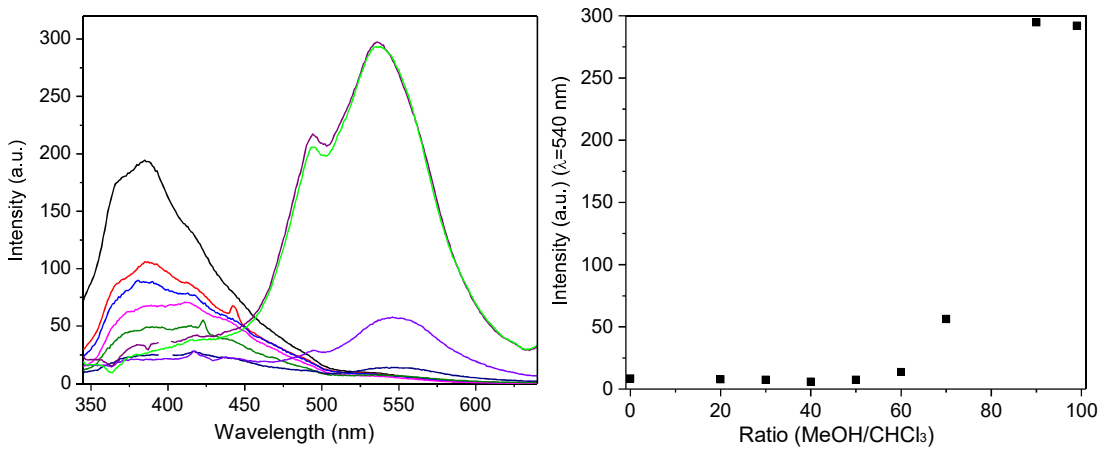


Figure 46. Emission spectra of aged 10^{-5} M solutions of (+)-**C1** (exc.: 330 nm) and plots of the emission intensities at 540 nm for (+)-**C1** as a function of the MeOH/$CHCl_3$ ratio, v/v.

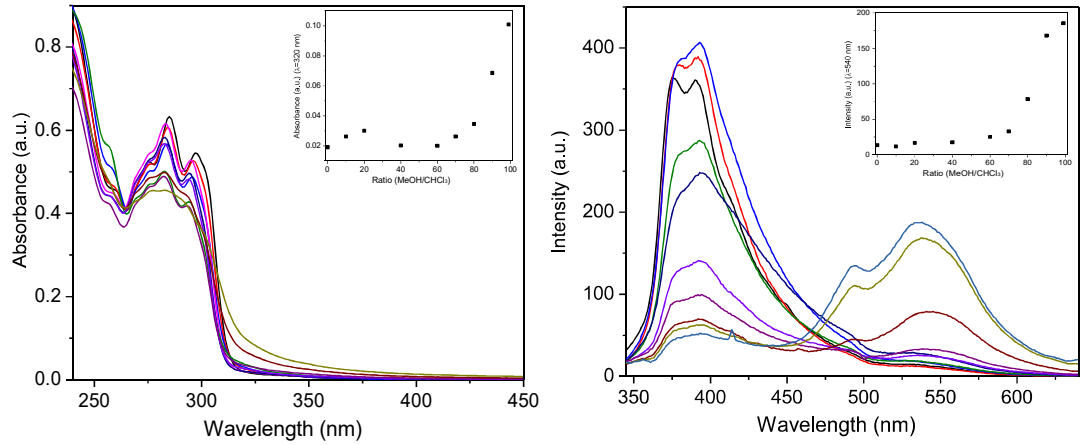


Figure 47. Absorption spectra of aged 10^{-5} M solutions of (–)-**C8** in $CHCl_3$/MeOH, inset: Absorbance in function of the solvent ratio at 320 nm. Emission spectra of 10^{-5} M solutions of (–)-**C8** in $CHCl_3$/MeOH (exc.: 330 nm), inset: Emission in function of the solvent ratio at 540 nm.

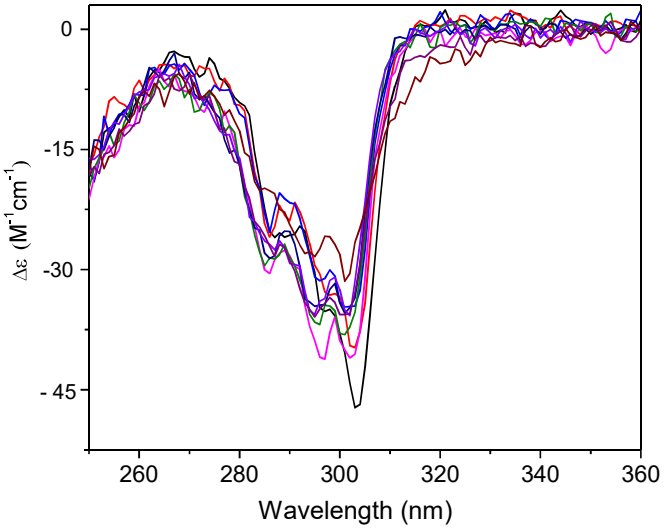


Figure 48. ECD spectra of aged 10^{-5} M solutions of (–)-**C8** in $CHCl_3$/MeOH

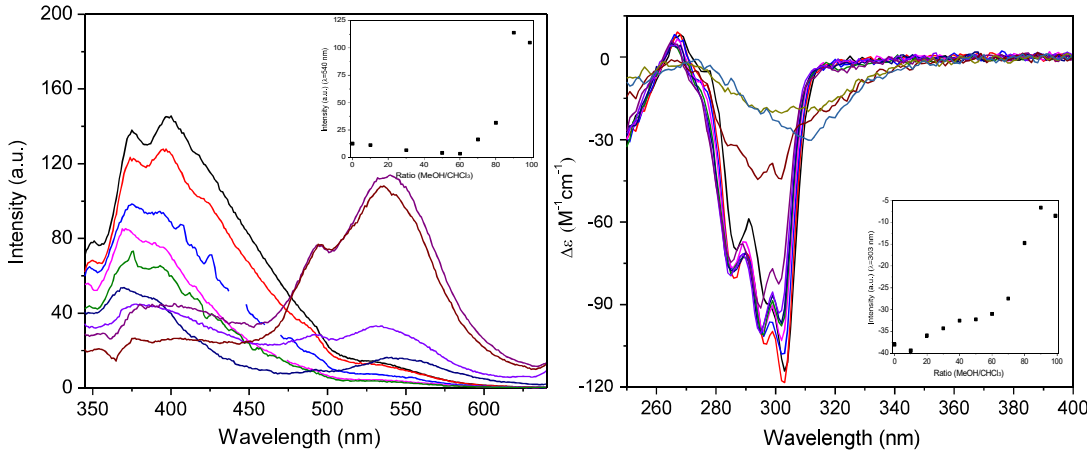


Figure 49. Emission and ECD spectra of aged 10^{-5} M solutions of (–)-**C2** in $CHCl_3$/MeOH

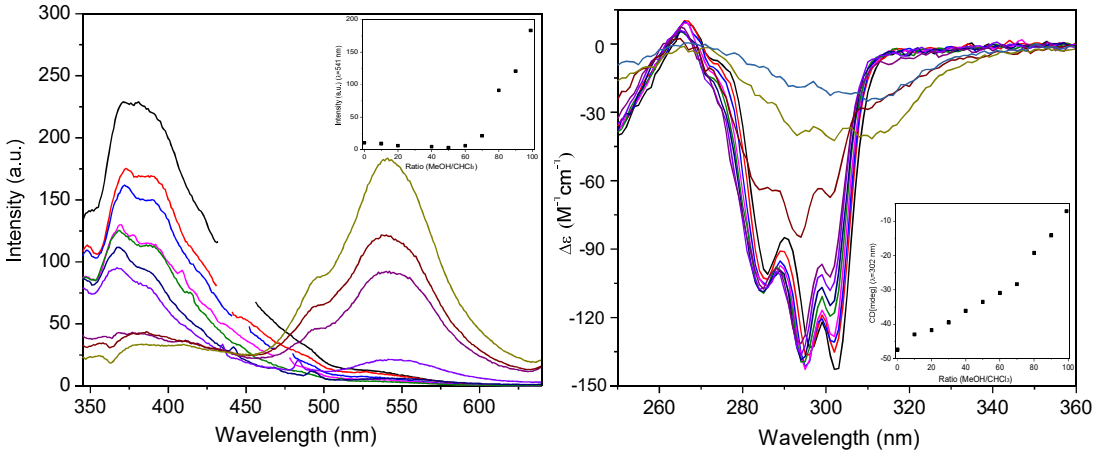


Figure 50. Emission and ECD spectra of aged 10^{-5} M solutions of (–)-**C3** in $CHCl_3$/MeOH

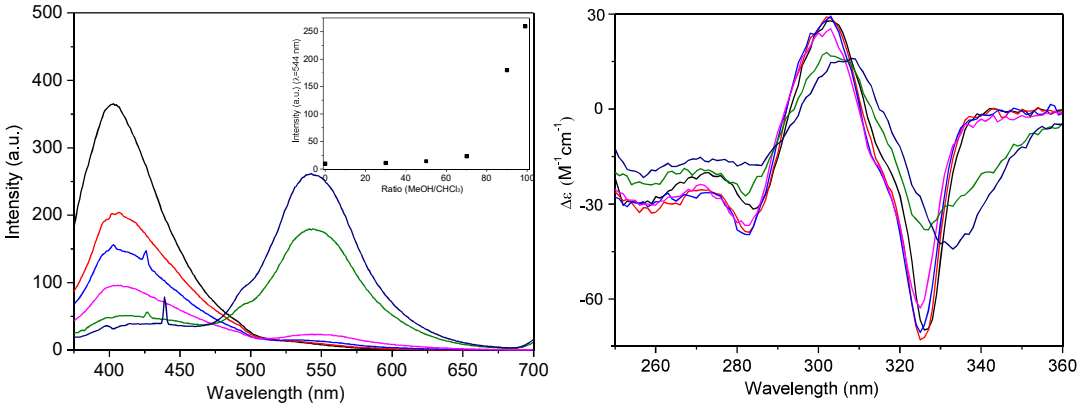


Figure 51. Emission and ECD spectra of fresh 10^{-5} M solutions of (–)-**C5** in $CHCl_3$/MeOH

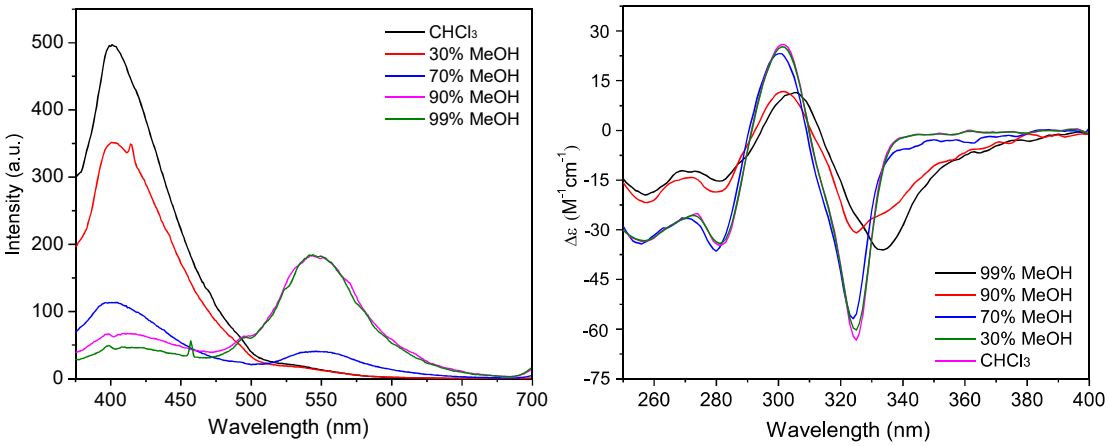
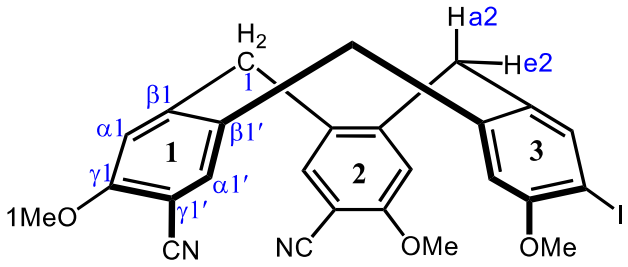


Figure 52. Emission and ECD spectra of fresh 10^{-5} M solutions of (−)**-C6** in $CHCl_3$/MeOH

Part II:

CTB(3OMe;2CN, I) 6



$C_{26}H_{21}IN_2O_3$
MW: 536.37

CTB(OMe,I) (0.5 g, 0.68 mmol), $Pd(PPh_3)_4$ (0.04 g, 0.034 mmol, 0.05 equiv) and zinc cyanide (0.085 g, 0.68 mmol, 1 equiv) were dissolved in 20 mL of dimethylformamide. The resulting mixture was allowed to react at 120 °C. After 2 hours, the solution was cooled to room temperature and dried under vacuum to give dark brown solid, which was purified by column chromatography on silica gel, using cyclohexane/dichloromethane/ethyl acetate (from 6:10:0 to 6:10:1.5) as eluent. The **CTB(3OMe;2CN,I)** target was afforded as a white solid power (0.127 g, 35%) along with the **CTB(3OMe;CN,2I)** by product (0.92 g, 21%).

^{1}H NMR (500 MHz, $CDCl_3$, 298 K): δ = 7.735 (s, 1 H; α3'-H), 7.526 (s, 3 H, α1'-H), 7.509 (s, 3 H, α2'-H), 6.906 (s, 3 H, α2-H), 6.870 (s, 3 H, α1-H), 6.720 (s, 3 H, α3-H), 4.780 (d, $^2J_{H,H}$ = 14.0 Hz, 1 H; a1-H), 4.710 (d, $^2J_{H,H}$ = 14.0 Hz, 1 H; a2-H), 4.684 (d, $^2J_{H,H}$ = 14.0 Hz, 1 H; a3-H), 3.939 (s, 3 H; OMe1-H), 3.935 (s, 3 H; OMe2-H), 3.882 (s, 3 H; OMe3-H), 3.688 (d, $^2J_{H,H}$ = 14.0 Hz, 1 H; e1-H), 3.668 (d, $^2J_{H,H}$ = 14.0 Hz, 1 H; e2-H), 3.651 (d, $^2J_{H,H}$ = 14.0 Hz, 1 H; e3-H) ppm.

^{13}C NMR (125 MHz, $CDCl_3$, 298 K): δ = 160.3 (γ1-C), 160.2 (γ2-C), 157.7 (γ3-C), 146.6 (β2-C), 145.7 (β1-C), 140.7 (α3'-C), 140.3 (β3-C), 135.2 (α1'-C), 135.1 (α2'-C), 131.8 (β1'-C), 131.6 (β3'-C), 130.5 (β2'-C), 116.4 (C≡N), 112.8 (α2-C), 112.6 (α1-C), 112.1 (α3-C), 101.1 (γ1'-C), 100.9 (γ2'-C), 84.8 (γ3'-C), 56.7 ($OCH_3$1), 56.5 ($OCH_3$2), 56.4 ($OCH_3$3), 36.7 ($CH_2$1, $CH_2$2), 37.4 ($CH_2$3) ppm.

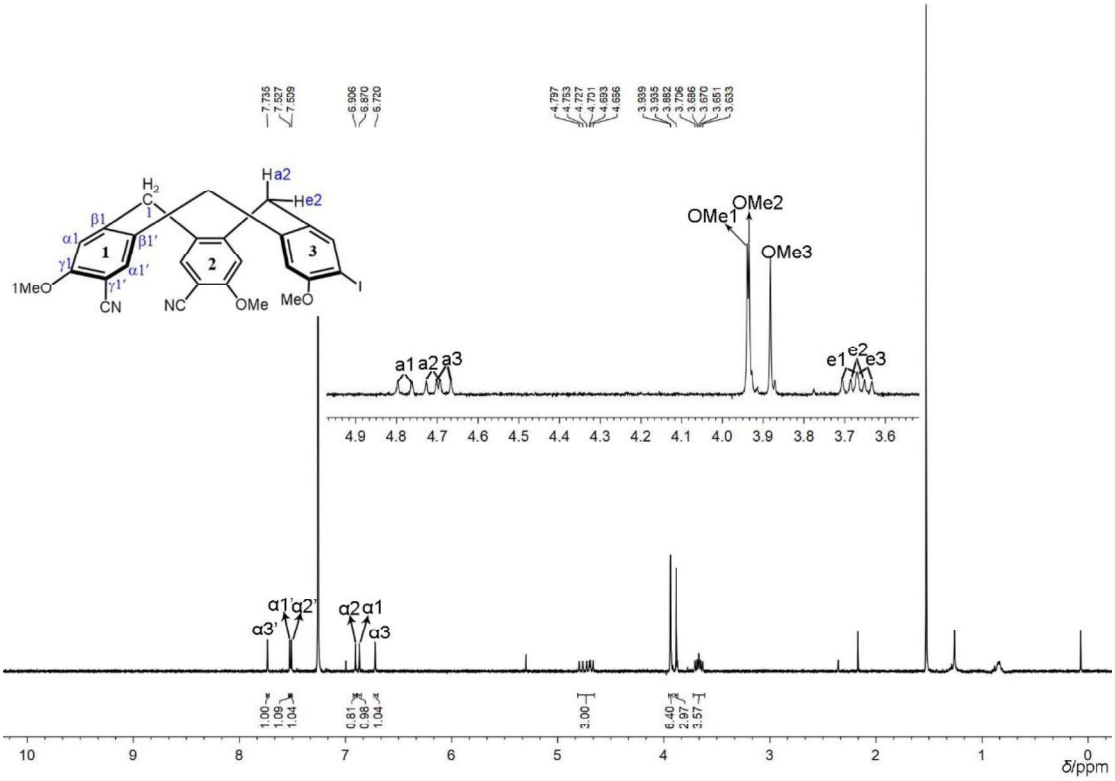
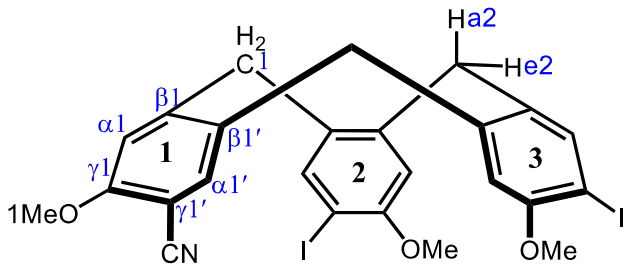


Figure 53. ^{1}H NMR spectrum of **CTB(3OMe;2CN,I)** in $CDCl_3$ at 298K.

CTB(3OMe;CN,2I) 7



$C_{25}H_{21}I_2NO_3$
MW: 637.26

^{1}H NMR (500 MHz, $CDCl_3$, 298 K): δ = 7.736 (s, 1 H; α3'-H), 7.717 (s, 3 H, α2'-H), 7.511 (s, 3 H, α1'-H), 6.885 (s, 3 H, α1-H), 6.743 (s, 3 H, α2-H), 6.706 (s, 3 H, α3-H), 4.720 (d, $^{2}J_{H,H}$ = 13.4 Hz, 1 H; a3-H), 4.693 (d, $^{2}J_{H,H}$ = 13.5 Hz, 1 H; a2-H), 4.624 (d, $^{2}J_{H,H}$ = 13.8 Hz, 1 H; a1-H), 3.922 (s, 3 H; OMe1-H), 3.872 (s, 6 H; OMe2, OMe3-H), 3.637 (d, $^{2}J_{H,H}$ = 13.4 Hz, 1 H; e3-H), 3.621 (d, $^{2}J_{H,H}$ = 13.5 Hz, 1 H; e2-H), 3.600 (d, $^{2}J_{H,H}$ = 13.8 Hz, 1 H; e1-H) ppm.

^{13}C NMR (125 MHz, $CDCl_3$, 298 K): δ= 160.0 (γ1-C), 157.4 (γ2, γ3-C), 146.4 (β1-C), 141.0 (β3-C), 140.6 (α3'-C),140.5 (α2'-C), 140.1 (β2-C), 135.0 (α1'-C), 132.8 (β3'-C), 131.7 (β1'-C), 131.5 (β2'-C), 116.4 (C≡N), 112.6(α1-C), 112.2 (α2-C), 112.0 (α3-C), 100.6 (γ1'-C), 84.6 (γ3'-C), 84.3 (γ2'-C), 56.6 ($OCH_3$2, $OCH_3$3), 56.2 ($OCH_3$1), 36.5 ($CH_2$3), 36.1 ($CH_2$1, $CH_2$2) ppm.

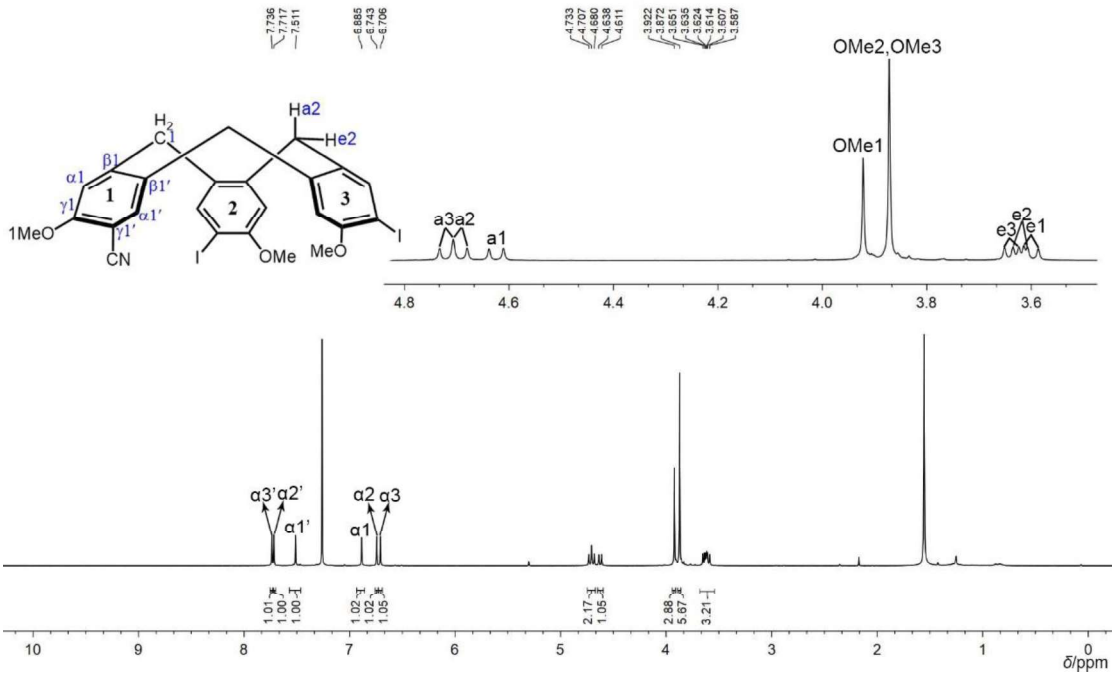
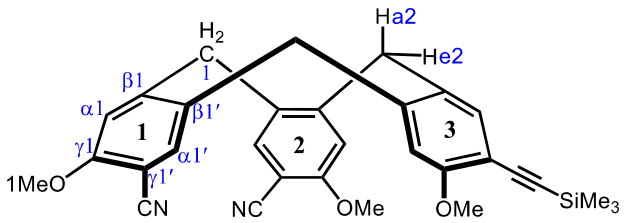


Figure 54. ^{1}H NMR spectrum of **CTB(3OMe;CN,2I)** in $CDCl_3$ at 298K.

CTB(3OMe;2CN,C$_2$TMS) 8



$C_{31}H_{30}N_2O_3Si$
MW: 506.68

CTB(3OMe;2CN,I) (0.085 g, 0.158 mmol), copper iodide (0.010 g, 0.0474, 0.3 equiv) and $PdCl_2(PPh_3)_2$ (0.031 g, 0.0474 mmol, 0.3 equiv) were dissolved in 18 mL of dimethylformamide, (trimethylsilyl) acetylene (0.046 g, 0.07 mL, 0.474 mmol, 3 equiv) and dried triethylamine 3.0 mL were added, and the resulting mixture was heated to 40 °C. After 2 hours, the solution was cooled to room temperature and dried under vacuum to give a dark brown solid, which was purified by column chromatography on silica gel, using toluene/ethyl acetate (9:1) as eluent, to give a pale yellow solid powder of **CTB(3OMe;2CN,C$_2$TMS)** (0.056 g, 70% yield).

^{1}H NMR (500 MHz, $CDCl_3$, 298 K): δ = 7.517 (s, 1 H; α1'-H), 7.507 (s, 3 H, α2'-H), 7.375 (s, 3 H, α3'-H), 6.937 (s, 3 H, α2-H), 6.867 (s, 3 H, α1-H), 6.751 (s, 3 H, α3-H), 4.773 (d, $^2J_{H,H}$ = 13.6 Hz, 1 H; a1-H), 4.703 (d, $^2J_{H,H}$ = 13.6 Hz, 1 H; a2-H), 4.693 (d, $^2J_{H,H}$ = 13.8 Hz, 1 H; a3-H), 3.941 (s, 3 H; OMe1,2-H), 3.877 (s, 3 H; OMe3-H), 3.678 (d, $^2J_{H,H}$ = 13.6 Hz, 1 H; e1-H), 3.664 (d, $^2J_{H,H}$ = 13.6 Hz, 1 H; e2-H), 3.651 (d, $^2J_{H,H}$ = 13.8 Hz, 1 H; e3-H), 0.239 (s, 9 H; $SiMe_3$-H) ppm.

^{13}C NMR (125 MHz, $CDCl_3$, 298 K): δ = 160.1 (γ1-C), 160.0 (γ2-C), 159.5 (γ3-C), 146.6 (β2-C), 145.5 (β1-C), 140.5 (β3-C), 135.3 (α1'-C), 135.1 (α3'-C), 134.9 (α2'-C), 131.5 (β1'-C), 130.4 (β2'-C), 129.3 (β3'-C), 116.2 (C≡N), 112.8 (α2-C), 112.4 (α1-C), 112.0 (α3-C), 111.9 (γ3'-C), 100.9 (γ2'-C), 100.6 (γ1'-C), 100.5 (ArC≡), 98.8 (≡CTMS), 56.2 ($OCH_3$3), 56.1 ($OCH_3$1,2), 36.7 ($CH_2$2), 36.5 ($CH_2$1), 36.4 ($CH_2$3), 0.0 Si(CH_3)$_3$ ppm.

Elemental analysis: Calcd for. $C_{31}H_{30}N_2O_3Si\cdot 2/3H_2O$, C 71.79, H 6.09, N 5.40, found

C 71.76, H 5.88, N 5.35.

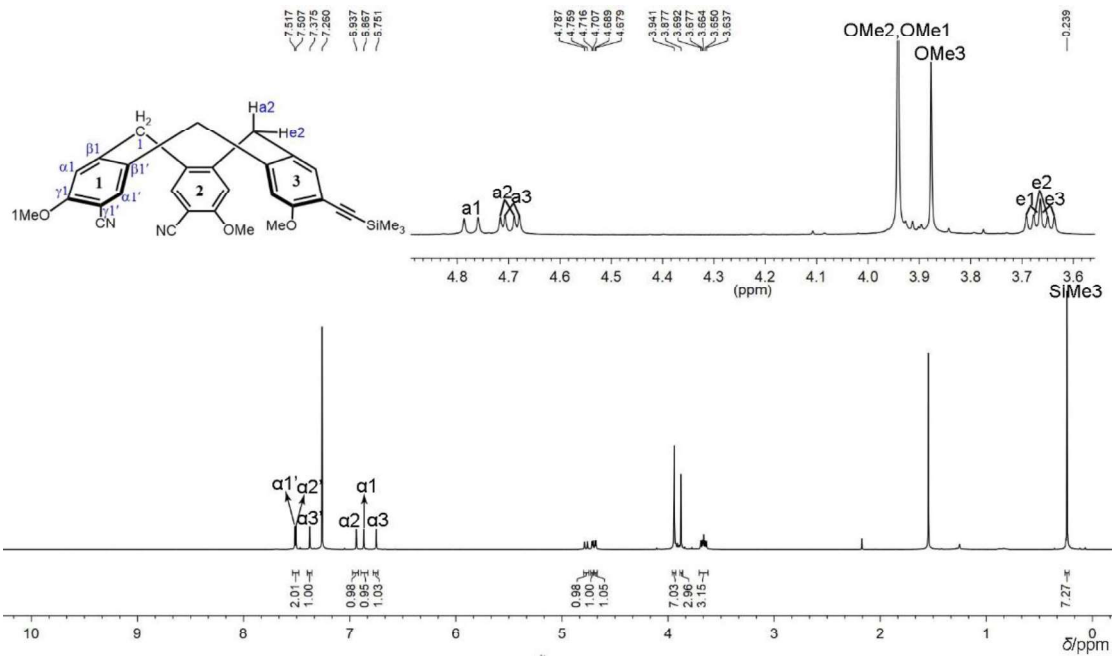
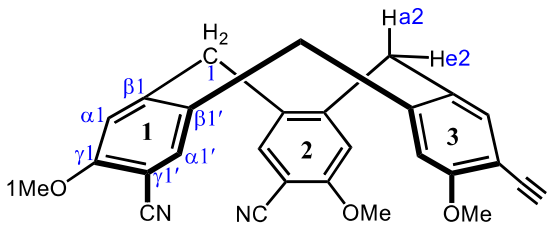


Figure 55. ^{1}H NMR spectrum of **CTB(3OMe;2CN,C$_2$TMS)** in $CDCl_3$ at 298K.

CTB(3OMe;2CN,C₂H) 10



$C_{28}H_{22}N_2O_3$
MW: 434.50

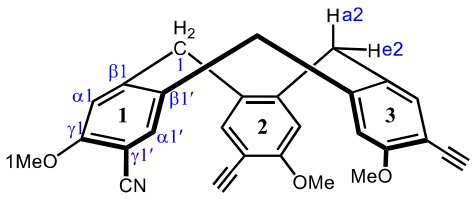
The intermediate **CTB(3OMe;2CN,C₂TMS)** (0.048 g, 0.1 mmol) was dissolved in 4 mL of THF. Tetrabutylammonium fluoride (0.5 mL of a 1 M solution in THF, 0.5 mmol) was added, and the mixture was allowed to react at room temperature for 4h. The THF was evaporated under vacuum, and distilled water (50 mL) was added. The resulting mixture was extracted three times (75 mL) with dichloromethane. The organic phases were washed with water, dried with anhydrous magnesium sulfate, and concentrated under vacuum to give a brown yellow solid powder **CTB(3OMe;2CN,C₂H)** (0.04 g, 97.5 % yield).

^{1}H NMR (500 MHz, $CDCl_3$, 298 K): δ = 7.535 (s, 1 H; α1'-H), 7.514 (s, 3 H, α2'-H), 7.421 (s, 3 H, α3'-H), 6.924 (s, 3 H, α2-H), 6.874 (s, 3 H, α1-H), 6.797 (s, 3 H, α3-H), 4.787 (d, $^2J_{H,H}$ = 14.0 Hz, 1 H; a1-H), 4.728 (d, $^2J_{H,H}$ = 14.0 Hz, 1 H; a2-H), 4.719 (d, $^2J_{H,H}$ = 14.0 Hz, 1 H; a3-H), 3.942 (s, 3 H; OMe1-H), 3.934 (s, 3 H; OMe2-H), 3.912 (s, 3 H; OMe3-H), 3.693 (d, $^2J_{H,H}$ = 14.0 Hz, 1 H; e1-H), 3.680 (d, $^2J_{H,H}$ = 14.0 Hz, 1 H; e2-H), 3.677 (d, $^2J_{H,H}$ = 14.0 Hz, 1 H; e3-H), 3.272 (s, 1 H, C_2H-H) ppm.

^{13}C NMR (125 MHz, $CDCl_3$, 298 K): δ = 160.3 (γ2-C), 160.2 (γ1-C), 159.9 (γ3-C), 146.7 (β2-C), 145.8 (β1-C), 141.1 (β3-C), 135.6 (α3'-C), 135.2 (α1'-C), 135.1 (α2'-C), 131.5 (β1'-C), 130.5 (β2'-C), 129.6 (β3'-C), 116.4 (C≡N), 112.9 (α2-C), 112.6 (α1-C), 112.1 (α3-C), 110.9 (γ3'-C), 101.2 (γ2'-C), 100.9 (γ1'-C), 81.5(≡CH), 79.6(ArC≡), 56.4 (O*C*H$_3$1, O*C*H$_3$2), 56.3 (O*C*H$_3$3), 36.9 (*C*H$_2$2), 36.8 (*C*H$_2$1), 37.6 (*C*H$_2$3) ppm.

Elemental analysis: Calcd for $C_{28}H_{22}N_2O_3 \cdot 1/3CH_2Cl_2 \cdot 1/3H_2O$, C 72.59, H 5.02, N 5.98, found C 72.77, H 4.98, N 6.03.

CTB(3OMe;CN,2C$_2$H) 11



$C_{29}H_{23}NO_3$
MW: 433.51

CTB(3OMe;CN,2I) (0.083 g, 0.13 mmol), copper iodide (0.003 g, 0.013 mmol, 0.1 equiv) and $PdCl_2(PPh_3)_2$ (0.009 g, 0.013 mmol, 0.1 equiv) were dissolved in 20 mL of dimethylformamide. (Trimethylsilyl) acetylene (0.038 g, 0.18 mL, 0.39 mmol, 3 equiv) and dried triethylamine 2.0 mL were added, and the mixture was heated to 40 °C. After 2 hours, the solution was cooled to room temperature and dried under vacuum to give a dark brown solid, which was purified by column chromatography on silica gel, using cyclohexane/ethyl acetate (7:2) as eluent, to give a pale yellow solid powder **CTB(3OMe;CN,2C$_2$TMS)** (0.045 g, 60% yield).

This intermediate **CTB(3OMe;CN,2C$_2$TMS)** (0.055 g, 0.1 mmol) was dissolved in 8 mL of THF. Tetrabutylammonium fluoride (1.0 mL of a 1 M solution in THF, 1.0 mmol) was added, and the mixture was allowed to react at room temperature for 4h. The THF was evaporated under vacuum, and distilled water (50 mL) was added. The resulting mixture was extracted three times (75 mL) with dichloromethane. The organic phases were washed with water, dried with anhydrous magnesium sulfate, and concentrated under vacuum to give a brown yellow solid powder **CTB(3OMe;2 CN,C$_2$H)** (0.04 g, 92.5 % yield).

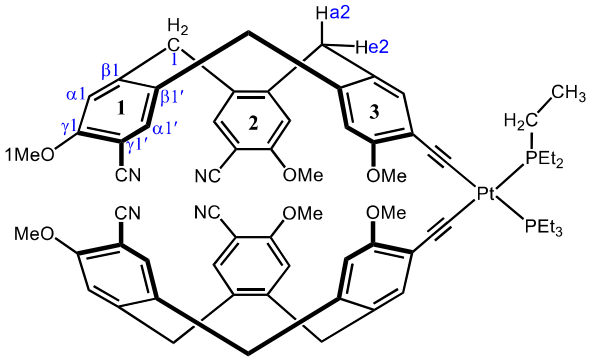
^{1}H NMR (500 MHz, $CDCl_3$, 298 K): δ = 7.521 (s, 1 H; α1'-H), 7.434 (s, 3 H, α3'-H), 7.411 (s, 3 H, α2'-H), 6.912 (s, 3 H, α1-H), 6.840 (s, 3 H, α2-H), 6.791 (s, 3 H, α3-H), 4.751 (d, $^2J_{H,H}$ = 13.8 Hz, 1 H; a3-H), 4.741 (d, $^2J_{H,H}$ = 13.5 Hz, 1 H; a2-H), 4.659 (d, $^2J_{H,H}$ = 13.8 Hz, 1 H; a1-H), 3.926 (s, 3 H; OMe1-H), 3.905 (s, 3 H; OMe3-H), 3.901 (s, 3 H; OMe2-H), 3.654 (d, $^2J_{H,H}$ = 13.8 Hz, 1 H; e3-H), 3.650 (d, $^2J_{H,H}$ = 13.5 Hz, 1 H; e2-H), 3.640 (d, $^2J_{H,H}$ = 13.8 Hz, 1 H; e1-H), 3.262 (s, 1 H, C_2H-H), 3.259 (s, 1 H,

C_2H-H) ppm.

^{13}C NMR (125 MHz, $CDCl_3$, 298 K): δ= 160.0 (γ1-C), 159.6 (γ2, γ3-C), 146.5 (β1-C), 141.8 (β2-C), 141.0 (β3-C), 135.6 (α2'-C), 135.4 (α3'-C), 135.0 (α1'-C), 131.4 (β1'-C), 130.5 (β3'-C), 129.6 (β2'-C), 116.4 (*C*≡N), 112.7 (α1-C), 112.2 (α2-C), 111.9 (α3-C), 110.5 (γ2'-C), 110.3 (γ3'-C), 100.5 (γ1'-C), 79.7(*C*≡*C*H), 56.2 (O*C*$H_3$1), 56.1 (O*C*$H_3$2, O*C*$H_3$3), 36.8 (*C*$H_2$1), 36.6 (*C*$H_2$2), 37.4 (*C*$H_2$3) ppm.

Elemental analysis: Calcd for $C_{29}H_{23}NO_3 \cdot 1/3CH_2Cl_2$, C 76.29, H 5.17, N 3.03, found C 76.23, H 5.31, N 3.11.

[*cis*-Pt(PEt$_3$)$_2$(CTB(3OMe; 2CN, C$_2$))$_2$Cu$^+$]Cl/I 12



$C_{68}H_{72}N_4O_6P_2Pt$
MW: 1298.38

CTB(3OMe;2CN,C$_2$H) (0.042 g, 0.1 mmol), *cis*-Pt(PEt$_3$)$_2$Cl$_2$ (0.025 g, 0.05 mmol, 0.5 equiv), copper iodide (0.002 g, 0.01 mmol, 0.2 equiv) and Et$_3$N (2.8 mmol, 400 µL, 28 equiv) were dissolved in 10 mL of dimethylformamide. The solution was allowed to react at room temperature. After 2 days, the solution was dried under vacuum to give a brown solid, which was purified by column chromatography on silica gel, using cyclohexane/dichloromethane/ethyl acetate (from 6:10:1 to 6:10:6 v/v) as eluent to give a pale yellow solid powder of **[*cis*-Pt(PEt$_3$)$_2$(CTB(3OMe;2CN,C$_2$))$_2$Cu$^+$]**Cl/I (0.032 g, 50%).

^{1}H NMR (Major isomer, 600 MHz, CD_2Cl_2, 298 K): δ = 8.559 (s, 2 H; α3'M-H), 7.591 (s, 2 H; α1'M-H), 7.435 (s, 2 H; α2'M-H), 7.423 (s, 2 H; α2M-H), 6.881 (s, 2 H; α1M-H), 6.715 (s, 2 H; α3M-H), 4.760 (d, $^2J_{H,H}$ = 13.5 Hz, 2 H; a3M-H), 4.738 (d, $^2J_{H,H}$ = 13.8 Hz, 2 H; a1M -H), 4.715 (d, $^2J_{H,H}$ = 13.5 Hz, 2 H; a2M-H), 4.042 (s, 6 H; OMe2M-H), 3.977 (s, 6 H; OMe1M-H), 3.808 (s, 6 H; OMe3M-H), 3.808 (d, $^2J_{H,H}$ = 13.5 Hz, 2 H; e2M-H), 3.721 (d, $^2J_{H,H}$ = 13.5 Hz, 2 H; e3M-H), 3.557 (d, $^2J_{H,H}$ = 13.8 Hz, 2 H; e1M-H), 2.071 (m, 12 H; CH_2-H), 1.162 (m, 18 H; CH_3-H) ppm.

^{1}H NMR (Minor isomer, 600 MHz, CD_2Cl_2, 298 K): δ = 8.443 (s, 2 H; α3'm-H), 7.594 (s, 2 H; α1'm-H), 7.527 (s, 2 H; α2'm-H), 7.351 (s, 2 H; α2m-H), 6.946 (s, 2 H; α1m-H), 6.754 (s, 2 H; α3m-H), 4.787 (d, $^2J_{H,H}$ = 13.8 Hz, 2 H; a1m-H), 4.765 (d, $^2J_{H,H}$ = 13.8 Hz, 2 H; a3m-H), 4.738 (d, $^2J_{H,H}$ = 13.8 Hz, 2 H; a2m-H), 3.967 (s, 6 H; OMe1m-H), 3.945 (s, 6 H; OMe2m-H), 3.863 (s, 6 H; OMe3m-H), 3.828 (d, $^2J_{H,H}$ = 13.8 Hz, 2

H; e2m-H), 3.714 (d, $^{2}J_{H,H}$ = 13.8 Hz, 2 H; e1m-H), 3.688 (d, $^{2}J_{H,H}$ = 13.8 Hz, 2 H; e3m-H), 2.071 (m, 12 H; CH_2-H), 1.162 (m, 18 H; CH_3-H) ppm.

^{31}P NMR (121 MHz, CD_2Cl_2, 298 K) δ = 4.18 ppm (M).

^{31}P NMR (121 MHz, CD_2Cl_2, 298 K) δ = 4.23 ppm (m).

Q-Tof-MS: Calcd. for $[C_{68}H_{72}N_4O_6P_2PtCu]^+$, 1361.92; found: 1361.38.

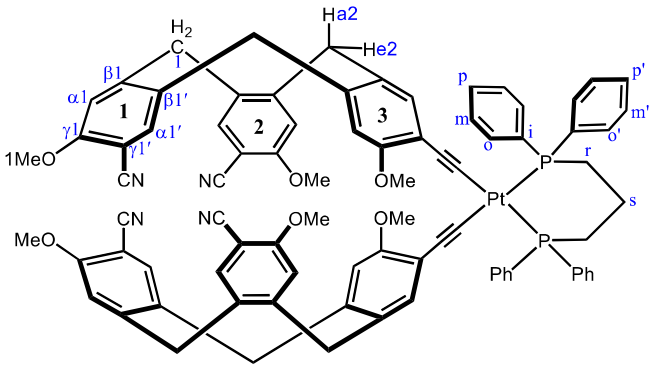
[*cis*-Pt(PEt$_3$)$_2$(Pd$_2$(dppp)$_2$ (CTB(3OMe;2CN,C$_2$))Cu$^+$](OTf)$_5$

[*cis*-Pt(PEt$_3$)$_2$(Pd$_2$(dppp)$_2$(CTB(3OMe;2CN,C$_2$))Cu$^+$](OTf)$_5$ (1.01 mg, 0.75 µmol) and [Pd(dppp)][OTf]$_2$ (1.25 mg, 1.5 µmol, 2 equiv) were mixed in CD_2Cl_2 (0.6 mL), and the suspension was stirred for 1.5 h to give a clear solution, which was analyzed by ^{1}H NMR spectroscopy (Manuscript **Figure 110**, **Page 133**)

Preparative separation for compound (±)-CTB(3OMe;2CN,C$_2$H)

About 57 mg of compound (±)-**CTB(3OMe;2CN,C$_2$H)** was dissolved in 65 mL of dichloromethane and applied to a (*S*,*S*)-Whelk-O1 (250 × 10 mm) column, using hexane/ethanol/dichloromethane 30:10:60 v/v/v as mobile phase; the flow-rate was 5 mL/min, and the UV detection was at 254 nm (Injections: 800 µL, every 6.0 minutes). Obtained 20.0 mg of the first eluted enantiomer with ee > 99%, 17.8 mg of the second eluted enantiomer with ee > 99% and 18 mg of a mixture.

[(Pt(dppp)((+)-CTB(3OMe;2CN,C$_2$))Cu$^+$]Cl/I 13



$C_{83}H_{68}N_4O_6P_2Pt$
MW: 1474.51

(+)-**CTB(3OMe;2CN,C$_2$H)** (0.008 g, 0.018 mmol), Pt(dppp)Cl$_2$ (0.006 g, 0.009 mmol,

0.5 equiv), copper iodide (0.001 g, 0.005 mmol, 0.25 equiv) and Et_3N (1.82 mmol, 250 μL) were dissolved in 6 mL of THF. The solution was allowed to react at room temperature. After 6 hours, the solvent was evaporated in vacuum and the residue futher dried under vacuum to give a yellow solid, which was purified by column chromatography on silica gel, using cyclohexane/acetone (4:3 v/v) as eluent. Obtained a pale yellow solid powder of **[(Pt(dppp)((+)-CTB(3OMe;2CN,C_2))Cu^+]**Cl/I (0.011 g, 81%).

^{1}H NMR (500 MHz, $CDCl_3$, 298 K): δ = 8.261 (s, 2 H; α3'-H), 7.742 (t, $^2J_{H,H}$ = 7.8 Hz, $^2J_{H,H}$ = 7.8 Hz, 4 H, o-H), 7.655 (t, $^2J_{H,H}$ = 7.4 Hz, 4 H, o'-H), 7.446 (s, 2 H, α1'-H), 7.435 (s, 2 H, α2'-H), 7.367 (d, $^2J_{H,H}$ = 7.5 Hz, 2 H, p-H), 7.310 (t, $^2J_{H,H}$ = 7.5 Hz, 4 H, m-H), 7.235 (s, 2 H, α2-H), 7.104 (dt, 6 H, p', m'-H), 6.847 (s, 2 H, α1-H), 6.415 (s, 2 H, α3-H), 4.752 (d, $^2J_{H,H}$ = 13.6 Hz, 2 H; a1-H), 4.623 (d, $^2J_{H,H}$ = 13.8 Hz, 2 H; a3-H), 4.565 (d, $^2J_{H,H}$ = 13.3 Hz, 2 H; a2-H), 3.927 (s, 6 H; OMe1-H), 3.867 (s, 6 H; OMe2-H), 3.730 (d, $^2J_{H,H}$ = 13.3 Hz, 2 H; e2-H), 3.608 (d, $^2J_{H,H}$ = 13.6 Hz, 2 H; e1-H), 3.537 (d, $^2J_{H,H}$ = 13.8 Hz, 2 H; e3-H), 3.170 (s, 6 H; OMe3-H), 2.481 (m, 4 H; r-H), 2.056 (m, 2 H; s-H) ppm.

^{31}P NMR (162 MHz, CD_2Cl_2, 298 K) δ = –9.36 ppm.

Q-Tof-MS: Calcd. for $[C_{83}H_{68}N_4O_6P_2PtCu]^+$ 1538.06 and $[(C_{83}H_{68}N_4O_6P_2Pt)Na^+]$ 1497.50; found 1537.38 and 1497.42.

[(Pt(dppp)(Pd_2(dppp)$_2$((+)-CTB(3OMe;2CN,C_2))Cu^+](OTf)$_5$

[(Pt(dppp)((+)-CTB(3OMe;2CN,C_2))Cu]Cl/I (1.51 mg, 1.0 μmol) and [Pd(dppp)][OTf]$_2$ (1.78 mg, 2.17 μmol, 2 equiv) were mixed in CD_2Cl_2 (0.6 mL), and the suspension was stirred for 1.5h to give a clear yellow solution, which was analyzed by ^{1}H NMR spectroscopy (Manuscript **Figure 111**, **Page 134**)

[(Pt(dppp)(CTB(3OMe;2CN,C_2))] and **[(Pt(dppp) (CTB(3OMe;2CN,C_2))Cu]Cl/I 18**

CTB(3OMe;2CN,C_2H) (0.044 g, 0.101 mmol), Pt(dppp)Cl_2 (0.047 g, 0.0767 mmol,

0.75 equiv), Et_3N (2.64 mmol, 360 µL) and copper iodide (0.002 g, 0.010 mmol, 0.1 equiv) were dissolved in 15 mL of THF. The solution was allowed to react at 45 ˚C. After 2 days, the solvent was evaporated under vacuum and the residue further dried under vacuum to give a yellow solid, which was purified by column chromatography on silica gel, using CyH/CH_2Cl_2/EtOAc (3:5:0-2 v/v) as eluent. Obtained a pale yellow solid powder of **[(Pt(dppp)(CTB(3OMe;2CN,C2))Cu]**Cl/I (0.025 g, 32%) and **[(Pt(dppp) (CTB(3OMe;2CN,C2))]** (0.024 g, 32%).

^{1}H NMR (Minor isomer, 400 MHz, $CDCl_3$, 298 K): δ = 7.913-7.708 (t, 8 H, o-H), 7.466 (s, 2 H; α1'm-H), 7.446 (s, 2 H; α2'm-H), 7.390-7.215 (t, 12 H, p, m-H), 6.830 (s, 2 H; α1m-H), 6.756 (s, 2 H; α3'm-H), 6.667 (s, 2 H; α2m-H), 6.524 (s, 2 H; α3m-H), 4.744 (d, $^2J_{H,H}$ = 13.4 Hz, 2 H; a1m-H), 4.566 (d, $^2J_{H,H}$ = 14.0 Hz, 2 H; a3m-H), 4.539 (d, $^2J_{H,H}$ = 13.2 Hz, 2 H; a2m-H), 3.915 (s, 6 H; OMe1m-H), 3.580 (s, 6 H; OMe2m-H), 3.539 (s, 6 H; OMe3m-H), 3.610(d, $^2J_{H,H}$ = 13.4 Hz, 2 H; e1m-H), 3.526 (d, $^2J_{H,H}$ = 14.0 Hz, 2 H; e3m-H), 3.388 (d, $^2J_{H,H}$ = 13.2 Hz, 2 H; e2m-H), 2.442 (m, 12 H; r-H), 2.045 (m, 18 H; s-H) ppm.

^{1}H NMR (Major isomer, 400 MHz, $CDCl_3$, 298 K): δ = 7.913-7.708 (t, 8 H, o-H), 7.466 (s, 4 H; α1', 2'M-H), 7.390-7.215 (t, 12 H, p, m-H), 6.855 (s, 2 H; α1M-H), 6.848 (s, 2 H; α3'M-H), 6.635 (s, 2 H; α2M-H), 6.529 (s, 2 H; α3M-H), 4.743 (d, $^2J_{H,H}$ = 13.4 Hz, 2 H; a1M-H), 4.569 (d, $^2J_{H,H}$ = 14.0 Hz, 2 H; a3M-H), 4.535 (d, $^2J_{H,H}$ = 13.2 Hz, 2 H; a2M-H), 3.930 (s, 6 H; OMe1M-H), 3.530 (s, 6 H; OMe3M-H), 3.399 (s, 6 H; OMe2M-H), 3.610(d, $^2J_{H,H}$ = 13.4 Hz, 2 H; e1M-H), 3.526 (d, $^2J_{H,H}$ = 14.0 Hz, 2 H; e3M-H), 3.415 (d, $^2J_{H,H}$ = 13.2 Hz, 2 H; e2M-H), 2.452 (m, 12 H; r-H), 2.072 (m, 18 H; s-H) ppm.

^{1}H NMR (Minor isomer, 600 MHz, $C_2D_2Cl_4$, 298 K): δ= 7.765-7.674 (t, 8 H, o-H), 7.492 (s, 2 H; α1'm-H), 7.483 (s, 2 H; α2'm-H), 7.366-7.122 (t, 12 H, p, m-H), 6.851 (s, 2 H; α1m-H), 6.793 (s, 2 H; α3'm-H), 6.749 (s, 2 H; α2m-H), 6.507 (s, 2 H; α3m-H), 4.772 (d, $^2J_{H,H}$ = 13.2 Hz, 2 H; a1m-H), 4.616 (d, $^2J_{H,H}$ = 13.5 Hz, 2 H; a3m-H), 4.568 (d, $^2J_{H,H}$ = 13.2 Hz, 2 H; a2m -H), 3.928 (s, 6 H; OMe1m-H), 3.685 (s, 6 H;

OMe2m-H), 3.550 (s, 6 H; OMe3m-H), 3.645(d, $^{2}J_{H,H}$ = 13.2 Hz, 2 H; e1m-H), 3.545 (d, $^{2}J_{H,H}$ = 13.5 Hz, 2 H; e3m-H), 3.464 (d, $^{2}J_{H,H}$ = 13.2 Hz, 2 H; e2m-H), 2.452 (m, 12 H; r-H), 2.072 (m, 18 H; s-H) ppm.

^{1}H NMR (Major isomer, 600 MHz, $C_2D_2Cl_4$, 298 K): δ = 7.765-7.674 (t, 8 H, o-H), 7.496 (s, 2 H; α2'M-H), 7.492 (s, 2 H; α1'M-H), 7.366-7.122 (t, 12 H, p, m-H), 6.862 (s, 2 H; α1M-H), 6.809 (s, 2 H; α3'M-H), 6.738 (s, 2 H; α2M-H), 6.507 (s, 2 H; α3M-H), 4.772 (d, $^{2}J_{H,H}$ = 13.2 Hz, 2 H; a1M-H), 4.607 (d, $^{2}J_{H,H}$ = 13.5 Hz, 2 H; a3M-H), 4.568 (d, $^{2}J_{H,H}$ = 13.2 Hz, 2 H; a2M-H), 3.936 (s, 6 H; OMe1M-H), 3.611 (s, 6 H; OMe2M-H), 3.574 (s, 6 H; OMe3M-H), 3.645(d, $^{2}J_{H,H}$ = 13.2 Hz, 2 H; e1M-H), 3.545 (d, $^{2}J_{H,H}$ = 13.5 Hz, 2 H; e3M-H), 3.464 (d, $^{2}J_{H,H}$ = 13.2 Hz, 2 H; e2M-H), 2.452 (m, 12 H; r-H), 2.072 (m, 18 H; s-H) ppm.

^{1}H NMR (Minor isomer, 400 MHz, CD_2Cl_2, 298 K): δ = 7.834-7.751 (t, 8 H, o-H), 7.508 (s, 2 H; α1'm-H), 7.503 (s, 2 H; α2'm-H), 7.366-7.254 (t, 12 H, p, m-H), 6.877 (s, 2 H; α1m-H), 6.626 (s, 2 H; α3'm-H), 6.702 (s, 2 H; α2m-H), 6.586 (s, 2 H; α3m-H), 4.760 (d, $^{2}J_{H,H}$ = 13.4 Hz, 2 H; a1m-H), 4.614 (d, $^{2}J_{H,H}$ = 14.0 Hz, 2 H; a3m-H), 4.587 (d, $^{2}J_{H,H}$ = 13.2 Hz, 2 H; a2m-H), 3.909 (s, 6 H; OMe1m-H), 3.641 (s, 6 H; OMe3m-H), 3.621 (s, 6 H; OMe2m-H), 3.648 (d, $^{2}J_{H,H}$ = 13.4 Hz, 2 H; e1m-H), 3.568 (d, $^{2}J_{H,H}$ = 14.0 Hz, 2 H; e3m-H), 3.434 (d, $^{2}J_{H,H}$ = 13.2 Hz, 2 H; e2m-H), 2.426 (m, 12 H; r-H), 2.005 (m, 18 H; s-H) ppm.

^{1}H NMR (Major isomer, 400 MHz, CD_2Cl_2, 298 K): δ = 7.834-7.751 (t, 8 H, o-H), 7.512 (s, 4 H; α 2'M-H), 7.508 (s, 4 H; α1'M-H), 7.366-7.254 (t, 12 H, p, m-H), 6.889 (s, 2 H; α1M-H), 6.675 (s, 2 H; α3'M-H), 6.709 (s, 2 H; α2M-H), 6.586 (s, 2 H; α3M-H), 4.760 (d, $^{2}J_{H,H}$ = 13.4 Hz, 2 H; a1M-H), 4.614 (d, $^{2}J_{H,H}$ = 13.6 Hz, 2 H; a3M -H), 4.594 (d, $^{2}J_{H,H}$ = 13.2 Hz, 2 H; a2M-H), 3.918 (s, 6 H; OMe1M-H), 3.636 (s, 6 H; OMe3M-H), 3.571 (s, 6 H; OMe2M-H), 3.648 (d, $^{2}J_{H,H}$ = 13.6 Hz, 2 H; e1M-H), 3.568 (d, $^{2}J_{H,H}$ = 14.0 Hz, 2 H; e3M-H), 3.458 (d, $^{2}J_{H,H}$ = 13.4 Hz, 2 H; e2M-H), 2.426 (m, 12 H; r-H), 2.00 (m, 18 H; s-H) ppm.

^{13}C NMR (Minor isomer, 125 MHz, $CDCl_3$, 298 K): δ= 159.98 (γ1m-C), 159.87 (γ2m-

C), 158.94 (γ3m-C), 147.41 (β2m-C), 145.65 (β1m-C), 136.38 (β3m-C), 135.17 (α1'm-C), 134.83 (α2'm-C), 134.83 (α3'm-C), 134.05-133.59 (o-C), 132.26 (β1'm -C), 130.56 (β2'm-C), 130.39 (p-C), 128.48 (β3'm-C), 117.36 (mm-C), 117.36 (γ3'm-C),116.59/116.57 (*C*m≡N), 112.93 (α2m -C), 112.46 (α1m-C), 112.29 (α3m-C), 105.41 (*C*≡*C*), 100.60 (γ1'm-C), 100.18 (γ2'm-C), 56.29-55.99 (O*C*$H_3$1,2,3), 36.55 (*C*$H_2$2), 36.90 (*C*$H_2$1), 36.27 (*C*$H_2$3), 26.41 (*C*$H_2$$CH_3$), 20.50 ($CH_2$*C*$H_3$) ppm.

^{13}C NMR (Major isomer, 125 MHz, $CDCl_3$, 298 K): δ = 159.96 (γ1M-C), 159.83 (γ2M-C), 158.94 (γ3M-C), 147.22 (β2M-C), 145.63 (β1M-C), 136.33 (β3M-C), 135.27 (α1'M-C), 134.65 (α2'M-C), 134.65 (α3'M-C), 134.05-133.59 (o-C), 132.14 (β1'M-C), 130.18 (β2'M-C), 130.39 (p-C), 128.43 (β3'M-C), 117.36 (mM-C), 117.36 (γ3'M-C),116.51/116.46 (*C*M≡N), 113.07 (α2M-C), 112.29 (α1M-C), 112.24 (α3M-C), 105.41 (*C*≡*C*M), 100.66 (γ1'M-C), 100.12 (γ2'M-C), 56.29-55.99 (O*C*$H_3$1,2,3), 36.55 (*C*$H_2$1), 36.90 (*C*$H_2$2), 36.27 (*C*$H_2$3), 26.41 (*C*$H_2$$CH_3$), 20.50 ($CH_2$*C*$H_3$) ppm.

[*cis*-Pt(PEt_3)$_2$(CTB(3OMe;2CN,C_2))$_2$] 20

CTB(3OMe;2 CN, C_2H) (0.060 g, 0.138 mmol), *cis*-Pt(PEt_3)$_2$$Cl_2$ (0.034 g, 0.069 mmol, 0.5 equiv.), Et_3N (2.76 mmol, 380 μL) and copper iodide (0.0027 g, 0.014 mmol, 0.1 equiv) were dissolved in 20 mL of THF. The solution was allowed to react at 55 ˚C. After 8 hours, the solvent was evaporated under vacuum and the residue further dried under vacuum to give a yellow solid, which then was dissolved in 30 mL $CHCl_3$. 20 mg NaCN dissolved in 20 mL of distilled water were added into the $CHCl_3$ solution and the reaction mixture stirred overnight. The organic phase was separeated, the aqueous phase was washed with $CHCl_3$, and the combined organic phases were dried with anhydrous magnesium sulfate, filtered, then concentrated to give a yellow solid powder, which was purified by column chromatography on silica gel, using CyH/CH_2Cl_2/EtOAc (3:5:0-1 v/v) as eluent. Obtained a pale yellow solid powder of **[*cis*-Pt(PEt_3)$_2$(CTB(3OMe; 2CN,C_2))$_2$]** (0.058 g, 66%).

^{1}H NMR (Minor isomer, 500 MHz, $CDCl_3$, 298 K): δ = 7.532 (s, 2 H; α1'm-H), 7.504 (s, 2 H; α2'm-H), 7.446 (s, 2 H; α3'm-H), 6.893 (s, 2 H; α1m-H), 6.788 (s, 2 H; α2m-

H); 6.673 (s, 2 H; α3m-H), 4.799 (d, $^{2}J_{H,H}$ = 13.3 Hz, 2 H; a1m-H), 4.660 (d, $^{2}J_{H,H}$ = 14.0 Hz, 2 H; a3m -H), 4.654 (d, $^{2}J_{H,H}$ = 13.5 Hz, 2 H; a2m-H), 3.955 (s, 6 H; OMe1m-H), 3.803 (s, 6 H; OMe3m-H), 3.386 (s, 6 H; OMe2m-H), 3.650 (d, $^{2}J_{H,H}$ = 13.3 Hz, 2 H; e1m-H), 3.612 (d, $^{2}J_{H,H}$ = 14.0 Hz, 2 H; e3m-H), 3.579 (d, $^{2}J_{H,H}$ = 13.5 Hz, 2 H; e2m-H), 2.065 (m, 12 H; CH_2-H), 1.102 (m, 18 H; CH_3-H) ppm.

^{1}H NMR (Major isomer, 500 MHz, $CDCl_3$, 298 K): δ = 7.523 (s, 2 H; α1'M-H), 7.466 (s, 2 H; α2'M-H), 7.393 (s, 2 H; α3'M-H), 6.855 (s, 2 H; α1M-H); 6.865 (s, 2 H; α2M-H), 6.674 (s, 2 H; α3M-H), 4.799 (d, $^{2}J_{H,H}$ = 13.5 Hz, 2 H; a1M-H), 4.669 (d, $^{2}J_{H,H}$ = 14.0 Hz, 2 H; a3M-H), 4.622 (d, $^{2}J_{H,H}$ = 13.5 Hz, 2 H; a2M-H), 3.928 (s, 6 H; OMe1M-H), 3.796 (s, 6 H; OMe3M-H), 3.707 (s, 6 H; OMe2M-H), 3.650 (d, $^{2}J_{H,H}$ = 13.5 Hz, 2 H; e1M-H), 3.612 (d, $^{2}J_{H,H}$ = 14.0 Hz, 2 H; e3M-H), 3.573 (d, $^{2}J_{H,H}$ = 13.5 Hz, 2 H; e2M-H), 2.065 (m, 12 H; CH_2-H), 1.102 (m, 18 H; CH_3-H) ppm.

^{13}C NMR (Minor isomer, 125 MHz, $CDCl_3$, 298 K): δ = 160.23 (γ1m-C), 160.08 (γ2m-C), 159.43 (γ3m-C), 147.15 (β2m-C), 145.82 (β1m-C), 136.79 (β3m-C), 135.22 (α1'm-C), 134.84 (α2'm-C), 134.83 (α1'm-C), 134.84 (α3'm-C), 132.15 (β1'm-C), 130.58 (β2'm-C), 128.80 (β3'm-C), 117.62 (γ3'm-C), 116.75 (*C*1m ≡N), 116.75 (*C*2m ≡N), 113.16 (α2m-C), 112.84 (α1m-C), 111.67 (α3m-C), 101.45(*C*≡*C*m), 100.76 (γ1'm-C), 100.47 (γ2'm-C), 56.51 (O*C*$H_3$1m), 56.03 (O*C*$H_3$2m), 55.85 (O*C*$H_3$3m), 36.77 (*C*$H_2$1m), 36.51 (*C*$H_2$3m), 37.17 (*C*$H_2$2m), 17.16 (*C*$H_2$$CH_3$), 8.61 ($CH_2$*C*$H_3$) ppm.

^{13}C NMR (Major isomer, 125 MHz, $CDCl_3$, 298 K): δ= 160.24 (γ1M-C), 160.08 (γ2M-C), 159.38 (γ3M-C), 147.53 (β2M-C), 145.85 (β1M-C), 136.79 (β3M-C), 135.22 (α1'M-C), 134.84 (α1'M-C), 134.68 (α3' M-C), 134.84 (α2'M-C), 132.40 (β1'M -C), 130.58 (β2' M-C), 128.91 (β3'M-C), 117.62 (γ3'M-C), 116.64 (*C*1M ≡N),116.64 (*C*2M ≡N), 113.41 (α2M-C), 112.56 (α1M-C), 111.69 (α3M-C), 101.45(*C*≡*C*M), 100.85 (γ1'M-C), 100.38 (γ2'M-C), 56.44 (O*C*$H_3$1M), 56.43 (O*C*$H_3$2M), 55.83 (O*C*$H_3$3M), 36.77 (*C*$H_2$1M), 36.51 (*C*$H_2$3M), 37.17 (*C*$H_2$2M), 17.16 (*C*$H_2$$CH_3$), 8.61 ($CH_2$*C*$H_3$) ppm.

^{1}H NMR (Minor isomer, 500 MHz, $C_2D_2Cl_4$, 298 K): δ = 7.561 (s, 2 H; α1'm-H), 7.511

(s, 2 H; α2'm-H), 7.496 (s, 2 H; α3'm-H), 6.917 (s, 2 H; α2m-H), 6.890 (s, 2 H; α1m-H), 6.701 (s, 2 H; α3m-H), 4.817 (d, $^{2}J_{H,H}$ = 13.2 Hz, 2 H; a1m-H); 4.694 ($^{2}J_{H,H}$ = 13.2 Hz, 2 H; a3m-H); 4.667 (d, $^{2}J_{H,H}$ = 13.2 Hz, 2 H; a2m-H); 3.956 (s, 6 H; OMe1m-H), 3.858 (s, 6 H; OMe3m -H), 3.733 (s, 6 H; OMe2m-H); 3.679 (d, $^{2}J_{H,H}$ = 13.2 Hz, 2 H; e1m-H); 3.654 (d, $^{2}J_{H,H}$ = 13.2 Hz, 2 H; e3m-H); 3.630 (d, $^{2}J_{H,H}$ = 13.2 Hz, 2 H; e2m-H); 2.016 (m, 12 H; CH_2-H), 1.084 (m, 18 H; CH_3-H) ppm.

^{1}H NMR (Major isomer, 500 MHz, $C_2D_2Cl_4$, 298 K): δ = 7.557 (s, 2 H; α1'M-H), 7.496 (s, 2 H; α2'M-H), 7.448 (s, 2 H; α3'M-H), 6.901 (s, 2 H; α2M-H), 6.874 (s, 2 H; α1M-H), 6.695 (s, 2 H; α3M-H); 4.817 (d, $^{2}J_{H,H}$ = 13.2 Hz, 2 H; a1M-H); 4.694 ($^{2}J_{H,H}$ = 13.2 Hz, 2 H; a3M-H); 4.667 (d, $^{2}J_{H,H}$ = 13.2 Hz, 2 H; a2M-H); 3.942 (s, 6 H; OMe1M-H), 3.858 (s, 6 H; OMe3M -H), 3.700 (s, 6 H; OMe2M-H), 3.679 (d, $^{2}J_{H,H}$ = 13.2 Hz, 2 H; e1M-H); 3.654 (d, $^{2}J_{H,H}$ = 13.2 Hz, 2 H; e3M-H); 3.630 (d, $^{2}J_{H,H}$ = 13.2 Hz, 2 H; e2M-H), 2.016 (m, 12 H; CH_2-H), 1.084 (m, 18 H; CH_3-H) ppm.

^{13}C NMR (Minor isomer, 125 MHz, $C_2D_2Cl_4$, 298 K): δ = 159.92 (γ1m-C), 159.74 (γ2m-C), 158.60 (γ3m-C), 147.17 (β2m-C), 145.87 (β1m-C), 136.62 (β3m-C), 135.04 (α1'm-C), 134.66 (α2'm-C), 134.36 (α3'm-C), 132.02 (β1'm-C), 130.41 (β2'm-C), 128.74 (β3'm-C), 116.69 (γ3'm-C), 116.55 (*C*1,2m ≡N), 113.30 (α2m-C), 112.35 (α1m-C), 111.00 (α3m-C), 101.45(*C*≡*C*m), 100.26 (γ1'm-C), 99.98 (γ2'm-C), 56.31 (O*C*H$_3$1m), 56.25 (O*C*H$_3$2m), 55.50 (O*C*H$_3$3m), 37.00 (*C*H$_2$3m), 36.48 (*C*H$_2$1m), 36.28 (*C*H$_2$2m), 16.76 (*C*H$_2$CH$_3$), 8.30 (CH$_2$*C*H$_3$) ppm.

^{13}C NMR (Major isomer, 125 MHz, $C_2D_2Cl_4$, 298 K): δ = 159.89 (γ1M-C), 159.72 (γ2M-C), 158.60 (γ3M-C), 147.30 (β2M-C), 145.87 (β1M-C), 136.55 (β3m-C), 135.01 (α1'M-C), 134.66 (α2'M-C), 134.36 (α3' M-C), 132.12 (β1'M -C), 130.38 (β2' M-C), 128.78 (β3'M-C), 116.60 (γ3'M-C), 116.50 (*C*1,2M ≡N), 113.25 (α2M-C), 112.35 (α1M-C), 111.96 (α3M-C), 101.45(*C*≡*C*M), 100.24 (γ1'M-C), 99.89 (γ2'M-C), 56.31 (O*C*H$_3$1M), 56.25 (O*C*H$_3$2M), 55.50 (O*C*H$_3$3M), 36.92 (*C*H$_2$3M), 36.48 (*C*H$_2$1M), 36.28 (*C*H$_2$2M), 16.76 (*C*H$_2$CH$_3$), 8.30 (CH$_2$*C*H$_3$) ppm.

^{1}H NMR (Minor isomer, 500 MHz, CD_2Cl_2, 298 K): δ = 7.568 (s, 2 H; α1'm-H), 7.547

(s, 2 H; α2'm-H), 7.386 (s, 2 H; α3'm-H), 6.928 (s, 2 H; α2m-H), 6.926 (s, 2 H; α1m-H), 6.732 (s, 2 H; α3m-H), 4.804 (d, $^{2}J_{H,H}$ = 14.0 Hz, 2 H; a1m -H); 4.702 ($^{2}J_{H,H}$ = 14.2 Hz, 2 H; a3m-H); 4.684 (d, $^{2}J_{H,H}$ = 14.0 Hz, 2 H; a2m-H); 3.943 (s, 6 H; OMe1m-H), 3.834 (s, 6 H; OMe3m -H), 3.623 (s, 6 H; OMe2m-H); 3.682 (d, $^{2}J_{H,H}$ = 14.0 Hz, 2 H; e1m-H); 3.648 (d, $^{2}J_{H,H}$ = 14.2 Hz, 2 H; e3m-H); 3.642 (d, $^{2}J_{H,H}$ = 14.0 Hz, 2 H; e2m-H); 2.016 (m, 12 H; CH_2-H), 1.084 (m, 18 H; CH_3-H) ppm.

^{1}H NMR (500 MHz, $C_2D_2Cl_4$, 298 K): δ = 7.568 (s, 2 H; α1'M-H), 7.532 (s, 2 H; α2'M-H), 7.362 (s, 2 H; α3'M-H), 6.938 (s, 2 H; α2M-H), 6.911 (s, 2 H; α1M-H), 6.723 (s, 2 H; α3M-H); 4.804 (d, $^{2}J_{H,H}$ = 14.0 Hz, 2 H; a1M-H); 4.695 ($^{2}J_{H,H}$ = 14.2 Hz, 2 H; a3M-H); 4.695 (d, $^{2}J_{H,H}$ = 14.0 Hz, 4 H; a2M-H); 3.930 (s, 6 H; OMe1M-H), 3.834 (s, 6 H; OMe3M -H), 3.735 (s, 6 H; OMe2M-H), 3.682 (d, $^{2}J_{H,H}$ = 14.0 Hz, 2 H; e1M-H); 3.648 (d, $^{2}J_{H,H}$ = 14.2 Hz, 2 H; e3M-H); 3.631 (d, $^{2}J_{H,H}$ = 14.0 Hz, 2 H; e2M-H), 2.016 (m, 12 H; CH_2-H), 1.084 (m, 18 H; CH_3-H) ppm.

^{13}C NMR (Minor isomer, 125 MHz, $C_2D_2Cl_4$, 298 K): δ = 160.57 (γ2m-C), 160.38 (γ1m-C), 159.48 (γ3m-C), 147.90 (β2m-C), 146.34 (β1m-C), 137.23 (β3m-C), 135.64 (α1'm-C), 135.38 (α2'm-C), 134.50 (α3'm-C), 132.86 (β1'm-C), 131.07 (β2'm-C), 129.53 (β3'm-C), 116.72 (γ3'm-C), 116.89 (*C*1m ≡N), 116.79 (*C*2m ≡N), 113.49 (α2m-C), 113.17 (α1m -C), 112.00 (α3m-C), 101.42(*C*≡*C*m), 101.00 (γ1'm-C), 100.62 (γ2'm-C), 56.90 (O*C*H$_3$1m), 56.55 (O*C*H$_3$2m), 56.28 (O*C*H$_3$3m), 37.25 (*C*H$_2$2m), 36.96 (*C*H$_2$1m), 36.70 (*C*H$_2$3m), 17.40 (*C*H$_2$CH$_3$), 8.76 (CH$_2$*C*H$_3$) ppm.

^{13}C NMR (Major isomer, 125 MHz, $C_2D_2Cl_4$, 298 K): δ = 160.57 (γ2M-C), 160.38 (γ1M-C), 159.52 (γ3M-C), 147.05 (β2M-C), 146.34 (β1M-C), 137.27 (β3M-C), 135.68 (α1'M-C), 135.51 (α2'M-C), 134.50 (α3'M-C), 132.95 (β1'M-C), 131.09 (β2'M-C), 129.57 (β3'M-C), 116.72 (γ3'M-C), 116.82 (*C*1M ≡N), 116.77 (*C*2M ≡N), 113.39 (α2M-C), 113.05 (α1M-C), 112.01 (α3M-C), 101.45(*C*≡*C*M), 101.46 (γ1'M-C), 100.62 (γ2'M-C), 56.90 (O*C*H$_3$1M), 56.71 (O*C*H$_3$2M), 56.28 (O*C*H$_3$3M), 37.25 (*C*H$_2$2M), 36.96 (*C*H$_2$1M), 36.70 (*C*H$_2$3M), 17.40 (*C*H$_2$CH$_3$), 8.76 (CH$_2$*C*H$_3$) ppm.

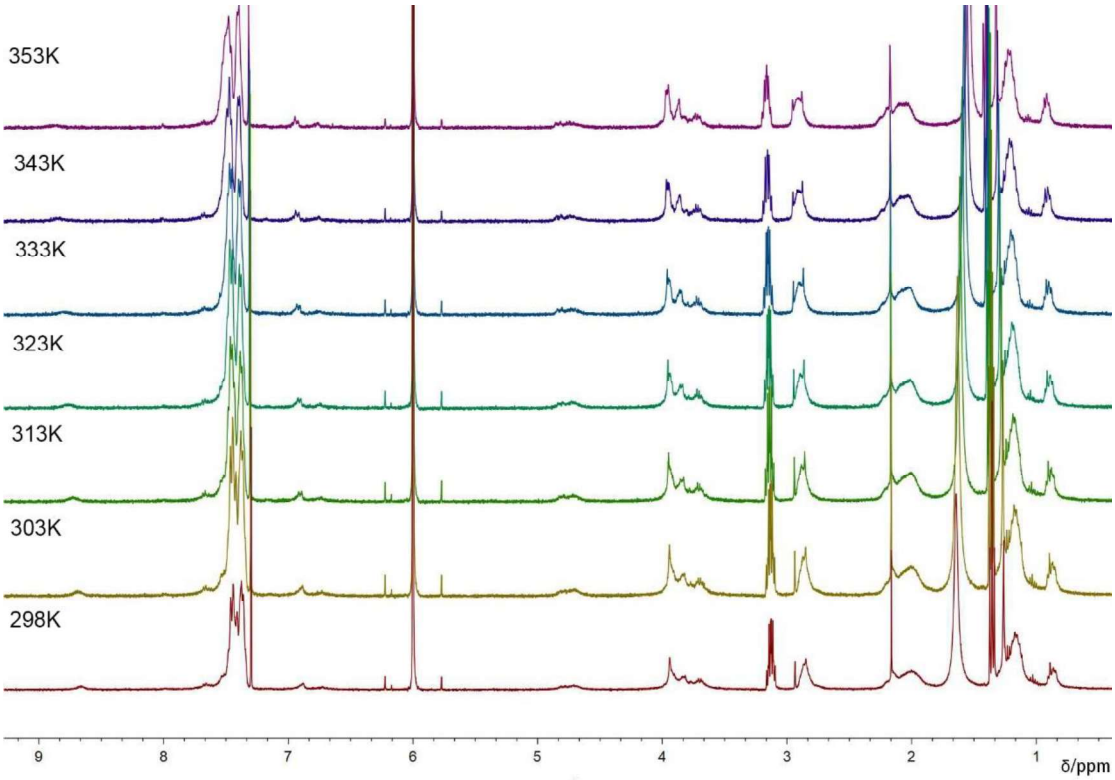


Figure 56: VT ^{1}H NMR spectra of compound **[*cis*-Pt(PEt$_3$)$_2$(Pd$_2$(dppp)$_2$(CTB(3OMe;2CN,C$_2$))Cu$^+$]**(OTf)$_5$ in $C_2D_2Cl_4$ (298-353K).

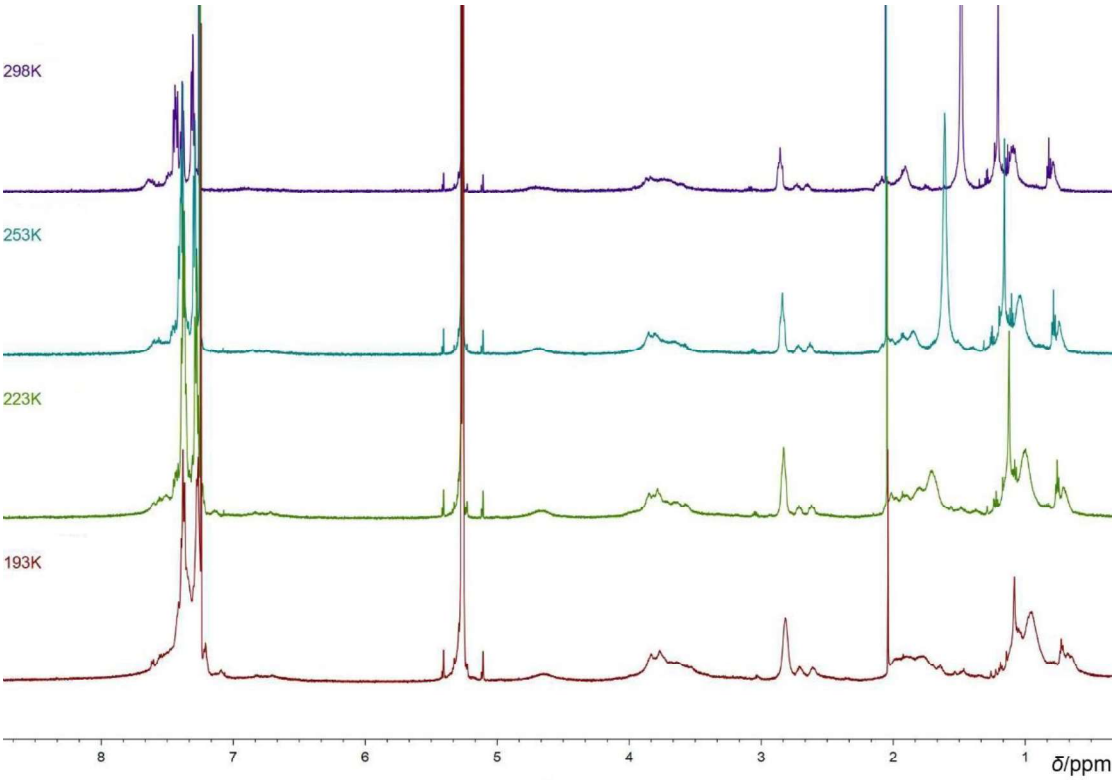


Figure 57: VT ^{1}H NMR spectra of compound **[*cis*-Pt(PEt$_3$)$_2$(Pd$_2$(dppp)$_2$(CTB(3OMe;2CN,C$_2$))Cu$^+$]**(OTf)$_5$ in CD_2Cl_2 (193-298K).

General Conclusion

Initially, cryptophanes are organic hosts designed by André Collet in the early 1980s, and capable of encapsulating a variety of species such as the xenon atom, alkanes, halogenated solvents, quaternary ammonium and fullerenes. It is also important that when chiral cryptophanes are used as host, enantioselective recognition has been observed. Metallo-cryptophanes are compounds obtained by face-to-face dimerization of CTBs using coordination bonds, in which the CTB ligands are linked by metal cations to form M_3L_2 cage species. The first metallo-cryptophanes were reported by Yamaguchi and Shinkai in 2001 and have been then developed by Hardie's group. However, there are only a few reports on luminescent metallo-cryptophanes and their application in host and guest recognition by electronic spectroscopy. In order to expand the application of metallo-cryptophanes in molecular recognition, two different series of light-emitting molecular precursors of metallo-cryptophanes were synthesized and characterized.

First, a series of chiral trinuclear phosphine gold(I) alkynyl complexes derived from CTB have been synthesized and characterized by NMR. The complexes were found mainly in monomeric form in the solution state. In the gas phase, the dimerization was obsered and the proportions of dimers were found to be related to the nature of the precursor CTB and of the phosphane ligands as well. In addition, there existed exchange phenomena between two different phosphane ligands in the gas phase. The ^{1}H NMR titration experiments showed that these gold CTB complexes could be used to host quaternary ammoniums as illustrated by the case of Et_4NI. The complexes showed long-lived phosphorescence in degassed chlorinated solvents; in addition, weak fluorescence in non-degassed solutions were observed. The luminescence properties of these complexes in the solid state were investigated as well, and dramatic red shifts were observed, especially for **C3** and **C6**, for which emission bands at 550 nm were observed. These bands were often, in literature examples, assigned to Au···Au interactions. The luminescence properties of these complexes in solvent mixtures were studied. Whereas acetonitrile only slightly perturbed the absorption and emission spectra of **C1** and **C4** in $CH_3CN/CHCl_3$ mixtures, the gradual addition of methanol had very different effects:

We found that with the increase of MeOH content, a green emission band centered around 540 nm developed. This luminescence switch was due to the formation of aggregates, which were investigated by dynamic light scattering and STEM microscopy. As aggregate formation does not occur in $CHCl_3$/MeCN, even at high MeCN content, it is likely that it results from solvophobic interactions. The CTB complexes being highly lipophilic, they form compacted supramolecular assemblies in order to minimize their exposition to methanol. The aggregation-induced emission (AIE) observed is likely to arise from electronic excited states involving contributions from Au···Au bonds, due to the constrained proximity of the complexes in the aggregates. The enantiomers of the ligand precursor as well as their gold complexes **C1** and **C5** have been separated by chiral HPLC. Studies of solvent-induced self-assembly studies on chiral gold CTB complexes indicated that the behavior of homochiral nanoparticles was different from the nanoparticles by comparison with nanoparticles obtained from racemic gold CTB complexes, suggesting that the latter are true racemates rather than conglomerates.

The precryptophanes were constructed from asymmetric CTBs which were linked by strong platinum(II)-acetylide organometallic bonds, and contained two identical monodentate metal binding sites, which are capable of forming weak coordination bonds as well. The precryptophanes provided two diastereomers: the achiral *meso* form, which showed a C_s-symmetry, and the chiral forms, which had a C_2-symmetry. For precryptophanes **12** and **13**, the large shifts of the signals of the protons α3', α2 and OMe3 were considered to be due to coordination between Cu^+ and alkynyl fragment and H-bonds between coordinated iodide and α3'. These interactions had a direct effect on α3', and indirect effect on the chemical shifts of -OMe3 and α2. Coordination polymers were presumably formed when the precryptophanes were equilibrated with $[Pd(dppp)](OTf)_2$. The Cu^+ cation could be removed by the addition of NaCN to provide us the Cu-free precryptophanes **18** and **20**. According to our studies, these precryptophanes could exist different conformers in different solvents. ^{1}H NMR spectroscopy showed that the –OMe2 substituent of one CTB of compounds **18** and **20**

could be positionned in the shielding field of the cavity of the other CTB, because the CTB could rotate around the Pt-Ar(C) axis. In addition, it showed that the interactions between –OMe2 of one CTB and the cavity of the other CTB were stronger in $CDCl_3$ than in $C_2D_2Cl_4$ and CD_2Cl_2. The shielding of the –OMe2 protons was stronger for the chiral forms by comparison with the *meso* form, which indicated that this group fitted better in the concavity of the other CTB in the chiral diastereomeric pair. Moreover, the saddle forms **19** of precryptophanes **18**, and **21** of precryptophanes **20** were observed. The spontaneous conversions of **19** into **18**, and of **21** into **20** were studied, which showed there was an equilibrium between their saddle and crown forms.

Appendix

Determination of the ratio between $[M + H]^+$ and $[2M + 2H]^{2+}$

The intensity I_1 of the superposed lowest mass peaks of the singly charged $[M + H]^+$ (M) and doubly charged $[2M + 2H]^{2+}$ (D) ions is:

(1) $$I_1 = xI_{100}(\mathrm{M}) + (1-x)I_n(\mathrm{D})$$

where $I_{100}(\mathrm{M})$ is the nominal intensity of the highest peak of $[M + H]^+$ and $I_n(\mathrm{D})$ the intensity of the lowest mass peak of $[2M + 2H]^{2+}$. By definition:

(2) $$I_n = \frac{n}{100} I_{1+\frac{1}{2}}$$

where:

(3) $$I_{1+\frac{1}{2}} = I_{100}(\mathrm{D}) = I_{100}(\mathrm{M})$$

By combinaison of these equations we can calculate x as function of I_1 and $I_{1+\frac{1}{2}}$:

(4) $$x = \frac{I_1 - \frac{n}{100} I_{1+\frac{1}{2}}}{I_{1+\frac{1}{2}}}$$

Application to the analysis of **C1**: Dimer to monomer ratio.

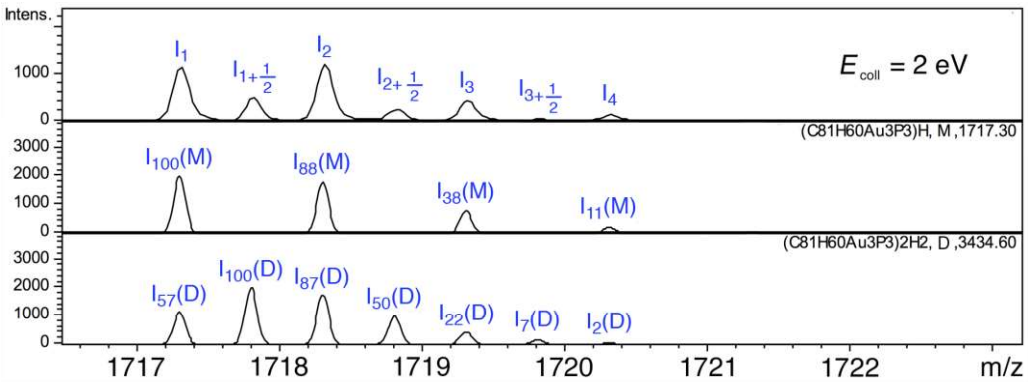


Figure 57. Experimental (a) and theoretical isotopic profiles (b) of the $[M + H]^+$ and (c) $[2M + 2H]^{2+}$ signals of **C1** illustrating the labelling of the peak intensities

References

1. A. J. Ewin, The action of phosphorus pentacholoride on the methylene ethers of catechol derivatives. *J. Chem. Soc. Trans.* **1909**, *95*, 1482–1488.

2. G. M. Robinson, A reaction of homopiperonyl and of homoveratryl alcohols. *J. Chem. Soc. Trans.* **1915**, *107*, 267–276.

3. A. S. Lindsey, The structure of cyclotriveratrylene (10,15-dihydro-2,3,7,8,12,13-hexamethoxy-5*H*-tribenzo[*a*,*d*,*g*]cyclononene) and related compounds. *J. Chem. Soc.* **1965**, 1685–1692.

4. B. Miller, B. M. Gesner, Conformation of cyclotriveratrylene by nuclear magnetic resonance measurements. *Tetrahedron Lett.* **1965**, *38*, 3351–3354.

5. A. S. Lindsey, Cyclotriveratrylene and related compounds. *J. Chem. Soc.* **1965**, 3864–3865.

6. M. J. Hardie, Recent advances in the chemistry of cyclotriveratrylene. *Chem. Soc. Rev.* **2010**, *39*, 516–527.

7. S. Lefevre, A. Héloin, D. Pitrat, J. C. Mulatier, N. Vanthuyne, M. Jean, J. P. Dutasta, L. Guy, A. Martinez, Cyclotriveratrylene-BINOL-based host compounds: synthesis, absolute configuration assignment, and recognition properties. *J. Org. Chem.* **2016**, *81*, 3199–3205.

8. A. Collet, Cyclotriveratrylenes and cryptophanes. *Tetrahedron* **1987**, *43*, 5725–5759.

9. J. Canceill, G. Gottarelli, Optical activity due to isotopic substitution. *J. Am. Chem. Soc.* **1984**, *106*, 5997–6003.

10. J. Canceill, A. Collet, J. Gabard, G. Gottarelli, G. P. Spada, Exciton approach to the optical activity of C_3-cyclotriveratrylene derivatives. *J. Am. Chem. Soc.* **1985**, *107*, 1299–1308.

11. A. Long, C. Colomban, M. Jean, M. Albalat, N. Vanthuyne, M. Giorgi, L. Di Bari, M. Górecki, J. P. Dutasta, A. M. Enantiopure, C_1-cyclotriveratrylene with a reversed spatial arrangement of the substituents. *Org. Lett.* **2019**, 160–165.

12. J. Canceill, A. Collet, J. Gabard, G. Gottarelli, G. P. Spada. Exciton approach to the optical activity of C_3-cyclotriveratrylene derivatives. *J. Am. Chem. Soc.* **1985**, *107*, 1299–1308.

13. A. Collet, J. Jacques, M. Cesario, C. Pascard, Synthesis and absolute configuration of chiral (C_3) cyclotriveratrylene derivatives. Crystal structure of (*M*)-(–)-2,7,12-triethoxy-3,8,13-tris-[(*R*)-1-methoxycarbonylethoxy]-10,15-dihydro-5*H*-tribenzo[*a*,*d*,*g*]-cyclononene. *J. Chem. Soc. Perkin Trans.* **1981**, 1630-1638.

14. S. F. Mason, Optical rotatory power. *Q. Rev. Chem. Soc.* **1963**, *17*, 20-66

15. H. Zimmermann, V. Bader, R. Poupko, E. J. Wachtel, Z. Luz, Mesomorphism, isomerization, and dynamics in a new series of pyramidic liquid crystals. *J. Am.*

Chem. Soc. **2002**, *124*, 15286–15301.

16. H. Zimmermann, P. Tolstoy, H. H. Limbach, R. Poupko, Z. Luz, The saddle form of cyclotriveratrylene. *J. Phys. Chem. B* **2004**, *108*, 18772–18778.

17. T. Brotin, J. P. Dutasta, Cryptophanes and their complexes - present and future. *Chem. Rev.* **2009**, *109*, 88–130.

18. J. F. Manville, G. E. Troughton, Synthesis, structure, and conformation of 10,15-dihydro-1,6,11-trihydroxy- 2,7,12-trimethoxy-4,9,14-trimethyl-5*H*-ribenzo[*a*,*d*,*g*] -cyclononene and its tripropyl analog. *J. Org. Chem.* **1973**, *38*, 4278–4281.

19. K. Frensch, F. Vögtle, Ligand structure and complexation. LII. Note on crown ethers with triveratrylene skeleton. *Liebigs Ann. Chem.* **1979**, 2121–2123.

20. N. L. Drake, W. B. Tuemmler, Podophyllotoxin and picropodophyllin. III.[1] The synthesis of a stripped analog[2]. *J. Am. Chem. Soc.* **1955**, *77*, 1209–1212.

21. J. Canceill, J. Gabard, A. Collet. (*C3*)-tris-(*O*-allyl)-cyclotriguaiacylene, a key intermediate in cyclotriveratrylene chemistry. Short and efficient synthesis of cyclotriguaiacylene. *J. Chem. Soc. Chem. Commun.* **1983**, 122–123.

22. T. Sato, K. Uno, M. Kainosho, A new synthesis of bridged aromatics: 10,15-dihydro-5*H*-tribenzo[*a*,*d*,*g*]cyclononene and its analogues. *J. Chem. Soc. Chem. Commun.* **1972**, 579–580.

23. T. Sato, T. Akima, K. Uno, Medium-sized cyclophanes. Part XIV. An aromatic displacement reaction in veratrylic compounds. Attempted nitration and halogenation of cyclotriveratrylene (10,15- dihydro-2,3,7,8,12,13- hexamethoxy-5*H*-tri-benzo[*a*,*d*,*g*]cyclononene). *J. Chem. Soc. Perkin Trans.* **1973**, 891–895.

24. T. Sato, K. Uno, Medium-sized cyclophanes. Part XV. 10,15-dihydro-5*H*-tribenzo-[*a*,*d*,*g*]cyclononene and analogues. *J. Chem. Soc. Perkin Trans.* **1973**, 895–900.

25. N. J. Cookson, J. M. Fowler, D. P. Martin, J. Fisher, J. J. Henkelis, T. K. Ronson, F. L. Thorp-Greenwood, C. E. Willans, M. J. Hardie, Metallo-cryptophane cages from *cis*-linked and *trans*-linked strategies. *Supramol. Chem.* **2018**, *30*, 255–266.

26. A. M. Bond, W. Miao, C. L. Raston, T. J. Ness, M. J. Barnes, J. L. Atwood, Electrochemical and structural studies on microcrystals of the $(C_{60})_x$(CTV) inclusion complexes (x =1, 1.5; CTV = cyclotriveratrylene). *J. Phys. Chem. B* **2001**, *105*, 1687–1695.

27. M. J. Hardie, C. L. Raston, Confinement and recognition of icosahedral main group cage molecules: fullerene C_{60} and *o*-, *m*-, *p*- dicarbadodecaborane(12). *Chem. Commun.* **1999**, *60*, 1153–1163.

28. J. F. Eckert, D. Byrne, J. F. Nicoud, L. Oswald, J. F. Nierengarten, M. Numata, A. Ikeda, S. Shinkai, N. Armaroli, Polybenzyl ether dendrimers for the complexation of [60]fullerenes. *New J. Chem.* **2000**, *24*, 749–758.

29. E. Huerta, E. Cequier, J. De Mendoza, Preferential separation of fullerene[84] from fullerene mixtures by encapsulation. *Chem. Commun.* **2007**, 5016–5018.

30. E. Huerta, G. A. Metselaar, A. Fragoso, E. Santos, C. Bo, J. de Mendoza, Selective binding and easy separation of C_{70} by nanoscale self-assembled capsules. *Angew. Chem. Int. Ed.* **2007**, *46*, 202–205.

31. L. Peyrard, S. Chierici, S. Pinet, P. Batat, G. Jonusauskas, N. Pinaud, P. Meyrande, I. Gosse. *C_3*-triiodocyclotriveratrylene as a key intermediate to fluorescent probes: application to selective choline recognition. *Org. Biomol. Chem.* **2011**, *9*, 8489–8494.

32. M. L. Dumartin, C. Givelet, P. Meyrand, B. Bibal, I. Gosse, A fluorescent cyclotriveratrylene: synthesis, emission properties and acetylcholine recognition in water. *Org. Biomol. Chem.* **2009**, *7*, 2725–2728.

33. T. Moriuchi-Kawakami, Y. Mizuno, T. Inoue, S. Matsubara, T. Moriuchi, A: *C_3*-substituted cyclotriveratrylene derivative with 8-quinolinyl groups as a fluorescence-enhanced probe for the sensing of Cu^{2+} ions. *Analyst* **2019**, *144*, 1140–1146.

34. J. Cancelli, M. Cesario, A. Collet, J. Guilhem, P. C. A new bis-cyclotribenzyl cavitand capable of selective inclusion of neutral molecules in solution. Crystal structure of its CH_2Cl_2 cavitate. *J. Chem. Soc. Chem. Commun.* **1985**, 361–363.

35. J. Canceill, L. Lacombe, A. Collet, New cryptophane forming unusually stable inclusion complexes with neutral guests in a lipophilic solvent. *J. Am. Chem. Soc.* **1986**, *108*, 4230–4232.

36. J. Gabard, A. Collet, Synthesis of a (*D_3*)-bis(cyclotriveratrylenyl) macrocage by stereospecific replication of a (*C_3*)-subunit. *J. Chem. Soc. Chem. Commun.* **1981**, 1137–1139.

37. J. J. Henkelis, M. J. Hardie, Controlling the assembly of cyclotriveratrylene-derived coordination cages. *Chem. Commun.* **2015**, *51*, 11929–11943.

38. G. Gottarelli, A. Collet, Exciton optical activity of molecules containing three and six coupled oscillators belonging to *C_3* and *D_3* point groups: applications to cyclotriveratrylenes and cryptophanes. *Croatica Chem. Acta.* **1989**, *62*, 279–292.

39. G. El-Ayle, K. T. Holman, Cryptophanes. Comprehensive Supramolecular Chemistry II. **2017**, *6*, 199–249.

40. C. J. Sumby, M. J. Hardie, Capsules and star-burst polyhedra: an $[Ag_2L_2]$ capsule and a tetrahedral $[Ag_4L_4]$ metallosupramolecular prism with cyclotriveratrylene-type ligands. *Angew. Chem. Int Ed.* **2005**, *44*, 6395–6399.

41. D. Scott Bohle, D. J. Stasko, Salicylaldiminato derivatives of cyclotriveratrylene: flexible strategy for new rim-metalated CTV complexes. *Inorg. Chem.* **2000**, *39*, 25, 5768–5770.

42. T. Brotin, V. Roy, J. P. Dutasta, Improved synthesis of functional CTVs and cryptophanes using $Sc(OTf)_3$ as catalyst. *J. Org. Chem.* **2005**, *70*, 6187–6195.

43. M. Miura, S. Yuzawa, M. Takeda, Y. Habata, T. Tanase, S. Akabori, Syntheses of aromatic bridged cryptophanes and their complexing abilities with alkyl ammonium cations. *Supramol. Chem*. **1996**, *8*, 53–66.

44. S. T. Mough, J. C. Goeltz, K. T. Holman, Isolation and structure of an 'Imploded' cryptophane. *Angew. Chem. Int Ed.* **2004**, *43*, 5631–5635.

45. A. Collet, J. P. Dutasta, B. Lozach, J. Canceill, Cyclotriveratrylenes and cryptophanes: their synthesis and applications to host-guest chemistry and to the design of new materials. *Top in Cur Chem* **1993**, *165*, 104–129.

46. S. B. Lee, J. I. Hong, Encapsulation of small organic molecules by a self-assembled molecular capsule through charged hydrogen bonding interaction. *Tetrahedron Lett.* **1996**, *37*, 8501–8504.

47. Z. Zhong, A. Ikeda, S. Shinkai, S. Sakamoto, K. Yamaguchi, Creation of novel chiral cryptophanes by a self-assembling method utilizing a pyridyl-Pd(II) interaction. *Org. Lett.* **2001**, *3*, 1085–1087.

48. D. J. Cram, M. E. Tanner, S. J. Keipert, C. B. Knobler, Two chiral [1.1.1]orthocyclophane units bridged by three biacetylene units as a host which binds medium-sized organic guests. *J. Am. Chem. Soc.* **1991**, *113*, 8909–8916.

49. F. Brégier, O. Hudeček, F. Chaux, M. J. Penouilh, J. C. Chambron, P. Lhoták, E. Aubert, E. Espinosa, Generation of cryptophanes in water by disulfide bridge formation. *Eur. J. Org. Chem.* **2017**, 3795–3811.

50. A. Collet, J. P. Dutasta, B. Lozach, Design, Synthesis, and properties of macrocyclic receptors for tetrahedral substrates. *Bull. Soc. Chim. Belg.* **1990**. *99*, 617–633.

51. J. Canceill, L. Lacombe, A. Collet, Water-soluble cryptophane binding lipophilic guests in aqueous solution. *J. Chem. Soc. Chem. Commun.* **1987**, 219–221.

52. L. Garel, B. Lozach, J. P. Dutasta, A. Collet, Remarkable effect of receptor size in the binding of acetylcholine and related ammonium ions to water-soluble cryptophanes. *J. Am. Chem. Soc.* **1993**, *115*, 11652–11653.

53. M. Darzac, T. Brotin, L. Rousset-Arzel, D. Bouchu, J. P. Dutasta, Synthesis and application of cryptophanol hosts: ^{129}Xe NMR spectroscopy of a deuterium-labeled $(Xe)_2$@bis-cryptophane complex. *New J. Chem.* **2004**, ***28***, 502–512.

54. M. Darzac, T. Brotin, D. Bouchu, J. P. Dutasta, Cryptophanols, new versatile compounds for the synthesis of functionalized cryptophanes and polycryptophanes. *Chem. Commun.* **2002**, *2*, 48–49.

55. A. Colbet, J. Gabard, Optically active (C_3)-cyclotriveratrylene-d_9. Energy barrier for the "crown to crown" conformational interconversion of its nine-membered-

ring system. *J. Org. Chem.* **1980**, *45*, 5400–5401.

56. C. Garcia, A. Aubry, A. Collet. Stereoselectivity in the template-directed synthesis of D_3 (chiral) and C_{3h} (achiral) cryptophanes with long $O(CH_2)_nO$ spacer bridges. *Bull. Soc. Chim. Fr.* **1996**, *133*, 853–867.

57. G. Huber, T. Brotin, L. Dubois, H. Desvaux, J. P. Dutasta, P. Berthault, Water soluble cryptophanes showing unprecedented affinity for xenon: candidates as NMR-based biosensors. *J. Am. Chem. Soc.* **2006**, *128*, 6239–6246.

58. Akabori, S. M. Miura, M. Takeda, S. Yuzawa, Y. Habata, T. Ishii, Syntheses of diethyleneoxy bridged cryptophanes and their complexing abilities with alkali metal and alkylammonium cations. *Supramol. Chem.* **1996**, *7*, 187–193.

59. R. M. Fairchild, K. T. Holman, Selective anion encapsulation by a metalated cryptophane with a π-acidic interior. *J. Am. Chem. Soc.* **2005**, *127*, 16364–16365.

60. J. Canceill, L. Lacombe, A. Collet, Analytical optical resolution of bromochlorofluoromethane by enantioselective inclusion into a tailor-made "cryptophane" and determination of its maximum rotation. *J. Am. Chem. Soc.* **1985**, 6993–6996.

61. J. Canceill, M. Cesario, A. Collet, J. Guilhem, C. Riche, C. Pascard, Selective recognition of neutral molecules: ^{1}H N.M.R. study of the complexation of CH_2Cl_2 and CH_2Br_2 by cryptophane-D in solution and crystal structure of its CH_2Cl_2 cavitate. *J. Chem. Soc. Chem. Commun.* **1986**, 339–341.

62. J. Canceill, M. Cesario, A. Collet, J. Guilhem, L. Lacombe, B. Lozach, C. Pascard, Structure and properties of the cryptophane-E/$CHCl_3$, complex, a stable van der waals molecule. *Angew. Chem. Int. Ed. Engl*. **1989**, *8*, 1246–1248.

63. Z. Tošner, J. Lang, D. Sandström, O. Petrov, J. Kowalewski, Dynamics of an inclusion complex of dichloromethane and cryptophane-E. *J. Phys. Chem. A* **2002**, *106*, 8870–8875.

64. S. Akabori, M. Takeda, M. Miura, The complexing abilities of diethyleneoxy- and xylene-bridged cryptophanes with alkanes. *Supramol. Chem.* **1999**, *10*, 253–262.

65. O. Petrov, Z. Tošner, I. Csöregh, J. Kowalewski, D. Sandström, Dynamics of chloromethanes in cryptophane-E inclusion complexes: a ^{2}H solid-state NMR and X-ray diffraction study. *J. Phys. Chem. A* **2005**, *109*, 4442–4451.

66. L. Garel, H. Vezin, J. P. Dutasta, A. Collet, Piperidine aminoxyl radicals as EPR probes for exploring the cavity of a water-soluble cryptophane. *Chem. Commun.* **1996**, 719–720.

67. S. Mecozzi, J. Rebek, The 55% solution: a formula for molecular recognition in the liquid state. *Chem. Eur. J.* **1998**, *4*, 1016–1022.

68. C. Garcia, D. Humilière, N. Riva, A. Collet, J. P. Dutasta, Kinetic and thermodynamic consequences of the substitution of SMe for OMe substituents of

cryptophane hosts on the binding of neutral and cationic guests. *Org. Biomol. Chem.* **2003**, *1*, 2207–2216.

69. C. E. O. Roesky, E. Weber, T, Rambusc, H. Stephan, K. Gloe, M. Czugler, A new cryptophane receptor featuring three endo-carboxylic acid groups: synthesis, host behavior and structural study. *Chem. Eur. J.* **2003**, *9*, 1104–1112.

70. R. M. Fairchild, K. T. Holman, Selective anion encapsulation by a metalated cryptophane with a π-acidic interior. *J. Am. Chem. Soc.* **2005**, *127*, 16364–16365.

71. P. Soular, P. Asseli, A. Cuisset, J. R. A. Moreno, T. R. Huet, D. Petitprez, J. Demaison, T. B. Freedman, X. Cao, L. A. Nafie, J. Crassous, Chlorofluoroiodomethane as a potential candidate for parity violation measurements. *Phys. Chem. Chem. Phys.* **2006**, *8*, 79–92.

72. B. S. Kim, Y. H. Ko, Y. Kim, H. J. Lee, N. Selvapalam, H. C. Lee, K. Kim, Water soluble cucurbit[6]uril derivative as a potential Xe carrier for ^{129}Xe NMR-based biosensors. *Chem. Commun.* **2008**, 2756–2758.

73. T. A. Robbins, C. B. Knobler, D. R. Bellew, D. J. Cram, A highly adaptive and strongly binding hemicarcerand. *J. Am. Chem. Soc.* **1994**, *116*, 111–122.

74. D. J. Cram, M. E. Tanner, C. B. Knobler, Guest release and capture by hemicarcerands introduces the phenomenon of constrictive binding. *J. Am. Chem. Soc.* **1991**, *113*, 7717–7727.

75. D. Ajami, J. Rebek, Multicomponent, hydrogen-bonded cylindrical capsules. *J. Org. Chem.* **2009**, *74*, 6584–6591.

76. R. M. Fairchild, A. I. Joseph, K. T. Holman, H. A. Fogarty, T. Brotin, J. P. Dutasta, C. Boutin, G. Huber, P. Berthault, A water-soluble Xe@cryptophane-111 complex exhibits very high thermodynamic stability and a peculiar ^{129}Xe NMR chemical shift. *J. Am. Chem. Soc.* **2010**, *132*, 15505–15507.

77. G. Huber, L. Beguin, H. Desvaux, T. Brotin, H. A. Fogarty, J. P. Dutasta, P. Berthault, Cryptophane-xenon complexes in organic solvents observed through NMR spectroscopy. *J. Phys. Chem. A* **2008**, *112*, 11363–11372.

78. D. R. Jacobson, N. S. Khan, R. Collé, R. Fitzgerald, L. Laureano-Pérez, Y. Bai, I. J. Dmochowski, Measurement of radon and xenon binding to a cryptophane molecular host. *PNAS* **2011**, *108*, 10969–10973.

79. K. Bartik, M. Luhmer, J. P. Dutasta, A. Collet, J. Reisse, ^{129}Xe and ^{1}H NMR study of the reversible trapping of xenon by cryptophane-A in organic solution. *J. Am. Chem. Soc.* **1998**, *120*, 784–791.

80. T. K. Ronson, H. Nowell, M. J. Hardie, Bow-tie metallo-cryptophanes from a carboxylate derived cavitand. *Chem. Commun.* **2011**, *47*, 176–178.

81. A. Schaly, Y. Rousselin, J. C. Chambron, E. Aubert, E. Espinosa, The stereoselective self-Assembly of chiral metallo-organic cryptophanes. *Eur. J.*

Inorg. Chem. **2016**, 832–843.

82. J. J. Henkelis, T. K. Ronson, L. P. Harding, M. J. Hardie, M_3L_2 metallo-cryptophanes: [2]catenane and simple cages. *Chem. Commun.* **2011**, *47*, 6560–6562.

83. C. J. Sumby, J. Fisher, T. J. Prior, M. J. Hardie, Tris(pyridylmethylamino)-cyclotriguaiacylene cavitands: an investigation of the solution and solid-state behaviour of metallo-supramolecular cages and cavitand-based coordination polymers. *Chem. Eur. J.* **2006**, *12*, 2945–2959.

84. J. J. Henkelis, C. J. Carruthers, S. E. Chambers, R. Clowes, A. I. Cooper, J. Fisher, M. J. Hardie, Metallo-cryptophanes decorated with bis-N-heterocyclic carbene ligands: self-assembly and guest uptake into a nonporous crystalline lattice. *J. Am. Chem. Soc.* **2014**, *136*, 14393–14396.

85. K. Caprice, D. Pál, C. Besnard, B. Galmés, A. Frontera, F. B. L. Cougnon, Diastereoselective amplification of a mechanically chiral [2]catenane. *J. Am. Chem. Soc.* **2021**, *143*, 11957–11962.

86. Y. Y. Zhang, F. Y. Qiu, H. T. Shi, W. Yu, Self-assembly and guest-induced disassembly of triply interlocked [2]catenanes. *Chem. Commun.* **2021**, *57*, 3010–3013.

87. S. Pilon, S. I. Jørgensen, J. H. van Maarseveen, Covalent [2]catenane and [2]rotaxane synthesis via a δ-amino acid template. *ACS Org. Inorg. Au* (**2021**) doi:10.1021/acsorginorgau.1c00017.

88. M. C. Jimenez-Molero, C. Dietrich-Buchecker, J. P. Sauvage, Chemically induced contraction and stretching of a linear rotaxane dimer. *Chem. Eur. J.* **2002**, *8*, 1456–1466.

89. A. Westcott, J. Fisher, L. P. Harding, P. Rizkallah, M. J. Hardie, Self-assembly of a 3-D triply interlocked chiral [2]catenane. *J. Am. Chem. Soc.* **2008**, *130*, 2950–2951.

90. J. R. Piper, L. Cletheroe, C. G. P. Taylor, A. J. Metherell, J. A. Weinstein, I. V. Sazanovich, M. D. Ward, Photoinduced energy- and electron-transfer from a photoactive coordination cage to bound guests. *Chem. Commun.* **2017**, *53*, 408–411.

91. N. K. Al-Rasbi, C. Sabatini, F. Barigelletti, M. D. Ward, Red-shifted luminescence from naphthalene-containing ligands due to π-stacking in self-assembled coordination cages. *J. Chem. Soc. Dalt. Trans.* **2006**, *2*, 4769–4772.

92. X. Yan, T. R. Cook, P. Wang, F. Huang, P. J. Stang, Highly emissive platinum(II) metallacages. *Nat. Chem.* **2015**, *7*, 342–348.

93. V. E. Pritchard, D. R. Martir, S. Oldknow, S. Kai, S. Hiraoka, N. J. Cookson, E. Zysman-Colman, M. J. Hardie, Homochiral self-sorted and emissive Ir^{III} metallo-

cryptophanes. *Chem. Eur. J.* **2017**, *23*, 6290–6294.

94. H. Schmidbaur, A. Schier, Aurophilic interactions as a subject of current research: an up-date. *Chem. Soc. Rev.* **2012**, *41*, 370–412.

95. M. Pujadas, L. Rodríguez, Luminescent phosphine gold(I) alkynyl complexes. Highlights from 2010 to 2018. *Coord. Chem. Rev.* **2020**, *408*, 213179.

96. J. C. Lima, L. Rodríguez, Applications of gold(I) alkynyl systems: a growing field to explore. *Chem. Soc. Rev.* **2011**, *40*, 5442–5456.

97. H. Y. Chao, W. Lu, Y. Li, M. C. W. Chan, C. M. Che, K. K. Cheung, N. Zhu, Organic triplet emissions of arylacetylide moieties harnessed through coordination to $[Au(PCy_3)]^+$. Effect of molecular structure upon photoluminescent properties. *J. Am. Chem. Soc.* **2002**, *124*, 14696–14706.

98. W. Lu, N. Zhu, C. M. Che, Luminescent properties of carbon-rich starburst gold(I) acetylide complexes. Crystal structure of $[TEE][Au(PCy_3)]_4$([TEE]H_4= tetraethynylethene). *J. Organomet. Chem.* **2003**, *670*, 11–16.

99. M. J. Irwin, J. J. Vittal, R. J. Puddephatt, Luminescent gold(I) acetylides: from model compounds to polymers. *Organometallics* **1997**, *16*, 3541–3547.

100. M. C. Blanco, J. Cámara, V. Fernández-Moreira, A. Laguna, M. C. Gimeno, Gold(I), Phosphanes, and alkynyls: the perfect allies in the search for luminescent compounds. *Eur. J. Inorg. Chem.* **2018**, 2762–2767.

101. M. E. S. Moussa, H. Chen, Z. Wang, M. Srebro-Hooper, N. Vanthuyne, S. Chevance, C. Roussel, J. A. G. Williams, J. Autschbach, R. Réau, Z. Duan, C. Lescop, J. Crassous, Bimetallic gold(I) complexes with ethynyl-helicene and bis-phosphole ligands: understanding the role of aurophilic interactions in their chiroptical properties. *Chem. Eur. J.* **2016**, *22*, 6075–6086.

102. V. W. W. Yam, S. W. K. Choi, K. K. Cheung, Synthesis and design of novel tetranuclear and dinuclear gold(I) phosphine acetylide complexes. First X-ray crystal structures of a tetranuclear ($[Au_4(tppb)(C{\equiv}CPh)_4]$) and a related dinuclear ($[Au_2(dppb)(C{\equiv}CPh)_2]$) complex. *Organometallics* **1996**, *15*, 1734–1739.

103. H. B. Xu, L. Y. Zhang, J. Ni, H. Y. Chao, Z. N. Chen, Conformation changes and luminescent properties of Au-Ln (Ln = Nd, Eu, Er, Yb) arrays with 5-ethynyl-2,2′-bipyridine. *Inorg. Chem.* **2008**, *47*, 10744–10752.

104. V. W. W. Yam, K. L. Cheung, S. K. Yip, K. K. Cheung, Synthesis, characterization, structure and luminescence studies of mono-, di- and trinuclear gold(I) phosphine alkynyl complexes. *J. Organomet. Chem.* **2003**, *681*, 196–209.

105. D. Li, X. Hang, C. M. Che, W. C. Lo, S. M. Peng, Luminescent gold(I) acetylide complexes. Photophysical and photoredox properties and crystal structure of $[\{Au(C{\equiv}CPh)\}_2(\mu\text{-}Ph_2PCH_2CH_2PPh_2)]$. *J. Chem. Soc. Dalton. Trans.* **1993**, 2929–2932.

106. L. P. Yang, C. L. Li, Y. L. Yao, Z. J. Lin, Z. P. Qiao, H. Y. Chao, Mononuclear gold(I) acetylide complexes with carbonyl moiety: synthesis, characterization, and tunable emission energy. *Inorg. Chem. Commun.* **2020**, *112*, 107731.

107. W. Lu, H. F. Xiang, N. Zhu, C. M. Che, The $^3(\pi\pi^*)$ emission of $Cy_3PAu(C{\equiv}C)_nAuPCy_3$ (n = 3, 4). Effect of chain length upon acetylenic $^3(\pi\pi^*)$ emission. *Organometallics* **2002**, 2343–2346.

108. V. W. W. Yam, S. K. Yip, L. H. Yuan, K. L. Cheung, N. Zhu, K. K. Cheung, Synthesis, structure, and ion-binding properties of luminescent gold(I) alkynylcalix[4]crown-5 complexes. *Organometallics* **2003**, *22*, 2630–2637.

109. S. K. Yip, W. H. Lam, N. Zhu, V. W. W. Yam, Synthesis, characterization, structure and luminescence studies of dinuclear gold(I) alkynyls of bis(diphenylphosphino)alkyl- and aryl-amines. *Inorg. Chim. Acta* **2006**, *359*, 3639–3648.

110. C. P. McArdle, S. Van, M. C. Jennings, R. J. Puddephatt, Gold(I) macrocycles and topologically chiral [2]catenanes. *J. Am. Chem. Soc.* **2002**, *124*, 3959–3965.

111. Y. P. Zhou, E. B. Liu, J. Wang, H. Y. Chao, Highly Ag^+ selective tripodal gold(I) acetylide-based 'off-on' luminescence chemosensors based on $^3(\pi\pi^*)$ emission switching. *Inorg. Chem.* **2013**, *52*, 8629–8637.

112. Y. P. Zhou, M. Zhang, Y. H. Li, Q. R. Guan, F. Wang, Z. J. Lin, C. K. Lam, X. L. Feng, H. Y. Chao, Mononuclear gold(I) acetylide complexes with urea group: synthesis, characterization, photophysics, and anion sensing properties. *Inorg. Chem.* **2012**, *51*, 5099–5109.

113. L. Erieau-Peyrard, C. Coiffier, P. Bordat, D. Bégué, S. Chierici, S. Pinet, I. Gosse, I. Baraille, R. Brown, Selective, direct detection of acetylcholine in PBS solution, with self-assembled fluorescent nano-particles: experiment and modelling. *Phys. Chem. Chem. Phys.* **2015**, *17*, 4168–4174.

114. X. N. Han, J. M. Chen, Z. T. Huang, Q. Y. Zheng, Synthesis of cyclotriveratrylene-phenylacetylene derivatives and a photophysical investigation of rigid conjugated cyclotriveratrylene dendrimers. *Eur. J. Org. Chem.* **2012**, 6895–6903.

115. N. Fantozzi, R. Pétuya, A. Insuasty, A. Long, S. Lefevre, A. Schmitt, V. Robert, J. P. Dutasta, I. Baraille, L. Guy, E. Genin, D. Bégué, A. Martinez, S. Pinet, I. Gosse, A new fluorescent hemicryptophane for acetylcholine recognition with an unusual recognition mode. *New J. Chem.* **2020**, *44*, 11853–11860.

116. F. Brégier, J. Lavalle, J. C. Chambron, Capping α-cyclodextrin with cyclotriveratrylene by triple disulfide-bridge formation. *Eur. J. Org. Chem.* **2013**, 2666–2671.

117. D. L. Musso, M. J. Clarke, J. L. Kelley, G. E. Boswell, G. Chen, Novel 3-phenylprop-2-ynylamines as inhibitors of mammalian squalene epoxidase. *Org. Biomol. Chem.* **2003**, *1*, 498–506.

118. L. Peyrard, M. L. Dumartin, S. Chierici, S. Pinet, G. Jonusauskas, P. Meyrand, I. Gosse, Development of functionalized cyclotriveratrylene analogues: introduction of withdrawing and π-conjugated groups. *J. Org. Chem.* **2012**, *77*, 7023–7027.

119. R. J. Cross, M. F. Davidson, Preparation and ligand-exchange reactions of phosphinegold ethynyl complexes. *J. Chem. Soc. Dalt. Trans.* **1986**, 411–414.

120. G. Jia, R. J. Puddephatt, J. D. Scott, J. J. Vittal, Organometallic polymers with gold(I) centers bridged by diphosphines and diacetylides. *Organometallics* **1993**, *12*, 3565–3574.

121. W. J. Hunks, M. A. MacDonald, M. C. Jennings, R. J. Puddephatt, Luminescent binuclear gold(I) ring complexes. *Organometallics* **2000**, *19*, 5063–5070.

122. G. E. Coates, C. Parkin, Gold(1) alkynyls and their co-ordination complexes. *J. Chem. Soc.* **1962**, 3220–3226.

123. Q. Y. Hu, W. X. Lu, H. D. Tang, H. H. Y. Sung, T. B. Wen, I. D. Williams, G. K. L. Wong, Z. Lin, G. Jia, Synthesis and photophysical properties of trimetallic acetylide complexes with a 1,3,5-triazine core. *Organometallics* **2005**, *24*, 3966–3973.

124. W. Lu, N. Zhu, C. M. Che, Polymorphic forms of a gold(I) arylacetylide complex with contrasting phosphorescent characteristics. *J. Am. Chem. Soc.* **200**3, *125*, 16081–16088.

125. M. Głodek, S. Pawlędzio, A. Makal, D. Plażuk, The impact of crystal packing and aurophilic interactions on the luminescence properties in polymorphs and solvate of aroylacetylide–gold(I) complexes. *Chem. Eur. J.* **2019**, *25*, 13131–13145.

126. F. K. W. Hau, K. L. Cheung, N. Zhu, V. W. W. Yam, Calixarene-based alkynyl-bridged gold(I) isocyanide and phosphine complexes as building motifs for the construction of chemosensors and supramolecular architectures. *Org. Chem. Front.* **2019**, *6*, 1205–1213.

127. A. Macchioni, G. Ciancaleoni, C. Zuccaccia, D. Zuccaccia, Determining accurate molecular sizes in solution through NMR diffusion spectroscopy. *Chem. Soc. Rev.* **2008**, *37*, 479–489.

128. B. M. Schulze, D. L. Watkins, J. Zhang, I. Ghiviriga, R. K. Castellano, Estimating the shape and size of supramolecular assemblies by variable temperature diffusion ordered spectroscopy. *Org. Biomol. Chem.* **2014**, *12*, 7932–7936.

129. K. T. Chan, G. S. M. Ton, W. P. To, C. Yang, L. Du, D. L. Phillips, C. M. Che, The interplay between fluorescence and phosphorescence with luminescent gold(I) and gold(III) complexes bearing heterocyclic arylacetylide ligands. *Chem. Sci.* **2017**, *8*, 2352–2364.

130. A. L. Sadowy, M. J. Ferguson, R. McDonald, R. R. Tykwinski, Chiral *cis*-platinum acetylide complexes via diphosphine ligand exchange: effect of the ligand.

Organometallics **2008**, *27*, 6321–6325.

131. K. Campbell, R. McDonald, M. J. Ferguson, R. R. Tykwinski, Using ligand exchange reactions to control the coordination environment of Pt(II) acetylide complexes: applications to conjugated metallacyclynes. *J. Organomet. Chem.* **2003**, *683*, 379–387.

132. V. Cámara, N. Barquero, D. Bautista, J. Gil-Rubio, J. Vicente, Heterometallic complexes with gold(I) metalloligands: self-assembly of helical dimers stabilized by weak intermolecular interactions and solvophobic effects. *Chem. Eur. J.* **2015**, *21*, 1992–2002.

133. P. Thordarson, Determining association constants from titration experiments in supramolecular chemistry. *Chem. Soc. Rev.* **2011**, *40*, 1305–1323.

134. K. Kataoka, T. D. James, Y. Kubo, Ion pair-driven heterodimeric capsule based on boronate esterification: construction and the dynamic behavior. *J. Am. Chem. Soc.* **2007**, *129*, 15126–15127.

135. H. de la Riva, M. Nieuwhuyzen, C. M. Fierro, P. R. Raithby, L. Male, M. C. Lagunas, A new type of luminescent alkynyl Au_4Cu_2 cluster. *Inorg. Chem.* **2006**, *45*, 1418–1420.

136. D. Li, X. Hong, C. M. Che, W. C. Lo, S. M. Peng, Luminescent gold(I) acetylide complexes. Photophysical and photoredox properties and crystal structure of $[\{Au(C{\equiv}CPh)\}_2(\mu\text{-}Ph_2PCH_2CH_2PPh_2)]$. *J. Chem. Soc. Dalton Trans.* **1993**, 2929–2932.

137. S. Y. Poon, W. Y. Wong, K. W. Cheah, J. X. Shi, Spatial extent of the singlet and triplet excitons in luminescent angular-shaped transition-metal diynes and polyynes comprising non-π-conjugated group 16 main group elements. *Chem. Eur. J.* **2006**, *12*, 2550–2563.

138. W. Y. Wong, Y. Guo, C. L. Ho, Synthesis, optical properties and photophysics of group 10-12 transition metal complexes and polymer derived from a central tris(p-ethynylphenyl)amine unit. *J. Inorg. Organomet. Polym. Mater.* **2009**, *19*, 46–54.

139. H. S. Lo, N. Zhu, V. K. M. Au, V. W. W. Yam, Synthesis, characterization, photophysics and electrochemistry of polynuclear copper(I) and gold(I) alkynyl phosphine complexes. *Polyhedron* **2014**, *83*, 178–184.

140. E. Aguiló, A. J. Moro, M. Outis, J. Pina, D. Sarmento, J. S. S. de Melo, L. Rodríguez, J. C. Lima, Deactivation routes in gold(I) polypyridyl complexes: internal conversion vs fast intersystem crossing. *Inorg. Chem.* **2018**, *57*, 13423–13430.

141. I. Kondrasenko, K. Chung, Y. T. Chen, J. Koivistoinen, E. V. Grachova, A. J. Karttunen, P. T. Chou, I. O. Koshevoy, Harnessing fluorescence versus phosphorescence ratio via ancillary ligand fine-tuned MLCT contribution. *J. Phys. Chem. C* **2016**, *120*, 12196–12206.

142. Y. C. Chang, K. C. Tang, H. A. Pan, S. H. Liu, I. O. Koshevoy, A. J. Karttunen, W. Y Hung, M. H. Cheng, P. T. Chou, Harnessing fluorescence versus phosphorescence branching ratio in (phenyl)$_n$-bridged (n = 0-5) bimetallic Au(I) complexes. *J. Phys. Chem. C* **2013**, *117*, 9623–9632.

143. W. Y. Wong, K. H. Choi, G. L. Lu, J. X. Shi, P. Y. Lai, S. M. Chan, Z. Lin, Binuclear gold(I) and mercury(II) derivatives of diethynylfluorenes. *Organometallics* **2001**, *20*, 5446–5454.

144. W. Lu, W. M. Kwok, C. Ma, C. T. L. Chan, M. X. Zhu, C. M. Che, Organic triplet excited states of gold(I) complexes with oligo(o- or m-phenyleneethynylene) ligands: conjunction of steady-state and time-resolved spectroscopic studies on exciton delocalization and emission pathways. *J. Am. Chem. Soc.* **2011**, *133*, 14120–14135.

145. V. W. Yam, S. W. Choi, Synthesis, photophysics and photochemistry of alkynylgold(1) phosphine complexes. *J. Chem. Soc. Dalton Trans.* **1996**, 4227–4232.

146. C. M. Che, H. K. Yip, W. C. Lo, S. M. Peng, Luminescent metal clusters. spectroscopic properties and X-ray structure of a bis(diphenylphosphino) methane and phenylacetylide. *Polyhedron* **1994**, *13*, 887–890.

147. G. Mie, Beiträge zur optik trüber medien, speziell kolloidaler metallösungen. *Ann. Phys.* **1908**, *330*, 377–445.

148. B. Zhao, J. Deng, J. Deng, Emulsification-induced homohelicity in racemic helical polymer for preparing optically active helical polymer nanoparticles. *Macromol. Rapid Commun.* **2016**, *37*, 568–574.

149. L. Yang, J. Liu, P. Sun, Z. Ni, Y. Ma, Z. Huang, Chiral nanoparticles: chiral ligand-free, optically active nanoparticles inherently composed of chiral lattices at the atomic scale. *Small* **2020**, *16*, 2001473 (1-14).

150. D. J. Gordon, Mie scattering by optically active particles. *Biochemistry 11*, **1972**, 413–420.

151. E. Y. H. Hong, V. W. W. Yam, Triindole-tris-alkynyl-bridged trinuclear gold(I) complexes for cooperative supramolecular self-assembly and small-molecule solution-processable resistive memories. *ACS Appl. Mater. Interfaces* **2017**, *9*, 2616–2624.

152. F. C. M. Leung, V. W. W. Yam, Cation- and solvent-induced supramolecular aggregation studies of crown ether-containing dinuclear alkynylgold(I) isocyanide complexes. *Eur. J. Inorg. Chem.* **2017**, 5271–5278.

153. A. Chu, F. K. W. Hau, V. W. W. Yam, $Au^{I} \cdots Au^{I}$ interaction assisted host–guest interactions and stimuli-responsive self-assembly in tetranuclear alkynylgold(I) calix[4]arene-based isocyanide complexes. *Chem. Eur. J.* **2017**, *23*, 11076–11084.

154. J. J. Henkelis, J. Fisher, S. L. Warriner, M. J. Hardie, Solvent-dependent self-assembly behaviour and speciation control of Pd_6L_8 metallo-supramolecular cages. *Chem. Eur. J.* **2014**, *20*, 4117–4125.

155. Y. Jiao, Y. Zuo, H. Yang, X. Gao, C. Duan, Photoresponse within dye-incorporated metal-organic architectures. *Coord. Chem. Rev.* **2021**, *430*, 213648.

156. S. L. Huang, T. S. A. Hor, G. X. Jin, Metallacyclic assembly of interlocked superstructures. *Coord. Chem. Rev.* **2017**, *333*, 1–26.

157. V. W. W. Yam, V. K. M. Au, S. Y. L. Leung, Light-emitting self-assembled materials based on d^8 and d^{10} transition metal complexes. *Chem. Rev.* **2015**, *115*, 7589–7728.

158. V. W. W. Yam, Molecular design of transition metal alkynyl complexes as building blocks for luminescent metal-based materials: structural and photophysical aspects. *Acc. Chem. Res.* **2002**, *35*, 555–563.

159. S. Y. L. Leung, S. Evariste, C. Lescop, M. Hissler, V. W. W. Yam, Supramolecular assembly of a phosphole-based moiety into nanostructures dictated by alkynylplatinum(II) terpyridine complexes through non-covalent Pt···Pt and π-π Stacking interactions: synthesis, characterization, photophysics and self-assembly behaviors. *Chem. Sci.* **2017**, *8*, 4264–4273.

160. C. H. Tao, H. Yang, N. Zhu, V. W. W. Yam, S. J. Xu, Branched luminescent multinuclear platinum(II) alkynyl complexes: candidates for efficient two-photon induced luminescence. *Organometallics* **2008**, *27*, 5453–5458.

161. V. W. W. Yam, A. S. Y. Law, Luminescent d_8 metal complexes of platinum(II) and gold(III): from photophysics to photofunctional materials and probes. *Coord. Chem. Rev.* **2020**, *414*, 213298.

162. S. Y. L. Leung, W. H. Lam, N. Zhu, V. W. W. Yam, Synthesis, structural characterization, and photophysical study of luminescent face-to-face dinuclear platinum(II) alkynyl phosphine complexes and their tetranuclear mixed-metal platinum(II)-silver(I) and -copper(I) complexes. *Organometallics* **2010**, *29*, 5558–5569.

163. V. W. Yam, L. P. Chan, T. E. Lai, Syntheses, photophysics, and X-ray structural characterization of dinuclear platinum(II) acetylide complexes, $[Pt_2(\mu\text{-dppm})_2(\mu\text{-PhC} \equiv C)(PhC \equiv C)_2]ClO_4$ and $[Pt_2(\mu\text{-dppm})_2(\mu\text{-}^tBuC \equiv C)(^tBuC \equiv C)Cl]ClO_4$. *Organometallics* **1993**, *2*, 2197–2202.

164. Y. S. Wong, M. Ng, M. C. L. Yeung, V. W. W. Yam, Platinum(II)-based host-guest coordination-driven supramolecular co-assembly assisted by Pt···Pt and π-π stacking interactions: a dual-selective luminescence sensor for cations and anions. *J. Am. Chem. Soc.* **2021**, *143*, 973–982.

165. A. K. W. Chan, V. W. W. Yam, Precise modulation of molecular building blocks from tweezers to rectangles for recognition and stimuli-responsive processes. *Acc.*

Chem. Res. **2018**, *51*, 3041–3051.

166. Z. M. Hudson, C. Sun, K. J. Harris, B. E. G. Lucier, R. W. Schurko, S. Wang, Probing the structural origins of vapochromism of a triarylboron-functionalized platinum(II) acetylide by optical and multinuclear solid-state NMR spectroscopy. *Inorg. Chem.* **2011**, *50*, 3447–3457.

167. C. M. Álvarez, L. A. García-Escudero, R. García-Rodríguez, J. M. Martín-Álvarez, D. Miguela, V. M. Rayón. Enhanced association for C_{70} over C_{60} with a metal complex with corannulene derivate ligands. *Dalton Trans.* **2014**, *43*, 15693–15696.

168. H. Jiang, W. Lin, Chiral metallacyclophanes: self-assembly, characterization, and application in asymmetric catalysis. *Org. Lett.* **2004**, *6*, 861–864.

169. H. Jiang, A. Hu, W. Lin, A chiral metallacyclophane for asymmetric catalysis. *Chem. Commun.* **2003**, 96–97.

170. Y. Yin, Z. Chen, R. H. Li, C. Yuan, T. Y. Shao, K. Wang, H. Tan, Y. Sun, Ligand-triggered platinum(II) metallacycle with mechanochromic and vapochromic responses. *Inorg. Chem.* **2021**, *60*, 9387–9393.

171. J. A. Whiteford, C. V. Lu, P. J. Stang, Molecular architecture via coordination: Self-assembly, characterization, and host-guest chemistry of mixed, neutral-charged, Pt-Pt and Pt-Pd macrocyclic tetranuclear complexes. X-ray crystal structure of cyclobis[[*cis*-Pt(dppp)(4-ethynylpyridine)$_2$][*cis*-$Pd^{2+}(PEt_3)_2$2$^-$ OSO_2CF_3]]. *J. Am. Chem. Soc.* **1997**, *119*, 2524–2533.

172. J. A. Whiteford, P. J. Stang, S. D. Huang, Neutral guest capture via lewis acid/base molecular square receptors. X-ray crystal structure of {ccyclobis[(cis-(dppp)Pt(4-ethynylpyridyl)$_2$)(*cis*-$(PEt_3)_2$Pt)]Ag_2}$^{+6}$(phenazine)($^-OSO_2CF_3$)$_6$. *Inorg. Chem.* **1998**, *37*, 5595–5601.

173. B. A. Anderson, E. C. Bell, F. O. Ginah, N. K. Harn, L. M. Pagh, J. P. Wepsiec, Cooperative catalyst effects in palladium-mediated cyanation reactions of aryl halides and triflates. *J. Org. Chem.* **1998**, *63*, 8224–8228.

174. N. Mézailles, L. Ricard, F. Gagosz, Phosphine gold(I) bis-(trifluoromethanesulfonyl)imidate complexes as new highly efficient and air-stable catalysts for the cycloisomerization of enynes. *Org. Lett.* **2005**, *7*, 4133–4136.

175. A. Tamaki, J. K. Kochi, Oxidative addition in the coupling of alkylgold(I) with alkyl halides. *J. Organomet. Chem.* **1974**, *64*, 411–425.

Jing ZHANG

TITRE de la thèse

Résumé

Nous avons exploré deux voies de synthèse de métallo-cryptophanes dans le but de créer des récepteurs doués de propriétés photophysiques originales. Dans une première partie nous avons synthétisé des complexes de Au(I) avec des cyclotribenzylènes (CTB) à fonctions alcynes afin dévaluer la capacité de ces composés à former des cryptophanes par interactions aurophiles. Les complexes sont luminescents dans $CHCl_3$ et complexent les ammoniums quaternaires comme Et_4N^+. Les complexes dans MeOH/ $CHCl_3$ s'auto-assemblent stéréosélectivement pour former des agrégats sphériques à des taux de MeOH élevés, le début de l'agrégation dépendant de la nature des ligands. Dans la deuxième partie, nous présentons la synthèse de pré-cryptophanes de platine à partir d'un CTB substitué par une fonction alcyne vraie et deux fonctions carbonitrile. Ces composés ont été isolés, de manière inattendue, sous forme de complexes de Cu(I). Les conformations des pré-cryptophanes sans Cu ont été étudiées dans différents solvants et dépendent des configurations relatives des CTB. Ces études ont ouvert la voie à de nouvelles approches synthétiques de crytophanes organométalliques.

Mots clés : Cyclotribenzylène, Complexe alcyne-metal noble, émission induite par l'agrégation, chiralité, pré-cryptophane

Résumé en anglais

We explored two ways for new approaches of metallo-cryptophane design and synthesis to create receptors endowed with original photophysical properties. In Part I, we synthesized alkynyl cyclotribenzylene (CTB) gold(I) complexes for evaluating their ability to form cryptophanes using aurophilic interactions. The organometallic CTBs were found to be luminescent in $CHCl_3$ and able to host quaternary ammoniums like Et_4N^+. Studies of optically-active and racemic gold CTB complexes in MeOH/$CHCl_3$ showed that they self-assembled stereoselectively into spherical nanoparticles at high MeOH content, the onset of nanoparticle formation depending on the nature of the metal ligands. In Part Ⅱ, luminescent organoplatinum precryptophanes were synthe-sized from a CTB containing an alkynyl and two carbonitrile substituents. They were unexpectedly isolated as Cu(I) complexes. The conformations of the Cu-free precryptophanes were studied in different solvents and were shown to depend also on the relative configurations of the two CTBs. These experiments paved the way for finding new strategies for the synthesis of organometallic cryptophanes.

Keywords : Cyclotribenzylene, Alkynyl noble metal complex, Aggregation-induced emission, Chirality, Precryptophane.

UNIVERSITE DE STRASBOURG

ECOLE DOCTORALE DES SCIENCES CHIMIQUES

RESUME DE LA THESE DE DOCTORAT

Mme ZHANG Jing

Titre : Composés organométalliques concaves chiraux: propriétés supramoléculaires et de luminescence

---

1) Introduction

La chimie supramoléculaire s'intéresse d'une part aux interactions entre un nombre limité de molécules, par exemple deux dans le cas de la formation d'un complexe entre un récepteur et un substrat, d'autre part aux assemblées moléculaires mettant en jeu un nombre élevé de molécules, par exemple dans la formation d'agrégats de morphologie et de taille diverses.[1] Les espèces supramoléculaires, qu'elles soient de simples complexes binaires ou des assemblées de molécules, sont mises en jeu notamment en analyse et en catalyse. Il est important de pouvoir détecter la formation de "supramolécules". De ce point de vue, l'émission de lumière (UV, mais surtout visible) est un phénomène particulièrement utile, grâce à sa grande sensibilité, son caractère non destructif, son inocuité, et sa facilité de mise en œuvre. Afin de pouvoir utiliser cette propriété lors de la manipulation des supramolécules il est nécessaire d'une part que les sous-unités moléculaires soient douées de luminescence et d'autre part que les phénomènes de piégeage de luminescence par agrégation soient inhibés.

Au cours de ce travail de thèse, nous nous sommes intéressés à une famille de récepteurs moléculaires concaves, les cyclotribenzylènes (CTB) et les cryptophanes (Figure 1).[2] Si les propriétés de complexation des CTB sont limitées, les cryptophanes, du fait de leur structure fermée, ont la capacité de complexer, avec de fortes affinités, une plus grande variété de substrats: Des molécules apolaires neutres, comme les petits alcanes, dont le méthane, les organohalogénés comme le chloroforme, mais aussi des cations organiques comme les ammoniums quaternaires. Il a été récemment démontré que les cryptophanes à cycles phénolate formaient des complexes avec les cations mous,[3] comme Cs^+ et Tl^+ et que les cryptophanes à cycles portant une charge positive complexaient les anions.[4] Depuis la découverte de l'aptitude des petits cryptophanes à complexer l'atome de Xe,[5] de nombreux travaux actuels ont pour objectif le développement de sondes au ^{129}Xe, notamment pour l'IRM,[6] car le déplacement chimique de cet atome est très sensible à son environnement.

Les cryptophanes, décrits pour la première fois par Collet au début des années 1980, peuvent être décrits comme des dimères de CTB face-à-face. Jusqu'à une vingtaine d'années, les cryptophanes étaient uniquement des composés organiques, mais depuis, il a été montré que ces composés pouvaient être obtenus, de manière expéditive, par auto-assemblage dirigé par des fragments de complexes de métaux de transition.[7] Certains de ces fragments sont

intrinsèquement luminescents et confèrent cette propriété aux cryptophanes correspondants. Une autre propriété des CTB et des cryptophanes est la chiralité. Sont chiraux les CTB portant au moins deux substituants différents sur l'une des sous-unités benzylène. En général les CTB chiraux comportent trois sous-unités benzylène identiques, dont les deux substituants sont disposés dans le même ordre, conférant à la molécule la symétrie C_3. Les cryptophanes, quant à eux, sont préparés sous deux formes diastéréoisomères, la forme *syn* ou *méso*, constituée de CTB de sens de chiralité opposés et la forme *anti*, constituée de CTB homochiraux. Ces derniers ont fait preuve d'intéressantes propriétés de reconnaissance énantiosélective.[8]

Au cours des vingt dernières années, de nouvelles approches de synthèse des cryptophanes ont été décrites. Celles-ci utilisent notamment les cations de certains métaux de transition (principalement Pd^{2+} et Pt^{2+}) pour assembler deux CTB face-à-face (Figure 2).[7,9] L'intérêt de cette approche est de réduire le nombre d'étapes de synthèse, mais aussi de permettre de travailler dans des conditions d'équilibre thermodynamique, qui vont, dans certains cas, favoriser la formation quasi-exclusive de l'isomère chiral. Notons que parallèlement à cette approche ont été développées des méthodes utilisant la formation de liaisons covalentes réversibles, qui permettent, elles aussi, d'opérer à l'équilibre thermodynamique et ont conduit au même résultat.[10]

Jusqu'à présent, les cyclotribenzylènes et les cryptophanes incorporant des cations de métaux de transition le faisaient grâce à des groupements fonctionnels de type ligand à atomes donneurs d'azote ou d'oxygène.[7] Nous avons donc décidé d'explorer, dans cette thèse, l'intérêt d'utiliser des ligands carbonés de type acétylure. En effet ces ligands conduisent, notamment avec les cations métalliques de la 3^e série des éléments de transition comme Pt^{2+} et Au^+, à des complexes stables de géométrie simple (carré-plan ou linéaire) et surtout, doués de propriétés de luminescence.[11] Nous présentons donc, dans les deux parties ci-après, d'une part des cyclotribenzylènes fonctionnalisés par des complexes acétylure d'or, d'autre part des cyclotribenzylènes pontés par des complexes acétylure de platine, dans les deux cas à ligands auxiliaires phosphine. Nous décrirons la synthèse de ces nouveaux composés et apporterons les preuves de leur identité chimique. Dans un second temps, nous étudierons leurs propriétés supramoléculaires en relation avec leurs propriétés de luminescence.

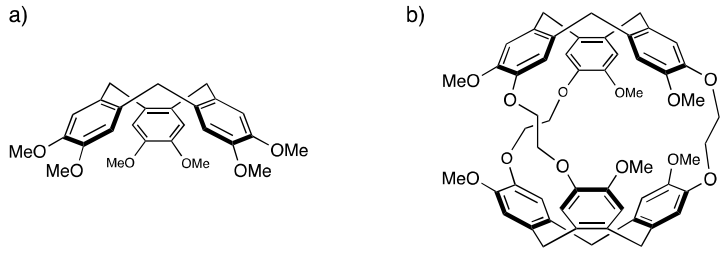


Figure 1. a) Un cyclotribenzylène achiral, le cyclotrivératrylène; b) Le cryptophane A, récepteur chiral de symétrie C_3 obtenu par triple pontage de deux sous-unités de type cyclotrivératrylène, en remplaçant un substituant méthoxy sur deux par une chaîne 1,2-dioxyéthylène.

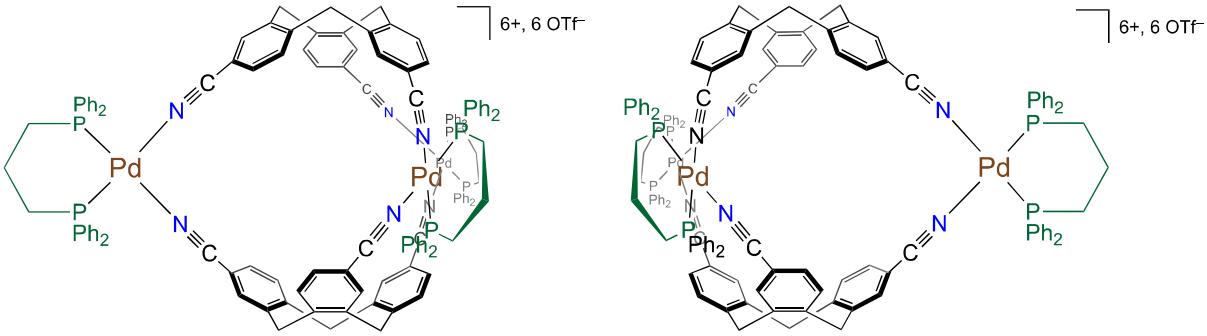


Figure 2. Un exemple de métallo-cryptophane ou cryptophane assemblé par des fragments de complexes de métaux de transition, ici $[Pd(dppp)]^{2+}$ (dppp = 1,3-bis(diphénylphosphino)propane).[9]

2) Résultats et discussion

2.1) Des cyclotribenzylènes fonctionalisés par des complexes acétylure de $[Au(PR_3)]^+$. La structure chimique générique de cette famille de composés est montrée à la Figure 3. Ces complexes trinucléaires d'or sont obtenus à partir des cyclotribenzylènes **1** et **2** incorporant trois entités phenylacétylène, le second se distinguant du premier par les substituants methoxy adjacents. Le cyclotribenzylène **2** avait été décrit dans la littérature,[12] mais **1** est un composé nouveau que nous avons synthétisé en cinq étapes à partir de l'alcool 3-méthoxy benzylique. La complexation du fragment $[AuPR_3]^+$ est effectuée soit en une étape, par réaction du cyclotribenzylène avec $[Au(Cl)PR_3]$ en présence de NaOMe, soit en deux étapes, par réaction du cyclotribenzylène avec $[Au(Cl)(SMe_2)]$ pour former d'abord un polymère de coordination organométallique qui est ensuite fragmenté par la phosphine.[13] Cette dernière voie se déroule à température ambiante. Elle sera utilisée, en particulier, pour la complexation de cyclotribenzylènes énantiomériquement purs, afin d'éviter la racémisation du ligand. Nous avons utilisé des phosphines de tailles et de propriétés életroniques différentes, afin de pouvoir éventuellement d'identifier l'influence de ces caractéristiques sur les propriétés des CTB organo-métalliques. Les huit composés **C1**, **C2**, **C3**, **C4**, **C5**, **C6, C7** et **C9** ont été isolés par précipitation sélective et obtenus avec des rendements s'échelonnant de 53 à 80%, selon la voie suivie et la nature de la phosphine. Dans les séries **C1** - **C3** et **C4** - **C6** la taille et le caractère électrodonneur du ligand phosphine varient en ordre inverse. **C7** et **C9** permettent d'étudier les complexes à ligands phosphine PEt_3 (**C7**) et PCy_3 (**C9**) plus basiques que $PPh_{3-n}Me_n$, mais de tailles très différentes. Notons qu'un complexe **C8** (non représenté), non symétrique, a été isolé au cours de la séparation directe des énantiomères de **C1** par HPLC sur phase stationnaire chirale. Les complexes **C1** à **C6** ont été obtenus sous forme énantiomériquement pure, soit de manière directe, par HPLC sur phase stationnaire chirale, soit de manière indirecte, à partir des versions optiquement pures des cyclotribenzylènes **1** et **2**. Ce travail, ainsi que la caractérisation chiroptique des complexes énantiopurs obtenus, a été effectué grâce à une collaboration avec le laboratoire du Dr. Nicolas Vanthuyne (UMR 7313, Aix-Marseille Université).

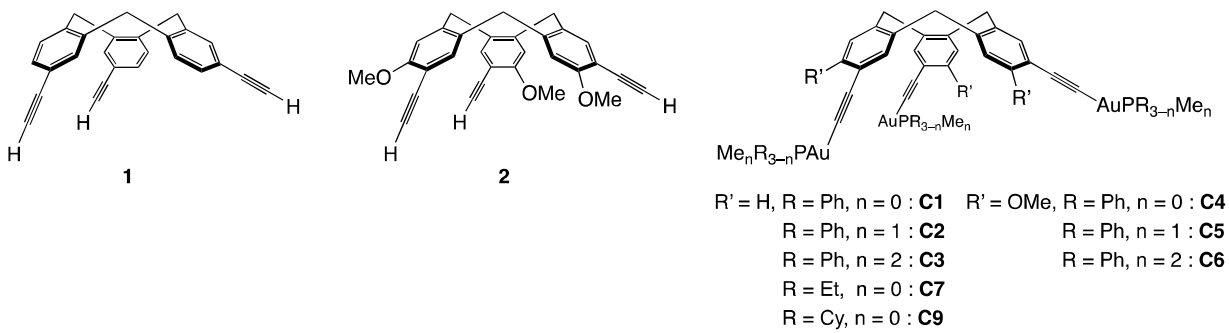


Figure 3. Structures des cyclotribenzylènes de départ **1** et **2** et des complexes trinucléaires d'or dérivés, **C1** - **C3**, **C7**, et **C9** pour **1**, et **C4** - **C6** pour **2**, respectivement.

Tous les complexes ont été caractérisés de manière exhaustive par RMN (^{1}H, ^{13}C et ^{31}P), IR, et analyse élémentaire. Nous avons ensuite examiné s'ils pouvaient donner lieu à la formation de dimères face-à-face, grâce à l'établissement d'interactions aurophiles intermoléculaires entre les atomes d'or de deux cyclotribenzylènes, en solution (RMN DOSY) ou en phase gaz (spectrométrie de masse). Ces études ont fait l'objet d'une collaboration avec le Service de RMN de la Fédération de Recherche Chimie "Le Bel" (Dr. Bruno Vincent) pour la mesure des constantes de diffusion et avec le Laboratoire de Spectrométrie de Masse des Interactions et des Systèmes (Dr. Emmanuelle Leize-Wagner, UMR 7140, Université de Strasbourg) pour les mesures de spectrométrie de masse par la technique d'ionisation "electrospray". Les mesures de diffusion sur des solutions de **C1**, **C7** et **C9** ont montré que les cyclotribenzylènes étaient sous forme monomère prédominante en solution, pour **C1** jusqu'à une concentration de 10^{-2} M. Les mesures de masse moléculaire en phase gaz ont permis de détecter la forme dimère sous forme d'adduit dichargé $[2M + 2H]^{2+}$ pour tous les composés sauf **C7** et **C8**. Cette forme est observée aux faibles énergies de collision (E_{coll}) et disparaît quand E_{coll} > 10 eV. Des hétérodimères ont été observés en injectant des solutions équimolaires de CTB différents. Les liaisons Au···Au sont sensibles au compromis entre une minimisation de l'encombrement stérique à leur proximité et une maximisation du caractère électro-accepteur de PR_3.

Les propriétés de spectroscopie électronique (absorption, émission) des complexes **C1** - **C9** ont été déterminées pour des solutions diluées (10^{-5} M) dans un premier temps dans le chloroforme. En absorption, nous observons des signatures typiques et différentes, selon que les complexes sont obtenus à partir du cyclotribenzylène **1** ou du cyclotribenzylène **2**. Tous les complexes sont émissifs. A l'air, ils présentent une émission faible, mais détectable dans le proche UV avec un maximum vers 375 nm et de durée de vie courte (1 ns), dont l'origine est un état excité singulet. En l'absence d'oxygène, sous argon, ils présentent une émission dans le visible vers 425 nm et de durée de vie longue (30 μs), provenant de l'état triplet. Ces émissions sont en accord avec les nombreux comptes-rendus de la littérature sur les propriétés spectroscopiques des complexes ArC_2AuPPh_3, qu'ils soient mononucléaires ou polynucléaires.[14]

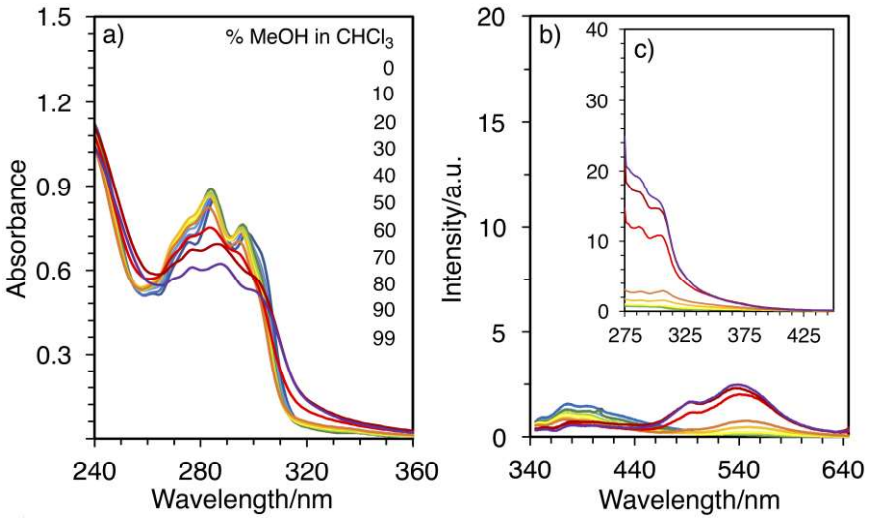


Figure 4. Spectres électroniques de solutions 10^{-5} M du composé **1** dans des mélanges $CHCl_3$/MeOH de différentes composition: (a) absorption; (b) emission; (c) excitation.

Dans un second temps, nous avons enregistré les spectres électroniques des complexes **C1** - **C9** dans des mélanges de chloroforme et de méthanol afin d'examiner si les complexes donnaient lieu au phénomène de solvatochromisme. Nous avons effectué cette étude en solution non dégazée. Pour tous les complexes, nous avons observé que lorsque la proportion de méthanol augmentait les bandes d'absorption s'élargissaient et, aux proportions élevées de méthanol, subissaient un déplacement bathochrome significatif. En émission, les complexes donnent lieu à un phénomène de luminescence duale : lorsque la proportion de méthanol augmente à partir d'un seuil, dont la valeur précise dépend du complexe (entre 50 et 70%), l'émission dans le proche UV à 375 nm décroît au profit d'une émission dans le visible, vers 540 nm. Elle est à son maximum pour un rapport MeOH/$CHCl_3$ de 90:10, v/v. En outre, nous avons observé que ces solutions diffusaient la lumière, ce qui nous a suggéré qu'elles étaient constituées d'agrégats. Les solutions des complexes **C1** et **C4** ont été examinées par diffusion de la lumière (technique dite DLS), ce qui nous a permis de déterminer la distribution des tailles des nanoparticules (plusieurs dizaines de nm) en fonction du taux de méthanol. En outre, comme indiqué par des images par microscopie électronique obtenues grâce à la collaboration du Dr. Eloïse Devaux (Laboratoire des nanostructures ISIS/Unistra), les nanoparticules sont de morphologie sphérique.

Le remplacement du méthanol par l'acétonitrile (étudié dans le cas de **C1**) ne conduit pas à des changements significatifs des spectres électroniques qui avaient été enregistrés dans le chloroforme pur. Ceci confirme que ce que nous observons dans le cas des solutions à taux élevé de méthanol n'est pas un effet du solvatochromisme, mais est lié à la solvophobie des complexes. Plutôt que d'être solvatées par le méthanol, les molécules de complexe s'agrègent de manière à présenter la surface minimale à ce solvant. Nous avons vu, par microscopie STEM, que les agrégats étaient de forme sphérique. Afin d'essayer de préciser la manière dont les molécules de complexe sont arrangées dans les agrégats, nous avons enregistré les spectres de dichroïsme circulaire des complexes **C1** et **C4** optiquement purs dans des mélanges $CHCl_3$/MeOH. Lorsque la proportion de méthanol augmente, on observe, comme en

spectroscopie d'absorption UV-visible, une diminution de l'intensité des bandes, leur élargissement, ainsi que le déplacement bathochrome de leur maxima (Figure 5), ce qui suggère la formation d'agrégats J entre les noyaux aromatiques des cyclotribenzylènes.

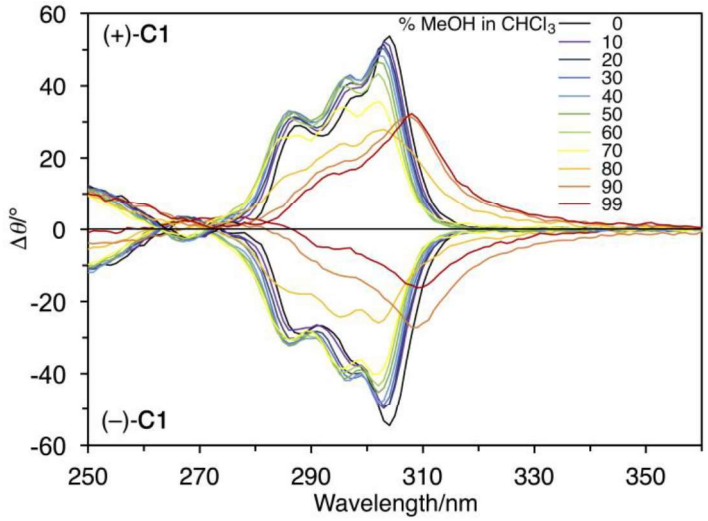


Figure 5. Evolution des spectres de dichroïsme circulaire des cyclotribenzylènes énantiomères (+)-**C1** et(–)-**C1** en fonction du taux de méthanol dans le chloroforme.

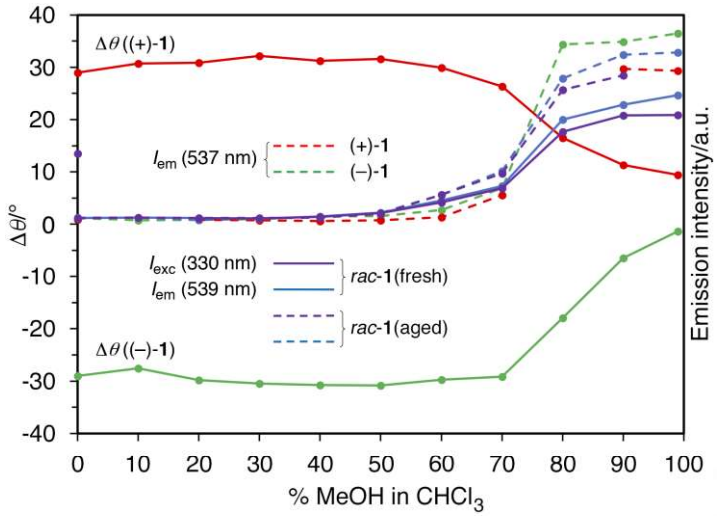


Figure 6. Evolution, en fonction du pourcentage de MeOH dans le chloroforme, du dichroïsme circulaire $\Delta\theta$, et de l'intensité d'émission vers 540 nm de solutions 10^{-5} M du complexe **1** sous forme énantiomériquement pure ((+)-**1** et (–)-**1**) et racémique.

Il est intéressant de comparer l'évolution, en fonction de la proportion de méthanol dans le chloroforme, de l'intensité d'émission de la bande vers 540 nm du complexe **1** sous forme racémique et sous forme énantiomériquement pure. Comme le montre la Figure 6, le pourcentage de méthanol à partir duquel cette émission apparaît, est plus élevé dans la cas de (+)-**1** et (–)-**1** par comparaison avec *rac*-**1**, que la solution ait été fraîchement préparée ou ait quelques jours. Plus précisément le seuil est de 60% pour les formes énantiomériquement

pures et de 50% pour le mélange racémique. La Figure 6 montre aussi l'évolution concomitante du dichroïsme circulaire à 330 nm, longueur d'onde à laquelle l'effet Mie (élargissement et déplacement des bandes dus à la formation de nanoagrégats[15]) est particulièrement sensible. Les différences de valeurs de seuils pourraient indiquer que la composition des agrégats formés à partir de *rac*-**1** diffère de celle des agrégats formés à partir des versions énantiopures de **1**. Ces dernières donnant lieu à des agrégats homochiraux, les agrégats formés à partir de *rac*-**1** sont hétérochiraux, donc des racémates plutôt que des conglomérats.

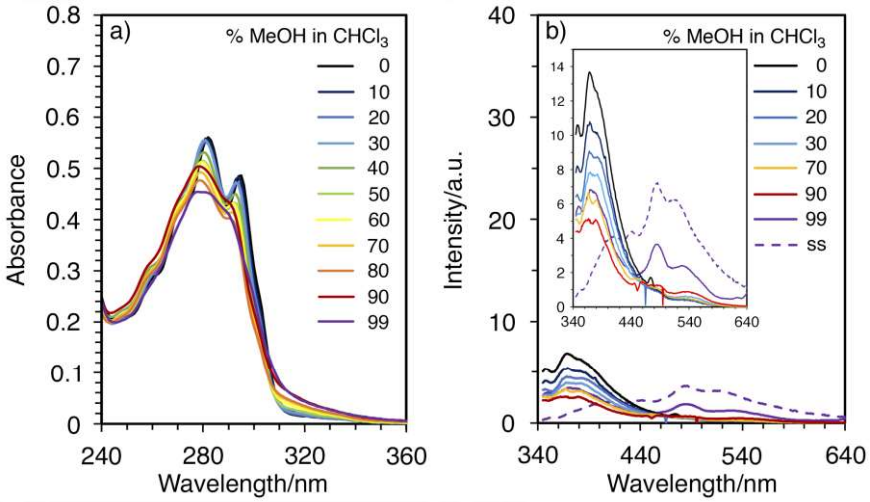


Figure 7. Spectres électroniques de solutions 10^{-5} M du composé C**9** dans des mélanges $CHCl_3$/MeOH de différentes compositions: (a) absorption; (b) émission. Dans le tracé des spectres d'émission nous avons inséré les spectre d'émission de C**9** à l'état solide (tirets violets).

Les cyclotribenzylènes **C1** - **C7** donnent tous lieu au phénomène d'émission induite par l'agrégation (AIE en anglais), ce qui n'est pas le cas de leurs précurseurs **1** et **2**. En particulier, la valeur de la longueur d'onde de cette émission (autour de 540 nm) est indépendante de la nature du complexe. Les évolutions spectrales enregistrées en fonction du pourcentage de méthanol dans le chloroforme diffèrent dans le détail d'un composé à l'autre, notamment en termes de seuil d'agrégation et de rapport entre l'intensité initiale d'émission vers 380 nm (mesurée dans $CHCl_3$ pur) et l'intensité d'émission à 540 nm (mesurée à 90 ou 99% de MeOH). Des phénomènes similaires ont été mis en évidence pour des complexes acétylure d'or amphiphiles, mais en milieu aqueux. L'émission de lumière visible induite par l'agrégation a été interprétée par la mise en place d'interactions aurophiles entre les molécules agrégées.[16] Par analogie nous proposons d'interpréter l'appartition d'une bande à 540 nm lorsque les complexes **C1** - **C7** ont été dissous dans des solutions de chloroforme diluées avec des proportions élevées de méthanol par l'émission résultant de transitions du type $^3(d_\sigma^* \rightarrow p_\sigma)$. Le cas du complexe **C9** est à traiter à part, car l'évolution de son spectre d'émission en fonction du pourcentage de méthanol est différente de celle des sept autres. En effet, l'émission induite par l'agrégation reste très faible, même jusqu'à 90% de méthanol. Ce n'est qu'à 99% de méthanol que son intensité devient notable, mais la forme de la bande diffère de celle des autres composés, puisque deux maxima sont identifiables, l'un à 485, l'autre à 529

nm (Figure 7). Nous avons, dans ce cas particulier, enregistré le spectre d'émission à l'état solide de **C9**. Celui-ci est superposé à celui obtenu dans le mélange $CHCl_3$/MeOH 1:99. Les deux spectres présentent des similitudes frappantes qui confirment que l'émission des complexes dans le visible est due au rapprochement des molécules par agrégation, en solution ou à l'état solide.

Les cryptophanes, comme le cryptophane A de la Figure 1, sont des récepteurs particulièrement affins des cations ammoniums, la reconnaissance ayant lieu grâce à des interactions de type cation-électrons π.[17] Les cyclotribenzylènes n'ont pas fait l'objet d'autant d'études. Néanmoins, des cyclotribenzylènes fluorescents porteurs de groupements anioniques ont été utilisés comme sondes de l'acétylcholine (neurotransmetteur contenant une fonction ammonium) en milieu aqueux.[18] Nous avons étudié la capacité du cyclotribenzylène **C1** à complexer le tétraéthylammonium dans le chloroforme en suivant par spectroscopie de RMN du proton le titrage de l'ammonium quaternaire par **C1** (Figure 8). A l'échelle de temps de la RMN, le substrat complexé est en échange rapide avec le substrat restant en solution. Le fait que les protons des groupes méthyle et méthylène du tétraéthylammonium subissent un blindage d'autant plus important que la quantité de **C1** est plus élevée atteste de la formation d'un complexe d'inclusion **C1**$\supset Et_4N^+$ dans lequel ces protons subissent un blindage induit par les sous-unités benzylène du récepteur. Le traitement des données au moyen du programme Bindfit nous a permis de montrer que le complexe était de stœchiométrie 1:1 et que la constante d'association correspondante K_a avait la valeur relativement élevée de 8900 M^{-1}. NEt_4^+ étant trop gros pour entrer dans la cavité du métallocryptophane virtuel obtenu par dimérisation de **C1**, des mesures de coefficients de diffusion de **C1** en présence du tétraéthylammonium par la technique DOSY nous ont permis de confirmer que **C1** était bien sous forme monomère dans la gamme de concentrations 10^{-3} - 10^{-2} M.

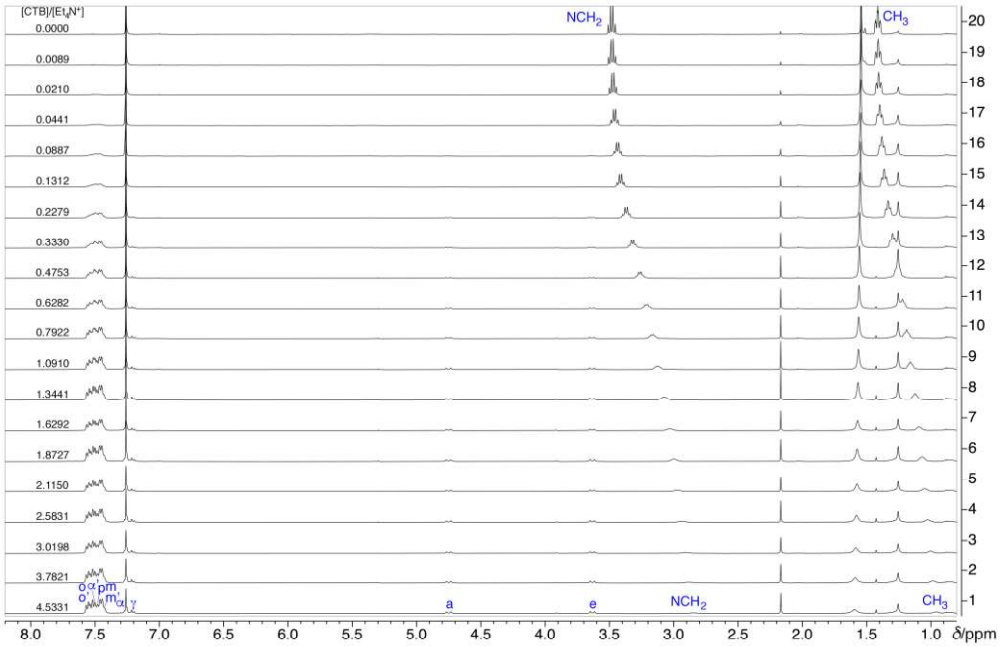


Figure 8. Titrage de **C1** par l'iodure de tétraéthylammonium dans $CDCl_3$.

En conclusion, la fonctionnalisation de cyclotribenzylènes par des acétylures de $[Au(PR_3)]^+$ conduit à des complexes trinucléaires de Au(I) présentant une concavité. En solution ces complexes ne forment pas, de manière notable et utilisable, des métallo-cryptophanes par dimérisation face-à-face induite par des interactions aurophiles. En revanche, ils donnent lieu à des phénomènes d'émission multiple en fonction de l'environnement (atmosphère, solvant) et de leur état (solution, solide). En particulier, dans des mélanges de chloroforme/méthanol riches en méthanol, ils donnent lieu au phénomène d'émission induite par l'agrégation. Cette émission provient vraisemblablement d'états excités résultant d'interactions aurophiles, ces dernières étant favorisées par la proximité contrainte des molécules dans les agrégats. Les complexes **C1** - **C9** sont chiraux, une propriété unique par rapport aux nombreux complexes acétylures d'or de la littérature. Certains d'entre eux ont été dédoublés en leurs énantiomères par HPLC ou préparés sous forme énantiopure à partir des précurseurs **1** et **2** eux-mêmes sous forme énantiopure. En milieu $CHCl_3$/MeOH 10:90 ils forment des nanoagrégats chiraux émettant de la lumière verte qui pourraient être exploités pour le développement de matériaux capables d'émettre de la lumière polarisée circulairement.

2.2) Vers des cryptophanes organométalliques à base d'acétylure de platine. La deuxième partie de notre travail de thèse examine la possibilité de préparer des cryptophanes organométalliques incorporant un fragment pontant de type bis-acétylure de Pt(II). Au laboratoire avaient été préparés des cryptophanes métallo-organiques dans lesquels deux molécules du cyclotribenzylène **5** de la Figure 9 ci-dessous portant trois fonctions carbonitriles étaient pontées par trois fragments complexes $[Pt(dppp)]^{2+}$, où dppp = 1,3-bis(diphenylphosphino)propane (Figure 2).[9] La formation des métallocryptophanes est quantitative et diastéréosélective en faveur des espèces chirales (par opposition à la forme *méso*, hétérochirale). Le succès de cette approche repose sur le caractère dynamique de la liaison Pt–N(C). Afin d'incorporer, dans ce type de cryptophane, un fragment complexe pontant luminescent, nous nous sommes lancés dans la synthèse du nouveau cyclotribenzylène **6** fonctionnalisé avec un substituant alcyne et deux substituants carbonitrile (Figure 9). Il n'était en effet pas réaliste d'envisager de synthétiser un cryptophane organométallique structuré exclusivement par des fragments complexes de type bis-acétylure de Pt(II), la liaison Pt–C(C) n'étant pas dynamique. L'idée était donc de synthétiser un cryptophane mixte incorporant un fragment complexe organométallique et deux fragments complexes à liaisons de coordination platine–carbonitrile. En conséquence, la voie de synthèse du métallocryptophane correspondant diffère de celle utilisée précédemment. Au lieu d'être assemblés de manière directe par couplage de type tripode-tripode, les métallo-cryptophanes organométalliques seront préparés en deux étapes, par l'intermédiaire de composés que nous appellerons "précryptophanes", comme indiqué sur la Figure 10 dans laquelle figurent les structures d'une forme chirale des précrytophanes [*cis*-$(Pt(PEt_3)_2)$(**4**–H)$_2$] et [P(dppp)(**4**–H)$_2$] (dppp est le chélate bidente 1,3-(bis(diphénylphosphino)propane) et des métallocryptophanes-cibles $[Pt_3(dppp)_3$(**4**–H)$_2]^{4+}$ et $[Pt(PEt_3)_2Pt_2(dppp)_2$(**4**–H)$_2]^{4+}$.

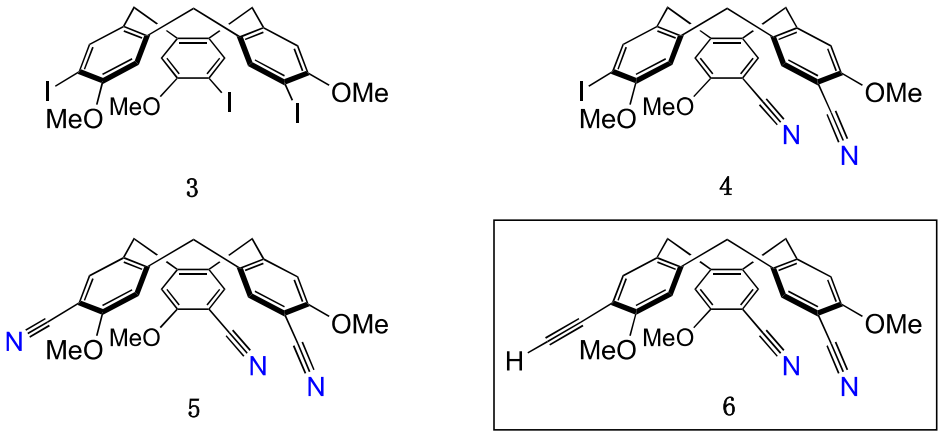


Figure 9. Structures du cyclotribenzylène-cible **6** (en encadré), de ses précurseurs **3** et **4**, et du sous-produit **5**.

Le cyclotribenzylène **6** a été préparé en trois étapes à partir du précurseur **3** connu.[19] La difficulté de sa préparation réside dans la substitution de deux atomes d'iode seulement de **3** par CN^-. Celle-ci est effectuée de manière statistique, par réaction de substitution nucléophile pallado-catalysée de **3** avec $[Zn(CN)_2]$.[20] Il est ensuite nécessaire de séparer le dérivé disubstitué **4** du composé trisubstitué **5**, ce qui est effectué par chromatographie sur colonne. **4** est obtenu avec un rendement de 34%. Le substituant -I restant est remplacé ensuite par -C≡C($SiMe_3$), par réaction de **4** avec le triméthylsilylacétylène (rendement: 78%).[21] Le composé-cible **6** est récupéré de manière quasi-quantitative par réaction avec les ions fluorure suivie d'une hydrolyse. Il représente un des rares exemples de cyclotrivératrylènes asymétriques. Ce composé a été dédoublé en ses énantiomères (+)-**4** et (–)-**4** par HPLC sur phase chirale et ses propriétés chiroptiques mesurées (Dr. N. Vanthuyne).

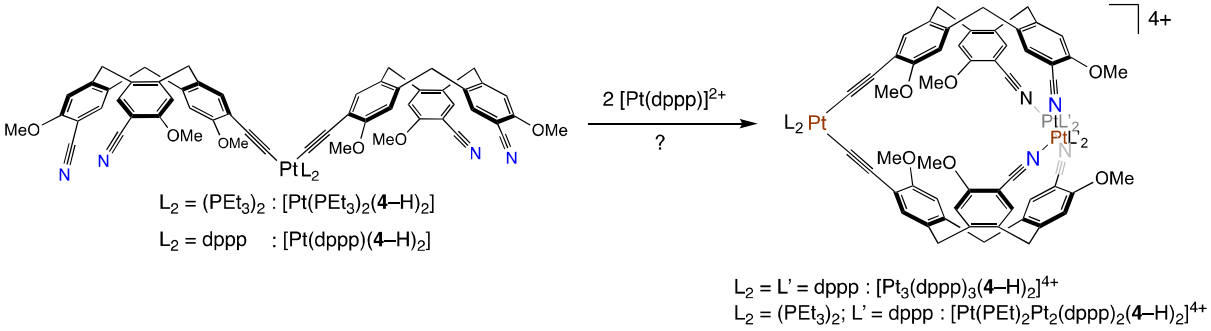


Figure 10. Structures des précryptophanes $[Pt(dppp)(\mathbf{4}–H)_2]^{4+}$ et $[Pt(PEt_3)_2(\mathbf{4}–H)_2]^{4+}$ et des métallocryptophanes-cibles $[Pt_3(dppp)_3(\mathbf{4}–H)_2]^{4+}$ et $[Pt(PEt_3)_2Pt_2(dppp)_2(\mathbf{4}–H)_2]^{4+}$. Seuls les isomères *anti* (chiraux) des précryptophanes et des métallocryptophanes sont représentés ici.

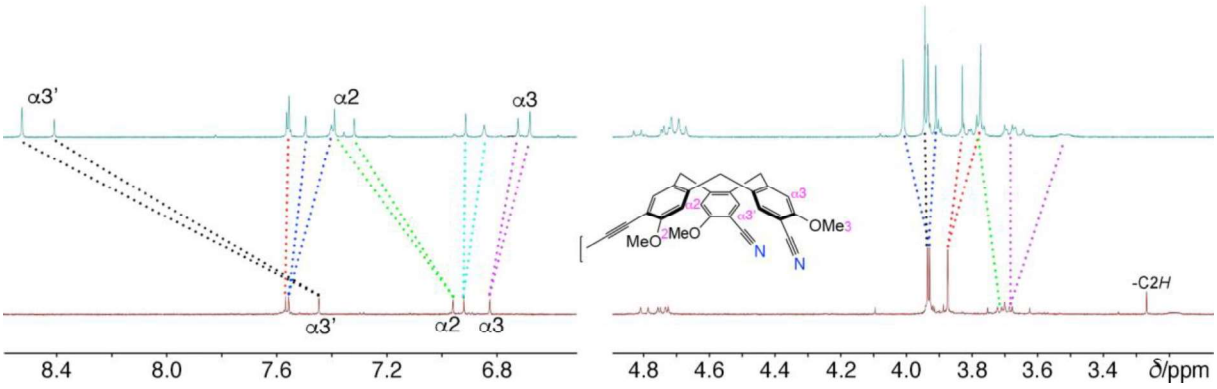


Figure 11. Spectres de RMN du proton des CTB **4** (bas) et précryptophane (haut) préparé à partir de *cis*-[Pt(PEt$_3$)$_2$Cl$_2$]. Les lignes en pointillés de couleur permettent de suivre les mouvements des signaux des différents protons lorsque l'on passe du CTB **4** au précryptophane. Seuls les labels des protons dont les signaux subissent des variations importantes de déplacement chimique sont indiqués. La structure chimique représentée est celle du CTB **4** après incorporation dans le précryptophane et donc perte du proton alcyne.

Nous avons utilisé le cyclotribenzylène **4** pour la préparation de deux précryptophanes par réaction avec *cis*-[Pt(PEt$_3$)$_2$Cl$_2$], d'une part et [Pt(dppp)Cl$_2$], d'autre part, dans les conditions du couplage de Sonogashira (CuI, NEt$_3$). Dans le cas de *cis*-[Pt(PEt$_3$)$_2$Cl$_2$], l'analyse du mélange réactionnel brut par RMN du proton avant purification par colonne de chromatographie a montré qu'il était constitué de deux espèces dans le rapport 1:1. Il n'a pas été possible de les séparer ensuite, mais le passage du mélange sur une colonne chromatographique a permis d'obtenir les composés **7M** (majeur) et **7m** (mineur), facilitant ainsi l'attribution des signaux à l'un et l'autre de ceux-ci. La Figure 11 montre les changements subis par le spectre de RMN du proton du CTB **4** après incorporation dans le précryptophane. Les faits les plus remarquables sont d'une part le déblindage important (> 1 ppm) des signaux des protons α3' des deux isomères, d'autre part le blindage des protons α3 et surtout des protons des substituants OMe3. Par ailleurs, l'examen du mélange par spectrométrie de masse a révélé que le signal moléculaire correspondait à l'adduit au cuivre $[M + Cu]^+$, principalement, celui-ci étant accompagné par le signal de l'adduit au sodium, $[M + Na]^+$.

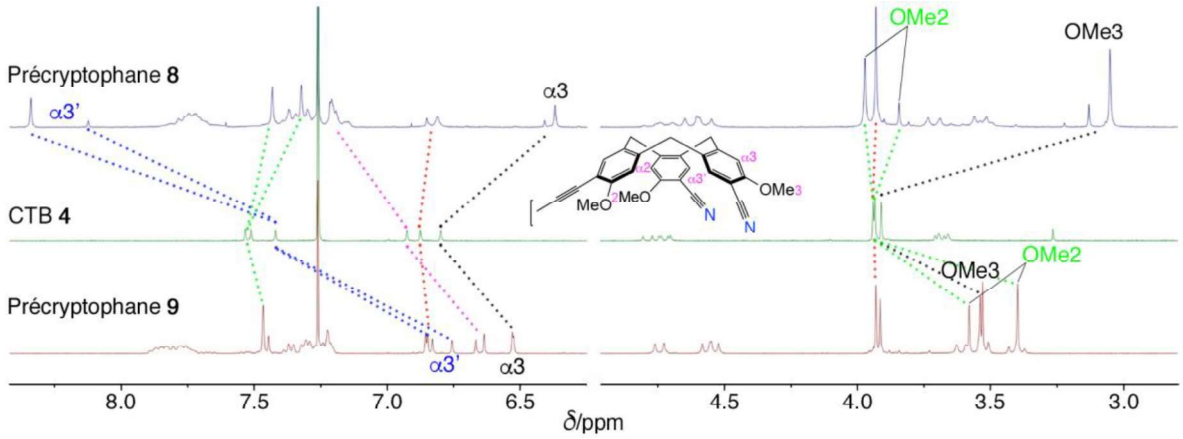


Figure 12. Spectres de RMN du proton obtenus après réaction du CTB **4** avec [Pt(dppp)Cl_2] en présence de CuI et de triéthylamine, et purification chromatographique du mélange réactionnel brut: (haut) composé **8**, (milieu) CTB **4**, (bas) composé **9**. Les lignes en pointillés de couleur permettent de suivre les mouvements des signaux des différents protons lorsque l'on passe du CTB **4** aux précryptophanes. Seuls les labels des protons dont les signaux subissent des variations importantes de déplacement chimique sont indiqués.

Le précryptophane [Pt(dppp)(**4**–H)$_2$] a été préparé de la même manière. Cependant, le passage du produit de réaction brut sur une colonne de chromatographie a permis, dans ce cas, de séparer deux composés (**8** et **9**) dont les spectres de RMN du proton, très différents, sont reproduits à la Figure 12. L'examen du spectre de RMN du proton du composé **8** montre que ce dernier est constitué d'un mélange de deux isomères **8M** et **8m**, mais fortement enrichi en **8M**. Ce spectre montre, par rapport à celui du CTB **4**, un déblindage important des protons α3', comme déjà observé dans le cas du mélange de **7M** et **7m**, ainsi qu'un blindage de même importance, en valeur absolue, des protons OMe3, situés sur le même noyau aromatique que les protons α3', celui portant la fonction alcyne. De telles variations de déplacement chimique ne sont pas observées dans le cas du composé **9**, isolé lui aussi sous forme de deux isomères, **9M** et **9m**, mais dans une proportion plus équilibrée. Toutefois, lorsque l'on passe du spectre du CTB **4** à **9**, on voit que les protons α3' subissent cette fois-ci un blindage de 0,75 ppm et les protons OMe2M, un blindage de 0,6 ppm, tout comme les protons OMe3M, d'ailleurs.

C'est l'examen des spectres de masse des mélanges de diastéréoisomères qui permet de déterminer la nature des complexes **8** et **9**. Le premier montre uniquement le signal moléculaire $[M + Cu]^+$ correspondant à l'adduit au cuivre, le second, uniquement le signal moléculaire $[M + Na]^+$ correspondant à l'adduit au sodium. Nous faisons donc l'hypothèse que **8** est le complexe de Cu(I) du précryptophane attendu. Il répond donc a priori à la formulation [Pt(dppp)(**4**–H)$_2$Cu]X, (X = Cl, I), alors que **9** est bien le précryptophane attendu, soit [Pt(dppp)(**4**–H)$_2$]. Le déblindage des protons α3' est donc caractéristique de la coordination de Cu(I) au cryptophane. La proximité de ces protons avec le fragment organométallique pontant (C≡C)$_2$Pt situé en *ortho* de chacun d'eux incite à penser que le cation Cu^+ est coordonné en mode bis(η^2-alcyne). Ce mode de coordination a été mis en évidence dans le cas de nombreux complexes bis(acétylure) de Pt^{2+}, notamment par Lang et van Koten.[22] Le déblindage des protons α3' pourrait être expliqué par des liaisons de type C–H···I$^-$, ce qui implique que

l'halogénure soit coordonné à Cu^+. La Figure 13 représente une structure du complexe [Pt(dppp)(**4**–H)$_2$CuI] sous forme chirale (symétrie C_2) intégrant ces hypothèses. On voit qu'une conséquence de ce modèle est le positionnement des substituants OMe3 occupant l'autre position *ortho* des fragments organométalliques pontants dans le cône de blindage du ligand auxiliaire dppp. Ceci rend compte de la résonance à champ fort de ces substituants.

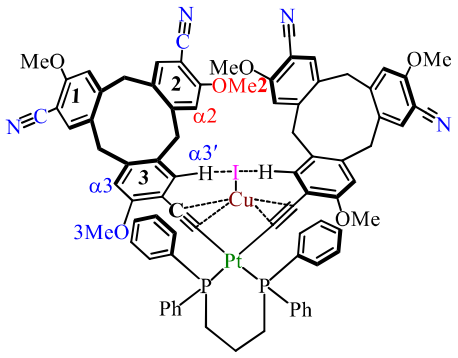


Figure 13. Structure possible du précryptophane complexé par le Cu(I), [Pt(dppp)(**4**–H)$_2$CuI] correspondant au précroptophane **8**. Cette structure rend compte du fort blindage des protons OMe3 par un substituant phényle du ligand dppp et du blindage moindre des protons α3 plus éloignés, ainsi que du fort déblindage des protons α3' dû à leur interaction avec l'ion iodure lié au cuivre(I) complexé aux fragments alcyne.

Le spectre de RMN du proton du produit de la réaction de formation du précryptophane [*cis*-(Pt(PEt$_3$)$_2$)(**4**–H)$_2$] montrant, on l'a vu, des signaux déblindés des protons α3' par rapport à leur position dans le spectre du CTB libre, ce produit correspond en fait au complexe de Cu(I) [*cis*-(Pt(PEt$_3$)$_2$)(**4**–H)$_2$CuI]. L'origine du cuivre étant CuI utilisé comme auxiliaire dans la réaction, nous avons, dans un deuxième temps, inclus un protocole de lavage du produit brut de réaction solubilisé dans le dichlorométhane avec un excès de cyanure de sodium en solution aqueuse, l'ion CN^- ayant une forte affinité pour Cu(I). Ce protocole nous a permis d'obtenir de manière univoque le précryptophane [*cis*-(Pt(PEt$_3$)$_2$)(**4**–H)$_2$] avec un rendement de 65% et un rapport diastéréomérique de 56:44. Il est intéressant de comparer le spectre de RMN du proton du précryptophane [*cis*-(Pt(PEt$_3$)$_2$)(**4**–H)$_2$] avec celui correspondant au précryptophane [Pt(dppp)(**4**–H)$_2$]. En effet, si l'on y retrouve le déplacement aux champs forts déjà noté des signaux des protons des groupes OMe2, on n'y retrouve pas un déplacement des mêmes ordre de grandeur et direction des signaux des protons α3', ainsi que OMe3. Il est donc probable que l'origine du blindage des protons α3' et OMe3 dans [Pt(dppp)(**4**–H)$_2$] provienne du fait que ces protons soient plongés dans le cône de blindage d'un substituant phényle du ligand auxiliaire dppp. Le blindage des protons OMe2 dans le cas des précryptophanes libres (c'est-à-dire ne complexant pas de Cu^+) peut être interprété comme résultant d'un changement de conformation. Comme représenté à la Figure 12, le précryptophane adopte un conformation de symétrie C_2 dans laquelle le substituant OMe2 d'un CTB est complexé par l'autre CTB, ce qui le situe dans la zone de blindage de ce dernier. Ce phénomène d'auto-complexation a déjà été observé dans le cas des cryptophanes dits "implosés".[23]

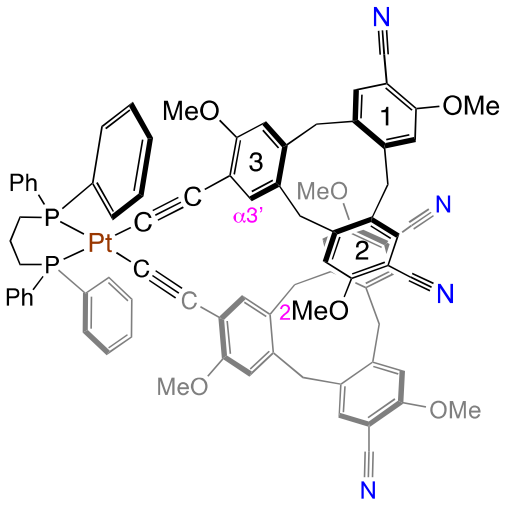


Figure 14. Proposition de modèle pour la structure du précryptophane [Pt(dppp)(**4**–H)$_2$] (composé **9** de la Figure 12). Cette vue montre clairement l'origine du blindage des protons OMe2 d'un CTB par l'autre CTB et du blindage des protons α3' par un substituant phényle du chélate dppp.

L'utilisation des isomères optiques de **4** nous a permis de préparer les précryptophanes énantiopurs sous forme des complexes de Cu(I) [*cis*-(Pt(PEt$_3$)$_2$)((–)-**4**–H)$_2$CuI] et [Pt(dppp)((+)-**4**–H)$_2$CuI].

En conclusion, l'approche "précryptophane" aux cryptophanes organométalliques s'est avérée plus ardue que prévu. Nous n'avons pas immédiatement pris conscience de la présence de Cu^+ dans la formulation de ces complexes, ce qui a été à l'origine de l'échec des premiers essais de fermeture des précryptophanes par des ions Pt^{2+}. Ce problème levé, nous nous employons actuellement à confirmer les résultats encourageants que nous avons récemment obtenus.

3) Conclusion générale

Notre travail a exploré pour la première fois la synthèse et les propriétés de cyclotribenzylènes chiraux comportant des substituants organométalliques de type acétylure d'or à ligand auxiliaire phosphine. Nous avons montré que ces cyclotribenzylènes étaient le siège de phénomènes de luminescence multiple, conférés par leur modification organométallique. Par ailleurs, ces cyclotribenzylènes, comportant des sous unités apolaires (squelette cyclotribenzylène et phosphines comme ligands auxiliaires terminaux), ont des propriétés solvophobiques en présence de solvants oxygénés comme le méthanol, donnant lieu à un phénomène d'agrégation. L'assemblage de métallocryptophanes à base de complexe bis-acétylure de platine a été exploré. Il met en jeu un intermédiaire de type "précryptophane", très rarement utilisé dans la synthèse organique des cryptophanes. Deux précryptophanes ont été préparés et caractérisés, sous forme de mélanges de diastéréoisomères et sous forme optiquement pure. L'étude de leur conversion en métallocryptophane est en cours.

4) Références

[1] J.-M. Lehn, Supramolecular Chemistry, John Wiley and Sons Inc, **1995**.

[2] (a) A. Collet, *Tetrahedron* **1987**, *43*, 5725; (b) T. Brotin, J.-P. Dutasta, *Chem. Rev*. **2009**, *109*, 88; (c) G. El-Ayle, K. T. Holman, in *Comprehensive Supramolecular Chemistry II*, **2017**, 199.

[3] T. Brotin, R. Montserret, A. Bouchet, D. Cavagnat, M. Linares, T. Buffeteau, *J. Org. Chem.* **2012**, *77*, 1198.

[4] R. M. Fairchild, K. T. Holman, *J. Am. Chem. Soc.* **2005**, *127*, 16364

[5] H. A. Fogarty, P. Berthault, T. Brotin, G. Huber, H. Desvaux, J.-P. Dutasta, *J. Am. Chem. Soc.* **2007**, *129*, 10332.

[6] N. S. Khan, B. A. Riggle, G. K. Seward, Y. Bai, I. J. Dmochowski, *Bioconjugate Chem.* **2015**, *26*, 101

[7] N. J. Cookson, J. M. Fowler, D. P. Martin, J. Fisher, J. J. Henkelis, T. K. Ronson, F. L. Thorp-Greenwood, C. E. Willans, M. J. Hardie, *Supramol. Chem.* **2018**, *30*, 255.

[8] J. Canceill, L. Lacombe, A. Collet, *J. Am. Chem. Soc.* **1985**, *107*, 6993.

[9] A. Schaly, Y. Rousselin, J.-C. Chambron, E. Aubert, E. Espinosa, *Eur. J. Inorg. Chem.* **2016**, 832.

[10] C. Givelet, J. Sun, D. Xu, T. J. Emge, A. Dhokte, R. Warmuth, *Chem. Commun.* **2011**, *47*, 4511.

[11] (a) F. Ling, H.-Y. Peng, J.-X. Chen, D. T. W. Chik, Z. Cai, K. M. C. Wong, V. W. W. Yam, H. N. C. Wong, *J. Am. Chem. Soc.* **2010**, *132*, 16383; (b) J. C. Lima, L. Rodriguez, *Chem. Soc. Rev.* **2011**, *40*, 5442.

[12] L. Peyrard, S. Chierici, S. Pinet, P. Batat, G. Jonusauskas, N. Pinaud, P. Meyrand, I. Gosse, *Org. Biomol. Chem.* **2011**, *9*, 8489.

[13] G. E. Coates, C. Parkin, *J. Chem. Soc.* **1962**, 3220.

[14] (a) D. Li, X. Hong, C.-M. Che, W.-C. Lo, S.-M. Peng, *J. Chem. Soc. Dalton Trans.* **1993**, 2929; (b) V. W.-W. Yam, S. W.-K. Choi, *J. Chem. Soc., Dalton Trans.* **1996**, 4227; (c) S.-Y. Poon, W.-Y. Wong, K.-W. Cheah, J.-X. Shi, *Chem. Eur. J.* **2006**, *12*, 2550.

[15] D. J. Gordon, *Biochemistry* **1972**, *11*, 413.

[16] A. Pinto, N. Svahn, J. C. Lima, L. Rodriguez, *Dalton Trans.* **2017**, *46*, 11125.

[17] D. A. Dougherty, D. A. Stauffer, *Science* **1990**, *250*, 1558.

[18] L. Peyrard, M.-L. Dumartin, S. Chierici, S. Pinet, G. Jonusauskas, P. Meyrand, I. Gosse, *J. Org. Chem.* **2012**, *77*, 7023.

[19] L. Peyrard, S. Chierici, S. Pinet, P. Batat, G. Jonusauskas, N. Pinaud, P. Meyrande, I. Gosse, *Org. Biomol. Chem.* **2011**, *9*, 8489.

[20] B. A. Anderson, E. C. Bell, F. O. Ginah, N. K. Harn, L. M. Pagh, J. P. Wepsiec, *J. Org. Chem.* **1998**, *63*, 8224.

[21] X. N. Han, J. M. Chen, Z. T. Huang, Q. Y. Zheng, *Eur. J. Inorg. Chem.* **2012**, 6895-6903.

[22] M. D. Janssen, M. Herres, L. Zsolnai, A. L. Spek, D. M. Grove, H. Lang, G. van Koten, *Inorg. Chem.* **1996**, *35*, 2476.

[23] S. T. Mough, J. C. Goeltz, K. T. Holman, *Angew. Chem. Int. Ed.* **2004**, *43*, 5631.